OXIDATION AND MECHANICAL BEHAVIOUR OF REACTION-BONDED SILICON CARBIDE–BORON CARBIDE AND THE CORROSION OF DIP-COATED RARE-EARTH SILICATE ENVIRONMENTAL BARRIER COATINGS UNDER CMAS EXPOSURE

Thesis by

Kareem Abdelhadi

In Partial Fulfilment of the Requirements for

the degree of

PhD in Mechanical Engineering

IMPERIAL COLLEGE LONDON

London, United Kingdom

2024

STATEMENT OF ORIGINALITY

I confirm that this thesis is my original work and written in my own words. I have properly referenced the research work of other authors following Imperial College London guidelines. This includes any reuse of materials such as images and figures.

COPYRIGHT DECLARATION

The copyright of this thesis rests with the author. Unless otherwise indicated, its contents are licensed under a Creative Commons Attribution-Non Commercial 4.0 International Licence (CC BY-NC).

Under this licence, you may copy and redistribute the material in any medium or format. You may also create and distribute modified versions of the work. This is on the condition that: you credit the author and do not use it, or any derivative works, for a commercial purpose.

When reusing or sharing this work, ensure you make the licence terms clear to others by naming the licence and linking to the licence text. Where a work has been adapted, you should indicate that the work has been changed and describe those changes.

Please seek permission from the copyright holder for uses of this work that are not included in this licence or permitted under UK Copyright Law.'

ACKNOWLEDGEMENTS

I would like to thank Prof. David Nowell (supervisor), Dr. Nasrin Al Nasiri (supervisor), Prof. John Dear, and Dr. Soraia Pimenta for their great help and support. I am grateful to Naomi Jackson-Macfarlane for her guidance and support. I would like to thank Prof. Stuart Lyon (University of Manchester), who taught me a lot about research. I want to thank Prof. Amal Esawi (American University in Cairo) and Prof. Mohamed Amr Serag-Eldin (American University in Cairo), who provided continuous support and encouragement.

I would like to thank the lovely Dr. Ecaterina (Cati) Ware, Dr. Mahmoud Ardakani, Dr. Gwilherm Kerherve, Dr. William Skinner, Dr. Andrea Berenov, Dr. Suresh Chettiar, Dr. Costas Elezoglou, Mr. Antonio De Sanctis, and Mr. Andy Pullen for their great support and help. I appreciate the generous support of Mr. John Boaler, Dr. Alex Charogiannis, and Dr. Dave Hollis (LaVision UK Ltd) for facilitating the use of LaVision DaVis DIC software which was of considerable help. Thanks and appreciations to Dr. Majed Almuslmani and Dr. Dimitrios Bikos for the insightful technical discussions.

I would like to thank Prof. Hisham Massoud (Duke University), Prof. Takayuki Narushima (Tohoku University), Prof. Yuri Gogotsi (Drexel University), and special thanks to Prof. Jonathan Stebbins (Stanford University) for their fruitful discussions in the field of oxidation.

I would also like to give special thanks to Prof. Petr Ptáček (Brno University of Technology), Dr. Zhe Cheng (Florida International University), Dr. Taylor Sparks (University of Utah), Dr. Gustavo Costa (NASA Glenn Research Center), Prof. Bernardo Cesare (University of Padua), Dr. Ravisankar Naraparaju (German Aerospace Center DLR), and Dr. Robert Golden (Rolls Royce Indianapolis USA) for their fruitful discussions in the field of coatings.

I would also like to thank Harjinder (Harry) Singh and Mark Holloway, from the Mechanical Engineering store, for their patience and great help with all the lab equipment.

ABSTRACT

The oxidation of reaction-bonded SiC–B_4C (RBSBC) in air was studied at 1250–1350°C for 5–96 hours. SEM showed a 3–5 μm uniform oxide layer after 48 h. TEM, Raman, and SIMS analyses revealed that the oxidation of 7 wt% B_4C with (SiC+ Si)/B_4C ratio of ~13 produced an amorphous Si-rich borosilicate layer. Oxidation followed a parabolic rate controlled by ionic oxygen transport, and with an activation energy of 353 kJ mol^{-1}. RBSBC with 7 wt% B_4C offers a cost-effective and lower-density alternative to SiC for oxidation-resistant applications.

The CMAS corrosion of three different (RE)-based (Yb, Lu and Er) EBCs was studied at 1300 °C for 1–48 h. The EBCs were applied on the RBSBC substrate using dip coating. At the CMAS–EBC interface, Yb and Lu formed protective garnet, while Er-silicate formed non-protective stoichiometric apatite. SEM and EDS showed that Yb and Lu had lower diffusion coefficients compared to Er-silicate, indicating higher CMAS resistance. XPS revealed that the Ca–Yb–Si oxyapatite phase was formed by substitutional diffusion that is controlled by vacancy formation in the RE_2O_3 lattice. Higher Ca content in the structure suppresses vacancy formation, which decreases Ca diffusion through the coat, thereby enhancing CMAS resistance.

DIC using high-speed camera was used to study the fracture behaviour of RBSBC. RBSBC failed transgranularly, where randomly-dispersed coarse B_4C grains deflects the crack path. R-curve for the stress intensity at the crack tip K_I was determined experimentally using the displacement values at the crack tip using virtual extensometers on the DIC images, and using the LEFM SENB theory based on the fracture load and crack length. The experimental K_I has higher values than the quasistatic because it reflects the actual conditions at the crack tip. Increasing B_4C content enhances crack resistance compared to SiC ceramics.

PUBLICATIONS

- Reem Kassem, **Kareem El Shafei**, Gareth M. Jones, Christopher D. Green, Nasrin Al Nasiri, "Contactless flash sintering of dip-coated environmental barrier coatings," in the process of being submitted, 2024.

- **Kareem El Shafei**, Reem Kassem, Philip Holloway, Ashraf Nayel, John P. Dear, and David Nowell, "Fracture behaviour of reaction-bonded silicon carbide–boron carbide using digital image correlation," *Engineering Fracture Mechanics*, vol. 37, pp. 110281–110303, 2024.

- **Kareem El Shafei**, "Investigating the mechanism of formation of Ca-rich Ca–Yb apatite that forms from the Yb-silicate–CMAS reaction at 1300 °C," *Materials Characterization*, vol. 210, pp. 113777–113787, 2024.

- **Kareem El Shafei**, Reem Kassem, and Nasrin Al Nasiri, "Diffusion behaviour and corrosion rate of rare earth monosilicate-based EBCs under CMAS exposure," *Ceramics International*, vol. 49, no. 23, Part B, pp. 38544–38555, 2023.

- **Kareem El Shafei** and Nasrin Al Nasiri, "Corrosion behaviour of rare-earth monosilicates in CMAS exposure," *Corrosion Science*, vol. 202, no. 2, pp. 110312–110322, 2022.

- **Kareem El Shafei** and Nasrin Al Nasiri, "Oxidation of reaction-bonded silicon carbide-boron carbide in air," *Ceramics International*, vol. 47, no. 12, pp. 17463–17470, 2021.

TABLE OF CONTENTS

STATEMENT OF ORIGINALITY i
COPYRIGHT DECLARATION ii
ACKNOWLEDGEMENTS iii
ABSTRACT iv
PUBLICATIONS v
TABLE OF CONTENTS vi
LIST OF FIGURES ix
LIST OF TABLES xvii
NOMENCLATURE xviii
1 INTRODUCTION 1
1.1 BACKGROUND 1
1.2 PROBLEM STATEMENT 2
1.3 OBJECTIVES AND OUTLINE 3
2 LITERATURE REVIEW 5
2.1 INTRODUCTION 5
2.2 REACTION-BONDED SiC–B_4C (RBSBC) 5
2.2.1 Development of RBSBC 5
2.2.2 Manufacturing 6
2.2.3 Structure and formation 8
2.2.4 Oxidation of Si and SiC 10
2.2.5 Oxygen diffusion in silica 12
2.2.6 Effects of B_4C, Si, and Al 13
2.3 ENVIRONMENTAL BARRIER COATINGS (EBCs) 14
2.3.1 Development of EBCs 14
2.3.2 Application of EBCs 19
2.3.3 Rare-earth silicates 22
2.3.4 Particle ingestion 24
2.3.5 Thermochemical interaction 27
2.3.6 Testing for EBCs 31
2.4 DIGITAL IMAGE CORRELATION (DIC) 35
2.5 SUMMARY 39
3 EXPERIMENTAL METHODS 40
3.1 MICROSTRUCTURE AND CHARACTERIZATION TECHNIQUES 40
3.1.1 Density measurement 40
3.1.2 Weight gain measurements 41

3.1.3 Grain size measurement 41
3.1.4 Mercury intrusion porosimetry (MIP) 42
3.1.5 X-ray diffraction (XRD) 43
3.1.6 X-ray photoelectron spectroscopy (XPS) 45
3.1.7 Scanning electron microscope (SEM) 47
3.1.8 Transmission electron microscopy (TEM) 49
3.1.9 Secondary ion mass spectrometry (SIMS) 52
3.1.10 Raman spectroscopy 53
3.2 MECHANICAL AND THERMAL TESTING 54
3.2.1 Fracture toughness K_{IC} 54
3.2.2 Coefficient of thermal expansion (CTE) 56
3.2.3 Vickers microindentation hardness 58
3.2.4 Impulse excitation technique (IET) 59
3.3 SUMMARY 61
4 OXIDATION OF REACTION BONDED SILICON CARBIDE-BORON CARBIDE IN AIR 62
4.1 INTRODUCTION 62
4.1.1 Microstructure 62
4.1.2 Oxidation 63
4.2 METHODOLOGY 65
4.3 RESULTS 66
4.3.1 Properties and microstructure 66
4.3.2 Oxidation kinetics 68
4.4 DISCUSSION 75
4.4.1 Substrate microstructure 75
4.4.2 Oxide layer 76
4.5 CONCLUSION 80
5 CORROSION BEHAVIOUR OF RARE-EARTH MONOSILICATE-BASED EBCs IN CMAS EXPOSURE 81
5.1 INTRODUCTION 81
5.1.1 EBC–CMAS thermochemical interaction 82
5.1.2 EBC–CMAS diffusion and infiltration time 83
5.1.3 EBC–CMAS thermodynamics 84
5.1.4 EBC–CMAS structure 86
5.2 METHODOLOGY 87
5.2.1 Rare-earth EBCs slurry 87
5.2.2 CMAS pellets preparation 87
5.2.3 Diffusion coefficient and corrosion rate 90
5.3 RESULTS 91

5.3.1 EBC and CMAS compositions 91
5.3.2 Yb-silicate and CMAS reaction 94
5.3.3 Lu-silicate and CMAS reaction 97
5.3.4 Er-silicate and CMAS reaction 100
5.3.5 RE-silicate and CMAS microstructure 103
5.3.6 RE-silicate and CMAS reaction kinetics 108
5.3.7 RE-silicate and CMAS diffusion 110
5.3.8 RE-silicate and CMAS structure 112
5.4 DISCUSSION 118
5.4.1 Corrosion composition 118
5.4.2 Corrosion mechanism 124
5.4.3 CMAS diffusion into RE-silicate 127
5.4.4 Infiltration time and corrosion rate 132
5.4.5 Real-life conditions versus CMAS pellets 134
5.4.6 Role of defects in CMAS diffusion 135
5.5 CONCLUSION 144
6 FRACTURE BEHAVIOUR OF REACTION-BONDED SILICON CARBIDE-BORON-CARBIDE USING DIGITAL IMAGE CORRELATION 145
6.1 INTRODUCTION 145
6.1.1 Fractography of brittle materials 145
6.1.2 Crack velocity 146
6.1.3 Crack-resistance plots 147
6.2 METHODOLOGY 148
6.3 RESULTS AND DISCUSSION 153
6.3.1 Fracture behaviour 153
6.3.2 DIC analysis 157
6.3.3 Crack velocity 161
6.3.4 Crack resistance behaviour 163
6.3.5 Testing conditions of K_I and J-integral 173
6.4 CONCLUSION 178
7 CONCLUSIONS 180
8 FUTURE WORK 182
8.1 INTRODUCTION 182
8.2 DIP COATING 182
8.3 DIC ON Yb_2SiO_5–Yb_2O_3/SiC WAFERS 184
REFERENCES 186

LIST OF FIGURES

Figure 1.1 (a) GE9x engine with SiC-based components [21, 22] and (b) F-16 Fighting Falcon F100 engine exhaust nozzle with SiC–B_4C divergent seals (yellow arrows) [19]. 1

Figure 1.2 F119 Pratt & Whitney engine uses SiC/SiC CMC (coated with EBC) [23]. 1

Figure 1.3 Substrate and coating system used in the current research (not to scale). 3

Figure 2.1 Graphical representation of reaction-bonded ceramic manufacturing unit. 7

Figure 2.2 (a) Infiltration of a SiC preform [35] (b) reaction-bonded structure [31]. 7

Figure 2.3 Microstructure of reaction-bonded SiC–B_4C (RBSBC) [36]. 8

Figure 2.4 Basic process for the oxidation of silicon, and the moving interface and volume expansion during Si oxidation. Courtesy of C. Hollauer [49]. 10

Figure 2.5 (a) SiO_2 volatilisation in $H_2O_{(g)}$ [13] (b) ΔW plot of SiC in a 50% H_2O–50% O_2 environment at 1200 °C [60, 63]. 12

Figure 2.6 Kinetics of SiO_2 oxidation and volatilisation in a $H_2O_{(g)}$ environment [61]. 12

Figure 2.7 Evolution of turbine blade materials and their coatings, where the inlet turbine gas temperature is plotted against the development year. Dashed line represents Gen. 2 and 3 EBCs [79, 80]. 16

Figure 2.8 Timeline of the evolution of EBC systems for SiC ceramics. Curved arrow indicates that EBC below the dashed is the latest development in each generation. 16

Figure 2.9 (a) Mullite + YSZ on a SiC substrate [81] (b) BSAS + Mullite + Si bond coat on SiC/SiC (MI) [82] (c) Yb_2SiO_5 + mullite + Si [4] (d) Yb_2SiO_5 + SiO_2 bond coat over SiC [83] (e) Yb–Gd–Y silicate + HfO_2–Si bond coat on SiC [77] (f) 3-layer HfO_2–Yb silicate–Si [23]. 17

Figure 2.10 The five requirements for EBCs and RE-silicates. Images courtesy of [7]. 18

Figure 2.11 (a) APS $Yb_2Si_2O_7$ on a SiC/Si susbstrate [104] (b) SHVOF $Yb_2Si_2O_7$ on a Si susbstrate [108] (c) EB-PVD HfO_2 topcoat on $Yb_2Si_2O_7$ [119] (d) dip coated Yb_2SiO_5-based coating on a SiC/SiC CMC substrate [114] (e) dip coated $Yb_2Si_2O_7$ on a SiC substrate [117] (f) NASA-developed EB-PVD HfO_2 topcoat over an APS middle coat [118]. 21

Figure 2.12 (a and b) Crystal structure of RE_2SiO_5 [125] (c) RE coordination numbers for REO_6 and REO_7 polyhedrons [125]. 23

Figure 2.13 (a) Boeing C-17 Globemaster ingesting sand [129] (b) Airbus A320 dusted by Calbuco volcano [139] (c) spread of volcanic ash from Calbuco volano in Chile to across the globe [140] (d) dust storm travelling across the Middle East [129, 141]. 25

Figure 2.14 (a) Schematic of ash ingestion in the gas turbine [128] (b) ash particles melt inside the combustor [128] molten ash adheres to coating surface (c) [128] (d) dust intake through the gas turbine engine [123] (e) CMAS molten deposit on airfoils [123, 137]. 26

Figure 2.15 (a) $Ca_2RE_8(SiO_4)_6O_2$ unit cell [148] (b) apatite structure along the c-axis [123]. 28

Figure 2.16 Profile of the reaction of CMAS pellet (dark grey) with a Y_2SiO_5 EBC (light grey) over 24 h [149] 30

Figure 2.17 (a) Ion transfer from the CMAS melt to Yb_2SiO_5 [76] (b) Image obtaied after Yb_2SiO_5–CMAS reaction at 1300 °C for 24 h, showing CMAS columnar apatite grains [76]. 30

Figure 2.18 (a) Ion transfer from the CMAS melt to $Yb_2Si_2O_7$ [76] (b) Image obtained after $Yb_2Si_2O_7$–CMAS reaction at 1300 °C for 100 h, depicting equiaxed apatite grains [76]. 30

Figure 2.19 Graphic representation of the damage mechanisms stated in Figure 2.20 and Figure 2.21. 33

Figure 2.20 Graphic representation (expansion of Figure 2.19) illustrating the key failure mechanisms in EBCs. Courtesy of Lee et al. [88]. 33

Figure 2.21 Block diagram showing the testing of EBCs. Red boxes represent the topics that are examined in this study. Blue boxes indicate the topics that are investigated by colleagues in the same reseach group. 34

Figure 2.22 Three main stages of the DIC experiment [187]. 36

Figure 2.23 A schematic table showing the pixel conversion to inches in addition to speckle and subset size with relation to camera resolution. 37

Figure 2.24 Principles of displacement calculation by correlating the subset in the deformed image with the initial subset in the reference image [192]. 38

Figure 2.25 Full-field displacement using multiple subsets, and the formation of a deformation vector field [187]. 38

Figure 3.1 Schematic showing the use of lineal intercept method to calculate grain size. 41

Figure 3.2 (a) Porosimetry cup with sample inside [205] (b) mercury intrusion [207]. 43

Figure 3.3 (a) XRD operating principle [210] (b) geometrical representation of Bragg's law [211]. 44

Figure 3.4 Schematic of the RIR method used to calculate X_m 45

Figure 3.5 Schematic showing the operating principle of XPS and its main components [219]. 46

Figure 3.6 XPS spectra obtained from the electrons that are excited from their electronic orbital shells including 1s, 2s, 2p, 3s and 3p orbitals. 47

Figure 3.7 (a) SEM components [223] (b) SEM scattering modes arising from electron beam-sample interaction [223]. 48

Figure 3.8 FIB sample preparation (a) Pt deposition (b) trench milling (c) lamella undercutting (d) lamella welding. 49

Figure 3.9 TEM components [223]. The detector detects electrons that pass through the sample instead of the electrons reflecting from the sample in the case of SEM. 51

Figure 3.10 (a) Difference between SEM and TEM [223] (b) TEM electron interaction [223]. 51

Figure 3.11 (a) Operating principle of SIMS [225] (b) sputtering of a sample surface [225]. 52

Figure 3.12 Schematic of the operation of Raman spectrometry showing the main components of the Raman microscope [229]. 54

Figure 3.13 Scattering of light because of laser-sample interaction [229]. 54

Figure 3.14 Dimensions of the fracture toughness specimen. 55

Figure 3.15 (a) Lengths of the sharpened samples, measured by optical microscope (b) SEM image of the fractured surface and measurement of the average crack length. 56

Figure 3.16 Schematic of the dilatometer in a horizontal configuration [238]. 57

Figure 3.17 Correction plot demonstrating the data obtianed from the dilatometer runs. 58

Figure 3.18 (a) Microhardness indenter [241] (b) Vickers indent (red) on RBSBC. 59

Figure 3.19 Schematic of IET and FFT signal processing [243, 244]. 59

Figure 3.20 Dimensions of the CMAS pellet for the IET technique. 61

Figure 3.21 Flowchart for the experiments (green) and characterisation (orange). 61

Figure 4.1 Top view of the sample arrangement for the oxidation tests. 65

Figure 4.2 (a) SEM image of RBSBC the microstructure (b) BEC of the SiC grains. 67

Figure 4.3 (a) Raman spectra for the SiC core and rim (b) B_4C core and rim. 67

Figure 4.4 XRD peaks of RBSBC showing crystalline SiC (α and β), $B_4Si_xAl_yC$, and Al. 68

Figure 4.5 XRD for the oxidised samples at (a) 1250 °C (b) 1350 °C. 69

Figure 4.6 SEM images of the oxide layer at 1250 °C (a) 24 h (b) 48 h (c) 72 h (d) 96 h. 70

Figure 4.7 SEM images of the oxide layer at 1300 °C (a) 24 h (b) 48 h (c) 72 h (d) 96 h. 71

Figure 4.8 SEM images of the oxide layer at 1350 °C (a) 24 h (b) 48 h (c) 72 h (d) 96 h. 71

Figure 4.9 TEM of the oxidised sample at 1350 °C for 72 h with FIB location and EDS. 72

Figure 4.10 Raman spectra of the oxide layer at 1350 °C for 72 h. 73

Figure 4.11 (a) SIMS profile for the oxide layer at 1350 °C after 72 h. (b) ΔW plot. 74

Figure 4.12 2D schematic of the vitreous borosilicate glass. 77

Figure 4.13 Comparison of parabolic rate constants for the oxidation of SiC. 79

Figure 5.1 (a) CMAS pellet that is ~8 mg with φ5 mm diameter (b) CMAS pellet placed on top of Er-silicate coated sample. 88

Figure 5.2 Yb, Lu, and Er-silicate coated samples before drying for 24 h. 88

Figure 5.3 Front view of the experimental setup of the CMAS experiments. 89

Figure 5.4 Yb, Er, and Lu-silicate samples out of furnace after CMAS corrosion. 89

Figure 5.5 XRD of CMAS pellet after heat treatment showing the presence of anorthite, diopside, and akermanite. 92

Figure 5.6 XRD of Yb, Lu and Er-silicates showing the presence of RE_2O_3, RE_2SiO_5, and $RE_2Si_2O_7$. 92

Figure 5.7 (a, b) Yb-silicate (c, d) Lu-silicate (e, f) Er-silicate on RBSBC substrate. 93

Figure 5.8 CMAS–Yb-silicate at 1300 °C after (a) 1 h (b) 6 h (c) 12 h (d) 24 h and (e) 48 h (f) 48 h showing the coating morphology after CMAS reaction. 95

Figure 5.9 (a) CMAS–Yb-silicate after 48 h (b) line scan at the CMAS–Yb_2O_3 interface and (c) EDS mapping at phases 1, 2 and 3. 96

Figure 5.10 (a) CMAS attack Yb_2SiO_5–$Yb_2Si_2O_7$ bottom coat after 48 h (b) magnified image showing the formation of apatite islands within the bottom coat in addition to lateral mud cracks at the substrate-bottom coat interface. 96

Figure 5.11 CMAS–Lu-silicate at 1300 °C after (a) 1 h (b) 6 h (c) 12 h (d) 24 h (e) 48 h (f) 48 h showing the morphology of the coat after CMAS reaction. 98

Figure 5.12 (a) CMAS–Lu-silicate at 1300 °C after 48 h (b) line scan. 99

Figure 5.13 (a) CMAS attack Lu_2SiO_5–$Lu_2Si_2O_7$ bottom coat after 48 h (b) magnified image with enhanced contrast (c) formaton of apatite at the surface of the Yb_2SiO_5–$Yb_2Si_2O_7$ bottom coat (d) formaton of apatite at the surface of the Lu_2SiO_5–$Lu_2Si_2O_7$ bottom coat. The figure shows the formation of vertical and laterial mud cracks. 99

Figure 5.14 CMAS–Er-silicate at 1300 °C after (a, b) 1 h (c, d) 6 h (e) 12 h (f) 24 h (g) 48 h (h) 48 h showing the morphology of the coat after CMAS reaction. 102

Figure 5.15 (a) CMAS–Er-silicate at 1300 °C after 48 h (b) line scan for Ca, Mg, and Si (c) corrosion of the Er_2SiO_5–$Er_2Si_2O_7$ bottom coat (d) magnified image. 102

Figure 5.16 TEM line scan at 1300 °C after 48 h for (a) Yb-silicate in Figure 5.17 (b) Lu-silicate in Figure 5.18. 104

Figure 5.17 TEM image for Yb-silicate at 1300 °C after 48 h (a) FIB lamella location (b) DP locations of (c) phase 3 (d) phase 2 (e) EDS on phase 2 grain (f) EDS analysis. 105

Figure 5.18 TEM image for Lu-silicate at 1300 °C after 48 h (a) phase 2 hexagonal grains (b) DP locations of (c) phase 3 (d) phase 2 (e) EDS on phases 2 and 3 grains (f) EDS analysis. 106

Figure 5.19 TEM image for Er-silicate at 1300 °C after 48 h (a) TEM sample top view (b) hexagonal equiaxed grains (c) hexagonal finger grains (d) hexagonal wide grains (e) phase 2 finger grains (f) molten CMAS. 107

Figure 5.20 (a) Reaction layer thickness (b) ΔW plot of CMAS–EBC reaction at 1300 °C..... 109

Figure 5.21 (a) Penetration depth of CMAS interaction with Yb, Lu and Er-silicates at 1300 °C (b) ΔW plot of CMAS–Yb-silicate reaction at 1250, 1300, and 1350 °C. 109

Figure 5.22 ΔW plot of CMAS reaction between 1250, 1300, and 1350 °C for (a) Lu-silicate (b) Er-silicate..... 110

Figure 5.23 D_{FSL} of Ca in Yb, Lu and Er-silicates after CMAS corrosion between 1–48 h at 1300 °C. Inset: D_{FSL} of Ca and Si (shown as dashed lines). 111

Figure 5.24 (a) optical image showing the location of XPS scans Ca–Yb apatite (b) XPS wide scan. 115

Figure 5.25 XPS scans on phase 2 Ca–Yb apatite for (a) Silicon Si2p (b) oxygen O1s (c) Calcium Ca2p (d) Ytterbium Yb4d. 115

Figure 5.26 (a) optical image showing the location of XPS scans Ca–Lu apatite (b) XPS wide scan. 116

Figure 5.27 XPS scans on phase 2 Ca–Lu apatite for (a) Silicon Si2p (b) oxygen O1s (c) Calcium Ca2p (d) Lutetium Lu4d. 116

Figure 5.28 (a) optical image showing the location of XPS scans for Ca–Er apatite (b) XPS wide scan. 117

Figure 5.29 XPS scans on phase 2 Ca–Er apatite for (a) Silicon Si2p (b) oxygen O1s (c) Calcium Ca2p (d) Erbium Er4d. 117

Figure 5.30 Coating failure sequence due to EBC–CMAS interaction at 1300 °C. 120

Figure 5.31 Redrawn ternary phase diagram [136] for the CMAS–RE_2O_3 reaction phases..... 121

Figure 5.32 (a) IR and IP of ions and oxides involved in CMAS–EBC reaction (b) Ionic radius vs. RL thickness and normalised penetration depth at 48 h. 123

Figure 5.33 (a) Arrhenius plot for the CMAS–EBC reaction at 1250, 1300, and 1350 °C (b) E values with respect RE-element ionic radius and IP. 123

Figure 5.34 The CMAS–RE_2O_3 reaction products (a) Yb and Lu-silicates (b) Er-silicate. 126

Figure 5.35 The CMAS–RE_2O_3 rection mechanism (a) coating morphology (b) infiltration (c) dissolution (d) precipitation of the dissolved CMAS–RE_2O_3. 126

Figure 5.36 Calculated D_{DAN} of Ca in RE-silicates under CMAS environment at 24 h. 129

Figure 5.37 Calculated D_{FSL} of Ca and Si in RE-silicates under CMAS environment. 129

Figure 5.38 Diffusion of Ca^{2+} and Si^{4+} from the melt to the RE_2O_3 grains. 131

Figure 5.39 The CMAS–Yb-silicate corrosion sequence from a point defect perspective showing the kinetics of corrosion-layer formation, the mechanics of defects (courtesy of Petr Ptáček), and the equations governing the mechanics of corrosion. 141

Figure 5.40 Pictorial translation of the Kröger-Vink equations in Figure 5.39. (a) during heating (b) substitutional diffusion (c) combined processes (d) lattice legend. 142

Figure 5.41 The chemical reaction resulting in Ca-rich apatite phase. 143

Figure 6.1 The dimension of the three-point bend sample with notch size. 152

Figure 6.2 Experimental setup of the bending test with DIC configuration using Photron Nova camera. The inset images show the three-point bend test, and the speckled sample. 152

Figure 6.3 Three-point bend behaviour of RBSBC until final fracture. The image was recorded by the Photron Nova HS camera at a framing rate of 137,500 fps. 155

Figure 6.4 Loading response: (a) load-displacement plot for RBSBC (b) schematic of the crack propagation shape. 156

Figure 6.5 Fracture surface morphology: (a) widefield image of the fractured specimen (b) magnified image of the fractured surface (c) SiC transgranular crack (d) crack deflection through the $B_4Si_xAl_yC$ grains. 156

Figure 6.6 Schematic of the RBSBC morphology under tension, where Si acts as bonds between individual SiC grains according to the bond-particle model [386]. 157

Figure 6.7 Strain mapping ε_{xx} for (a) 173 f and 1.26 ms (b) 181 f and 1.32 ms (c) 231 f and 1.68 ms (d) 320 f and 2.33 ms (there are 366 frames covering the time period 0–2.66 ms - top right gives frame number and time in ms). 158

Figure 6.8 Displacement in x-direction U at the onset of crack (Δa~0.2 mm) at 173 f and 1.26 ms: (a) displacement map by DIC software DaVis (b) contour map plot. (there are 366 frames covering the time period 0–2.66 ms - top right gives frame number and time in ms). 159

Figure 6.9 (a–f) show the U displacement maps between 173–278 f (1.26–2.02 ms), where the white circle shows the extent of the crack tip. (there are 366 frames covering the time period 0–2.66 ms - top right gives frame number and time in ms). 160

Figure 6.10 Plot of the compiled U versus r for the frames shown in Figure 6.9. 161

Figure 6.11 (a) crack length versus cracking time (b) cracking velocity versus crack length. Inset pictures show the crack propagation in relative scale until fracture. 163

Figure 6.12 Schematic of obtaining experimental K_I from the change of U across r. 165

Figure 6.13 Image of the crack at 278 f (2.01 ms) showing the grid of 67 extensometers placed at 0.1 mm equidistance along the crack flanks, where ΔU was measured. 166

Figure 6.14 Plots: (a) ΔU versus r for various frame rates (b) ΔU versus f for six equidistant extensometers, where r is 0 at the top of the sample, and 6 at the notch tip. 166

Figure 6.15 Plots of experimentally-obtained (measured using virtual extensometers form the DIC images): (a) K_I versus Δa (b) J versus Δa 167

Figure 6.16 Crack extension measurement and the formation of the R-curve [399]. 169

Figure 6.17 Plots of quasistatic calculation (according to LEFM SENB) for: (a) K_I versus Δa (b) J versus Δa. 169

Figure 6.18 Schematic of the crack and its related dimensions and properties. 171

Figure 6.19 Plots of: (a) CMOD versus Δa (b) CMOD versus δ_{ext}. 171

Figure 6.20 Plots of δ versus Δa for: (a) experimental (virtual extensometer) (b) quasistatic (LEFM SENB). 171

Figure 6.21 Plots of experimental (virtual extensometer) and quasistatic (LEFM SENB) analyses for: (a) K_I versus Δa (b) the linear region for the two K_I curves. 175

Figure 6.22 Plots of experimental (virtual extensometer) and quasistatic (LEFM SENB) analyses for: (a) J versus Δa (b) the linear region for the two J curves. 175

Figure 6.23 Plots of experimental (virtual extensometer) and quasistatic (LEFM SENB) analysis for (a) δ versus Δa (b) the linear region (from the K_I and J plots) for the two δ curves. 176

Figure 6.24 Difference in values and slopes between the experimental (virtual extensometer) and the quasistatic (LEFM SENB) K_I and J for the linear region. 176

Figure 6.25 Bar chart showing the slope of R-curves for various SiC-based materials..... 178

Figure 8.1 (a) Nadetech precision dip coater (b) dashes between specification numbers above show the ND-DC 150 / ND-DC 300 / ND-DC 600 dip coaters [455]. 183

Figure 8.2 Main objectives of dip coating method to produce corrosion-resistant EBCs. 183

Figure 8.3 (a) Uncoated SiC wafer on the left, and SiC wafer coated with Yb-silicate on the right (part of the wafer broke; therefore, it is shorter) (b) Deben four-point bend stage. 185

LIST OF TABLES

Table 1.1 Outline of the thesis chapters and chapter descriptions. 3

Table 4.1 Weight gain and thickness measurements for oxide layer between 5–96 h. 72

Table 4.2 Oxidation results for SiC and SiC–B_4C materials from previous authors. 79

Table 5.1 Coatings mixture (gm) for preparing Yb, Lu, and Er-silicate coatings [25]. 87

Table 5.2 EDS analysis (at%) for reaction phases of CMAS–RE silicates at 1300 °C. 103

Table 5.3 D_{FSL} and D_{DAN} of Ca and Si in Yb, Lu and Er-silicates. 111

Table 5.4 Fitting parameters from the XPS spectra for Si2p, O1s, Ca2p and RE4d. 114

Table 5.5 D_{DAN} for CMAS–RE_2SiO_5 corrosion in air; obtained from previous authors. 130

Table 5.6 Infiltration time and CR of different EBCs and TBCs in CMAS environment. 132

Table 6.1 Si, SiC and B_4C selected properties for residual stress calculation [429, 437]..... 154

Table 6.2 The values of V, δ, K_I and J at the measured Δa and CMOD within the captured recorded time and frame rate. 172

Table 6.3 Comparing R-curve for various SiC-based materials. 177

NOMENCLATURE

Symbol	Description	Units
ΔW	Weight change before and after oxidation	mg
A	Sample surface area	mm^2
t	Oxidation time	h
k_p	Parabolic rate constant	$kg^2\ m^{-4}\ s^{-1}$
L	Oxide layer thickness	μm
T	Absolute temperature	K
E	Activation energy	$kJ\ mol^{-1}$
R	Universal gas constant	$J\ k^{-1}\ mol^{-1}$
D_{FSL}	Diffusion coefficient based on Fick's Second Law	$m^2\ s^{-1}$
D_{DAN}	Diffusion coefficient based on Dayi and Al Nasiri	$m^2\ s^{-1}$
$\mathrm{erf}\,(z)$	Gaussian error function	–
X	Penetration depth of CMAS into coat	μm
C_s	Concentration of Ca or Si at CMAS–EBC interface	wt%
C_a	Concentration of Ca or Si at EBC–substrate interface	wt%
$C_{(x,t)}$	Concentration of Ca or Si at penetration depth X and time t	wt%
t_i	Infiltration time of CMAS into the coat	min
L_c	Coating thickness	μm
τ	Tortuosity factor	–
D_c	Capillary diameter	μm
ω	Fraction of coat pores open for CMAS infiltration	–
η	Viscosity of CMAS glass	$N\ s\ m^{-2}$
σ	Surface tension	$J\ m^{-2}$
D_o	Diffusion coefficient at zero porosity	$m^2\ s^{-1}$
ΔH_f	Enthalpy of formation	$kJ\ mol^{-1}$

1 INTRODUCTION

1.1 BACKGROUND

Gas turbine engines operate by compressing incoming air and directing it into a combustor, where it is mixed with atomized fuel and ignited. The resulting high-temperature, high-speed gas is then channelled to a turbine, where the kinetic energy of the gas is converted into mechanical energy: either shaft power for applications such as gas plants and turboprop engines or thrust for turbojet engines. Technological developments of high-temperature components for combustors and turbines are among the technological challenges hindering the performance improvement of gas turbines. Additionally, in the aircraft industry, thrust-to-weight ratios of the aircraft propulsion engines and thermal efficiencies of stationary engines always need to be increased. Thus, an increase in the efficiency of gas turbine engine would result in higher combustion temperature, which would then lead to higher turbine inlet temperature (TIT). TIT is particularly important because approximately 2/3 of the turbine power is used to run the compressor [10, 11].

Nowadays, high-temperature parts are manufactured from Ni-based superalloys coated with thermal barrier coatings (TBCs) such as yttria-stabilised zirconia (YSZ). This limits the combustion temperature to 1400–1500 °C, which results in a TBC surface temperature of 1000–1100 °C and heat-resistant alloy temperature of 800 °C [12]. Thus, the need for higher gas turbine operating temperatures has led to the development of silicon carbide (SiC)-based ceramics for use in the hot sections instead of Ni-based superalloys, which have reached the upper limits of their temperature capabilities [13]. SiC-based ceramics exhibit high thermal resistances and durabilities between 1000 and 1400 °C [12, 14].

Currently, SiC-based ceramics are crucial materials for aerospace applications. The increasing demand for higher-efficiency gas turbines has resulted in the development of these ceramics. In addition to excellent resistances to oxidation and corrosion, SiC-based ceramics demonstrate lower densities and higher specific strengths than those of metals [4, 15]. They are presently employed in combustor liners, shrouds, turbine inlet nozzles, and turbine blades (Figure 1.1a). Reaction bonded SiC–B_4C (RBSBC) is a compromise between reaction-bonded SiC (RBSC) and reaction-bonded B_4C (RBBC) [16], in which both SiC and B_4C particles are combined.

Addition of B_4C particles to SiC leads to a less dense material (RBSBC) with better hardness as compared to that of RBSC [16-18] and lower cost than that of RBBC [16]. Reaction-bonded ceramics are used in applications requiring heat-resistances and low densities, for example, in gas turbines, because of their high thermal and chemical stabilities. They protect the hot section components of aircraft turbine engines from high temperatures in the combustion environments. SiC–B_4C ceramics are specifically employed in the divergent seals in military gas turbine engines (Figure 1.1b) [19, 20].

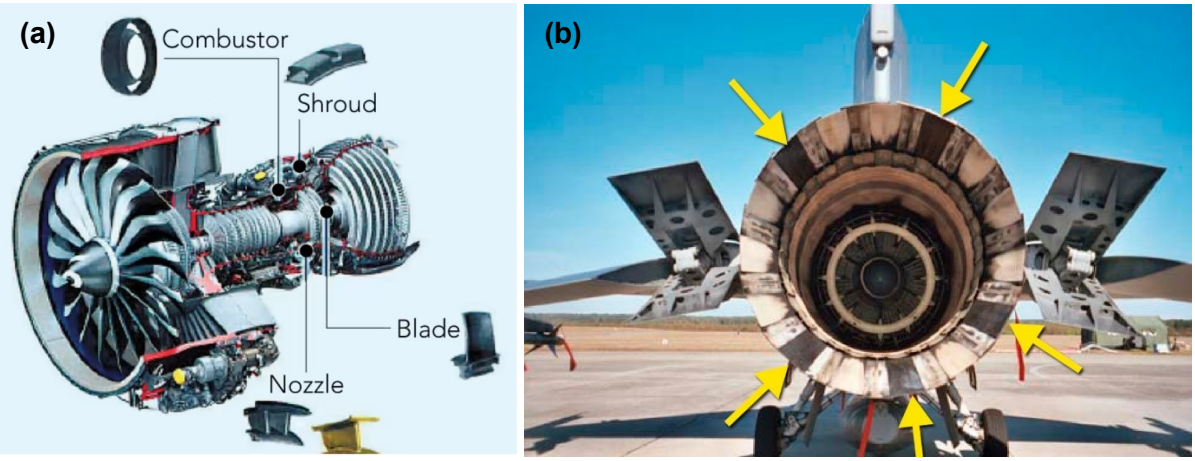


Figure 1.1 (a) GE9x engine with SiC-based components [21, 22] and (b) F-16 Fighting Falcon F100 engine exhaust nozzle with SiC–B_4C divergent seals (yellow arrows) [19].

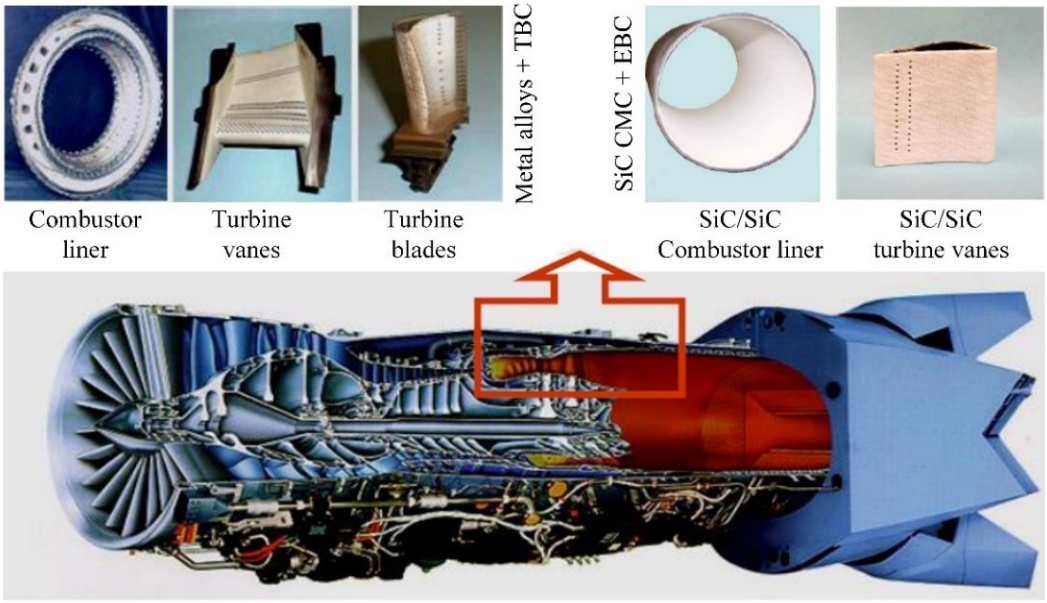


Figure 1.2 F119 Pratt & Whitney engine uses SiC/SiC CMC (coated with EBC) [23].

1.2 PROBLEM STATEMENT

As SiC corrodes in a gas turbine environment, it must be coated with environmental barrier coatings (EBCs). Moreover, the fouling and corrosion of stator turbine vanes due to inferior air quality are attributed to compressor power loss and engine efficiency reduction [11]. Thus, corrosion-resistant EBCs are essential for engine performance, particularly in demanding environments. EBCs are ceramic-based, contrary to thermal barrier coatings (TBCs) that are deposited on Ni-based superalloys. Development of SiC-based ceramics with EBCs is the next step in replacing metal alloys with TBCs in gas turbines, where high temperatures and severe corrosive areas exist. These areas include the combustor liners, turbine vanes, and blades (Figure 1.2). Silicates and oxides of rare-earth (RE) elements (that is, 15 elements from La to Lu) are among the latest generations of EBCs. RE-silicates are chosen because of their abilities to withstand temperatures above 1480 °C for thousands of hours [24], and they prove to be superior to previous coating systems in resisting water vapour corrosion and ash/salt corrosion.

The RBSBC substrate was received from M-Cubed Technologies, Inc. and designed for high-hardness and high-temperature (not exceeding 1300 °C) applications. The material was coated with patented slurry-based reaction-bonded rare-earth silicate EBCs developed by Nasiri et al., in co-operation with Rolls Royce USA [25]. The substrate/slurry method was designed for use in the stationary parts of a gas turbine hot section. Reaction between the slurry and silica oxide layer formed the RE-silicate bottom coat at the coat/substrate interface. The topcoat was a RE_2O_3 excess formed by dip coating method. This resulted in a coating architecture with two layers (Figure 1.3). As indicated by Rolls Royce, the excess topcoat is not intended to be scrapped but used as a first line of defence against environmental attack. Corrosion of the coating in a high-temperature sand environment was investigated because sand ingestion is an important industrial problem affecting the integrities of coatings.

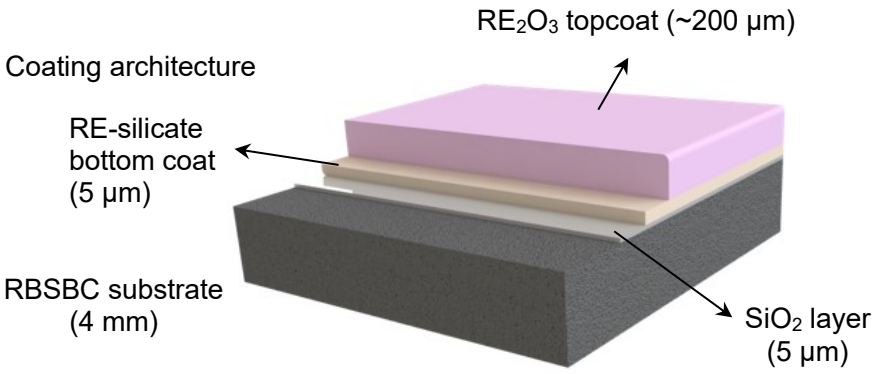


Figure 1.3 Substrate and coating system used in the current research (not to scale).

1.3 OBJECTIVES AND OUTLINE

An outline of the thesis chapters is provided in Table 1.1 below. The objectives of this study are stated in the introductions of Chapters 4, 5, and 6 ('Results and Discussion' chapters).

Table 1.1 Outline of the thesis chapters and chapter descriptions.

Ch.	Name	Description and Objectives
1	Introduction	Includes problem statement (background) on the current research, in addition to the main research objectives and thesis outline (this table).
2	Literature review	Introduces topics that are related to Chapters 4, 5, and 6 ('*Results and Discussion*' chapters). These topics comprise oxidations of SiC and RBSBC in addition to environmental barrier coatings, their developments, and corrosions of EBCs in sand environment.
3	Experimental methods	Explains the fundamentals of testing methods and characterisation techniques used for the analysis of the data presented in Chapters 4, 5, and 6. It also includes coating application and sample preparation methods.
4	Oxidation of reaction bonded silicon carbide-boron carbide in air (Results and Discussion)	Investigates the oxidation properties of RBSBC substrate and compares the formed oxide layer with those of monolithic SiC-ceramics. Assesses the potential application of RBSBC as a high-temperature substrate for EBCs.

5	Corrosion behaviour of rare-earth monosilicates in CMAS exposure (Results and Discussion)	Examines the corrosion resistances of the RE-silicate based EBCs prepared by dip coating method in a high-temperature sand environment. Provides an understanding of the corrosion mechanism, and damage morphology and determines the factors affecting the sand corrosion resistance. Develops an assessment methodology to rank the performances of EBCs in a corrosion environment. Determines the optimum RE element for use in CMAS-resistant RE-silicate EBCs.
6	Fracture behaviour of reaction bonded silicon carbide-boron carbide using digital image correlation (Results and Discussion)	Analyses the damage morphology and evaluates the crack resistance behaviour of the RBSBC substrate using a DIC setup equipped with an ultra-high-speed camera to assess the substrate behaviour under static tensile and flexural loadings.
7	Conclusions	Summarise the work performed in the current study.
8	Future Work	Proposes areas of future work for ceramic SiC-based substrates and EBCs. These areas include investigating dip coating of RE-silicate-based EBCs to produce a denser, thicker, and more corrosion-resistant coatings. Additionally, examining the mechanical responses of thin coatings using in-situ tensile beds in collaboration with a DIC setup will be a useful technique for investigating thin EBCs.

2 LITERATURE REVIEW

2.1 INTRODUCTION

Literature review in this chapter is tailored to the topics examined in this study and their background knowledge. Three main topics are analysed: reaction-bonded SiC–B_4C (RBSBC), oxidation of RBSBC, and environmental barrier coatings (EBCs). The first topic focuses on understanding the substrate used in this study. This includes properties, processing, and microstructure of RBSBC. In the second topic, oxidation properties of SiC and RBSBC are examined because oxidation is a pre-step for coating application. The third topic comprises the introduction of EBCs, including RE-silicates, followed by the corrosion of RE-silicate EBCs in a sand environment. Finally, digital image correlation (DIC) is briefly introduced.

2.2 REACTION-BONDED SiC–B_4C (RBSBC)

2.2.1 Development of RBSBC

SiC is primarily processed via chemical vapour deposition (CVD), solid-state sintering or reaction bonding. CVD SiC is produced by introducing a Si-containing gas (silane or silicon tetrachloride) and a C-containing gas (propane or methane) into the reaction chamber [26]. These gases react on the heated substrate to form a thin film of SiC, thereby generating ultra-pure SiC, which is used in optics/mirrors, semiconductors, and high-temperature electronics [26]. Sintered SiC is produced by initially mixing fine SiC powder with non-oxide sintering aids [27]. The powdered material is formed or compacted using die pressing, isostatic pressing, and injection moulding. Thereafter, the material is sintered under an inert atmosphere above 2000 °C [27]. Because of its their lower processing cost, high wear resistance, and thermal shock resistance, this material is employed in the automotive industry, armours, and for high-temperature heat exchangers. RBSC, also termed ‘reaction-sintered’ or ‘siliconised SiC’, is synthesized by infiltrating compacts composed of mixtures of SiC and C with liquid Si [28]. This reaction demonstrates the lowest cost and produces a dimensional change of < 1%; thus manufacturers possess excellent control of component tolerances [29].

2.2.2 Manufacturing

RBSBC comprises α-SiC, C or graphite, B_4C, a binder, and water, where C is added either in the form of powder or incorporated into a resin. These components are mixed in the desired ratio followed by ball-milling to obtain a slurry. Then, the slurry is dried, crushed to the required size powder, and pressed into dies. The final step leads to a green preform (Figure 2.2). This preform is called 'green' because of green-coloured α-SiC [30]. If the resin acts as a free C source, the green pre-form undergoes pyrolysis between 600 and 1000 °C, removing pure C particles [28, 31]. The preform is placed inside a furnace (Figure 2.1), where a solid Si block is put under the porous preform. The preform/Si block are placed inside an alloy container, which is encased within a retort chamber that prevents the ingress of contaminants [32]. The amount of Si used depends on the preform size and desired SiC–B_4C/Si ratio. At the furnace operating temperatures of 1400–1600 °C, the molten Si infiltrates the porous green body with no applied pressure such that infiltration occurs by capillary action (Figure 2.2a) [31]. Molten Si reacts with C particles to form β-SiC that precipitates on the original α-SiC particles and bonds with them (Figure 2.2b). Hence, the corresponding material is termed 'reaction-bonded SiC'. In the presence of B_4C, Si forms SiC–B_4C–Si compounds [28], where excess Si binds to SiC and B_4C grains, generating a matrix. Si infiltration increases the volume of the body because of the new reaction products and added Si. Therefore, certain initial amount of porosity in the green body is needed to accommodate the volume change and allow Si to infiltrate it [33]. High infiltration temperature results in lower Si viscosity, which facilitates the filling of the pores and free space in the green body by Si [34]. It also enhances the Si–C reaction. Infiltration time ranges from a few minutes to hours depending on the pre-form density, porosity, particle size, and Si viscosity [33]. Reaction-bonding demonstrates several advantages over conventional sintering. It leads to a denser product with near-zero porosity because of Si filling. It also reduces processing energy and time because conventional sintering occurs at ~2000 °C, resulting in lower production cost. It also produces complex shapes with a high precision of less than 1% volume change [28].

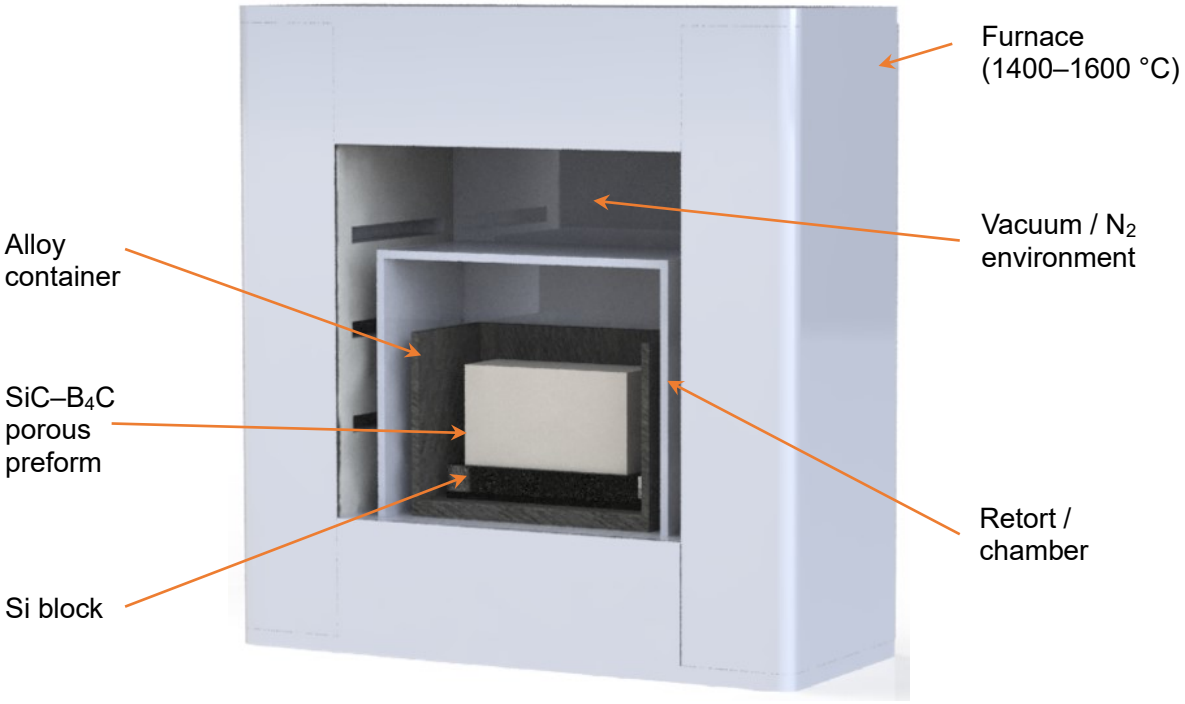


Figure 2.1 Graphical representation of reaction-bonded ceramic manufacturing unit.

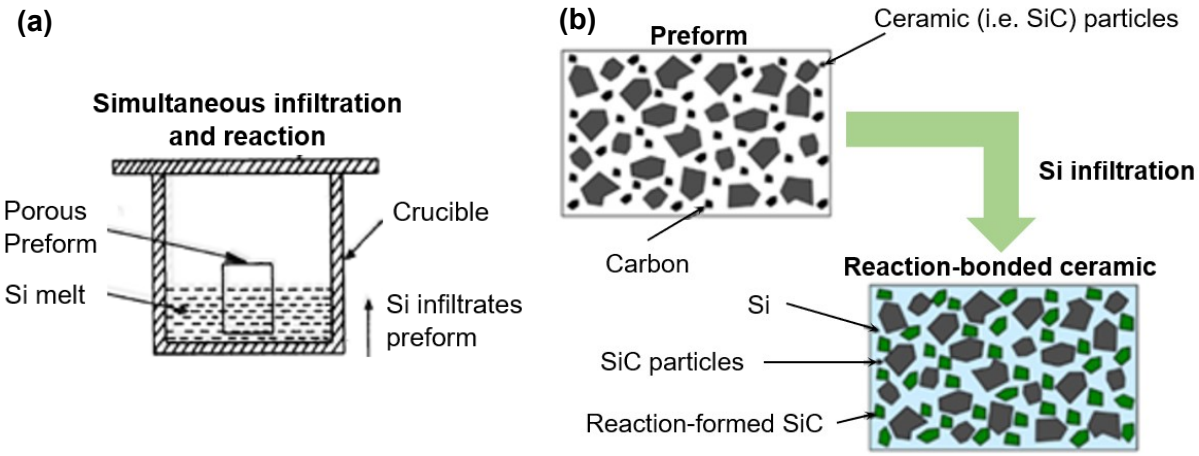


Figure 2.2 (a) Infiltration of a SiC preform [35] (b) reaction-bonded structure [31].

2.2.3 Structure and formation

Previous studies [16, 36] have reported that the microstructure of RBSBC consists of SiC, B_4C, B–C–Si ($B_xSi_yC_z$) and residual Si (Figure 2.3). It also comprises plate-like SiC inside large B_4C grains. A dissolution-precipitation model has been proposed for the reaction between Si and C [16, 30, 37]. At the beginning of infiltration, C dissolves in molten Si [Eq. (2.1)], generating heat during the process. This exothermic reaction increases the local infiltration temperature by ~400 °C [31], thereby increasing the solubility of C in Si by a factor of ten [16]. This local temperature increase also increases the diffusion coefficient of C in Si [36]. Consequently, a concentration gradient of C in Si forms between the reaction and non-reaction regions at the peripheries of the SiC grains [16]. However, Zhou et al. [38] have stated that the Si/C reaction is an electrochemical process [Eqs. (2.2) and (2.3)] that can be considered a redox reaction in which Si comes into contact with C and loses an electron because of its lower electronegativity, leading to oxidation. C is reduced to a negatively charged ion. Si and C ions react, producing a charged SiC layer around the C particles, and C particle diffusion through this layer governs the reaction kinetics.

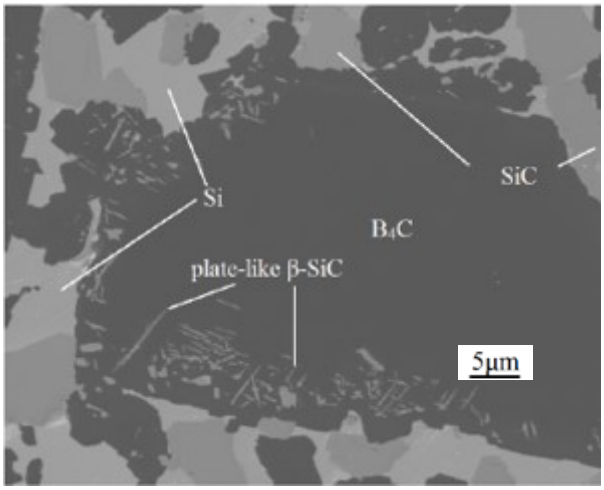


Figure 2.3 Microstructure of reaction-bonded SiC–B_4C (RBSBC) [36].

$$Si_{(l)} + C_{(graph)} \rightarrow Si/C_{(soln)} \tag{2.1}$$

$$Si \rightarrow Si^+ + e^- \ (oxidation) \mid C + e^- \rightarrow C^- \ (reduction) \tag{2.2}$$

$$Si^+ + C^- \rightarrow SiC \tag{2.3}$$

B_4C powder added to the reaction mixture serves as an alternative C source, thus reducing the amount of free Si [39]. Molten Si diffuses into the B_4C grains, where it is incorporated into the chain bonding the B_xC icosahedrons, thereby forming $B_xSi_yC_z$ [40]. B_xC prefers C over Si; this means that the amount of $B_xSi_yC_z$ generated decreases with an increase in the C content [41]. It is noted that B_4C is an acronym rather than a chemical formula because it exists over varying chemical compositions $B_{12+x}C_{3-x}$ ($0.06 < x < 1.7$) [39, 42, 43].

Increasing the amount of C in the preform results in a coarse-grained structure as C reacts more with Si, forming more SiC, which undergoes coalescence [28]. The amount of residual Si decreases with an increase in the C/Si ratio because of SiC production [44]. The amount of residual Si can be controlled by the weight % of the slurry components and packing density. This in turn depends on the element particle size and available porosity in the green body [45]. Residual Si negatively impacts the mechanical properties of the components and limits their use to 1400 °C. Concerning Al, it slows down Si/C formation, which can be advantageous for limiting SiC coalescence, thereby lowering the residual stresses in the process [28].

Regarding the effect of temperature, the solubility of Si in B_4C is low at infiltration temperatures less than 1550 °C [40]. This supresses the generation of B–C–Si [**i.e.** $B_{12}(B, C, Si)_3$] at infiltration temperatures less than 1600 °C owing to the limited C and B solubilities in Si [28, 41]. This indicates that infiltrating the preform below 1600 °C leads to lower B–C–Si content. With respect to the diffusion time, infiltrating the preform for more than 30 min supresses the formation of silicon borides SiB because there is sufficient time for the reaction to proceed towards the production of SiC and B–C–Si, as demonstrated in Eq. (2.4) [41].

$$2SiC + 3B_4C \rightarrow 2SiB_6 + 5C \tag{2.4}$$

2.2.4 Oxidation of Si and SiC

Oxidation of SiC is essentially the same as that of Si [46, 47]. Oxidation of Si has been extensively analysed, most famously by Deal and Grove [48], who derived a theoretical relationship for the calculation of oxide thickness with respect to time. Their study is also widely accepted for modelling the oxidation of SiC [48]. They conducted experiments on Si under dry air and wet conditions between 700 and 1300 °C. The main assumptions of their model are as follows: (a) oxidation proceeds by the inward movement of the oxidant O_2 rather than the outward movement of C or Si (b) O_2 completely reacts with Si on the substrate surface, forming SiO_2 (Figure 2.4). This results in the consumption of Si to form SiO_2 and recession of the initial Si surface with the loss of the newly formed oxide layer (Figure 2.4).

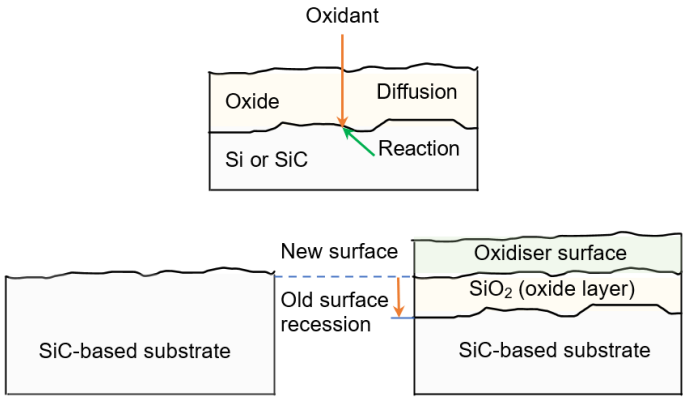


Figure 2.4 Basic process for the oxidation of silicon, and the moving interface and volume expansion during Si oxidation. Courtesy of C. Hollauer [49].

Ogbuji and Opila [47] compared their work with Deal and Grove and deduced that the mechanism controlling the oxidation rates of both Si and SiC is the permeation of O_2 through SiO_2 because these materials have the same activation energy E across the investigated temperature range. Most researchers support that O_2 transport through the oxide layer is the rate-limiting step for oxide growth on both Si and SiC, where the parabolic rate constant k_p depends on O_2 partial pressure $p(O_2)$. This results in a parabolic behavior that explains the oxide weight gain (or thickness increase) with respect to oxidation time. Putz and Hertl [50] suggested that the oxidation of SiC is controlled by CO desorption from the SiO_2/SiC interface, thereby opening more sites for further oxidation. Regardless of whether O_2 diffusion or CO desorption is the rate-limiting step, the behaviour of the resulting oxide does not change. Based

on the dependence of oxidation on O_2 concentration [O_2] and $p(O_2)$, Wagner [51] discussed the conditions for the production of volatile SiO (active oxide layer) or protective SiO_2 (passive oxide layer). At temperatures exceeding 900 °C [52] under atmospheric conditions, SiC is oxidised to form a protective silica layer, releasing gaseous CO as in Eq. (2.5). At lower $p(O_2)$ (< 1 atm), active oxidation leads to rapid weight loss by the formation of gaseous SiO instead of the protective SiO_2 because [O_2] is extremely low to form an SiO_2 protective oxide film, as shown in Eq. (2.6) [53, 54]. Subsequently, and based on this principle, Wagner [51] derived an active-to-passive transition pressure according to the supply of O_2 to the SiC surface [55].

$$2SiC_{(s)} + 3O_{2_{(g)}} \rightarrow 2SiO_{2_{(g)}} + 2CO_{(g)} \tag{2.5}$$

$$SiC_{(s)} + O_{2_{(g)}} \rightarrow SiO_{(s)} + CO_{(g)} \tag{2.6}$$

Under passive oxidation conditions, a protective SiO_2 layer will form on the ceramic substrate. However, in the presence of water vapour (major combustion product), the SiO_2 layer volatilises due to the hydrolysis of Si–O–Si bonds to form volatile Si–O–H molecules ($Si(OH)_{4(g)}$) resulting in SiC substrate recession [Eq. (2.7) and Figure 2.5a] [56, 57]. This is a function of $p(H_2O)$, where under a 4–10 bar combustor pressure, water vapor pressure is sufficient to generate $Si(OH)_{4(g)}$ leading to weight loss [57]. The recession kinetics follows a linear behaviour (Figure 2.5b) and can reach rates of 1 μm h^{-1} [4, 58, 59]. In the presence of water vapour, both behaviours simultaneously occur; parabolic silica formation and linear volatilisation (Figure 2.6). The sum of both processes results in paralinear kinetics, which eventually leads to component failure (Figure 2.5) [57, 60, 61]. It is noted that the parabolic growth rate of silica in steam in the absence of volatilisation is around one order of magnitude faster than that in dry O_2 because H_2O and OH^- molecules exhibit 10 times higher permeability in SiO_2 [61, 62]. SiO_2 volatilisation opens the way for the ingress of O_2 and water vapour (hydroxyl groups) through the substrate, allowing for further oxidation and substrate recession. It also opens the way for ionic compounds from the fuel ash and environment to form molten salts, resulting in hot corrosion. Thus, EBCs are developed to enable the protective silica layer to withstand the severity of the gas turbine environment and prolong its service life.

$$SiC_{(s)} + 2H_2O_{(g)} \rightarrow Si(OH)_{4_{(g)}} \tag{2.7}$$

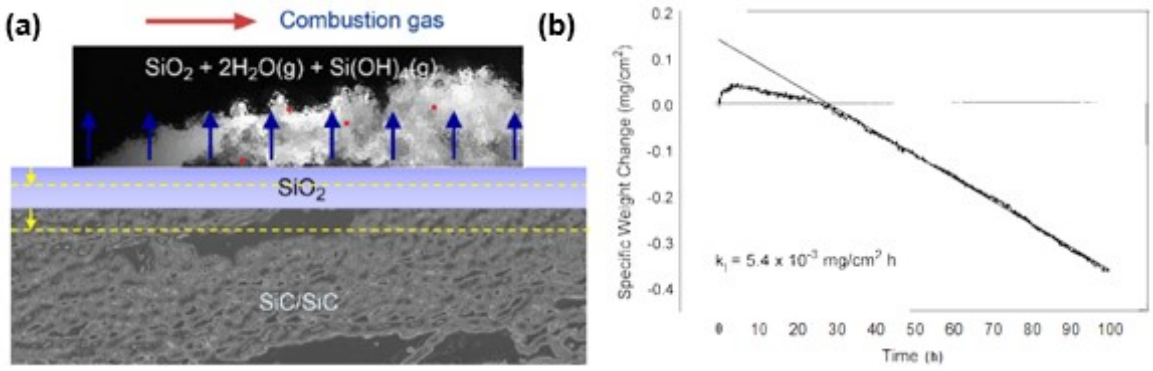


Figure 2.5 (a) SiO_2 volatilisation in $H_2O_{(g)}$ [13] (b) ΔW plot of SiC in a 50% H_2O–50% O_2 environment at 1200 °C [60, 63].

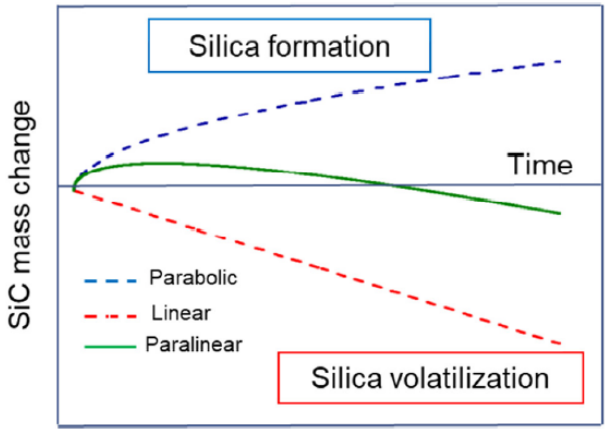


Figure 2.6 Kinetics of SiO_2 oxidation and volatilisation in a $H_2O_{(g)}$ environment [61].

2.2.5 Oxygen diffusion in silica

O_2 diffuses through silica either by the motion of molecular O_2 through voids or by the occupation of lattice vacancies in the SiO_4 tetrahedral network by ionic O (O^{2-}) [64, 65]. These two mechanisms demonstrate different temperature dependencies. At temperatures below 1300 °C, the diffusivity of molecular O_2 is significantly higher than that of O^{2-} because O^{2-} is scarce [64]. At temperatures above 1300 °C, network O^{2-} diffusion becomes dominant [64]. As the two mechanisms exhibit different temperature regimes, they demonstrate different activation energies. If O^{2-} is the dominant flux species, E of oxidation is expected to be higher because O^{2-} requires higher energy to form [64]. Understanding oxygen diffusion mechanism is important for comprehending how the oxide behaves under different [O_2] and $p(O_2)$ conditions depending on the environment, and this mechanism reflects the kinetics k_p of the oxide layer.

2.2.6 Effects of B_4C, Si, and Al

B_4C suppresses oxidation because of its low vacancy diffusion, and strong covalent bonds [41]. B_4C is oxidised to liquid boria $B_2O_{3(l)}$ at ~600 °C (~450 °C according to Wuchina et al. [66], as shown in Eq. (2.8), and evaporates at temperatures between 1200 and 1300 °C [67-69]. Boria mixes with SiO_2 to form borosilicate glass SiO_2–B_2O_3 [Eq. (2.8)] [66] or borate anions [Eqs. (2.9) and (2.10)] [67]. Borosilicate is a more effective passive layer than boria owing to its higher viscosity, which results in low O_2 diffusivity [70]. The oxidation of RBSBC is affected by the oxidation properties of SiC and B_4C. As with SiO_2, the rate-controlling step for SiO_2–B_2O_3 growth is O_2 diffusion [70]. However, the fluidity of B_2O_3 allows it to fill in the cracks, which makes B_4C useful for the self-healing properties of materials [34]. Self-healing materials can be achieved by mixing B_4C and SiC. At ~600 °C, the formation of B_2O_3 remains slow, whereas at temperatures higher than 1100 °C, the formation of less viscous Si–B–O increases its fluidity and helps seal the cracks [34, 71, 72].

$$B_4C_{(s)} + 4O_{2_{(s)}} \rightarrow 2B_2O_{3_{(l)}} + CO_{2_{(g)}} \tag{2.8}$$

$$B_4C_{(s)} + 3O_{2_{(s)}} \rightarrow 4BO_{(g)} + CO_{2_{(g)}} \tag{2.9}$$

$$B_4C_{(s)} + 5O_{2_{(s)}} \rightarrow 4BO_{(g)} + CO_{2_{(g)}} \tag{2.10}$$

The presence of residual Si in borosilicates positively impacts the oxidation of RBSC in two ways: at temperatures above 1410 °C, Si melts and provides short routes for O_2 diffusion, whereas at lower temperatures, the higher oxidation rate of Si compared to that of SiC increases the overall oxidation rate of RBSC [73]. The introduction of Al into the SiC matrix helps reduce the volatilisation of boron species at high temperatures [34]. Furthermore, SiO_2 can also react with SiC above 1250 °C, where SiO_2 reduction results in either CO bubbles at the SiC/SiO_2 interface [Eq. (2.11)], or form Si [Eq. (2.12)] [50]. This depends on the stoichiometry of the reaction; nevertheless the reaction producing CO is faster [50].

$$SiC_{(s)} + 2SiO_{2_{(s)}} \rightarrow 3SiO_{2_{(g)}} + CO_{(g)} \tag{2.11}$$

$$2SiC + SiO_2 \rightarrow 3Si + 2CO \tag{2.12}$$

2.3 ENVIRONMENTAL BARRIER COATINGS (EBCs)

2.3.1 Development of EBCs

The purpose of thermal barrier coatings (TBCs) is to protect metal-based superalloys, such as Ni and Co-based alloys, that are used in the hot section and the turbine, from high temperature combustion gases [12]. Their thicknesses are usually between 100 and 500 μm, and they consist of bond coat (**i.e.** NiCoCrAlY), thermally grown oxide as Al_2O_3, and a ceramic topcoat such as Y_2O_3-stabilized ZrO_2 (YSZ). They are also sometimes stabilised with other materials; for example, MgO, CaO and CeO_2 [74]. Nevertheless, TBCs usually fail prematurely in corrosive environments, which limits their use below their full temperature boundary [74]. Figure 2.7 shows the development of the turbine blade material + coating and turbine inlet temperature (TIT) (red lines) of each coating milestone, where SiC/EBCs are at the high end.

The need for high-temperature corrosion-resistant ceramic-based coatings for SiC-based ceramics has led to the establishment of EBCs. Major developments in EBCs can be categorised into four main generations (Figure 2.8) [7, 13]. This section only discusses the key milestones in the advancement of EBCs. Numerous other EBC compositions and architectures are available as the field of EBCs is still undergoing extensive research.

Generation I was developed in the early 1990s. Atmospheric plasma sprayed (APS) mullite ($3Al_2O_3–2SiO_2$ or $2Al_2O_3–SiO_2$) (Figure 2.9a) was used as a protective coating for SiC ceramics because its coefficient of thermal expansion (CTE) and chemical stability match those of SiC and Si-based ceramics. However, the exposure of mullite to temperatures above 1000 °C led to the crystallisation of the amorphous phases in mullite. Shrinkage accompanying crystallisation causes cracks and delamination [57, 75]. Mullite also suffers from recession in combustion environments owing to the selective volatilisation of silica in water vapour [4]. To overcome the recession of mullite, a YSZ topcoat was proposed (Figure 2.9a). Nevertheless, CTE mismatch between YSZ and SiC resulted in cracking and delamination. Generation II EBCs were developed from the mid-1990s to the early 2000, where the YSZ topcoat was replaced by barium-strontium-aluminosilicate (BSAS) $Ba_{(1-x)}Sr_xAl_2Si_2O_{10}$. CTE of BSAS is almost the same as that of SiC, and its silica activity is lower than that of mullite. Adding the BSAS second phase to the mullite bottom coat reduces the stresses and thus cracks and delamination. A further improvement was the introduction of a Si bond coat for adherence and

phase stability, forming three-layered structure Si bond coat + mullite/BSAS + BSAS topcoat (Figure 2.9b). However, BSAS demonstrated volatilisation due to SiO_2 activity in addition to BSAS–Si bond coat reaction at 1300 °C, resulting in degradation and spallation of the coating.

Based on the services of Gen. I and II EBCs, Gen. III must fulfil five main requirements (Figure 2.10), where the lifetime durability of the coat is expected to be between 5000 and 10,000 h [76] to last for thousands of take-offs and landings in commercial jets, or 30,000 h in case of industrial gas turbine engines [74]. A close CTE match between the coatings and SiC substrate, and between the layers themselves. Second, EBC must exhibit phase stability at temperatures exceeding 1300 °C. Third, they must possess low SiO_2 activity. Fourth, chemical compatibility should be present between the different layers of the coating and the environment. Fifth, the coatings must be dense (free of pores and cracks). These requirements are explained in the 'Rare-earth silicates' section.

RE-based EBCs have been constructed for these purposes as Gen. III EBCs using lanthanides (15 RE elements from La to Lu). Early Gen. III EBCs had RE-silicate topcoat above the mullite (or mullite + BSAS) middle coat and Si bond coat (Figure 2.9c). RE-silicates are either monosilicates, such as RE_2SiO_5 (one SiO_2 molecule), or disilicates $RE_2Si_2O_7$ (two SiO_2 molecules). Because of the integrity of RE-silicates at high temperatures [24], they were employed as the entire coating systems (Figure 2.9d). RE-silicates have proven to be superior to previous coating systems in resisting water vapour corrosion and ash/salt corrosion. Gen. IV EBCs comprised doped RE-silicates that increases their operating temperatures and improved their resistances to sand/dust/ash and molten salt corrosion, which are major factors in EBC design. A Hf–RE-silicate system, for example, plasma-sprayed HfO_2–RE_2O_2(silicate) exhibited high-temperature stability and improved calcium-magnesium-aluminosilicate (CMAS) resistance (Figure 2.9e–f) [77]. Another option is the multicomponent RE-silicate system such as $(Yb,Gd,Y)_2Si_{2-x}O_{7-2x}$ [77], which demonstrated excellent stability in steam tests at 1500 °C, and $(Er_{0.25}Tm_{0.25}Yb_{0.25}Lu_{0.25})_2Si_2O_7$ [78]. Both systems exhibited improved CMAS resistance. Nevertheless, the fields of Gens. III and IV EBCs are still novel.

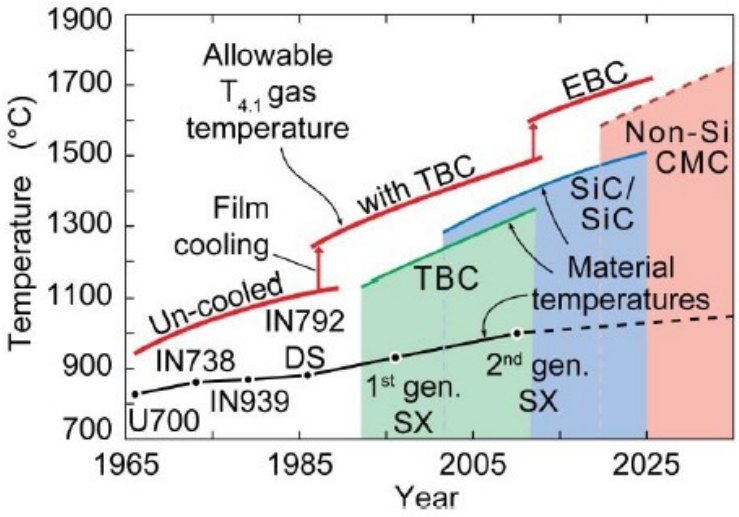


Figure 2.7 Evolution of turbine blade materials and their coatings, where the inlet turbine gas temperature is plotted against the development year. Dashed line represents Gen. 2 and 3 EBCs [79, 80].

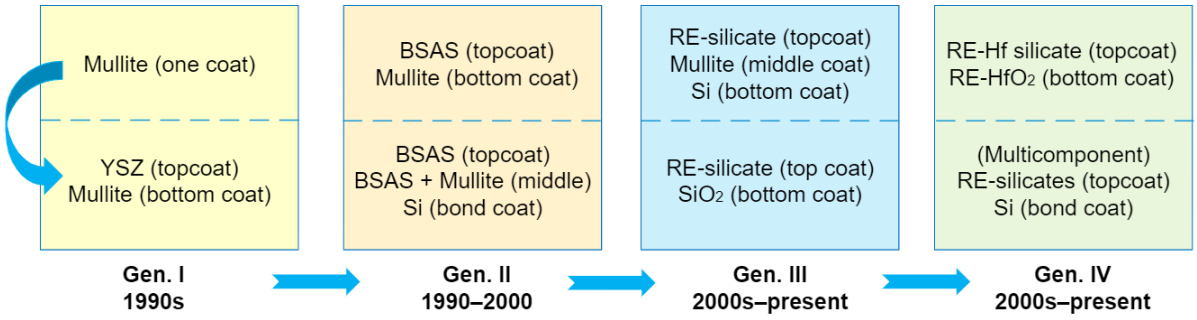


Figure 2.8 Timeline of the evolution of EBC systems for SiC ceramics. Curved arrow indicates that EBC below the dashed is the latest development in each generation.

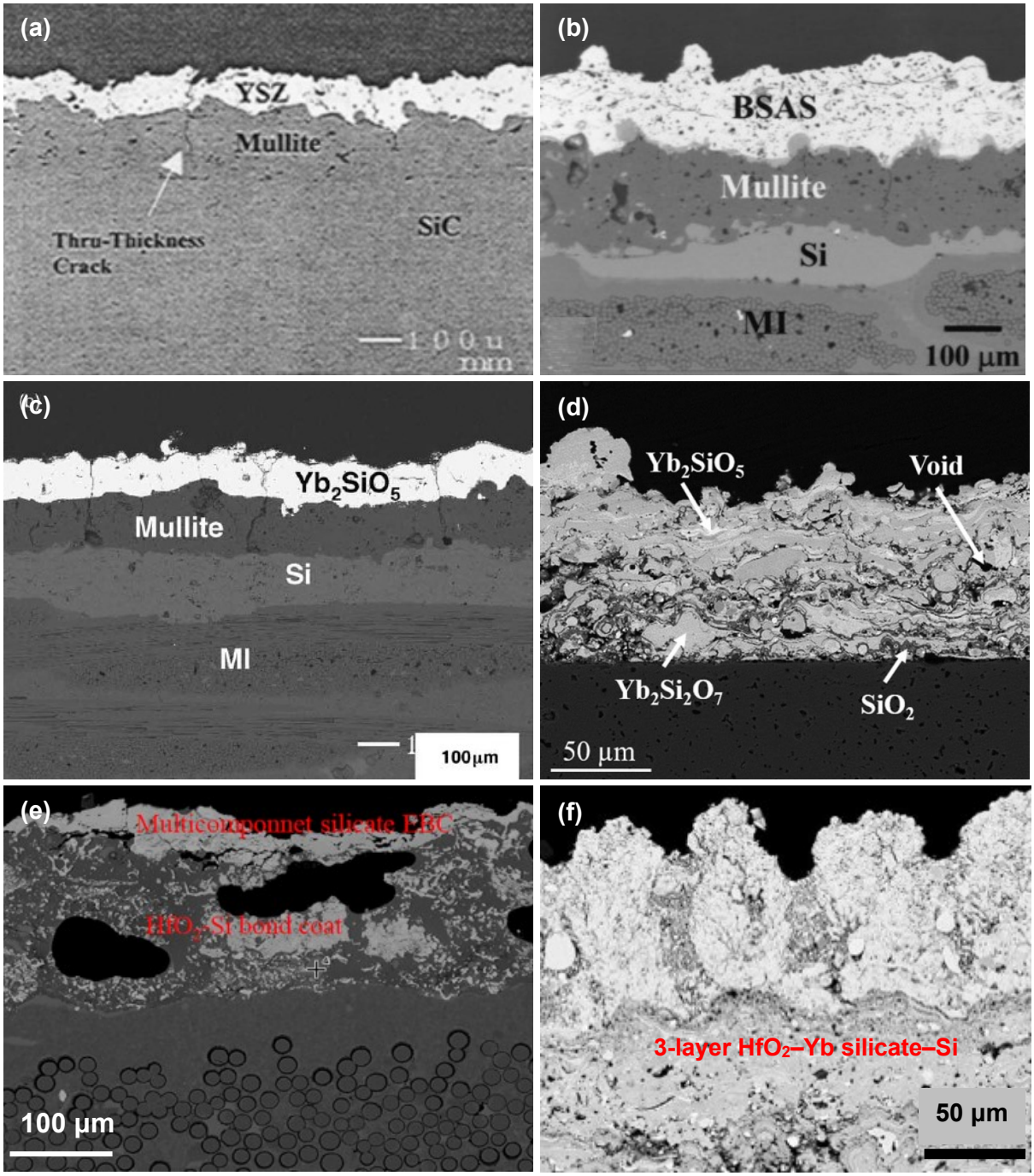
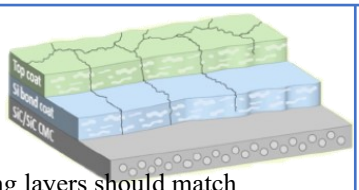


Figure 2.9 (a) Mullite + YSZ on a SiC substrate [81] (b) BSAS + Mullite + Si bond coat on SiC/SiC (MI) [82] (c) Yb_2SiO_5 + mullite + Si [4] (d) Yb_2SiO_5 + SiO_2 bond coat over SiC [83] (e) Yb–Gd–Y silicate + HfO_2–Si bond coat on SiC [77] (f) 3-layer HfO_2–Yb silicate–Si [23].

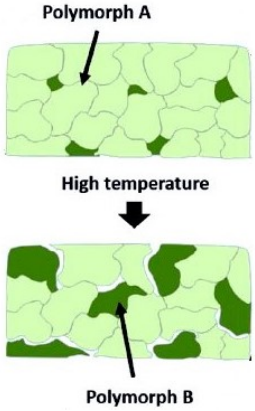
CTE match



- CTE of coating layers should match
- CTE of topcoat should match molten ash

Composition	CTE $\times 10^{-6}$ C^{-1}	T °C	Ref.
Lu_2SiO_5	6.1–7.3	1300	[3]
$Lu_2Si_2O_7$	5.2	1000	[2, 5]
Yb_2SiO_5	6.7–7.7	1300	[3]
$Yb_2Si_2O_7$	3.6–4.5	1500	[5]
Er_2SiO_5	5.4–6.4	1300	[3, 6]
$Er_2Si_2O_7$	3.9	1500	[7]
CMAS	9.8	700	[8]
RBSBC	4.8–5.2	1350	–
Si	3.5–4.5	–	[7]
SiO_2	10.3	–	[9, 10]

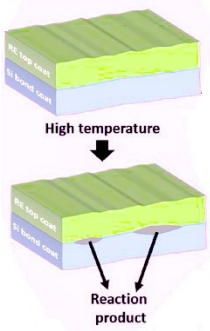
Phase stability



- Coat does not undergo phase transformation at high T
- Coat does not exhibit polymorphs
- CTE of polymorphs result in minimal volume change

Composition	Polymorphs	Ref.
RE_2SiO_5 (RE = Lu, Yb, Er)	N/A	[4]
$Lu_2Si_2O_7$	N/A	[2, 4]
$Yb_2Si_2O_7$	β, γ and δ	[4]
$Er_2Si_2O_7$	y, α, β and γ	[4]

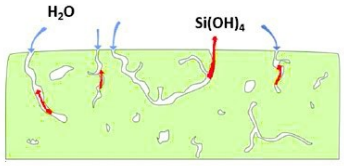
Chemical compatibility



- Coating layers should be chemically compatible
- Topcoat should resist corrosion due to combustion environment

Compatibility of RE-silicates	Ref.
- RE_2O_3, RE_2SiO_5, and $RE_2Si_2O_7$ are compatible together and with Si & SiC	
- RE-silicates are more resistant to $H_2O_{(g)}$ and ash/salt corrosion than Gen. I and II	[1, 2]

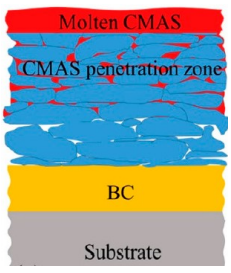
SiO_2 volatility



- Coat should have low a_{SiO_2} in dry, $H_2O_{(g)}$, molten ash/salt env. to avoid volatilization & coat recession

Volatility of RE-silicates	Ref.
- $RE_2Si_2O_7$ have high a_{SiO_2} than RE_2SiO_5	[4]
- $RE_2Si_2O_7$ decompose to RE_2SiO_5 + SiO_2 owing to selective volatilization of SiO_2	[2, 4]
- Decomposed SiO_2 can vapourize in $H_2O_{(g)}$	
- RE_2SiO_5 is less volatile than $RE_2Si_2O_7$	[4]
- Reduced a_{SiO_2} in Y_2O_3–SiO_2 system limits SiO_2 reactivity with water vapour	[1]
- Presence of RE_2O_3 reduces a_{SiO_2} (amount of $Si(OH)_{4(g)}$ released) in $H_2O_{(g)}$ environment	[2]

Permeability



- Coat should be dense
- Coat should resist O_2, OH^-, and H_2O ingress
- Topcoat should resist ash/salt penetration

- RE-silicates applied by APS, EB-PVD and dip coating
- RE-silicates are more resistant to CMAS penetration than Gen. I and II coatings

	RE_2O_3-based	RE_2SiO_5	$RE_2Si_2O_7$
CTE match (w/t RBSBC)			✓
Phase stability	✓	✓	
Chemical compatibility	✓	✓	
SiO_2 volatility	✓	✓	
Permeability			

Figure 2.10 The five requirements for EBCs and RE-silicates. Images courtesy of [7].

2.3.2 Application of EBCs

EBCs are applied using different techniques, each of which results in materials with different properties, microstructures, and defects. Therefore, they can be used in various different applications. This section presents the most common coating techniques for EBCs. Most general spraying processing techniques are categorised into thermal spray processing, colloidal processing, and vapour deposition. Thermal spray processing comprises atmospheric plasma spraying (APS) [80, 84-88], suspension plasma spraying (SPS) [86, 89, 90], and high velocity oxy-fuel coating spraying (HVOF) [84, 86]. Colloidal processing includes dip coating, whereas vapour deposition comprises chemical vapour deposition (CVD) [91, 92], electron-beam physical vapour deposition (EB-PVD) [93-97], and plasma spray PVD (PS-PVD) [59, 98-100]. Thicknesses of EBCs usually range from a few micrometers to millimetres.

APS is the most common processing technique, and it employs a high-power jet of ionised gas to melt the ceramic powder and propel molten particles to the substrate surface [101]. APS of RE-silicates on SiC ceramics forms a low-porosity homogenous structure that consists of splats (single impacted molten particles) (Figure 2.11a). High cooling rates from the plasma temperature lead to phase composition differences along the splats and the formation of thermal stresses, which induce vertical cracks [102-104]. These cracks in the topcoat lead to easy penetration of steam and O_2. The APS powder feedstock particle size is limited to 10–100 μm [105]. SPS utilises fine powders (nominal particle size less than 1 μm) dispersed in a liquid, such as alcohol, to produce a liquid feedstock that is injected into the plasma jet for melting and propulsion towards the sample [12]. This results in considerably finer molten splats, leading to denser coatings with fewer phase composition differences between splats [106]. Additionally, suspension control limits material loss during spraying [107]. HVOF uses the flame generated from the combustion of O_2 with a flammable gas to deposit a molten or semi-molten powder. HVOF produces dense coatings on SiC-based ceramics with porosities comparable to those of APS coatings and lower thermal stresses [86, 105, 108]. Suspension/solution HVOF (SHVOF) employs a liquid suspension of Yb-silicate, resulting in fewer microstructural defects, including microcracks and splat boundaries, than those in the case of APS (Figure 2.11b) [105, 108].

Vapour deposition involve vapour condensation on the substrates. CVD uses a precursor gas that chemically reacts with a base material to form a targeted coat. It is generally used to process

thin functional coatings similar to those used in the semiconductor industry. CVD is rarely used for EBCs because the induced chemical reaction results in undesired silicate phases [109]. EB-PVD is a non-line-of-sight technique that utilises an electron beam to bombard RE_2O_3 and SiO_2 ingots, in a vacuum environment, transforming them into one vapour cloud of RE-silicate. The vapour cloud is converted to a heated substrate, where the coating forms by condensate deposition. Subsequently, the coating is annealed. The EB-PVD microstructure densifies and shrinks after annealing, leading to a columnar structure with vertical gaps in between (Figure 2.11c). The advantage of this structure is that it improves the strain tolerance, which decreases thermal shock stress and results in a longer thermal life cycle [110]. However, these gaps cannot effectively impede the transfer of heat leading to high thermal conductivity [111]. Furthermore, the gaps result in inferior corrosion resistance. Nevertheless, the development of a feathery EB-PVD structure leads to a feather-like columnar structure with the ability to limit molten sand and salts through the columnar gaps by 56–72% [93-95]. PS-PVD uses a supersonic plasma jet in a very-low-pressure environment (0.5–10 Torr) at ultra-high temperatures (~5700 °C) to vaporise the injected ceramic powder followed by deposition on the substrate's surface [100, 112]. PS-PVD offers the advantage of varying the coating architecture by adjusting the processing conditions. It can produce both splat-like microstructures and columnar structures, thus bridging the gap between APS and EB-PVD, in addition to affording higher deposition rate than EB-PVD. Currently, both EB-PVD and APS are the most frequently used coatings techniques for TBCs and EBCs [74, 113].

Dip coating is a non-line-of-sight process that consists of dip coating the SiC-ceramic in a slurry of RE-silicates followed by sintering. The reaction of RE oxides with silica formed on the surface of SiC-based ceramics results in RE-monosilicate-based coatings [25, 114]. Compared to thermal spraying, fewer studies have been reported on dip coating of RE-silicates. The reported studies [114-117] indicate that dip coating produces dense microstructures (Figure 2.11d and e). However, these microstructures lead to porosities and cracks through the coatings, and with a maximum thickness of 200 μm [115, 116]. The advantages of dip coating is that it is a simple and low-cost method that allows the coatings of intricate parts that are otherwise difficult to coat with uniform thicknesses using spraying methods. Note that hybrid methods combining different coating application methods to form functionally graded EBCs have been reported (Figure 2.11f) [91, 118]. Additionally, the application of these EBCs is faster than APS and EB-PVD, and less sensitive to surface finish than those obtained using spraying techniques.

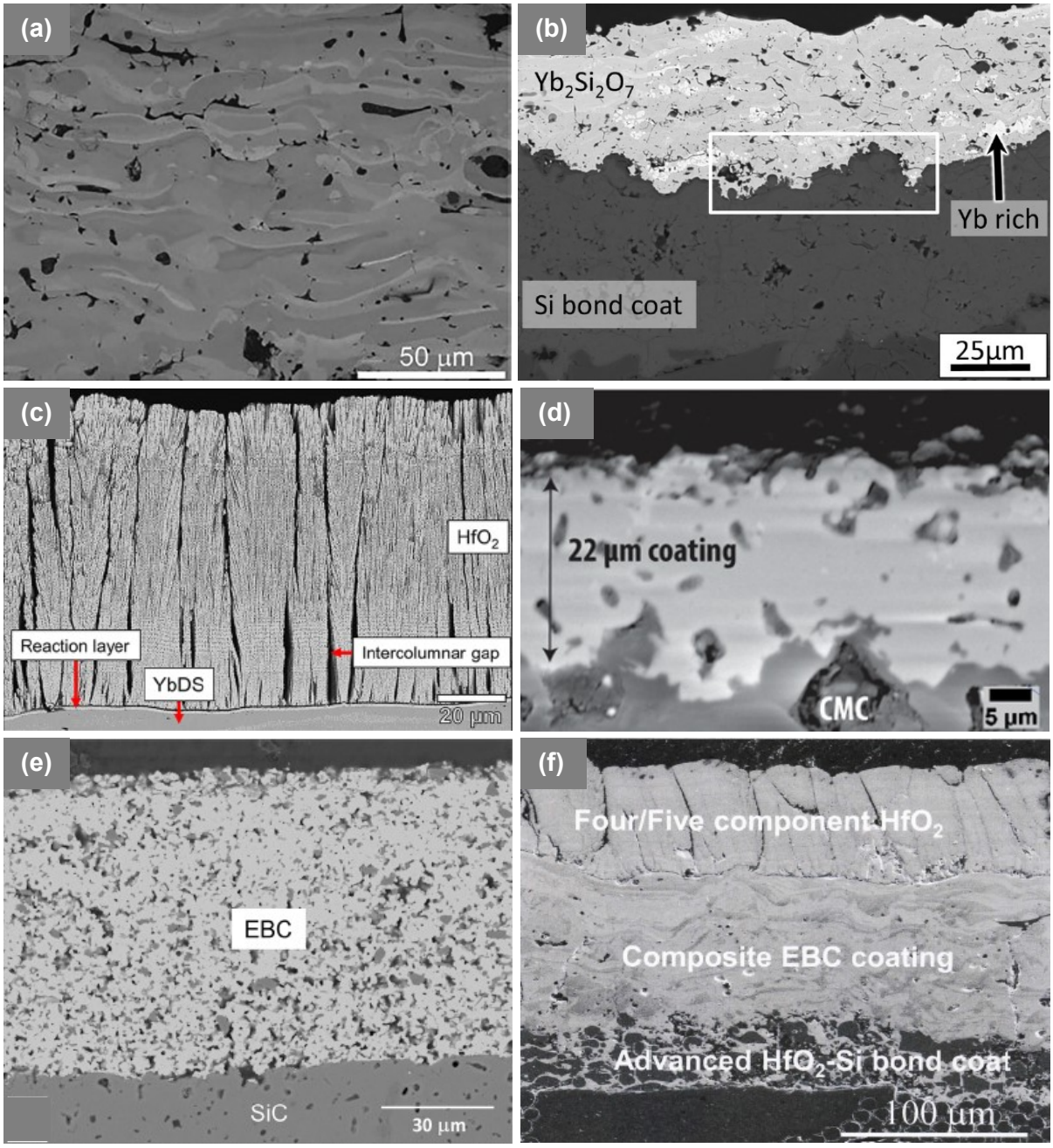


Figure 2.11 (a) APS $Yb_2Si_2O_7$ on a SiC/Si susbstrate [104] (b) SHVOF $Yb_2Si_2O_7$ on a Si susbstrate [108] (c) EB-PVD HfO_2 topcoat on $Yb_2Si_2O_7$ [119] (d) dip coated Yb_2SiO_5-based coating on a SiC/SiC CMC substrate [114] (e) dip coated $Yb_2Si_2O_7$ on a SiC substrate [117] (f) NASA-developed EB-PVD HfO_2 topcoat over an APS middle coat [118].

2.3.3 Rare-earth silicates

RE-disilicates can be formed by the direct reaction of RE oxides with silica, as presented in Eqs. (2.13) and (2.14), or through the generation of monosilicates at first, as demonstrated in Eq. (2.15) [120, 121]. RE-monosilicates and disilicates exhibit low silica activities and lower volatilisation rates as compared to those of corresponding previous generation materials [2, 13]. The higher SiO_2 content in $RE_2Si_2O_7$ results in higher silica activity than that of RE_2SiO_5. Thus, they are more prone to volatilisation and coating recession in water-vapour environments [122, 123]. This often leads to the decomposition of disilicates to monosilicates. The presence of large amounts of RE_2O_3 in the coatings further decreases a_{SiO_2} in the $H_2O_{(g)}$ environment. CTEs of disilicates are closer to those of SiC-based ceramics than those of monosilicates, which minimises thermal stresses and avoids cracking and delamination risks [124]. Among the RE-monosilicates, Sc, Lu, Yb, Tm, Er, and Dy do not exhibit polymorphs. Among RE-disilicates, only $Lu_2Si_2O_7$ demonstrates no polymorphs [4]. Materials with polymorphs of varying densities are not desirable because the coatings should not undergo any phase transformation that may cause volume changes and result in internal stresses [4]. RE-silicates and RE_2O_3 are chemically compatible with Si and SiC, facilitating their formation in several Si-based layers. Finally, RE-silicates are reactive coatings that reacts with molten salts and ash and form protective compounds that resist further salt ingress.

$$RE_2O_{3_{(s)}} + SiO_{2_{(g)}} \rightarrow RE_2SiO_{5_{(s)}} \tag{2.13}$$

$$RE_2O_{3_{(s)}} + 2SiO_{2_{(g)}} \rightarrow RE_2Si_2O_{7_{(s)}}\ or\ RE_2SiO_{5_{(s)}} + SiO_2 \tag{2.14}$$

$$RE_2SiO_{5_{(s)}} + SiO_{2_{(g)}} \leftrightarrow RE_2Si_2O_{7_{(s)}} \tag{2.15}$$

RE-monosilicates are divided into type A, from La to Tb, and type B, from Dy to Lu (including Yb and Er) [120]. Both types exhibit monoclinic structures. The coordination numbers for type-A RE cations are 7 and 9 [125], and their structures consist of isolated SiO_4 tetrahedra and RE–O polyhedra. The structures contain two RE sites: $RE_{(1)}$ and $RE_{(2)}$. $RE_{(1)}$ is coordinated to 9 O atoms, 8 of which are bonded to Si and the remaining O atom is Si-unbonded O atom. RE(2) is coordinated to 7 O atoms, 4 of which are bonded to Si and 3 are Si-unbonded O atoms [120]. Type-B, have coordination numbers of 6 and 7 [125]. They also comprise two RE sites: $RE_{(1)}$ and $RE_{(2)}$. RE(1) is coordinated to 7 O atoms, 5 of which are bonded to Si and 2 are Si-unbonded O atoms. $RE_{(2)}$ is coordinated to 6 O atoms, 4 of which are bonded to O and two are

Si-unbonded O atoms, forming an octahedron [125]. Figure 2.12 a, b and c show the structure of RE_2SiO_5, its projection along the b-axis, and the RE coordination numbers for REO_6 and REO_7 polyhedrons, respectively. Type B RE-silicates exhibit shorter atomic radii and stronger RE–O bonds.

RE elements can also be classified to light RE elements (LREEs) and heavy RE elements (HREEs) [126, 127]. LREEs include Sc, and elements ranging from La to Gd, whereas HREEs are elements ranging from Y to Lu. The definitions of LREEs and HREEs are based on the electron configuration, where LREEs possess unpaired 4*f* electrons (half-filled 4*f* electron shells), whereas HREEs contain paired electron configurations (clockwise and counter-clockwise spinning electrons) [126, 127].

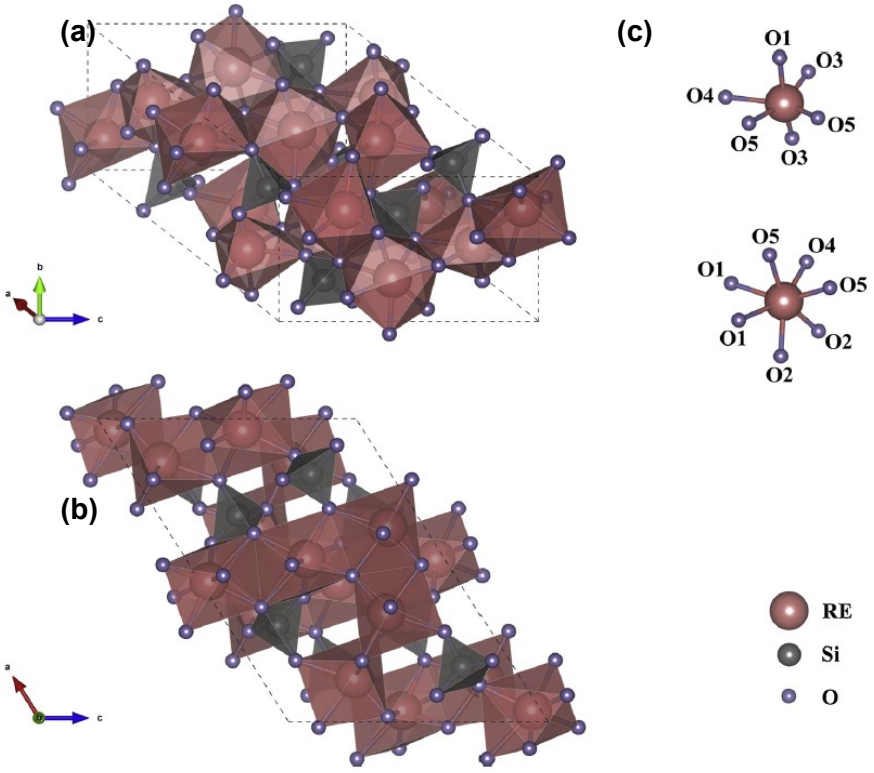


Figure 2.12 (a and b) Crystal structure of RE_2SiO_5 [125] (c) RE coordination numbers for REO_6 and REO_7 polyhedrons [125].

2.3.4 Particle ingestion

Engine damage owing to high-temperature corrosion can occur in two ways. First, hot corrosion from the fuel residues (including sulphates, such as Na_2SO_4, chlorides, such as NaCl, and vanadates, such as vanadium pentoxide V_2O_5) arising from combustion. The second way is the ingestion of particles, which is almost inevitable because the inertial particle separator is incapable of filtering-out particles less than 50 μm [128, 129]. Additionally, they can travel for thousands of kilometres (as shown in Figure 2.13c and d) and reach altitudes higher than 5500 m. Particles are either salicaceous sand particles that results from flying in desert areas or environmental ash such as volcanic ash, which are also salicaceous in nature. The earliest studies on particle ingestion investigated the damage to engines operating in the Middle East, including the study of military aircraft engines operating in the Arabian Gulf (Figure 2.14a) [130, 131] in addition to commercial liners (Figure 2.13b) [132]. This deposit-induced coating degradation has become increasingly relevant due to high engine operating temperatures and the growth of air transport within and through the Middle East and Asia [123]. Engine deposits from these regions are typically high in CaO content, with moderate amounts of Al_2O_3 and MgO. FeO, NiO and TiO_2 were detected in trace amounts, and they likely originated from the engine components. Alkali salts, such as Na_2O and K_2O, were also discovered in trace amounts, and they stemmed from fuel components. Contrarily, volcanic ash comprises a high SiO_2 content with less contribution from alkali-earth compounds such as CaO [133-135]. Understanding sand composition and type is important for assessing sand corrosion of EBCs. At high operating temperatures, siliceous oxides such as CMAS glass, with low melting points ~1200 °C, are ingested into the turbine (Figure 2.14a), where they melt in the hot section and gets propelled at high-speeds (Figure 2.14b) to deposit onto the EBCs in the hot section components in the form of sticky droplets that adheres to the surface (Figure 2.14c) [136]. Molten CMAS reacts with RE-silicates in the combustion environment and corrodes them, which affects the coating service life and leads to component failure. Figure 2.13a (inset) shows molten CMAS deposits on turbine guide vanes, and Figure 2.14d and e depicts CMAS molten deposits on Pratt & Whitney airfoils coated with 7–8% YSZ TBCs [123, 129, 137]. Siliceous oxide particles also cause abrasion of engine parts, particularly fan and compressor, and can destabilise combustion by affecting the fuel/air mixture [138]. Kueppers et al. [138] conducted a study on the compositional effects of volcanic ash and several types of ingested sands on gas turbine engines, and they noticed that glassy volcanic ash is rarer yet it is more dangerous

because it usually softens at temperatures approximately ~600 °C and melts at ~1059 °C, which is lower than the melting points of crystalline silicates [138].

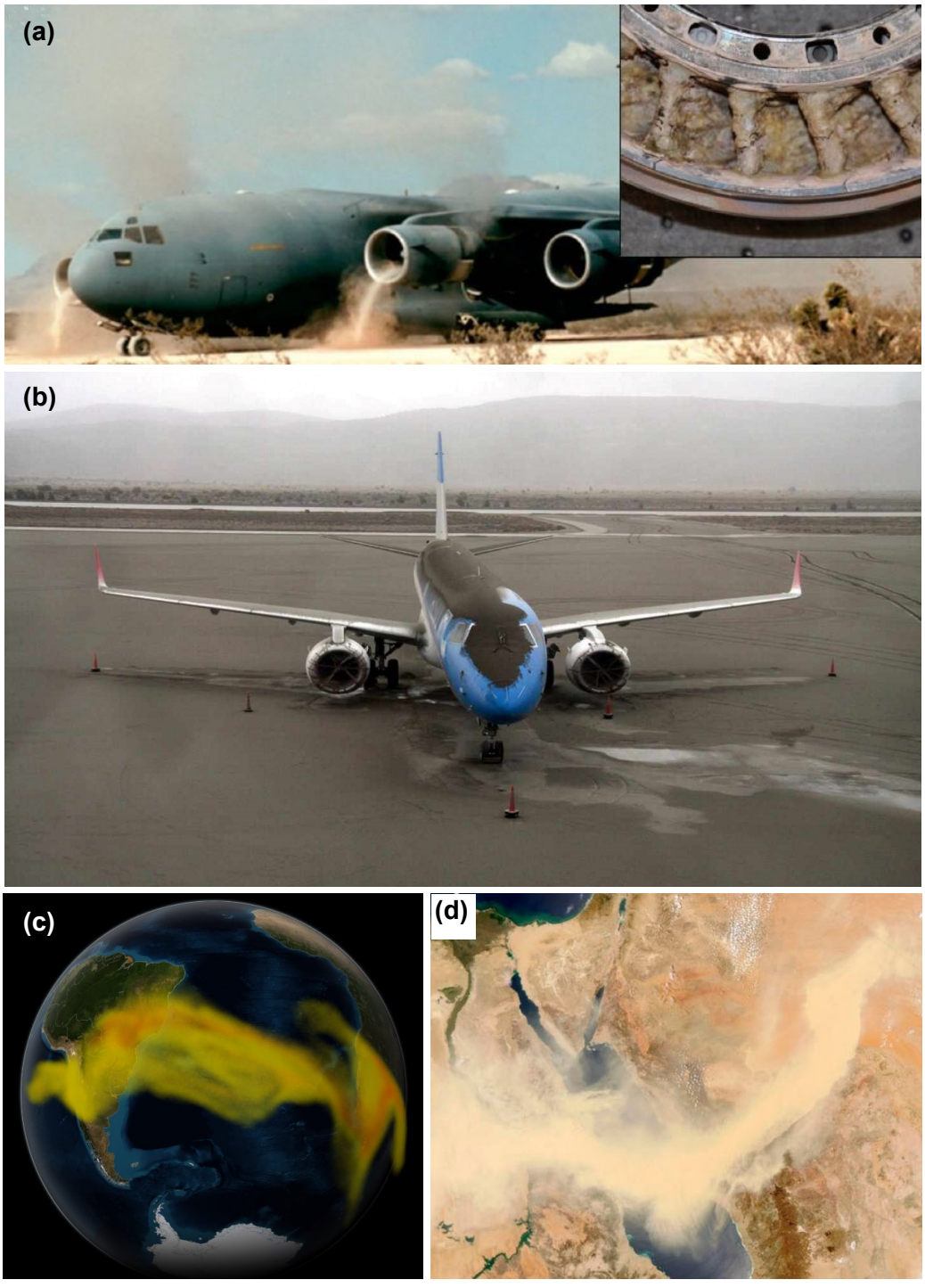


Figure 2.13 (a) Boeing C-17 Globemaster ingesting sand [129] (b) Airbus A320 dusted by Calbuco volcano [139] (c) spread of volcanic ash from Calbuco volano in Chile to across the globe [140] (d) dust storm travelling across the Middle East [129, 141].

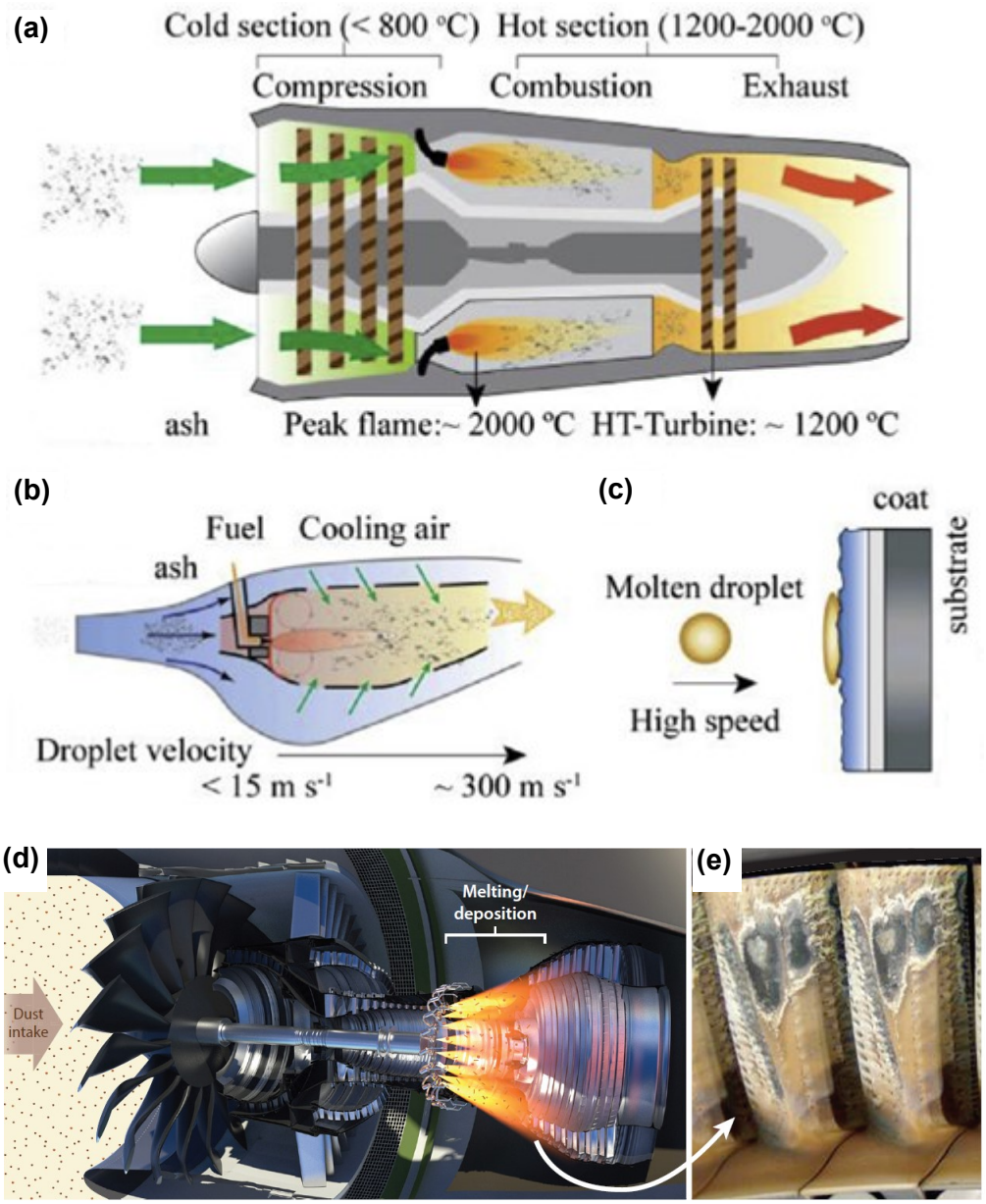


Figure 2.14 (a) Schematic of ash ingestion in the gas turbine [128] (b) ash particles melt inside the combustor [128] molten ash adheres to coating surface (c) [128] (d) dust intake through the gas turbine engine [123] (e) CMAS molten deposit on airfoils [123, 137].

2.3.5 Thermochemical interaction

This section introduces the morphology of CMAS and the mechanisms of reactions of CMAS with RE-monosilicates and RE-disilicates as an illustrative basis for the reaction of salicaceous sand with RE-silicate EBCs. This is because CMAS reaction with RE-silicates is the most deleterious and widely addressed EBC corrosion in literature. However, discrepancies exist in the literature concerning the reaction of RE-based EBCs with CMAS and volcanic ash. These discrepancies arise from numerous factors, which include, but are not limited to, the CMAS composition (desert sand or volcanic ash), coating microstructure, which is a function of the spraying method and its parameters, and the coating architecture and composition. Nevertheless, the corrosion of volcanic ash and salicaceous sands, such as CMAS, follows the same behaviour. CMAS reacts with RE-silicates [Eq. (2.16)], or the RE-apatite $RE_{9.33}(SiO_4)_6O_2$ [Eq. (2.17)], forming silica- and alkaline-earth-based RE-silicate oxyapatite (**i.e.** $Ca_2RE_8(SiO_4)_6O_2$) [142-144].

$$4RE_2Si_2O_7 + CMAS\ (2CaO) \rightarrow Ca_2RE_8(SiO_4)_6O_2 + 2SiO_2 \quad (2.16)$$

$$RE_{9.33}(SiO_4)_6O_2 + CMAS\ (2CaO) \leftrightarrow Ca_2RE_8(SiO_4)_6O_2 + 1.33RE_2O_3 \quad (2.17)$$

The general formula of apatite-type oxide is $M_{10}(XO_4)_6Z_2$, where M can be a RE or alkaline-earth element, X can include Si and P, and Z is an anionic site that can include O^{2-} and OH^- [145, 146]. The doping of RE apatite with alkaline-earth metals leads to the general formula $M^I_xM^{II}_{10-x}(XO_4)_6O_2$, where M^I is an alkaline-earth element and M^{II} is a RE element. Under CMAS corrosion, M^I_x is Ca^{2+}, which shares lattice sites with M^{II}_{10-x} (RE^{3+}) (Figure 2.15a). This results in crystalline calcium apatite that comprises SiO_4^{4-} tetrahedra surround by REO_x (RE^{3+}–O^{2-}) polyhedra, where RE^{3+} occupies two sites: $RE_{(1)}$ coordinated with seven oxygen anions and $RE_{(2)}$ coordinated with nine oxygen anions that are shared with Ca^{2+} cations [147, 148]. This is demonstrated by the apatite formula $RE_6[RE_2Ca_2](SiO_4)_6O_2$, where the cations surrounded by dashed circles correspond to the $RE_{(2)}$ sites and the remaining cations represent the $RE_{(1)}$ sites (Figure 2.15b) [147].

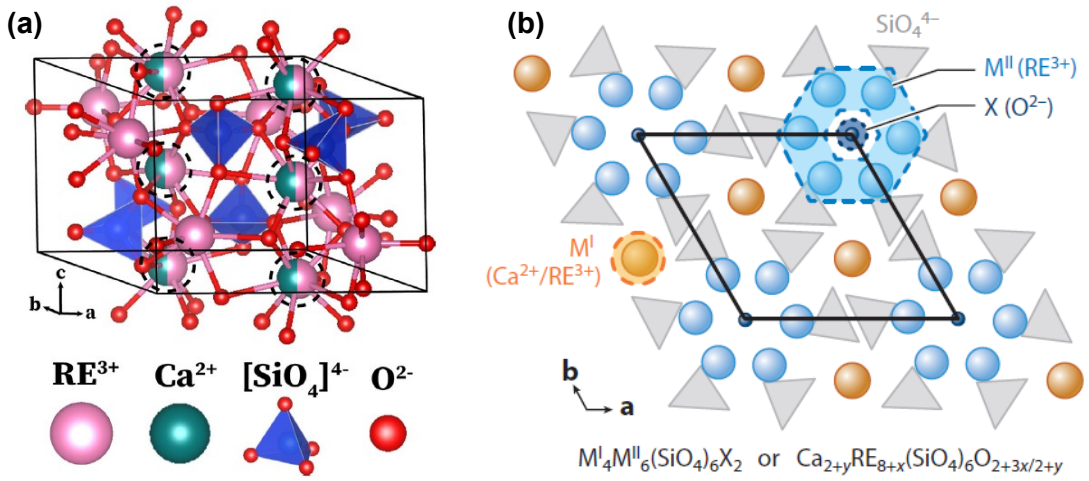


Figure 2.15 (a) $Ca_2RE_8(SiO_4)_6O_2$ unit cell [148] (b) apatite structure along the c-axis [123].

Previous researchers [58, 76, 136, 147, 149-156] have examined the corrosion of RE-monosilicates and RE-disilicates in a CMAS environment. They have observed that apatite forms by the diffusion of Ca, Mg, and SiO_2 from the CMAS melt into the reaction front at the Y_2SiO_5–CMAS interface, coupled with the outwards diffusion of RE ions into the CMAS melt (Figure 2.17a and Figure 2.18a). This leads to coating recession by the CMAS melt, whereby Si and Ca diffuse to the grain boundaries either between the columnar apatite grains (Figure 2.17b) or between the channels and through the grain boundaries in $RE_2Si_2O_7$ (Figure 2.18b). The reaction of Si and Ca with the coating results in the recession of the coating at the expense of the newly formed apatite layer.

Apatite can form columnar (Figure 2.17b) or equiaxed grains (Figure 2.18b) that are interpenetrated by an amorphous CMAS-based melt, which is the primary gate regulating the diffusions of Ca and Si through the apatite grains. The presence of molten CMAS glass between apatite grains allows the continuous transport of cations and anions to the reaction front, which results in the coarsening of apatite crystals over time until they fuse together (Figure 2.17b). The continuous diffusion of the melt also increases the proportion of the amorphous phase and substantially widens the gaps between apatite grains. The growth of columnar protruded apatite is usually based on the previously formed dense apatite, as shown by the white square in Figure 2.17b. This morphology is explained by the diffusion of ionic species through the narrow tunnels and intergranular paths of RE-silicates, where they form new apatite grains that are forced to grow vertically through these tunnels.

The final composition of apatite formed from the reaction of RE_2SiO_5 with CMAS melt [Eq. (2.18), where O_2 is omitted from the equations] consumes more SiO_2 from the melt than that in the case of $RE_2Si_2O_7$ [Eq. (2.19)] because of the higher SiO_2 activity in $RE_2Si_2O_7$ (the SiO_2 contents in disilicates are two-fold those in monosilicates). Thus, the reaction of CMAS with $RE_2Si_2O_7$ to form apatite products can proceed without the contribution of Si from the melt, as shown in Eq. (2.19). This indicates that more disilicate moles are required to produce the same amount of apatite produced by monosilicates. This results in higher disilicate recession [76, 136, 149]. Some authors, including Zhao et al. [76], have discovered that the apatite formed by the $Yb_2Si_2O_7$–CMAS interaction is less columnar and more equiaxed than that formed by the Yb_2SiO_5–CMAS interaction because of more CMAS consumption with $RE_2Si_2O_7$ (Figure 2.18a–b). This, supported by the fact that RE-monosilicates are less volatile in harsh environments because of their low silica activity [4, 150, 157], implies that RE_2SiO_5 provides higher resistance to CMAS corrosion. In contrast, some researchers, such as Stolzenburg et al. [150], have reported a slower reaction of CMAS with $Yb_2Si_2O_7$ than that with Yb_2SiO_5 by one order of magnitude, which was attributed to the lower Yb_2O_3 activity in disilicates, which stem from their lower Yb_2O_3/Si_2O ratio.

$$6Ca_{0.33}Mg_{0.09}Al_{0.13}Si_{0.45} + 4Yb_2Si \rightarrow Ca_2Yb_8Si_6 + 2[Mg_{0.26}Al_{0.39}Si_{0.35}] \quad (2.18)$$

$$6Ca_{0.33}Mg_{0.09}Al_{0.13}Si_{0.45} + 4Yb_2Si_2 \rightarrow Ca_2Yb_8Si_6 + 6[Mg_{0.09}Al_{0.13}Si_{0.78}] \quad (2.19)$$

$$13.3Ca_{0.33}Mg_{0.09}Al_{0.13}Si_{0.45} + 8Yb \rightarrow Ca_2Yb_8Si_6 + 5.33[Ca_{0.45}Mg_{0.23}Al_{0.32}] \quad (2.20)$$

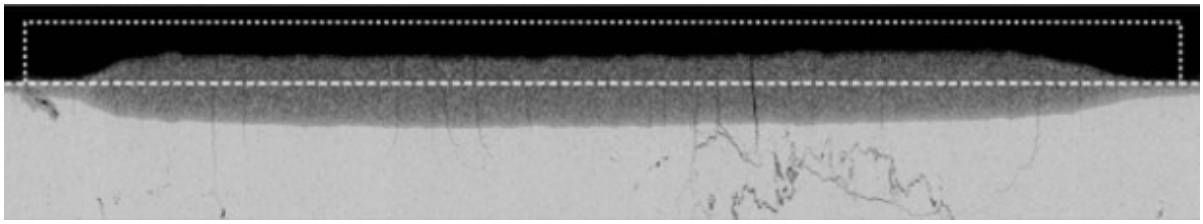


Figure 2.16 Profile of the reaction of CMAS pellet (dark grey) with a Y_2SiO_5 EBC (light grey) over 24 h [149]

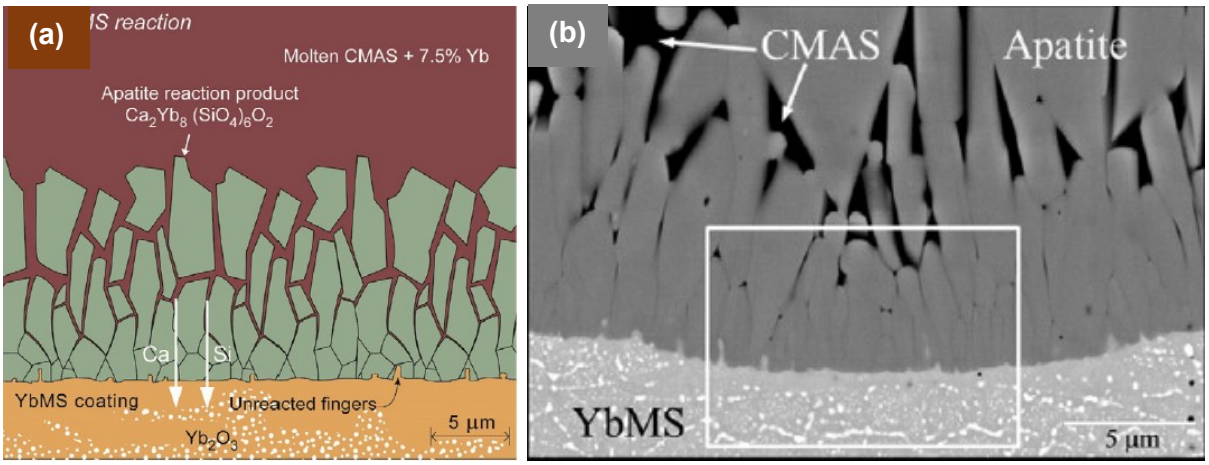


Figure 2.17 (a) Ion transfer from the CMAS melt to Yb_2SiO_5 [76] (b) Image obtaied after Yb_2SiO_5–CMAS reaction at 1300 °C for 24 h, showing CMAS columnar apatite grains [76].

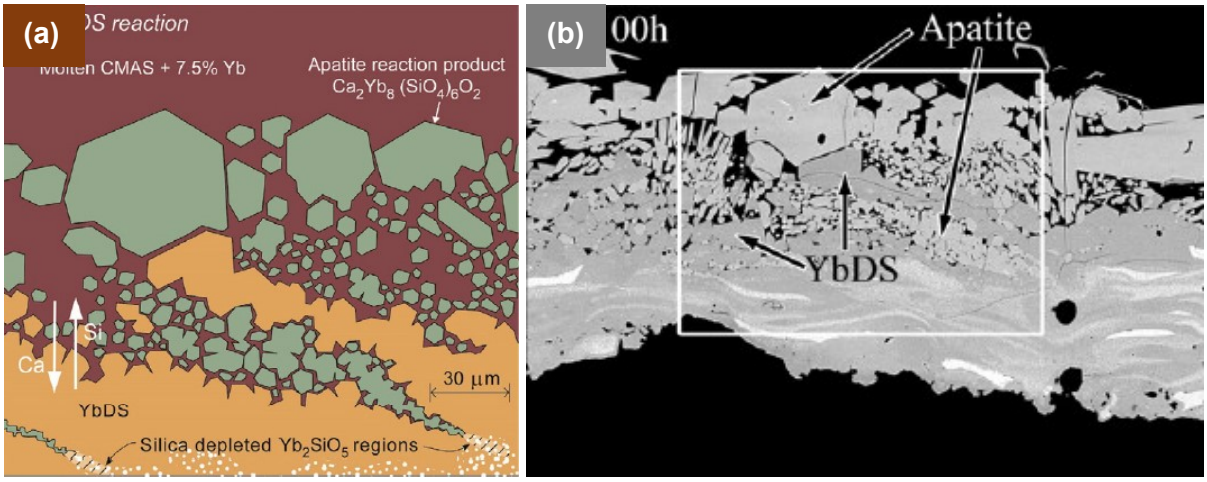


Figure 2.18 (a) Ion transfer from the CMAS melt to $Yb_2Si_2O_7$ [76] (b) Image obtained after $Yb_2Si_2O_7$–CMAS reaction at 1300 °C for 100 h, depicting equiaxed apatite grains [76].

2.3.6 Testing for EBCs

EBCs are initially processed using a certain system design, coating chemistry, and application technique that are expected to best fulfil the five main requirements shown in Figure 2.10. The CMAS–EBC corrosion tests of EBCs are analogous to the crucible tests of refractory materials, where molten CMAS corrosion of ceramic-based coatings can be compared to molten slag corrosion of ceramic-based refractories. Engineering tests are either thermochemical or thermomechanical (Figure 2.19 and Figure 2.21). Figure 2.19 depicts a graphical representation of the primary damage mechanisms explained in Figure 2.21, where (Comb.) is the chemical damage caused by the combustion environment and (Ext.) is the chemical damage induced by external factors.

Thermochemical testing includes humidity, water vapour, and corrosion testing. Humidity reflects the shutdown conditions, where water droplets collect on the coating surface and react with silica in the coating, forming $Si(OH)_{4(g)}$. This leads to the consumption of silica from EBC and its recession [158, 159]. Humidity tests are performed by placing the coatings in a beaker filled with water, where the coatings are exposed to water for prolonged periods at ~65 °C [56]. Water vapour, product of combustion environment, also lead to silica volatility in EBCs, in which SiO_2 volatility depends on various parameters, such as silica activity in EBC, gas velocity, the water vapour partial pressure, and the total pressure [60]. The volatility of various RE-silicates is determined using thermogravimetric analysis (TGA) [4, 88]. Steam tests can be conducted in a tube furnace [160] or in high steam test rigs [158, 159]. In these tests, O_2 partial pressure can also be adjusted to simulate several conditions. Corrosion testing evaluates the coating performance in the presence of fuel ash (hot corrosion), salts, and salicaceous dust particles (CMAS and volcanic ash). Corrosion testing is usually performed in a laboratory furnace using CMAS pellets or in burner rigs to simulate the actual operating environment [161-173]. The burner rig consists of a simulated combustion chamber in which jet fuel and air/O_2 are mixed to produce a high-temperature exhaust that is directed towards the sample. A disperser is typically used to disperse the ash between the sample and flame and control the particle size, distribution, and concentration of the dispersed ash. Because burner rigs are expensive and exhausting to build and operate, a microturbine [174, 175] or jet flame [176] can be employed as a middle ground between laboratory furnaces and burner rigs. The microturbine uses a jet turbine similar to those utilised in radio-controlled jet planes to direct

the exhaust towards the sample, whereas the flame jet is simpler and more common in academic laboratories; flame jet from a flame torch is directed towards the sample. Salicaceous particles are either placed on the sample before being exposed to the flame or dropped between the flame and sample surface. Microturbines are rare because most research groups prefer the safer and cheaper option of using a static furnace. In the cases of burner rigs and microturbines, jet fuel is used resulting in a complex corrosion setting because the actual combustion environment is a mixture of ash, water vapour, and fuel residues.

Mechanical testing is employed to analyse coating failure due to mechanical damage. The factors causing mechanical damage include residual stresses, stresses owing to thermal expansion mismatch, erosion from foreign objects and internal debris, and fracture mechanics as crack resistance behaviour and fitness for service, which induce delamination and cracking in the coating system. Thermal expansion mismatch is unavoidable and is usually the result of thermochemical interactions of the coating. It can also arise from phase instability owing to corrosion, which can be accompanied by volumetric shrinkage or expansion. The stresses in the coating can be calculated using LayerSlayer [79, 102, 177] or FEA [178-182]. Solid particle erosion occurs because of the ingestion of foreign particles, including ash, sand and debris, at speeds that can reach 300 m s^{-1}, and they particularly affect the fan and compressor blades. This results in mechanical damage indentation, impact damage, and possibly erosion-corrosion, in which the mechanical damage can tear away the coating surface and enhance corrosion, considerably impacting the lifetime of the coating and substrate. Erosion can be estimated by numerical methods [183] or tested using burner rigs or specially-manufactured erosion rigs [184, 185]. Testing for the fracture behaviour of the coating comprises conventional mechanical testing, for example, in-situ and ex-situ flexural bending, high-temperature fatigue test rigs, environmental fatigue test rigs to investigate the corrosion fatigue phenomenon, and high temperature fatigue to evaluate thermomechanical fatigue resistance [186]. Damage to EBCs is usually a complex process involving a multitude of mechanisms that can be thermochemical and/or thermomechanical in nature.

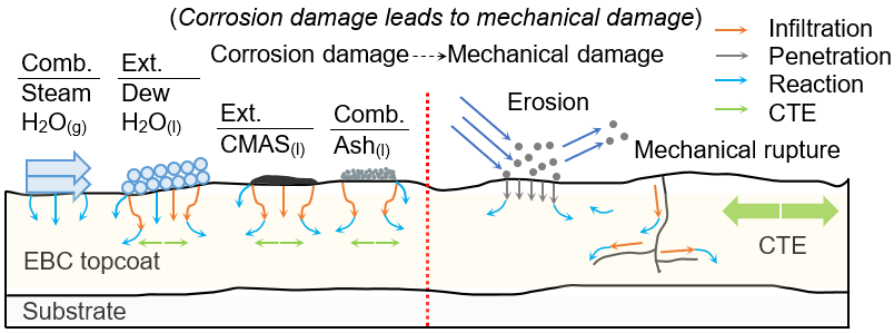


Figure 2.19 Graphic representation of the damage mechanisms stated in Figure 2.20 and Figure 2.21.

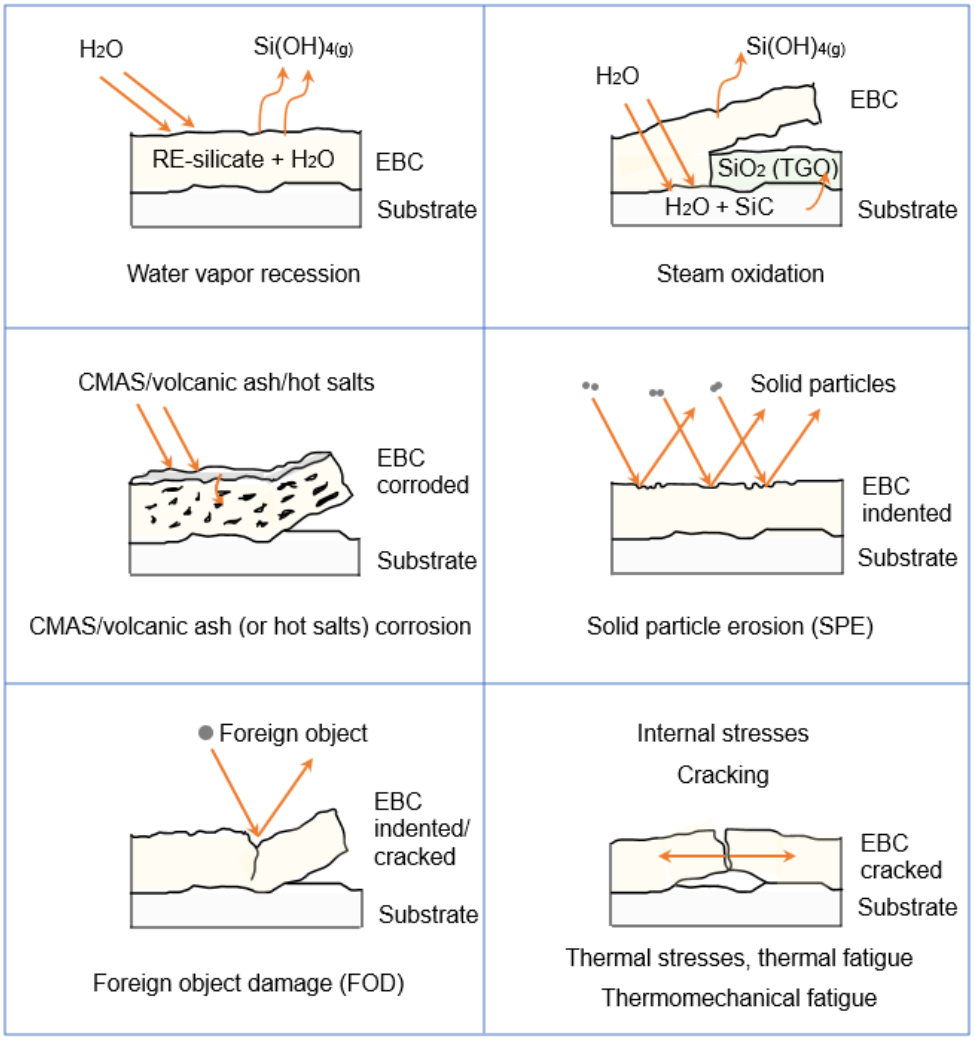


Figure 2.20 Graphic representation (expansion of Figure 2.19) illustrating the key failure mechanisms in EBCs. Courtesy of Lee et al. [88].

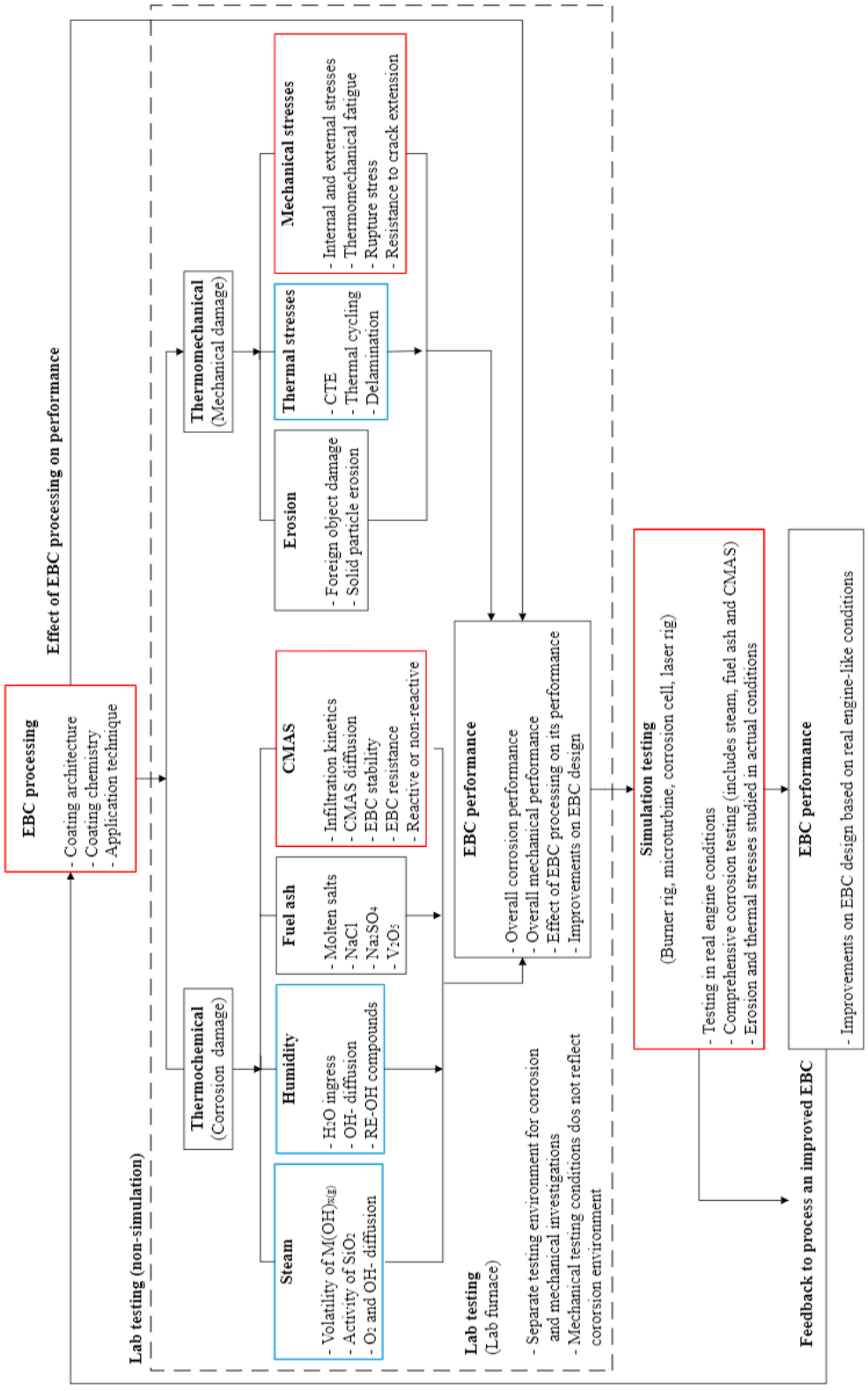


Figure 2.21 Block diagram showing the testing of EBCs. Red boxes represent the topics that are examined in this study. Blue boxes indicate the topics that are investigated by colleagues in the same reseach group.

2.4 DIGITAL IMAGE CORRELATION (DIC)

There are numerous methods to quantify the deformation of a material when a force is applied to it such as strain gauges, extensometers (mechanical, optical, and laser), linear variable differential transformers (LVDT), and DIC. The advantage of DIC over other methods is that it can provide displacement measurements across any point on the material as opposed to strain gauges and extensometers, which offer a single measurement per test. Additionally, DIC can determine local deformations caused by inhomogeneity, cracking, or stress concentrations across the material.

Digital image processing techniques are based on obtaining information by imaging a specific feature or area over a certain time frame and comparing the images. As such, DIC can evalate the full-field strain data and surface displacements of a material based on a series of images acquired using either one or two cameras. One camera obtains two-dimensional information because it does not possess the perspective for out-of-plane motion. Thus, the specimen should be flat, planar to the camera sensor, and at a constant distance from the camera to avoid errors in strain measurements, because if the specimen moves towards the sensor, it will appear larger in the image and lead to tensile strain bias in the data and vice versa. A three-dimensional DIC (also called digital volume correlation) uses a second camera to acquire perception such as having two eyes, which facilitates how an object moves out of plane.

DIC operates by tracking points across a series of images obtained over successive time frames. Therefore, a speckle pattern must be applied to the surface. The DIC experiment (Figure 2.22) can be divided into three main steps: (1) forming a speckled pattern on the tracked sample, (2) obtaining images during deformation, and (3) analysing the sample displacement data.

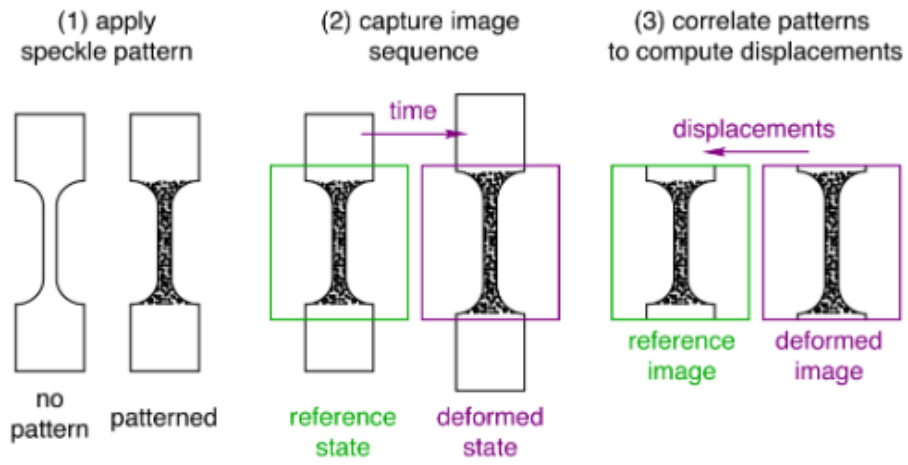


Figure 2.22 Three main stages of the DIC experiment [187].

The speckle pattern (Figure 2.25a) provides features and markers to track points across the sample surface. For the speckle pattern to be effective, it must deform with the specimen and resist testing conditions such as temperature and moisture. The pattern characteristic itself must be visible with a high contrast opposite to the specimen surface (**i.e.** black speckle on a white surface), 50% coverage with an approximately equal amount of black and white regions, consistent speckle size (3–5 pixels), and finally random speckle distribution that does not form a specific pattern [188]. Speckle patterns can be applied using different methods including spraying, printing, stamping, and manual application using a permanent marker [188]. DIC matches the speckle pattern of a deformed image with that of a reference or baseline image. The reference image is the initial undeformed image, and it has a number of speckled dots that can be tracked. A square section of the pattern is selected for tracking, which is termed 'subset' or 'facet'. Considering a field-of-view of 10″ using a 1 MP camera (1000 x 1000 pixels), 1 pixel = 0.01″. Thus, the ideal speckle size is between 0.03 and 0.05″ (3 and 5 pixels). A subset is selected such that its default size is a square of 20–30 pixels, which means that a single subset would contain approximately 6 speckles (Figure 2.23), which is twice the minimum number of speckles required within a subset [189, 190]. Thus, the speckle size is critical because it affects the subset accuracy. If the speckle size is significantly large or small, an entire subset may be in either the black or white region, respectively, which would prevent a suitable correlation. However, this can be compensated by increasing the subset size: nevertheless, this will be performed at the cost of spatial resolution and processing time. If the pattern is extremely small, the camera resolution may not be sufficient to accurately represent the specimen.

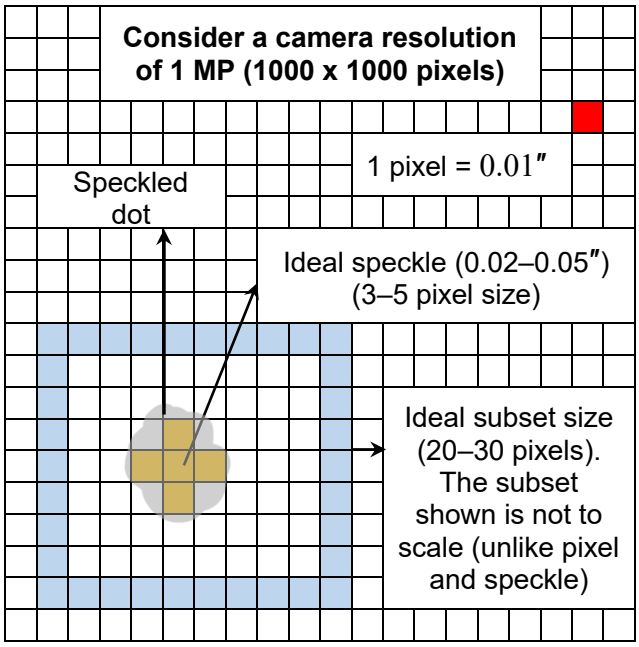


Figure 2.23 A schematic table showing the pixel conversion to inches in addition to speckle and subset size with relation to camera resolution.

After the material is deformed, the subset of the deformed image (post-event image) is correlated with that of the reference image (pre-event image). Once the subsets are matched, a new position is defined according to its displacement vector, (Figure 2.24). The centre of the subset (shown as a green dot in the pre-event image), which is not part of the speckled pattern, is the origin point from which the displacement is calculated (Figure 2.24). Then, the displacement vector can be decomposed into the Cartesian coordinates X and Y, where the displacement fields U and V can be determined. The subset is then repositioned with its centre at the new location to allow tracking points that are continuously moving away from the origin point in the reference image [191]. Figure 2.24 depicts the deformation of a single subset for illustrative purposes. The DIC however, calculates the displacement field for multiple subsets as shown in Figure 2.25, where four subsets are depicted and their origins appear as red dots, and the distance between the points of origins of subsets is called ‘step size’. Upon deformation, the new positions of the red dots are represented as blue dots, where the direction and distance between them are the vector fields (Figure 2.24). Then, magnitudes and directions of the strain fields are translated into a colour map.

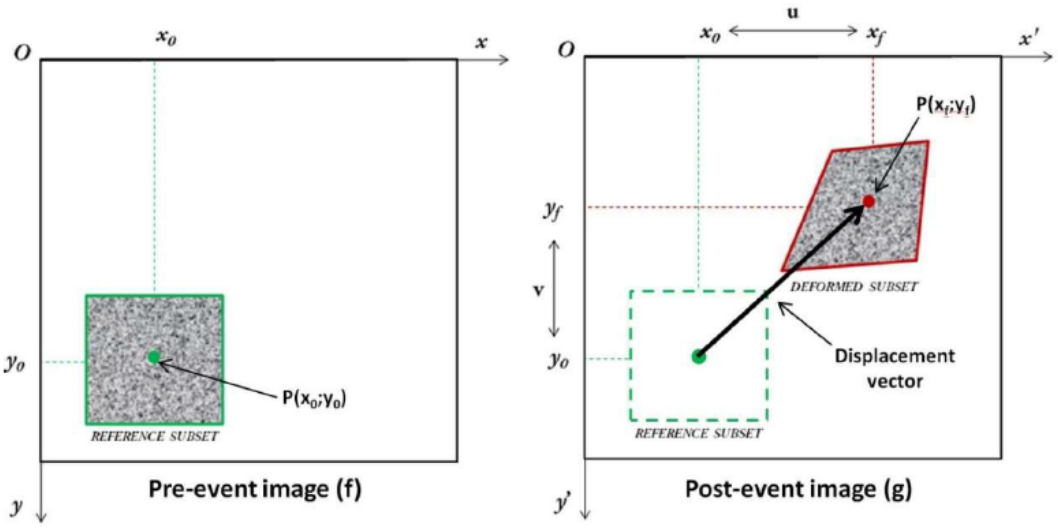


Figure 2.24 Principles of displacement calculation by correlating the subset in the deformed image with the initial subset in the reference image [192].

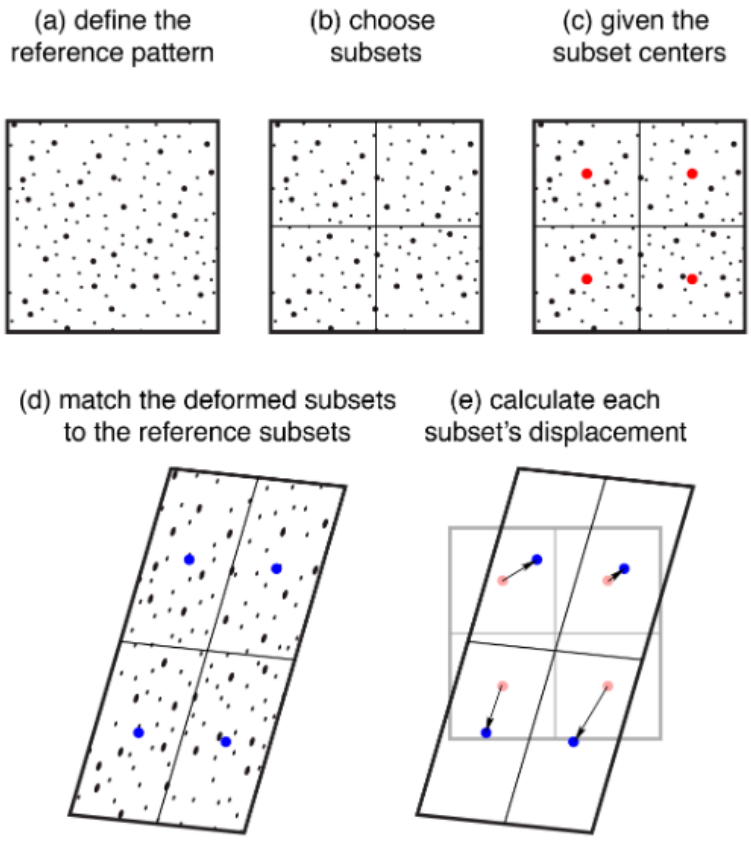


Figure 2.25 Full-field displacement using multiple subsets, and the formation of a deformation vector field [187].

Typical errors that affect DIC results include inadequately prepared sample surfaces or speckled patterns, improper camera focus, unevenly distributed lightening, poor image resolution that results in an inaccurate subset correlation, and out-of-plane motion, where the deformation of the sample is not constrained to a plane that is parallel to the camera [193-196].

2.5 SUMMARY

In summary, RBSBC is a SiC-based ceramic that falls between pure SiC and B_4C. RBSBC is designed for high-temperature low-load-bearing applications and is used in the hot-section components of gas turbines. Reaction-bonding process offers a low-cost and high-tolerance material with high density. The presence of B_4C decreases the material density and increases its hardness. The oxide formed from the oxidation of the RBSBC substrate is a SiO_2-based borosilicate SiO_2–B_2O_3 layer that is formed by the inward diffusion of O_2 through the oxide layer. Due to oxide layer recession in water vapour and salicaceous corrosive environment such as CMAS (sand), coatings are used to protect the RBSBC substrate from the deleterious effects of these environments.

Research on EBCs began in the early 1990s and four generations of EBCs have been developed. RE-silicates are among the most recent generations. The most promising RE-silicates are Yb, Lu, and Er-based coatings. RE coatings are applied using several techniques such as line-of-sight spraying, including APS, HVOF, and EB-PVD, and non-line-of-sight techniques such as dip coating. Dip coating provides a low-cost coating solution and can fully cover intricate parts better than spraying techniques. Regardless of their protective nature, RE-silicates corrode in a CMAS environment by forming an alkaline-earth metal-based RE-silicate structure Ca–RE–SiO_2 structure known as apatite. Apatite forms a hexagonal structure that incorporates elements from the CMAS melts as Ca and Si, which increases the protective nature of the coat and consumes the deleterious melt on the coating surface. Testing of EBC is broadly divided into corrosion and mechanical testing depending on the damage to the coating. Corrosion damage includes water vapour and humidity attack, in addition to high-temperature corrosion such as salicaceous sand (CMAS and volcanic ash) and molten salt corrosion. Mechanical testing includes impact from foreign object damage, erosion, thermal stresses and mechanical rupture. The mechanical stresses are also an important part for the substrate because it will hold most of the applied load.

3 EXPERIMENTAL METHODS

3.1 MICROSTRUCTURE AND CHARACTERIZATION TECHNIQUES

3.1.1 Density measurement

Experimental density ρ_{exp} [Eq. (3.1)] of the sample was measured using the Archimedes principle according to ASTM C830 [197]. ρ_{H_2O} (gm cm^{-3}) is the water density, W_{dry} (gm) denotes the sample weight measured in dry air, and W_{sub} is the weight of the sample recorded after submerging the sample in water. The samples used were 10 mm^3 cubes.

$$\rho_{exp} = \frac{W_{dry}}{W_{dry} - W_{sub}} x \rho_{H_2O} \tag{3.1}$$

The theoretical density ρ_{theo} of the sample is determined from the rules of mixtures [198] based on the volume fractions of phases (mass%) and density of each phase, as represented in Eq. (3.2). Both the experimental and theoretical densities are used to ultimately calculate the relative density ρ_{rel} (%), which is the ratio of the actual density of the material to the ideal density of the same material (theoretical density) as shown in Eq. (3.3). The relative density provides an indication of the percentage volume of voids in a ceramic, where the higher ρ_{rel}, the denser the ceramic [199]. Thus, relative density is used to determine the density of RBSBC with regard to its chemical composition. Moreover, ρ_{rel} assesses the reaction-bonding method in producing dense SiC–B_4C ceramics.

$$\rho_{theo} = [(mass\%) \times (\rho)]_{phase-1} + \cdots + [(mass\%) \times (\rho)]_{phase-n} \tag{3.2}$$

$$\rho_{rel} = \frac{\rho_{exp}}{\rho_{theo}} \times 100 \tag{3.3}$$

3.1.2 Weight gain measurements

Gravimetry is a quantitative chemical analysis that aims to estimate the kinetics of the chemical changes occurring in a sample during oxidation and corrosion experiments via weight gain or loss. The weight gain is measured using a mass balance (Ohaus Pioneer, USA) with an accuracy of ± 0.01 mg. The weight change ΔW is recorded as the difference between the masses of the sample before and after testing. Weight gain is used to determine the kinetics of the RBSBC oxidation and EBC–CMAS reactions.

3.1.3 Grain size measurement

Grain size is the diameter of an individual grains in addition to its aspect ratio [200]. The average grain size is evaluated using the Heyne linear intercept method according to BS EN 623-3:2001 [201]. This method depends on calculating the mean linear intercept length l over many grains by first drawing a line on the scanning electron microscope (SEM) image using ImageJ (Figure 3.1). The number of intersects ($n_1 + \cdots + n_2 = 6$ intersects in Figure 3.1) of the line with the grain boundaries are counted and divided by the line length, as shown in Eq. (3.4). The average grain size is considered $1.570l$ [198, 202, 203]. Four random lines are measured on the SEM images along the grain intersects, where each line crosses at least 50 grains [203, 204]. Approximately 200 grains were considered for the grain-size analysis. The grain-size method is used to calculate the size of the SiC and B_4C grains in RBSBC substrate.

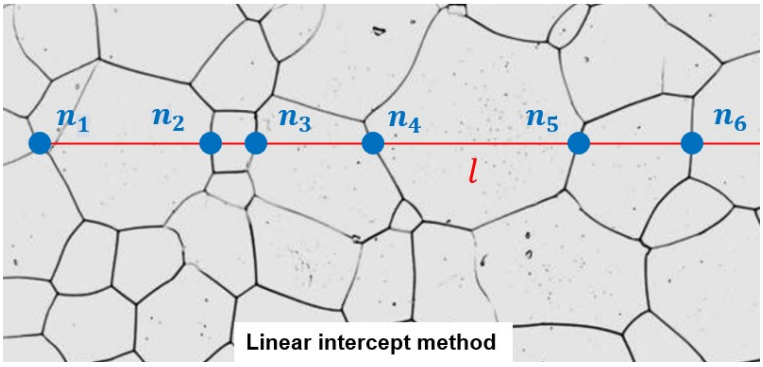


Figure 3.1 Schematic showing the use of lineal intercept method to calculate grain size.

$$Grain\ size = (n_1 + n_2 + \cdots + n_n)/l \tag{3.4}$$

3.1.4 Mercury intrusion porosimetry (MIP)

MIP is a technique used to measure pore size, volume, and distribution in porous materials. It involves the intrusion of Hg into the open pores of the samples. Pressure is applied to force Hg into the open pores of the samples. Hg is used because it is a non-wetting liquid, which means that it does not wet the sample or penetrate the pores through capillary action [205, 206], but rather require external pressure to fill the pores in the sample. The apparatus consists of a sealed glass connected to a stem filled with Hg (Figure 3.2). The stem acts as a Hg reservoir for measuring the intrusion volume. The sample is placed inside the glass, where Hg is pressed against it to fill the sealed sample.

The required pressure is inversely proportional to the sizes of the infiltrated pores according to the Washburn equation (Eq. 3.5), where P is the applied pressure, γ represents the surface tension of Hg, θ is the contact angle of Hg, and d denotes the pore diameter. Thus, the pore diameter can be estimated from the applied Hg pressure. The volume of the pores is determined based on the measured volume of the intruded Hg.

$$P = \frac{-4\gamma cos\theta}{d} \qquad 3.5)$$

The pore size and pore volume percentage of the coating are evaluated using MIP (Micromeritics AutoPore IV, Germany) that operates in a pressure range of 0–33,000 psi and exhibits a pore detection range from 0.003 to 360 μm. MIP is used to determine the pore size and percentage within the coating. The results are compared with the ImageJ analysis of the pore size obtained from the SEM images of the coating.

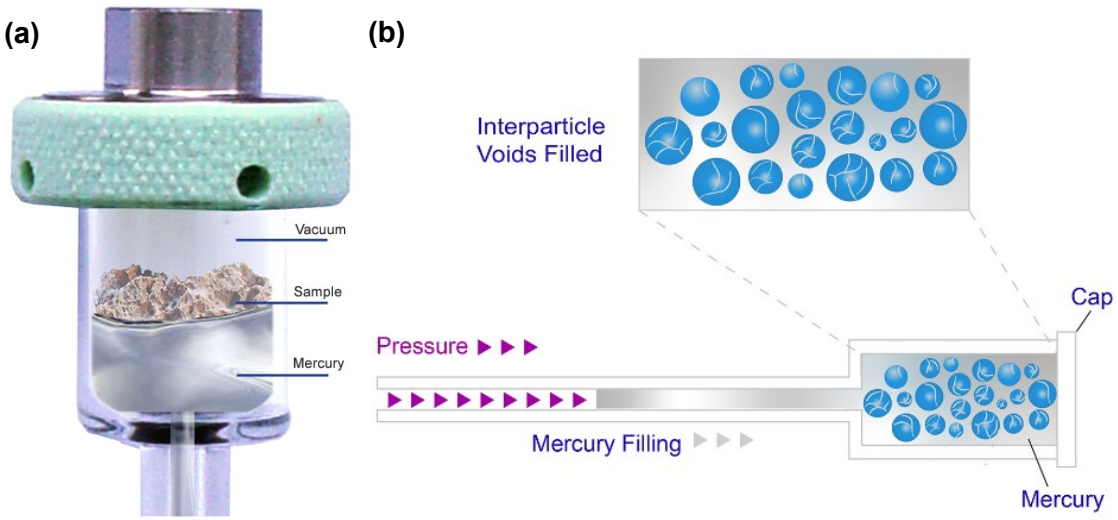


Figure 3.2 (a) Porosimetry cup with sample inside [205] (b) mercury intrusion [207].

3.1.5 X-ray diffraction (XRD)

XRD was used to determine the crystallographic structure, identify the polymorphs, and quantitatively analyse the samples. Its principle depends on bombarding a target with an X-ray (Figure 3.3a), which releases electrons from the inner K-shell of the target material, prompting electrons in higher-level shells to drop to its place, thus releasing X-rays in the process [198]. Therefore, the source is denoted as K_α. X-rays interact with the electron cloud in the atoms of a crystalline structure to cause elastic scattering of secondary waves in all directions [208], and only waves that undergo constructive interference produce a detectable peak. According to Bragg's law, diffraction occurs in the case of constructive interference when the phase shift between two parallel waves, diffracting from parallel crystallographic planes, is an integer n of wavelengths λ (multiple of 2π) (Figure 3.3b) [209]. Based on Bragg geometry [Eq. (3.6)], the phase shift between parallel reflected beams is $2dsin\theta$,

$$n\lambda = 2d_{hkl}sin\theta_{hkl} \tag{3.6}$$

where d is the interplanar distance considering the crystal structure to be modelled as a set of parallel crystallographic planes (hkl). It is proportional to the number of regularly-spaced electrons in the plane. Every crystalline solid exhibits a unique pattern of d spacings that can differentiate between compounds with the same chemical compositions yet different phases. θ represents the angle between the transmitted X-ray and diffracted plane. As the diffracted beam

is at the same angle as that of the incident beam, the angle between the incident and diffracted beams is 2θ.

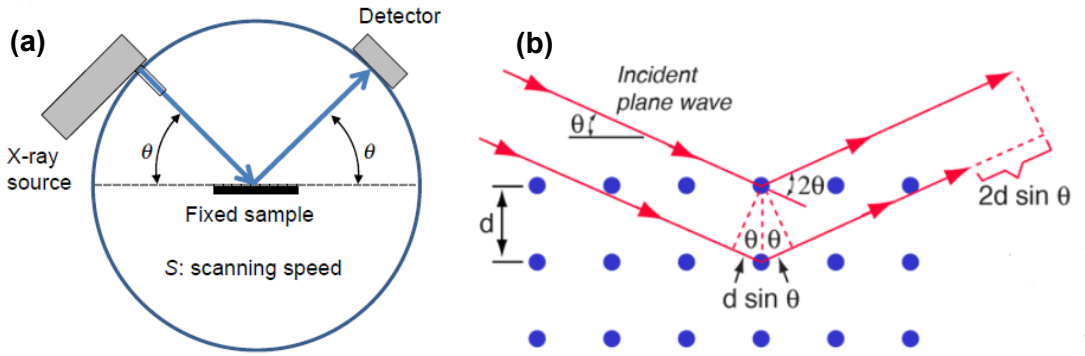


Figure 3.3 (a) XRD operating principle [210] (b) geometrical representation of Bragg's law [211].

Relative intensity ratio (RIR) is semi-quantitative analysis, where an integrated internal standard intensity of corundum (α-alumina) peak is normalised against the measured peaks at a 1:1 wt.% mixture [212]. Corundum was chosen as the reference crystal by the International Centre for Diffraction Data (ICDD) [213]. This means that the XRD measures the strongest peak intensity (intensity counts) I for the tested phase m (its amount X is unknown) and compares it with the strongest peak intensity I of α-alumina at a known amount of α-alumina (Figure 3.4). This results in four parameters, three of which are known: I_m is the maximum intensity for the measured phase m (measured from the XRD test run), I_c is the maximum intensity for the standard phase corundum (standard data in the XRD software), X_m is the relative percentage amount X of the measured phase m (it is the required data), X_c is the relative percentage amount X of the standard phase corundum (standard known amount of corundum in the XRD software that corresponds to I_c). Since I is proportional to X, Eq. (3.7) represents a direct relationship between the relative peak height intensities and weight fractions of phases [212-214]. The results are presented as a pie-chart.

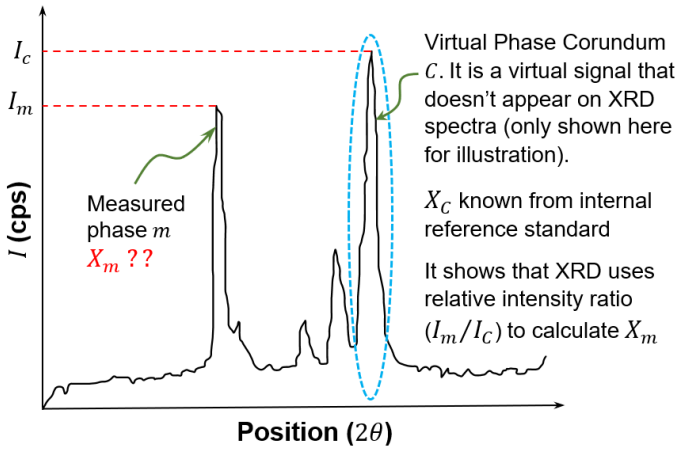


Figure 3.4 Schematic of the RIR method used to calculate X_m.

$$\frac{I_\alpha}{I_c} \cong \frac{X_\alpha}{X_c} \tag{3.7}$$

XRD instrument used in this study is a Bruker D2 Phaser, UK. Measurements were conducted in the 2θ range of 10°–90° at 0.0345 increments. The software used for the analysis is HighScore Plus, utilising ICDD database. HighScore Plus compares the obtained peaks with a dataset of peaks to assign the angle of each peak 2θ to its corresponding element or compound. XRD is used to determine the phases present in the RBSBC and EBC–CMAS corrosion.

3.1.6 X-ray photoelectron spectroscopy (XPS)

XPS is a surface analysis technique used to determine the elemental composition, in addition to the chemical and electronic states of the atoms and other elements to which they are bonded. The principle depends on irradiating the sample surface with a low-energy (~1.2–1.5 keV) X-ray beam, which ionises molecules or atoms by forcing electrons from the K-shell close to the nucleus to become excited and released (Figure 3.5). The released electrons emit kinetic energy as a result of being bombarded with X-ray photons, which reflects the electronic structure of the atoms present. The kinetic energy E_k is measured using a spectrometer. E_k is used to determine the binding energy E_b of electrons belonging to a specific core level according to the photoelectric equation [Eq. (3.8)], where ϕ is a function term for the spectrometer and E_{ph} represents the applied photon energy [215]. The electrons pass through an electrostatic lens that collects them and focuses them to a hemispherical analyser, which measures the kinetic energy of electrons (binding energy) and also counts the electrons. The binding energy is the

energy required to remove an electron from the atom, and it decreases at higher orbitals further from the nucleus. It is characteristic for each element, and its peaks reflect the electronic orbital shell, such as 1s, 2s, 2p orbitals, from which the electron is excited (Figure 3.6). The composition is assessed by quantifying the number of electrons, indicated as intensity, emitted from the top 1 to 10 nm of the analysed samples [216, 217]. XPS spectra are presented as count intensity vs. binding energy (keV). Note that all orbitals except for 1s yield doublet peaks [218]. The doublet peak is a peak that split into two smaller peaks. These two small peaks have the same oxidation states yet different binding energies. These peaks originate from the interaction between the electron spin around its axis and its orbital motion around the nucleus. For example, the spin states of the 2p orbital are $2p_{1/2}$ and $2p_{3/2}$, where $2p_{3/2}$ has a higher binding energy. The $2p_{1/2}$: $2p_{3/2}$ binding energy ratio is 1:2.

$$E_b = E_{ph} - E_k - \phi \tag{3.8}$$

XPS system used herein is K-Alpha$^+$ (Thermo Fischer Scientific, USA) operated at a 400 μm beam source and 200 eV for surveys. The samples were sputtered with electrons for 20 s before the XPS analysis to remove the surface layer containing contamination and C traces, which could block the X-ray beam and affect the accuracy of the acquired spectra. Curve fitting and analysis were conducted using 'Avantage' software (Thermo Scientific, USA). XPS was used to determine the oxidation state and bonding structure of the reaction product formed from the corrosion of RE-silicate EBCs in CMAS environment.

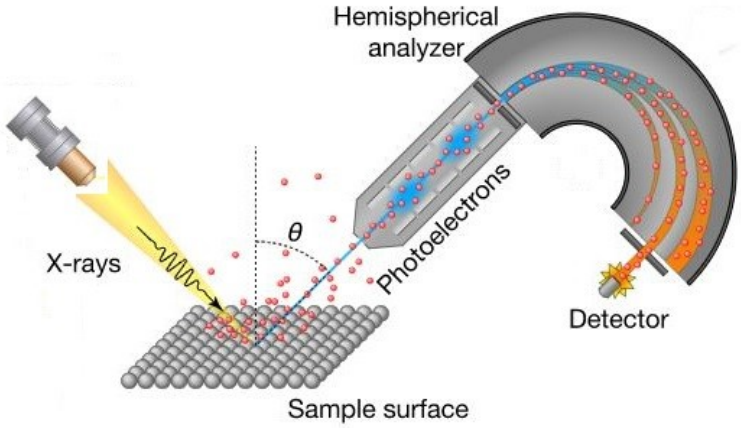


Figure 3.5 Schematic showing the operating principle of XPS and its main components [219].

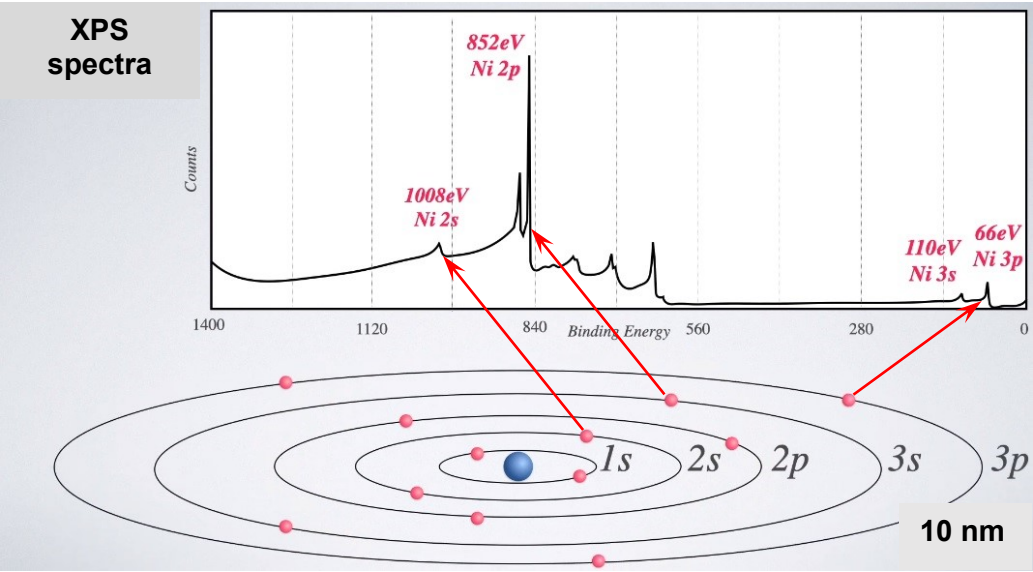


Figure 3.6 XPS spectra obtained from the electrons that are excited from their electronic orbital shells including 1s, 2s, 2p, 3s and 3p orbitals.

3.1.7 Scanning electron microscope (SEM)

Electron microscope directs an electron beam onto the sample, where the resultant of the beam-sample interaction is detected and analysed (Figure 3.7a). When the electron beam interacts with the target, elastic and inelastic scattering modes occur. Elastic scattering takes place when the electron retains its original energy after the scattering event, whereas inelastic scattering occurs when the electron hits the target and transfer some its energy to it, causing the electron to lose energy and change its energy state. Elastic scattering produces backscattering electrons (BSE), whereas inelastic scattering generates secondary electrons (SE) and X-rays (Figure 3.7b) [220]. SEs are weakly bonded outer shells, or valence electrons emitted in response to the ionisation of the sample by the electron beam. Their energies are low: thus, only SEs that are produced at the surface are released [221]. The emitted electrons are functions of the atomic number Z, atomic density, and topographic surface. Thus, SEs reflect the topographic surface of a material, resulting in secondary electron imaging (SEI). Some of the electrons are attracted to the nucleus, where they circle around it and return without slowing down or colliding with another electron and transferring all their kinetic energies to it, resulting in elastic scattering. These are BSEs or reflected electrons [222]. As they go deeper in the atom, and has higher energy than those of SEs, their intensities are more dependent on Z, where larger Z leads to the release of more electrons. Thus, they differentiate between phases based on contrast. Emitted

X-rays are at an energy and λ that are characteristic of the substrate allowing the detector to identify the composition of materials and amounts of elements using energy dispersive spectroscopy (EDS). As SEM uses electrons to produce an image, the sample must be conductive to obtain an SE image. Alternatively, beam electrons build up on the sample surface, and the number of electrons entering the specimen becomes higher than those exiting it resulting in a negatively charged sample surface [221]; resulting in bright image distortions.

Microstructures of the as-received, corroded, and oxidised materials were examined using SEM (JEOL JSM 6010LA, Japan, and TESCAN MIRA, Czech Republic) coupled with EDS at an accelerating voltage of 20 kV. All images were acquired using backscattering electron imaging (BEC) for phase contrasts. Prior to SEM, the samples were cross-sectioned, and polished to 1 µm using diamond suspension followed by cleaning in an acetone ultrasonic bath for 15 min to remove contaminants. The samples were gold sputtered (Emitech K575X, UK) to prevent electrical charging. ImageJ was used to analyse the SEM images, where each measurement represents the average of 20 points equally taken along the length of the sample.

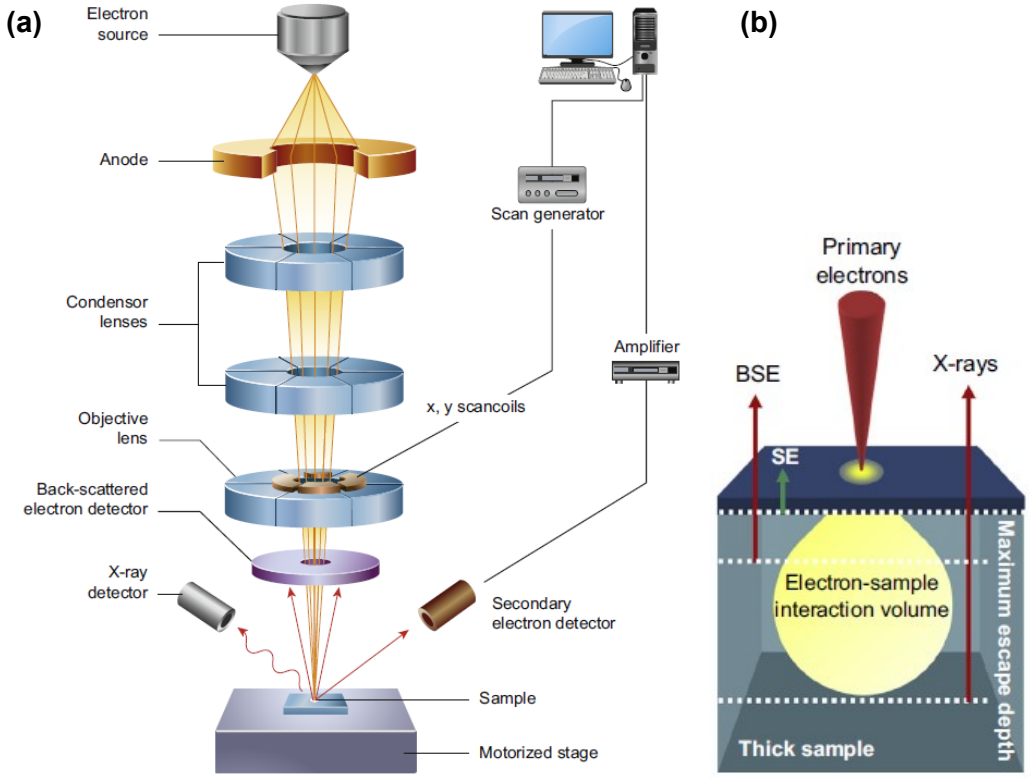


Figure 3.7 (a) SEM components [223] (b) SEM scattering modes arising from electron beam-sample interaction [223].

3.1.8 Transmission electron microscopy (TEM)

Transmission electron microscopy (TEM) lamella samples are prepared using focused ion beam (FIB). A Gallium ion Ga^+ beam is employed at low currents for imaging purposes, and at high currents for milling [198]. The FIB sample is processed through a series of steps (Figure 3.8). First, a rectangular area of interest is chosen on the sample where Pt is deposited to prevent damage from the Ga^+ beam. Second, horizontal trenches at the edges of the deposited area are milled using the Ga^+ beam, leaving a 1 μm thick lamella protected by a Pt layer on top. This lamella contains the features of interest. Finally, the areas under the lamella are cut while leaving only a small part attached to the actual substrate of the material. Finally, the lamella is lifted from the substrate, welded to the sample holder and surface-etched using Ga^+ beam until the lamella thickness is less than 120 nm. During each step, the stage is tilted such that the lamella is always normal to the incident ion beam.

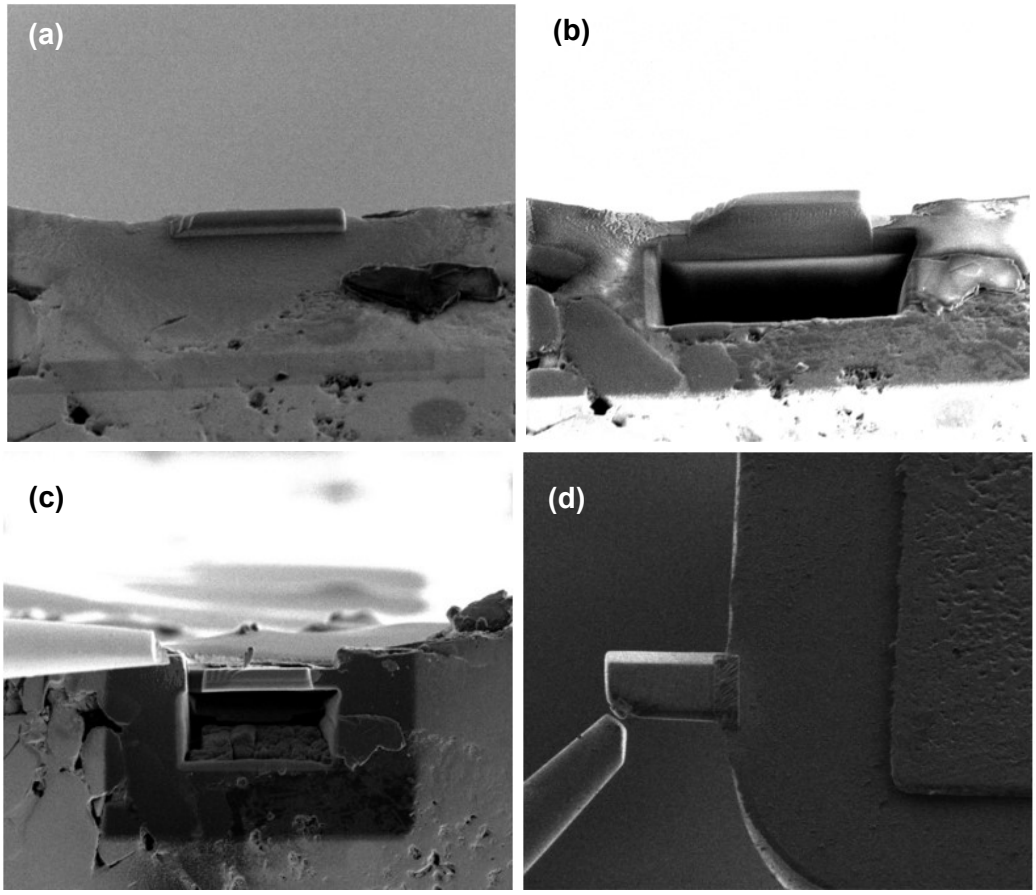


Figure 3.8 FIB sample preparation (a) Pt deposition (b) trench milling (c) lamella undercutting (d) lamella welding.

TEM investigates the internal details of the sample at near-atomic resolutions (1–10 nm) [223]. TEM has the same basic components as those of SEM (Figure 3.9) but TEM detects the electrons that pass through ultra-thin samples (< 120 nm), where they hold information on their internal structure (Figure 3.10b). The beam of electrons should be of high-energy of 60–300 kV to be transmitted through the sample. Dense or more crystalline phases appear darker because of fewer transmitted electrons, resulting in bright-field images in which transmitted electrons pass to the detector and backscattered electrons are blocked. A dark-field image is the opposite of the bright-field image, in which scattered electrons are detected; thus, denser areas appear brighter. TEM also acquires the diffraction pattern (DP) of a material giving information on its crystal structure and lattice parameters. The TEM beam is high-energy, and its wavelength is considerably lower than the spacings between atoms; thus, atoms act as diffraction gratings, where electron waves hitting the atoms are diffracted if they satisfy Bragg's law. This results in a spot image, in which each spot corresponds to an atom location.

Electron microscopes consist of the following main components (Figure 3.7 and Figure 3.9): electron gun, electromagnetic lens system (condenser and objective lenses), vacuum system, and a detector. The gun produces an electron beam by sending high electric current to a thin W filament (cathode), heating it to emit electrons. High voltage between the anode and cathode accelerates the electrons to form a beam, which is directed through a hole in the anode. Electromagnetic lenses create a magnetic field by passing a current around a magnet to manipulate the electron beam. The lens power can be adjusted by changing the current through the lens. The condenser lens focuses (by stretching the beam to control its width; demagnification) the beam through an aperture that lies between the condenser and objective lenses. This regulates the amount of beam heading towards the objective lens [224]. The objective lens controls the diameter of the electron beam (beam intensity) that hits the sample, which controls focus. The electromagnetic coils are used to shift or tilt the beam to the sides.

Bright-field imaging and diffraction patterns were obtained using TEM (JEOL JSM 2100F, Japan) equipped with EDS (INCA software, Oxford Instruments, UK). TEM lamella was prepared by FIB milling (Helios NanoLab 600, USA). TEM is used to investigate the structure of the reaction product formed by the corrosion of EBC in CMAS environment.

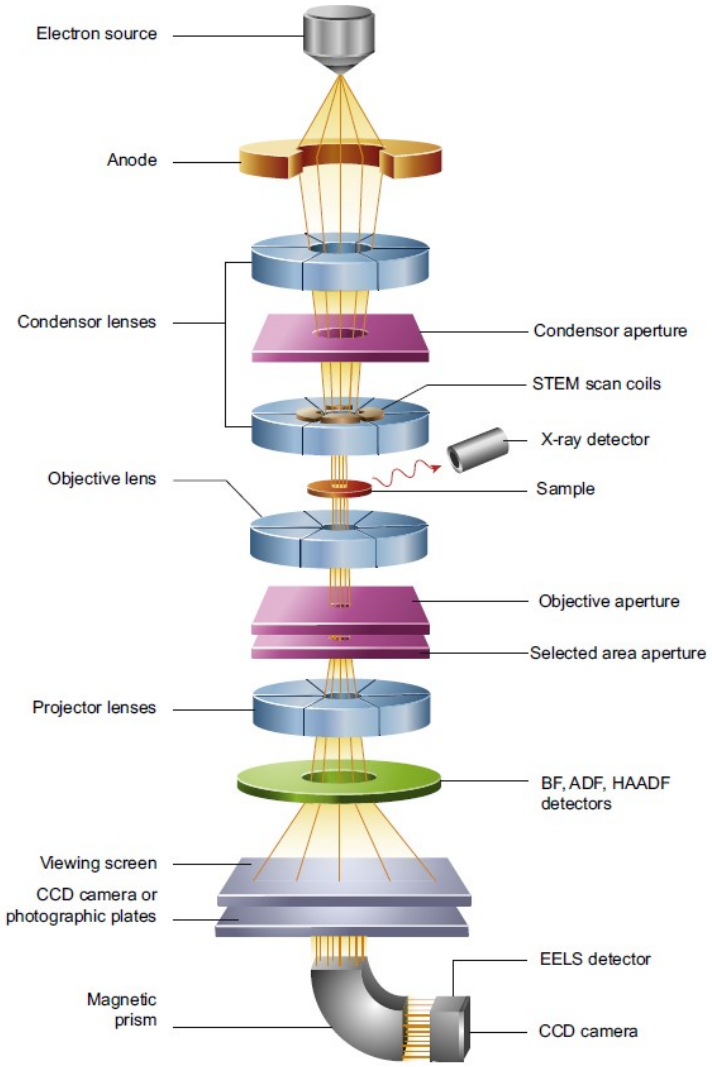


Figure 3.9 TEM components [223]. The detector detects electrons that pass through the sample instead of the electrons reflecting from the sample in the case of SEM.

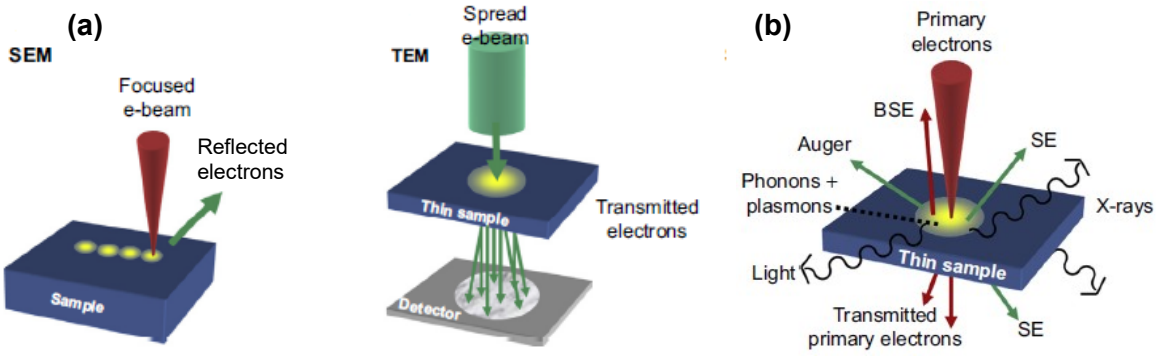


Figure 3.10 (a) Difference between SEM and TEM [223] (b) TEM electron interaction [223].

3.1.9 Secondary ion mass spectrometry (SIMS)

SIMS is a surface analysis technique that provides information on the composition of a sample surface. The sample is sputtered by a primary ion beam that is usually Cs or O_2 (Figure 3.11a). Interaction of the beam with the sample provides sufficient energy to ionise the sample and release secondary electrons, neutral particles, and secondary ions. If the primary beam is positively charged such as Cs^+ and O_2^+, the resultant ionisation will mostly be composed of negative ions and vice versa (Figure 3.11b). Thus, the choice of the primary ion beam is a function of the analysed sample and the expected charges of its ions. The secondary ions yield varies according to the sample and sputtering conditions such as beam source, energy and angle. Only secondary ions are detected, and the ejected ions are accelerated through a lens to a mass spectrometer for mass analysis. The ions are sorted according to their mass/charge ratio, their resonant electric fields or according to their velocity which is function of ion mass and time of flight. The types of results include mass spectrum and depth profile where counts are detected across a profile depth (µm).

A depth profile is used to detect B, Si, and O counts through the oxide layer depth using SIMS (Hidden SIMS Workstation, UK). B is particularly difficult to detect using EDS analysis; therefore, SIMS is required for this purpose. The analysis uses Cs^+ and O_2^- gases as the primary ions at 20 keV and 80 nA for a depth of 6 µm and crater size of 600 µm.

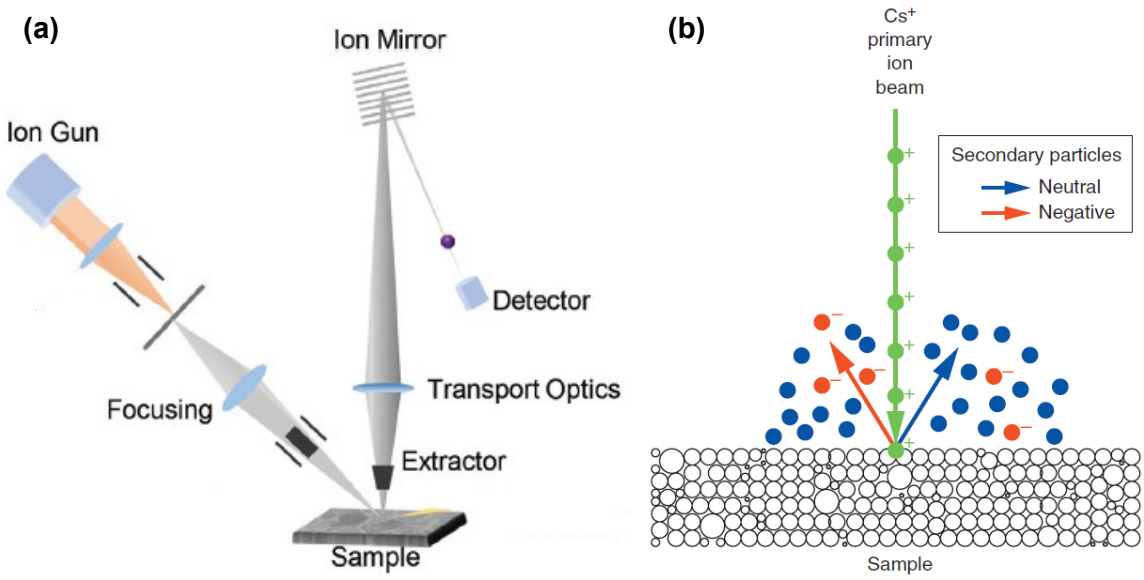


Figure 3.11 (a) Operating principle of SIMS [225] (b) sputtering of a sample surface [225].

3.1.10 Raman spectroscopy

Raman spectroscopy is a non-destructive tool that determines the chemical structure and identifies phases and atomic bonding properties. Raman microscope (micro Raman) comprises a laser source coupled with an optical microscope to facilitate visualisation the sample and performs analysis at specific spot locations (Figure 3.12a) [226]. Raman spectroscopy is a light-scattering technique, where a laser with a wavelength λ in the order of nanometres interacts with the electron cloud of the atom. Laser-atom interaction leads to elastic and inelastic scatterings. The elastic scattering (Rayleigh scattering) occurs when the scattered light has the same energy E as that of the laser source and it is filtered by the detector. Inelastic scattering (Raman scattering) takes place when the incident light photon E_o interacts with the atom, where it either transfers part of its energy to the atom raising the internal energy of the system, or part of the internal energy of the matter is transferred to the scattered photon E. Thus, the scattered photon has a different energy and frequency f than those of the incident photon. It can either be higher ($E > E_o$) or lower ($E < E_o$) as shown in Figure 3.12b. This difference amounts to the change in the internal state of the molecule, which is a function of the internal structure and bonding properties of the atom. The electrical field from the incident laser alters the charge distribution within the atom depending on the atomic properties such as bond strength, length and symmetry, resulting in rotational and vibrational modes in the atomic bonds [227, 228]. Additionally, when the laser hits the lattice, vibrations are created in the lattice which are a function of lattice parameters, resulting in multiple peaks for the same material depending on the mode of reaction of the lattice with the laser. The Raman spectrum is presented as Raman scattering (cm^{-1}) versus intensity. The reflected Raman-scattered light is obtained using a spectrometer.

Raman acquisition was obtained using a Raman microscope (Renishaw RE 04, UK) with a 532 nm laser source and acquisition time of 10 s at 50% laser power, within a scanning range of 100–1500 cm^{-1}. Raman spectroscopy was used to identify the elements present in RBSBC individual and the bond type of the formed oxide layer.

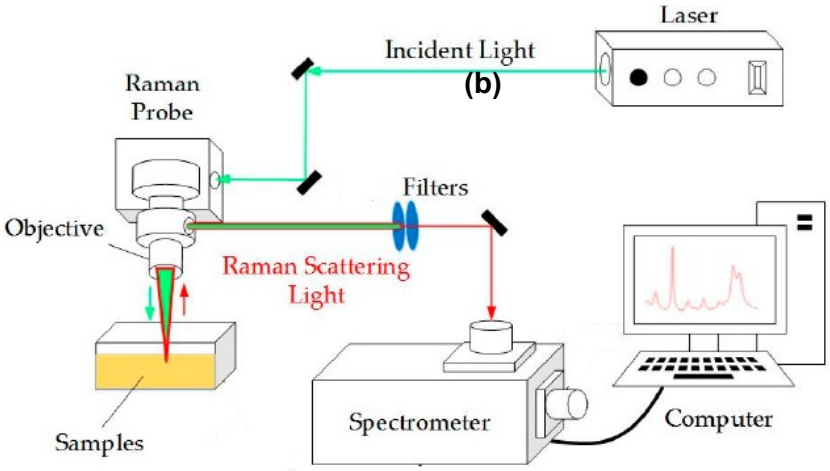


Figure 3.12 Schematic of the operation of Raman spectrometry showing the main components of the Raman microscope [229].

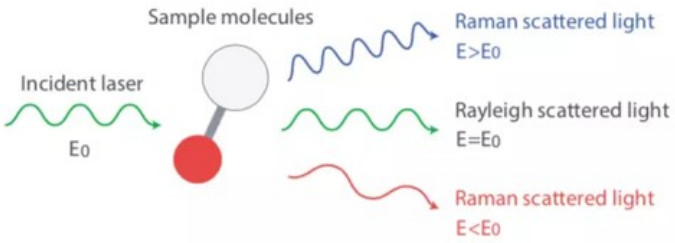


Figure 3.13 Scattering of light because of laser-sample interaction [229].

3.2 MECHANICAL AND THERMAL TESTING

3.2.1 Fracture toughness K_{IC}

Fracture toughness of ceramics reflects the ability of ceramics to resist fracture whether an indentation exists inside the material or on its surface. The fracture toughness is measured using the critical stress intensity factor K_{IC} (for Mode I fracture) at the crack ends, where fracture normally occurs. K_{IC} is the material's resistance to brittle fracture when a crack is present. Thus, higher fracture toughness indicates a higher resistance to fracture. K_{IC} is determined according to ASTM C1421-18 [230] based on three-point bending test. Samples are prepared according to the single-edge-V-notch beam (SEVNB) method following the requirements of Kübler [231] and CEN/TS 14425-5:2004 [232]. This method is also called '*precracked beam method (pb)*' in ASTM C1421-18. An 0.8 mm pre-notch is introduced into the sample centre, along the 3 mm face using a 0.3 mm diamond blade (Figure 3.14) to promote early crack initiation [230].

The stress field around the notch tip is related to the notch radius [233]. A critical notch radius that can simulate a sharp crack is required for accurate K_{IC} estimation [234]. Therefore, a razor blade is used that slides back and forth, using a motor, over a pre-notch while being lubricated with a 1 μm diamond suspension (Buehler MetaDi). The notch radius, measured using an optical microscope, is ~20–30 μm, which is almost equal to the average grain size of the material (~20 μm) because the defect size at the notch tip is proportional to the characteristic length of the material microstructure; namely the grain size [235]. The final notch length after sharpening is 1.20–1.25 mm.

The RBSBC specimen was loaded under tension during three three-point bending test. The tests were conducted using Zwick/Roell Z2.5 at ambient temperature with a 16 mm supporting span S_o and a 0.01 mm s^{-1} displacement rate [230]. Sample dimensions (mm) are 40 (length) l × 3 (width) B × 4 (height) W (Figure 3.14). After fracture, the average crack length a is measured on the fractured surface (Figure 3.15b) using ImageJ. It is calculated as the average of a_1, a_2 and a_3 measured at 0.25B, 0.5B and 0.75B respectively [232]. K_{IC} (MPa $m^{1/2}$) is calculated according to Eqs. (3.9) and (3.10), where P is the fracture load (N), α denotes the ratio of the average relative crack length to specimen height a/W, and g is the stress intensity shape factor, as notch geometry affects the stress distribution around it [233].

$$K_{IC} = \left[\frac{PS_o}{BW^{3/2}}\right]\left[\frac{3(\alpha)^{1/2}}{2(1-\alpha)^{3/2}}\right] f(a/W) \tag{3.9}$$

$$f(a/W) = \frac{1.99 - [\alpha][1-\alpha][2.15 - 3.93[\alpha] + 2.7[\alpha]^2]}{1 + 2[\alpha]} \tag{3.10}$$

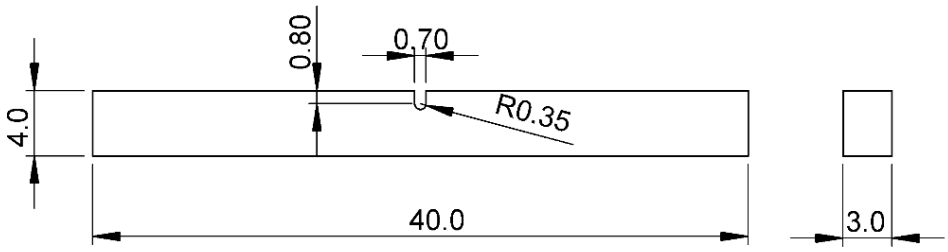


Figure 3.14 Dimensions of the fracture toughness specimen.

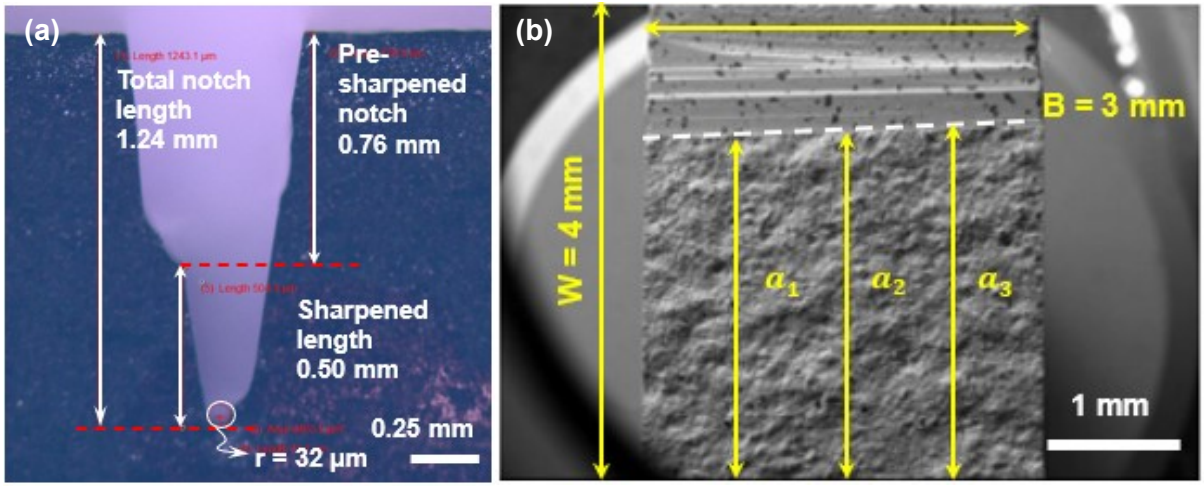


Figure 3.15 (a) Lengths of the sharpened samples, measured by optical microscope (b) SEM image of the fractured surface and measurement of the average crack length.

3.2.2 Coefficient of thermal expansion (CTE)

Thermal expansion coefficient represents the change in the sample dimensions with respect to temperature and is measured using a dilatometer according to ASTM E228-17 [236]. The push-rod dilatometer consists of an LVDT, pushrod, furnace, and a thermocouple (Figure 3.16). The sample is placed at the end of the pushrod, inside a furnace, where it is gradually heated to the desired temperature. As the sample expands, it pushes against the pushrod. The pushrod is connected to LVDT, which converts the pushrod displacement to a voltage, and the software convert the voltage to a readable displacement signal. The temperature of the sample is recorded using a thermocouple placed on the sample. In this technique, the linear change of sample length is recorded as $\Delta L/L_o$ versus temperature, where ΔL denotes the change in sample length and L_o is the original sample length.

Dilatometer components can be affected when changes in length are driven by the temperature changes [237]. Therefore, a 'correction' run, under the exact conditions and dimensions as those employed in the sample run, is performed using high-purity Al_2O_3 to negate the effect of sample expansion because the pushrod is made from high-purity Al_2O_3 [236]. The correction run facilitates the determination of the changes in the length of the pushrod material. The second run is the 'sample' run, in which the dilatometer reads the displacement of the sample and pushrod. Thus, to account for the changes in the length of the experimental sample only, the 'correction' run is subtracted from the 'sample' run.

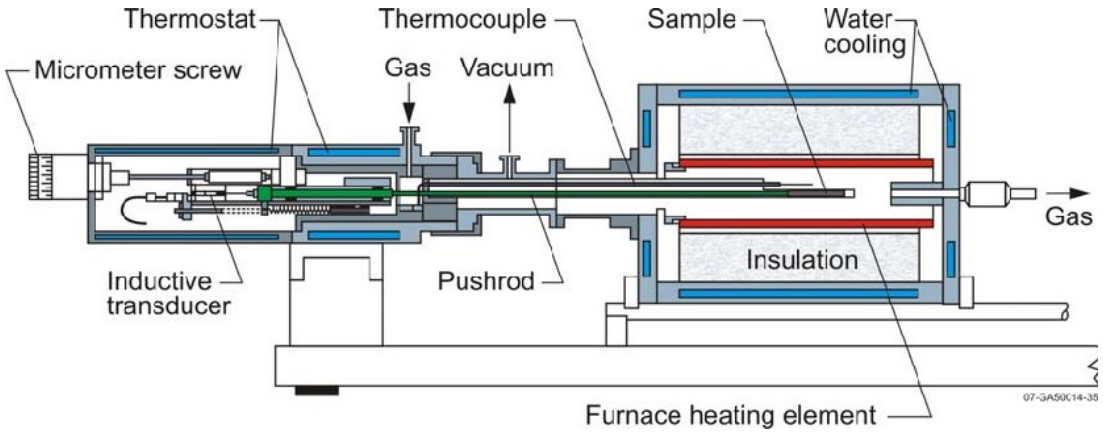


Figure 3.16 Schematic of the dilatometer in a horizontal configuration [238].

During the 'sample' run, the dilatometer signal reading for the strain $(\Delta L/L_o)_{samp}$ is the average of the readings of alumina push-rod and sample. To calculate the true sample strain $(\Delta L/L_o)_{true}$, and negate the effect of pushrod displacement, a calibration should be made, which is equal to the difference between the measured strain from 'correction run' $(\Delta L/L_o)_{corr}$ and true Al_2O_3 strain $(\Delta L/L_o)_{alum}$ [shown in small brackets in Eq. (3.11)]. Calibration subtracts the true alumina strain from the correction run to account for any errors caused by the expansion of the dilatometer components [238]. Note that the value obtained from the 'sample' run is negative in value (Figure 3.17) because the expansion of the Al_2O_3 pushrod is higher than that of RBSBC, and thus the machine reads a contraction in the sample materials. The correction in Eq. (3.11) is applied to each data point to acquire the true strain at each point. The CTE α for the measured sample [Eq. (3.12)] is obtained over the temperature range $(\Delta T = T_m - T_o)$, where T_m is the temperature at point m and true sample strain at point m is $(\Delta L/L_o)_{true,m}$.

$$\left(\frac{\Delta L}{L_o}\right)_{true} = \left[-\left(\frac{\Delta L}{L_o}\right)_{samp} + \left[\left(\frac{\Delta L}{L_o}\right)_{alum} - \left(\frac{\Delta L}{L_o}\right)_{corr}\right]\right] \tag{3.11}$$

$$\alpha = \left[\frac{1}{\Delta T} \times \left(\frac{\Delta L}{L_o}\right)_{true,m}\right]_m \tag{3.12}$$

CTE of the RBSBC substrate was measured using a pushrod dilatometer (Netzsch DIL 402, Germany). Sample dimensions (mm) are 25 (length) × 4 (width) × 4 (height). The operating conditions are 1 K min^{-1} to achieve an accuracy result of 0.1 × 10^{-6} K^{-1} [239] at a heating interval between 25 and 1350 °C.

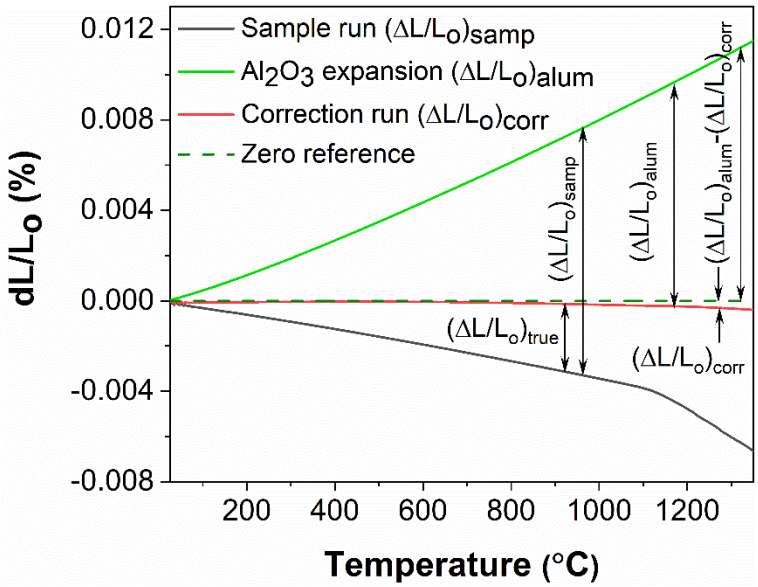


Figure 3.17 Correction plot demonstrating the data obtianed from the dilatometer runs.

3.2.3 Vickers microindentation hardness

Vickers microindentation testing is a hardness test method that differs from the standard Vickers testing in its ability to measure the hardness in localised areas as the crystal grains in the microstructure. It also uses a force of less than 10 N, which means a smaller indentation (hence the name 'microindentation') [240].

Vickers microindenter is an optical measurement system, in which an optical microscope is focused on a polished specimen and a pyramid-shaped diamond indenter makes an impression using a selected force that usually ranges from 2 to 10 N. Figure 3.18a shows a Vickers indent on a B–C–Si–Al grain on a RBSBC sample using a 2 N force. Vickers hardness HV (GPa) is calculated using Eq. (3.13), where F (N) is the applied load and d (mm) represents the average length of the two diagonals of the impression indent (Figure 3.18b).

$$HV = 0.0018544\left(\frac{F}{d^2}\right) \tag{3.13}$$

Vickers hardness HV indentation was conducted with a 2 N load using a Wilson VH1102 microhardness tester (Buehler, Germany) according to ASTM C1327-15 [21]. Vickers hardness was employed to determine the hardness values of B_4C grains in the RBSBC substrate.

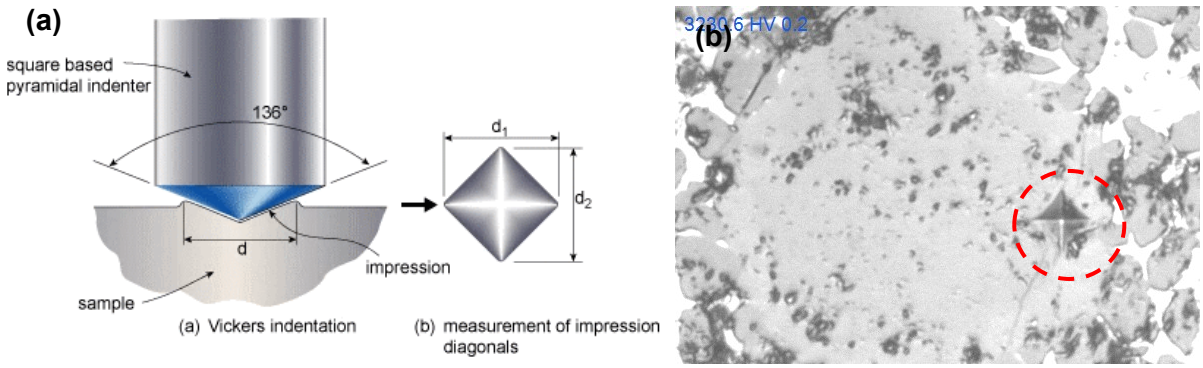


Figure 3.18 (a) Microhardness indenter [241] (b) Vickers indent (red) on RBSBC.

3.2.4 Impulse excitation technique (IET)

Impulse excitation technique (IET) is used for the non-destructive characterisation of the elastic properties of a material according to ASTM E1876-22 [242]. The obtained properties include the Young's modulus, shear modulus, and Poisson's ratio. The principle depends on the resonant frequency of each material. When a material is excited, it emits a sound that depends on its elastic properties, dimensions, and mass. The measurement principle involves hitting the sample with a ball and recording the induced vibration signal (amplitude) in the time domain using a microphone or laser vibrometer placed above the sample without contact. The vibration signal is transformed into frequency using fast Fourier transformation (FFT), where a software determines the resonant frequency and accordingly deduce the elastic properties (Figure 3.19).

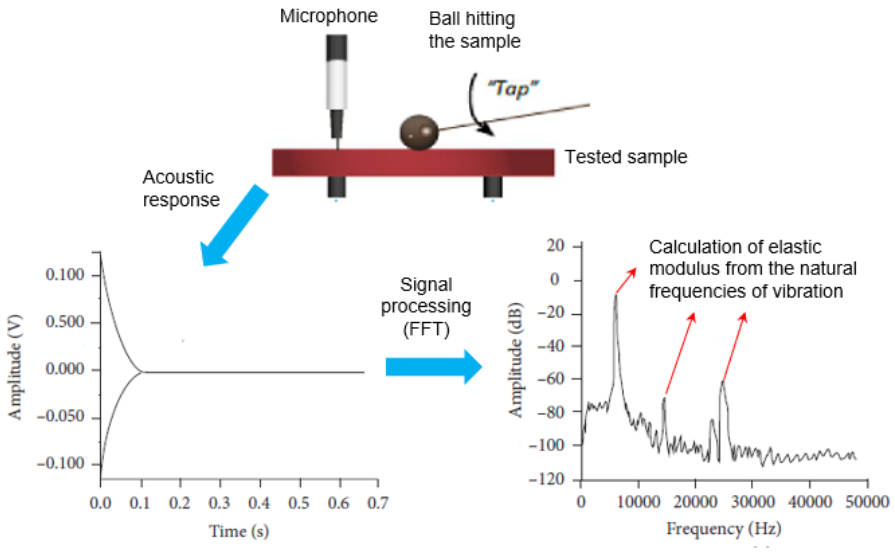


Figure 3.19 Schematic of IET and FFT signal processing [243, 244].

Based on the sample geometry and resonant frequency, the Young's modulus E (Pa) can be calculated using Eq. (3.14) [242], where m is the mass of the bar (g), f_t denotes the resonant frequency of the bar (Hz), B is the width of the bar (mm), L represents the length of the bar (mm), W is the thickness of the bar (mm), and T_1 is a correction factor that depends on the Poisson's ratio and thickness-to-length ratio as shown in Eq. (3.15).

$$E = 0.9465\left(\frac{mf_t^2}{B}\right)\left(\frac{L^3}{W^3}\right)T_1 \tag{3.14}$$

$$T_1 = \left[1.000 + 6.585\left(\frac{W}{l}\right)^2\right] \tag{3.15}$$

The shear modulus G (Pa) was calculated using Eq. (3.16) [245], where R is a factor that is a function of the bar width to thickness as shown in Eq. (3.17). The Poisson's ratio is calculated as a factor of the Young's modulus and shear modulus, as represented in Eq. (3.18) [245]. The abovementioned equations for E, G and v are for rectangular bar specimens.

$$G = \frac{4Lmf_t^2}{Bh}R \tag{3.16}$$

$$R = \left[\frac{1+\left(\frac{B}{W}\right)^2}{4 - 2.521\frac{W}{B}\left(1 - \frac{1.991}{e^{\pi(B/W)}+1}\right)}\right]\left[1 + \frac{0.00851B^2}{L^2}\right] - 0.060\left(\frac{B}{L}\right)^{3/2}\left(\frac{B}{W} - 1\right)^2 \tag{3.17}$$

$$v = \left(\frac{E}{2G}\right) - 1 \tag{3.18}$$

The samples (dimensions in Figure 3.20) were synthesized as 40 mm circular pellets from powder, then cut to the desired dimensions using a diamond saw blade. IET technique was used herein to obtain the E and v values for the RBSBC, Yb_2SiO_5, Yb_2O_3, and CMAS. The purpose of the acquired E, G, and v data is to be used for future work involving thermomechanical stresses and modelling.

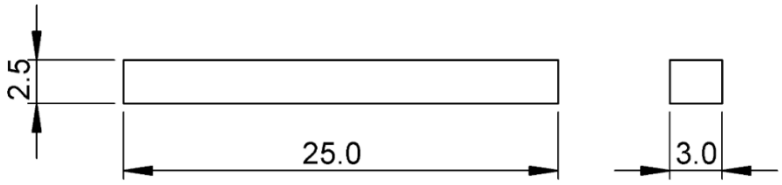


Figure 3.20 Dimensions of the CMAS pellet for the IET technique.

3.3 SUMMARY

The experimental work in this study was divided into four main stages: analysing the RBSBC substrate properties, investigating the oxidation of the substrate, preparing coatings, characterising the CMAS–EBC corrosion experiments. Figure 3.21 depicts a flow chart that summarises the experimental work performed and the characterisation methods used herein. The green boxes indicates the experiments for each stage, and the orange boxes represents the characterisation methods used for that stage. For example, for examining the oxidation properties of RBSBC, the oxidation experiments were conducted in a furnace, and the corresponding testing and characterisation techniques include weight gain measurements, XRD, SEM, TEM, SIMS, and Raman spectroscopy. After the oxidation experiments, the oxidised samples were dip-coated for 'EBC preparation', and then EBC was characterised using SEM and XRD.

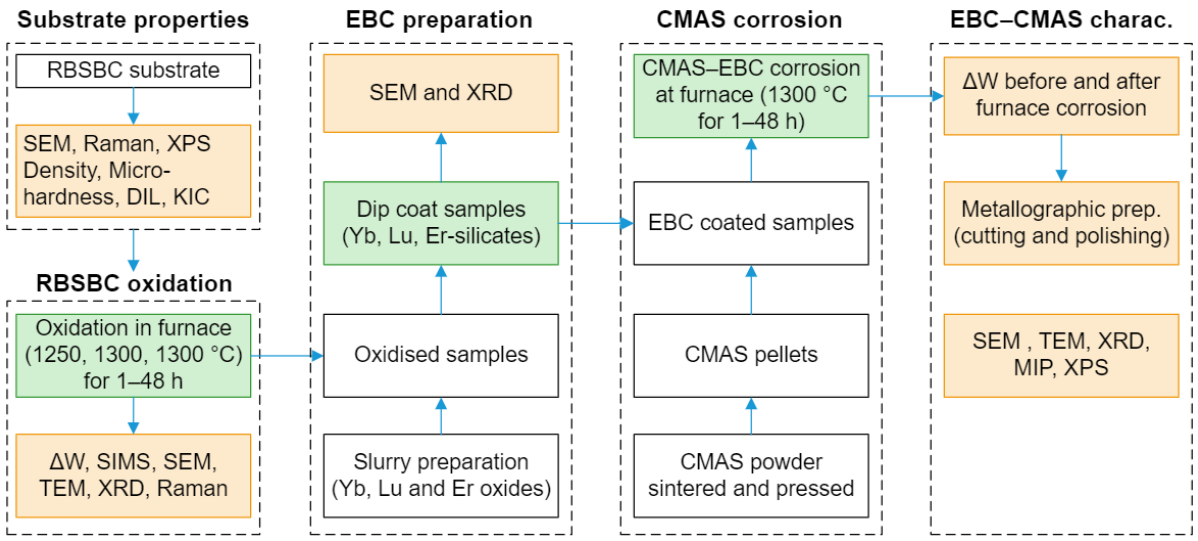


Figure 3.21 Flowchart for the experiments (green) and characterisation (orange).

4 OXIDATION OF REACTION BONDED SILICON CARBIDE-BORON CARBIDE IN AIR

K. El Shafei and N. Al Nasiri, "Oxidation of reaction-bonded silicon carbide-boron carbide in air," *Ceramics International*, vol. 47, no. 12, pp. 17463–17470, 2021.

4.1 INTRODUCTION

Oxidation studies of RBSBC have not been thoroughly addressed in the literature, particularly for low boron concentrations. Previous studies of SiC–B_4C materials incorporated high boron carbide, ranging from 25 to 67 wt% [246-248]. This chapter provides an insight into the oxidation behaviour of RBSBC with low B_4C content (~7 wt%) in order to examine the applicability of an economical and lightweight RBSBC with high oxidation resistance compared to SiC. In addition, the RBSBC substrate forms the basis of the coating system, discussed in chapter 5, so studying its microstructure and oxidation properties is essential in understating the substrate-coating interaction.

4.1.1 Microstructure

Previous authors [16, 30, 37, 38] recorded the morphology of RBSBC to consist of core-rim structure, where the original α-SiC is surrounded by a very thin rim of β-SiC. It was proposed that dissolution-precipitation is responsible for the formation of the core-rim morphology. Zhou et al. [38] however states that the Si/C reaction is an electrochemical process governed by redox reaction, whereby silicon is oxidised and C is reduced to form SiC. This assumption is refuted by Wang et al. [16] because, unlike the dissolution-precipitation model, it doesn't account for the formation of core-rim structure.

Regarding B–C–Si, Solodkyi et al. [41] stated that the formation of $B_{12}(B, C, Si)_3$ is diffusion controlled and therefore, it is affected by infiltration temperature and time. This assumption is in accordance with Zhang et al. [40], and Wang et al. [36], who proposed Si inward diffusion into the B_4C grain to explain $B_{12}(B, C, Si)_3$ phase formation at B_4C rim. Alternatively, other authors [37, 249-251] on the other hand, suggested dissolution-precipitation mechanism where B_4C dissolution by molten silicon results in the precipitation of silicon-rich $B_{12}(Si, B, C)_3$ phase at the B_4C rim.

According to Wang et al. [36] and Hayun et al. [37], the formation of β-SiC plates inside the B_4C grains, which they presumed to be formed by dissolution-precipitation. During cooling, C and B solubility in Si decreases and SiC supersaturates the liquid to precipitate β-SiC [16]. SiC forms because it is more stable than B_4C at 1600 °C [36]. This results in secondary phase β-SiC being trapped inside B_4C grains. Ness and Page [30] relate the β-SiC plate-like morphology growth to carbon concentration, where they tend to grow towards the carbon saturated areas creating an elongated structure in the process [36].

4.1.2 Oxidation

According to Lamkin et al. [65], oxygen diffuses through silica by the motion of molecular oxygen through the voids or via occupation of the lattice vacancies in the SiO_4 tetrahedral network by ionic oxygen O^{2-}.

Ramberg and Worrell [64] observed parabolic rate behaviour for Si–SiC, as well as for chemical vapor deposition CVD-SiC oxidised between 1200 and 1600 °C in dry oxygen. They observed the formation of amorphous SiO_2, with activation energy E of 361 kJ mol^{-1}, at temperatures above 1350 °C, which they attributed to O^{2-} diffusion through the silica scale as the rate-controlling step for oxidation. It was deduced that O^{2-} diffusion becomes dominant above 1300 °C, resulting in an increase in the activation energy. Costello and Tressler [252] oxidise single-crystal α-SiC in dry O_2 at temperatures of 1200–1500 °C and attributed the activation energy (289 kJ mol^{-1}) to O^{2-} diffusion through the oxide layer above 1400 °C. Narushima et al. [53] recorded a two-stage parabolic behaviour for CVD-SiC oxidised in dry oxygen at 1550–1675 °C, with activation energies of 345 and 387 kJ mol^{-1}. Their findings agree with those of the above-mentioned authors [64, 65, 252]. Narushima et al. [53] observed that the crystallisation of amorphous SiO_2 results in deviation from parabolic behaviour due to the change in oxidation kinetics and in E for O_2 transport through the oxide layer. Ogbuji and Opila [47] oxidised CVD-SiC cyclically at 1200–1500 °C in dry oxygen and found parabolic behaviour for the growth of amorphous SiO_2, with an activation energy of 118 kJ mol^{-1}. It was proposed that the permeation of molecular oxygen through silica dominates oxygen transport at the SiO_2/SiC interface. Ogbuji and Singh [73] also studied RBSC in dry air between 1100–1400 °C for 50 hrs and found parabolic oxidation behaviour. Costello and Tressler [252] oxidised single-crystal α-SiC in dry O_2 at temperatures of 1200–1500 °C and attributed the activation energy (289 kJ mol^{-1}) to O^{2-} diffusion through the oxide layer above 1400 °C.

On the other hand, Fitzer and Ebi [253] studied the oxidation of SiC in air and pure O_2, and reported O_2 diffusion to control the reaction process up until 1400 °C then CO diffusion out of the oxide is the rate-controlling step between 1400–1600 °C. This was confirmed by Pultz and Hertl [50] when they suggested that oxidation of SiC is controlled by CO desorption from the SiO_2/SiC interface thus opening more sites for further oxidation.

According to Telle [251], materials in which B_4C particles that are enveloped by SiC exhibit higher oxidation resistance than SiC materials. Ogawa et al. [254] oxidised C–SiC–B_4C at 1000–1300 °C in air and noticed that the SiO_2 content is proportional to the SiC/B_4C ratio, where a higher SiO_2 content results in a more protective oxide layer. This is due to the higher viscosity and lower vapour pressure of SiO_2 compared to those of B_2O_3 and SiO_2–B_2O_3. Narushima et al. [70] oxidised SiC–B_4C (35 wt%) in O_2-rich atmosphere at temperatures of 800–1500 °C. They considered the diffusion of molecular oxygen through the borosilicate layer to be the rate-controlling step for oxidation. They noted that increasing the SiO_2 content in SiO_2–B_2O_3 resulted in a protective SiO_2 layer dominating the oxide. Gogotsi et al. [68] studied the oxidation resistance of SiC–B_4C–AlON ceramics in air at 1500 °C. They observed that increasing SiC/B_4C ratio leads to the formation of borosilicates which extend the serviceability of B_4C-contained ceramics in oxidizing environments up to 1350 °C.

The presence of cracks in the amorphous oxide layer were observed by Narushima et al. [53], Ogbuji and Opila [47], and Ramberg and Worrell [64]. It was attributed to thermal stresses occurring between different SiO_2 polymorphs. They can be the result of CTE mismatch between amorphous and crystalline SiO_2 [64] or from internal stresses arising from volumetric expansion [47, 53].

4.2 METHODOLOGY

The oxidation kinetics are presented as the oxide weight gain vs. oxidation time. The weight gain was measured using a mass balance (Ohaus Pioneer, USA) with an accuracy of ± 0.01 mg. Samples of 10 × 10 × 4 mm were placed inside zirconia boats (Almath, UK) in a chamber lift-up furnace (Lenton, UK), where oxidation at 1250, 1300 and 1350 °C were conducted in laboratory air at a heating rate of 10 °C min^{-1} for 5, 24, 48, 72, and 96 h. The testing temperature of 1350 °C is chosen as the upper testing limits because the silicon present in the material melts at 1410 °C. The oxidation kinetics were analysed using the parabolic rate law [Eq. (4.1)], where ΔW (mg) is the weight change before and after oxidation, A (mm^2) is the sample surface area, and t is the oxidation time. The parabolic rate constant k_p ($kg^2\ m^{-4}\ s^{-1}$) was obtained from the weight gain versus time plot. The activation energy E (kJ mol^{-1}) was calculated using the Arrhenius equation [Eq. (4.2)], where A^* is a pre-exponential factor accounting for the initial rapid oxidation period (determined from experimental results) and R (J k^{-1} mol^{-1}) is the universal gas constant.

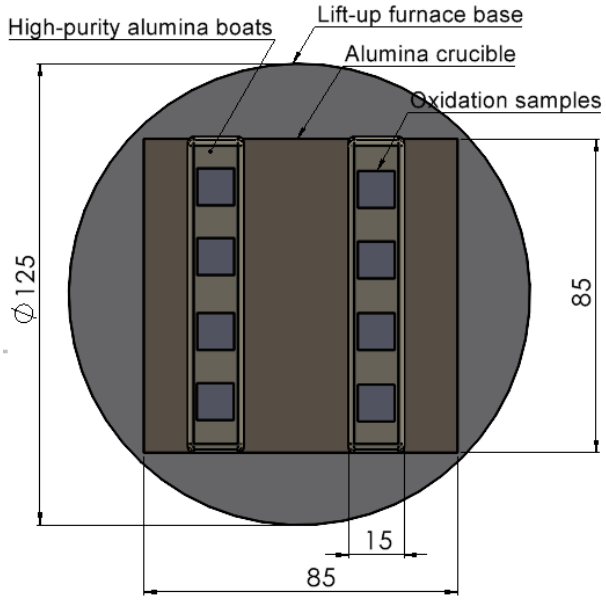


Figure 4.1 Top view of the sample arrangement for the oxidation tests.

$$(\Delta W/A) = \sqrt{k_p.t} \tag{4.1}$$

$$k_p = A^*.e^{(-E/RT)} \tag{4.2}$$

4.3 RESULTS

4.3.1 Properties and microstructure

The studied material is RBSBC supplied by M-Cubed Technologies, Inc. There was no provided data or catalogue for the received material, so testing was required to understand material properties. RBSBC has an experimental density of 2.915 gm cm^{-3}, theoretical density of 2.981 gm cm^{-3} and relative density of 90% making it a lightweight material, that falls between B_4C (~2.6 gm cm^{-3}) and SiC (~3.2 gm cm^{-3}). It is close to the value recorded by M-Cubed Technologies for reaction-bonded silicon carbide (2.8–3.0 gm cm^{-3}) [33, 36, 255]. The CTE calculated between 23–1350 °C is 4.8×10^{-6} $°C^{-1}$ which is between that of SiC (4.5×10^{-6} $°C^{-1}$) and B_4C (> 5×10^{-6} $°C^{-1}$). The measured young's modulus E is 370 GPa and the Poisson's ratio v is 0.18. The measured K_{IC} (3.2 MPa $m^{1/2}$) is slightly lower than the one recorded by M-Cubed for RBSBC (4 MPa $m^{1/2}$) [28, 255]. The grain size of SiC is between 15–20 μm, while B_4C is ~50 μm. The coarse grains matches those used by Aghajanian et al. [256] at M-cubed Technologies for SiC–B_4C–Si composites, which is ~50 μm. Thus, the original SiC particles are coarse and/or excess carbon was used in the slurry during fabrication. The material is designed for high temperatures and corrosion resistance [28].

SEM imaging (Figure 4.2a) shows that SiC and B_4C grains are connected by a residual silicon pool. The B_4C grains have plate-like α-and β-SiC trapped inside them. Figure 4.2b is a backscattering image (BEC) showing the core-rim structure of the original SiC surrounded by a secondary phase SiC. It also shows the B_4C grains to be surrounded by SiC particles across its perimeter. Based on EDS analysis, the B_4C grains contained Si (~4 %) and Al (~1 %), where Si and Al atoms occupy vacancies in the B_4C crystal structure forming a B_4C–Si–Al solid solution ($B_4Si_xAl_yC$). The Raman spectra in Figure 4.3a shows that the SiC core (point 1) is formed from α-SiC. This is evident form the Raman peaks at 149, 788 and 797 cm^{-1}. The rim of the structure (point 2) shows a notable decrease in the α-SiC peaks and a rise of the β-SiC peaks at 796 and 971 cm^{-1}, in addition to Si peak at 518 cm^{-1} and a small B peak at 240 cm^{-1}. The B peak is only noticed in few samples. Raman spectra on the B_4C core grains (Figure 4.3b point 3) shows the presence of B_4C through the 480 and 530 cm^{-1} twin peaks and 1060 cm^{-1} peak, in addition to small traces of SiC. Further from the B_4C core and towards the edges (points 4 and 5), the presence of Si (518 cm^{-1}) and SiC (797 and 971 cm^{-1}) becomes evident.

The SiC inside the B_4C grains (point 5) consists of α-SiC in addition high amount of β-SiC. Si is also detected at the SiC grains.

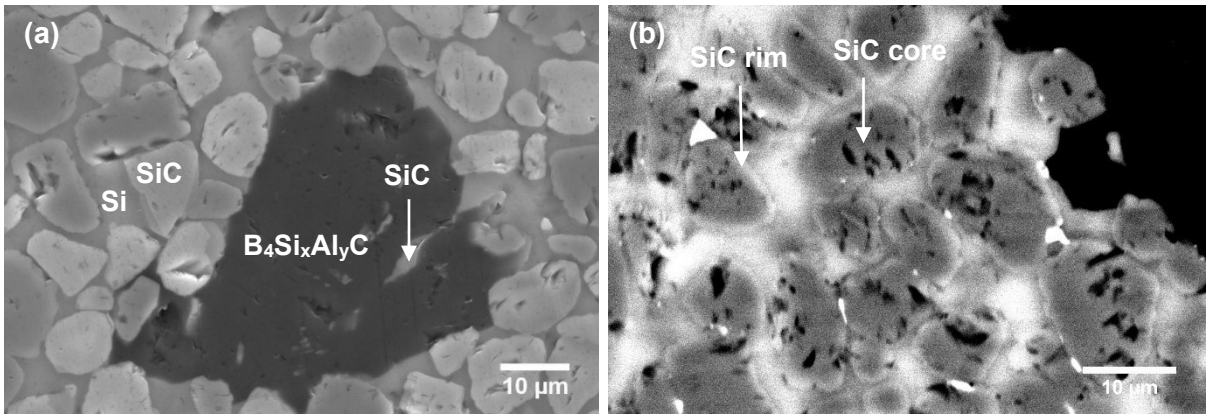


Figure 4.2 (a) SEM image of RBSBC the microstructure (b) BEC of the SiC grains.

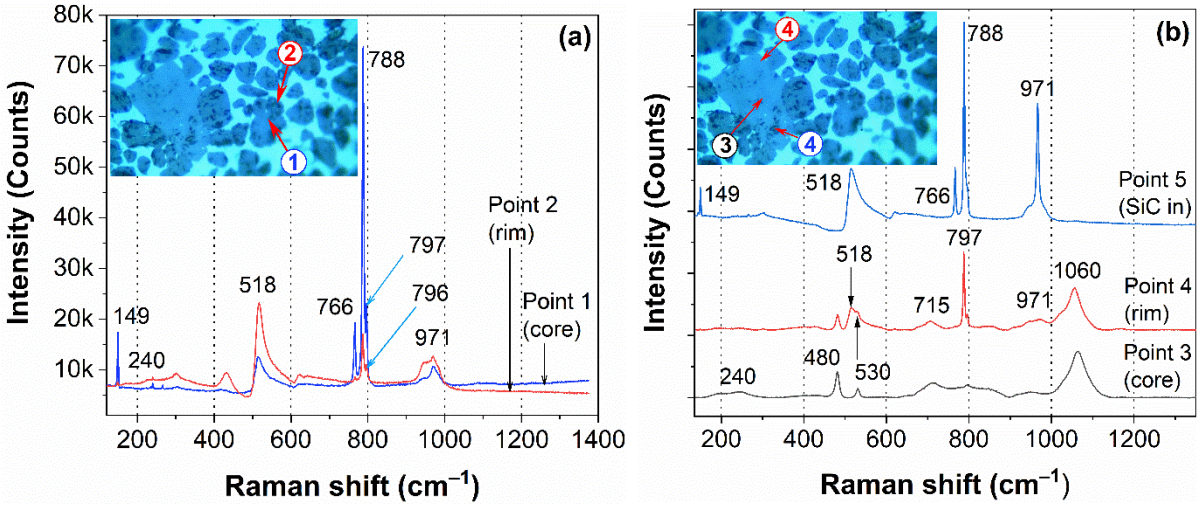


Figure 4.3 (a) Raman spectra for the SiC core and rim (b) B_4C core and rim.

XRD analysis (Figure 4.4) reveals the existence of α-SiC, β-SiC, $B_4Si_xAl_yC$, Si and Al, where all phases are crystalline. The main peak of $B_4Si_xAl_yC$ at 37.6° falls between the B_4C peak at 37.8° and that of the $B_{12}(B, C, Si)_3$ phase at 37.4°. This is attributed to the lower Si (~4%) concentration in $B_4Si_xAl_yC$ compared to 6% in $B_{12}(B, C, Si)_3$, which shifts the 2θ value towards that of B_4C. The composition of RBSBC obtained from RIR is: 82% SiC, 7% $B_4Si_xAl_yC$, 10% Si and 1% Al. This shows that RBSBC is formed using SiC as the main filler material with $B_4Si_xAl_yC$ acting as a reinforcement.

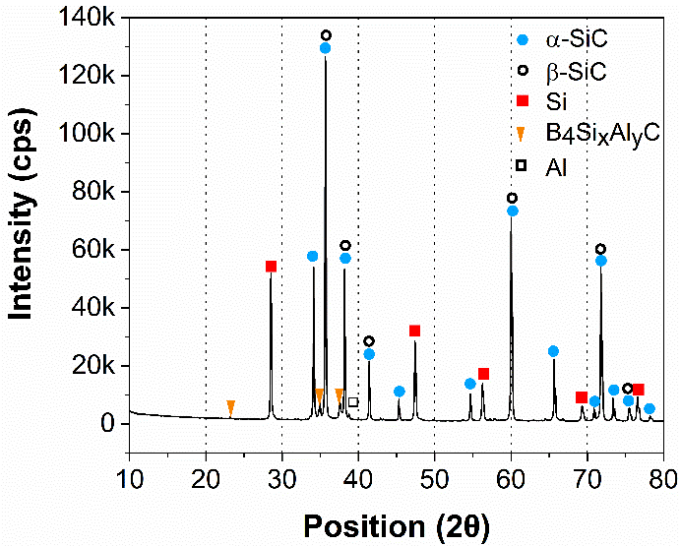


Figure 4.4 XRD peaks of RBSBC showing crystalline SiC (α and β), $B_4Si_xAl_yC$, and Al.

4.3.2 Oxidation kinetics

The XRD plots for the samples oxidised at 1250 °C (Figure 4.5a) and 1350 °C (Figure 4.5b) for 24–96 h shows an increase in silica content with increasing oxidation time. The growing SiO_2 peak at ~22° is associated with a decrease in the Si (28.5°) and SiC (35.7°) peaks. The silica peak is highest at 96 h, indicating the thickest oxide layer. This peak is more intense for the sample oxidised at 1350 °C than for the sample oxidised at 1250 °C, reflecting an increase in silica content with temperature, and higher oxidation rate. The intensity of the silicon peak at 28.5° declined to a greater extent with oxidation time compared to the SiC peaks, suggesting that silicon oxidation is predominant over SiC oxidation. The peak of $B_4Si_xAl_yC$ did not decline notably because this peak is small relative to those of the major phases. Borosilicates are not detected.

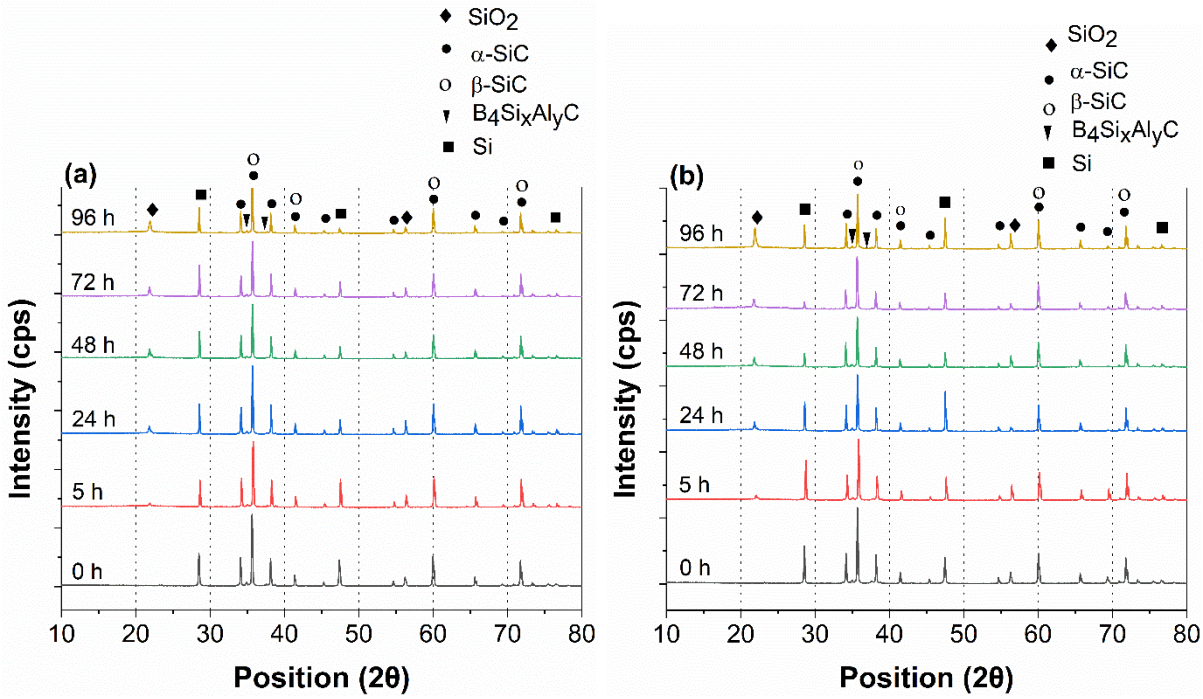


Figure 4.5 XRD for the oxidised samples at (a) 1250 °C (b) 1350 °C.

SEM images (Figure 4.6–Figure 4.8) show a proportional relationship between the oxide thickness and oxidation temperature and duration, which matches with the XRD results. The oxide (shown as white dahed line in Figure 4.6a) could barely be detected at 5 h of oxidation for the oxidation temperatures. With oxidation at 1250 °C (Figure 4.6), the oxide layer is thin and non-uniform after 24 h, consistent with almost non-observable SiO_2 peaks in the XRD pattern. The oxide became noticeable after 48 h and reached its maximum thickness after 96 h. The same pattern was observed at 1300 and 1350 °C (Figure 4.7 and Figure 4.8 respectively). Oxidation at 1350 °C results in a thicker and more uniform silica layer than that formed at 1250 and 1300 °C. This indicates a denser and more protective oxide layer. Table 4.1 shows the measured oxide thickness. Pores are observed at the SiO_2–SiC interface and around the $B_4Si_xAl_yC$ grains (Figure 4.6d, Figure 4.7c and Figure 4.8d) due to the evolution of CO and CO_2 gases as a result of SiC and O_2 reaction, and B_2O_3 formation from B_4C and O_2 reraction. In the case of the thin oxide layers formed at 5 and 24 h, rapid evolution of the gases disrupted the formation of a uniform and protective oxide layer. However, no cracks were observed in the substrate or the oxide layer.

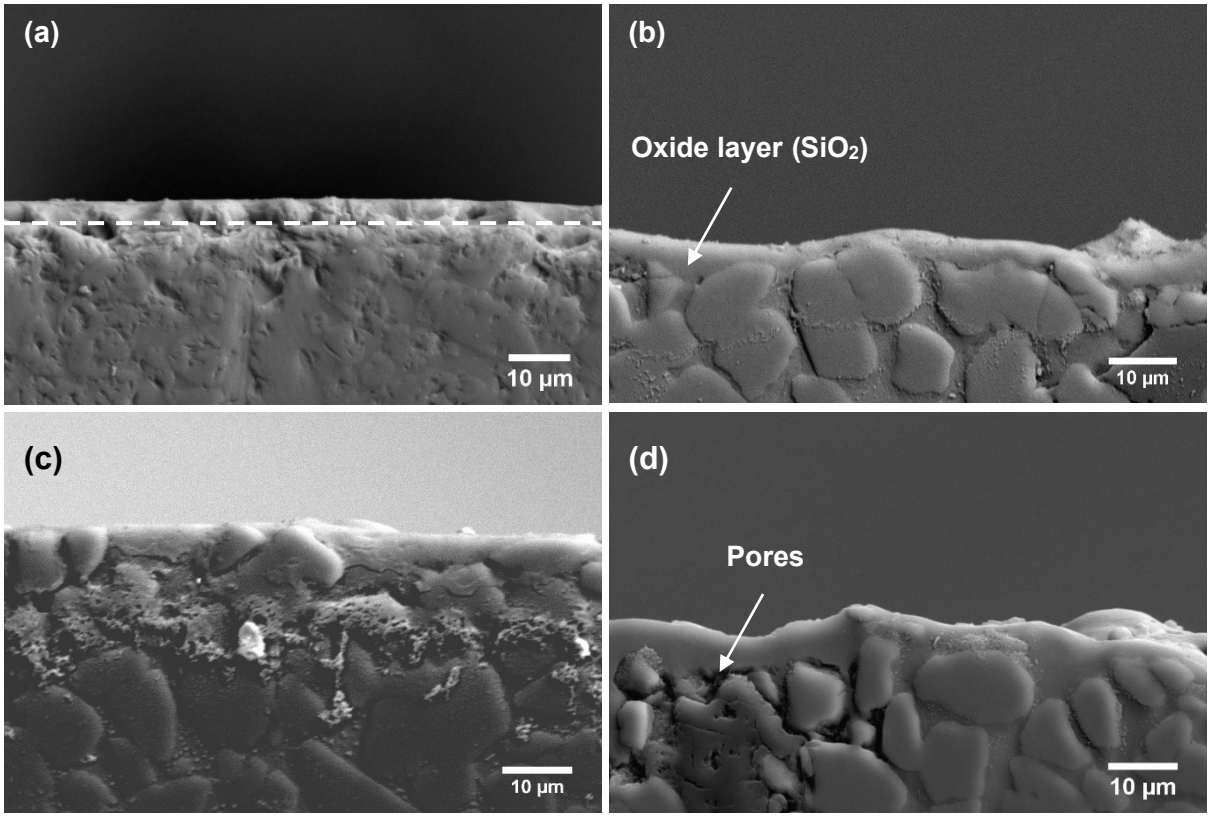
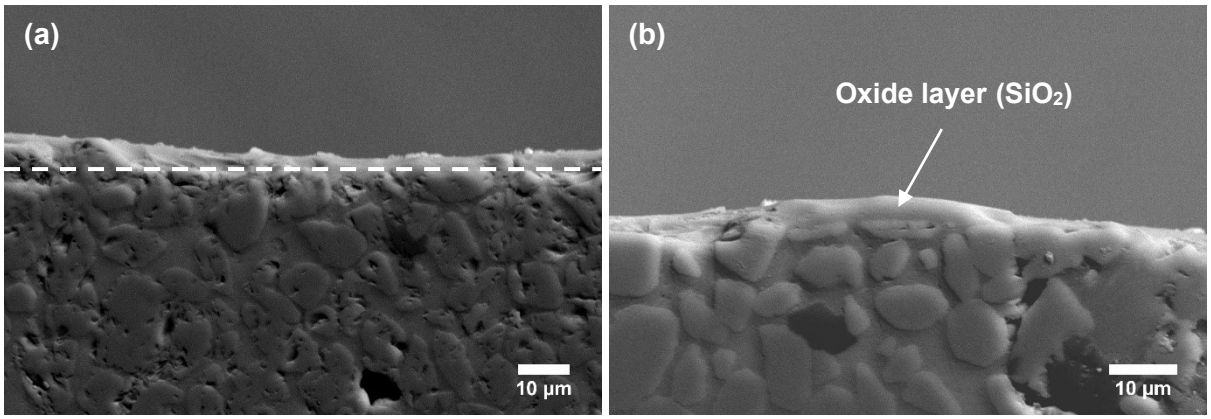


Figure 4.6 SEM images of the oxide layer at 1250 °C (a) 24 h (b) 48 h (c) 72 h (d) 96 h.



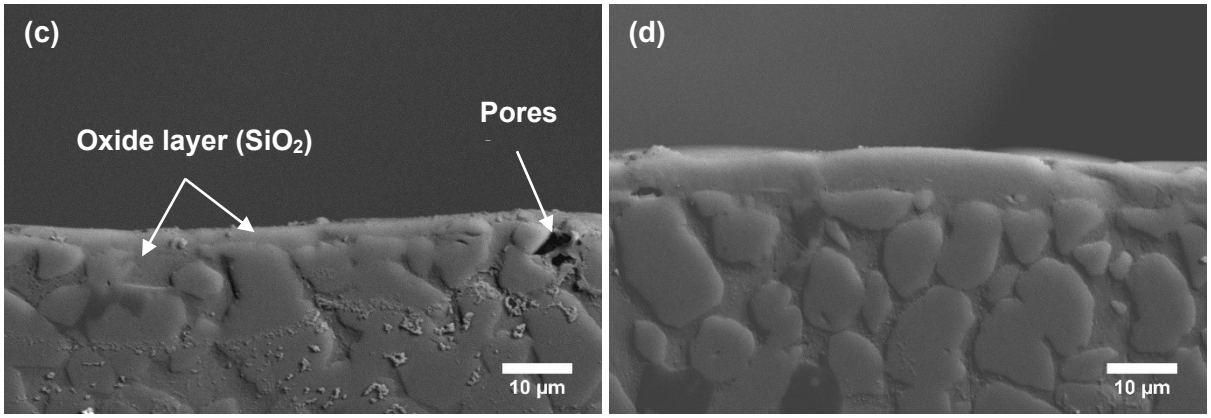


Figure 4.7 SEM images of the oxide layer at 1300 °C (a) 24 h (b) 48 h (c) 72 h (d) 96 h.

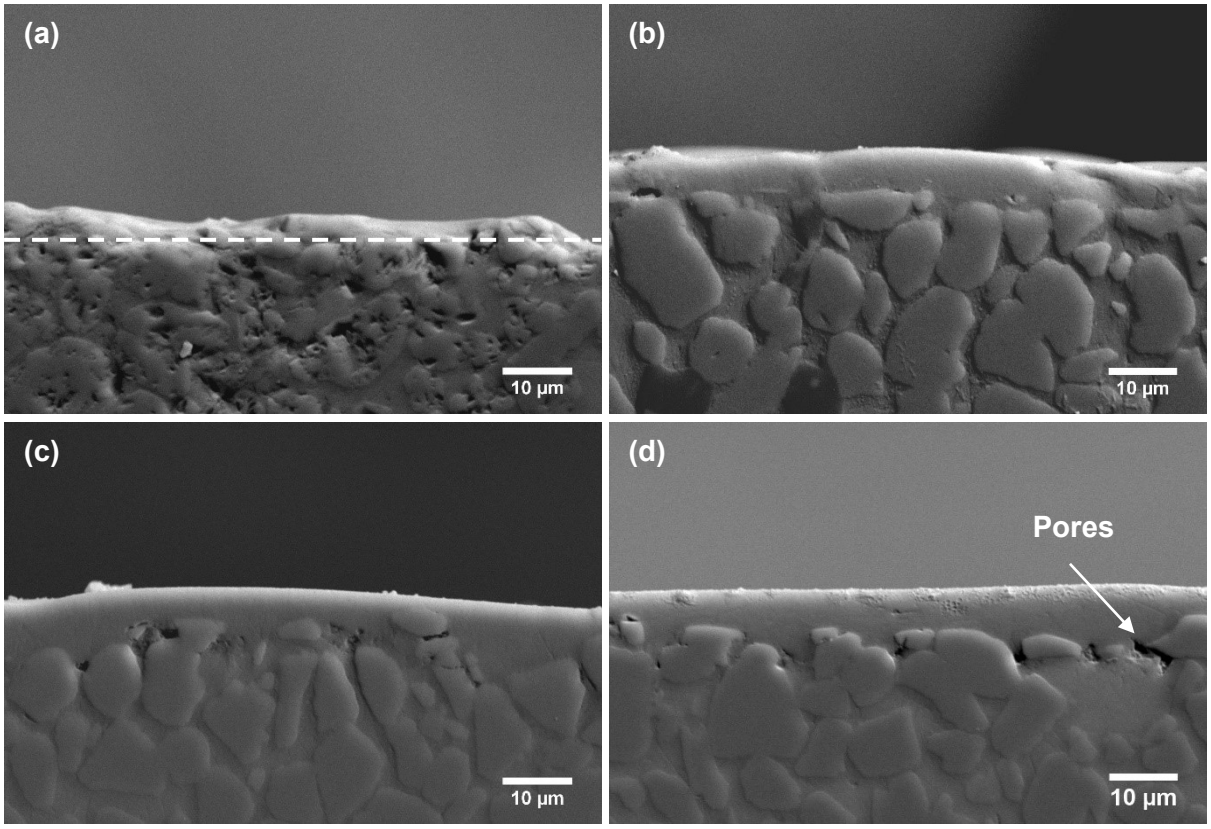


Figure 4.8 SEM images of the oxide layer at 1350 °C (a) 24 h (b) 48 h (c) 72 h (d) 96 h.

Table 4.1 Weight gain and thickness measurements for oxide layer between 5–96 h.

Time (h)	1250 °C		1300 °C		1350 °C	
	ΔW (mg)	L (μm)	ΔW (mg)	L (μm)	ΔW (mg)	L (μm)
5	0.00 ± 0.12	1.3 ± 0.43	0.00 ± 0.13	1.8 ± 0.53	0.00 ± 0.23	2.3 ± 0.54
24	0.20 ± 0.24	2.4 ± 0.47	0.27 ± 0.36	2.5 ± 0.83	0.45 ± 0.48	2.7 ± 0.93
48	0.30 ± 0.05	2.6 ± 0.8	0.50 ± 0.15	3.2 ± 1.02	0.70 ± 0.34	3.9 ± 1.40
72	0.35 ± 0.15	3.1 ± 1.2	0.60 ± 0.17	4.0 ± 1.33	0.90 ± 0.14	4.8 ± 1.58
96	0.45 ± 0.67	3.7 ± 1.0	0.70 ± 0.20	4.7 ± 1.22	1.03 ± 0.04	5.8 ± 1.52

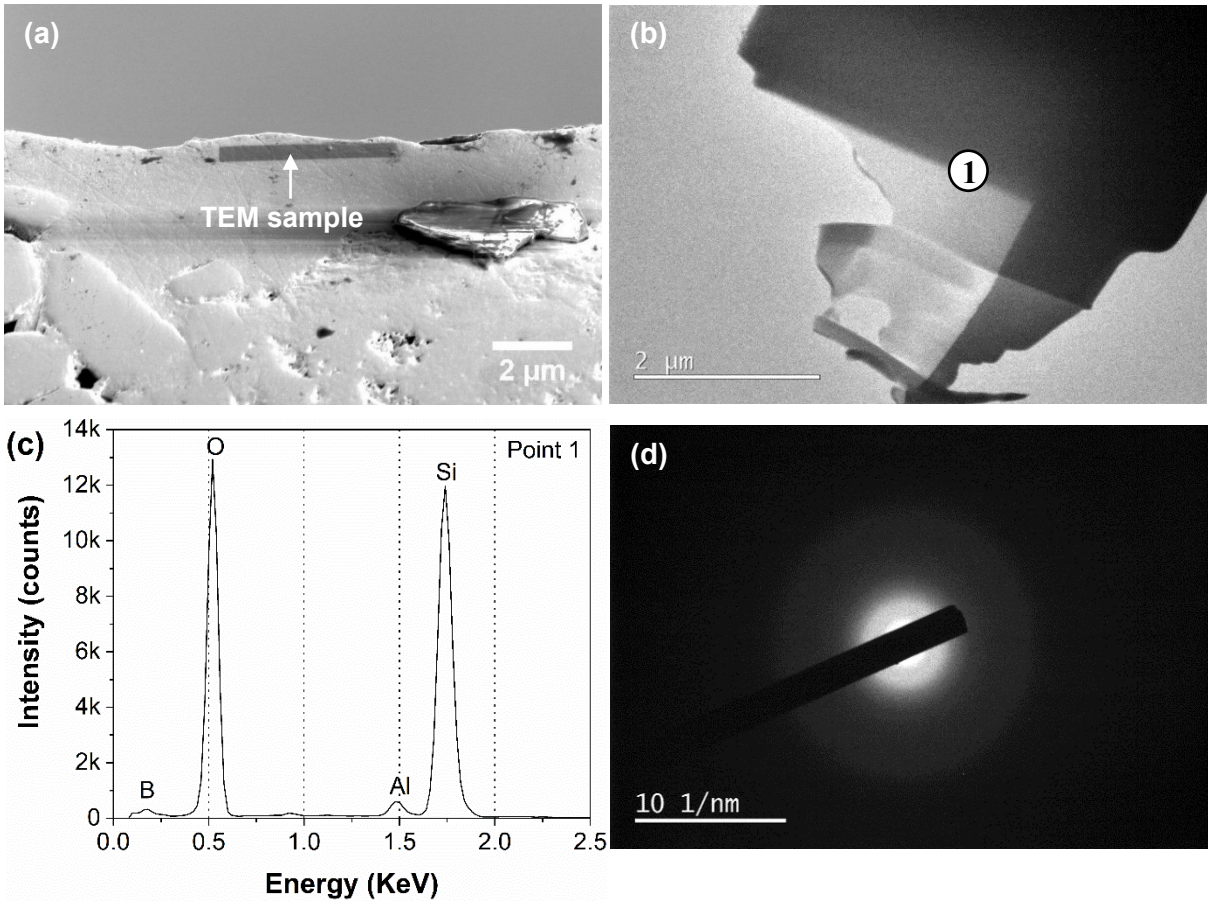


Figure 4.9 TEM of the oxidised sample at 1350 °C for 72 h with FIB location and EDS.

TEM images (Figure 4.9) of the oxidised samples at 1350 °C for 72 h show the location of the FIB lamella (Figure 4.9a) and an image of the oxide layer (Figure 4.9b) with the EDS location at point 1. Elemental analysis (Figure 4.9c) shows a composition of 8 mass% B, 57 mass% O, 33 mass% Si and 1.5 mass% Al. The detection of boron indicates the presence of borosilicate

or borate groups. The diffraction pattern (Figure 4.9d) lacks diffraction spots, which shows an amorphous oxide layer.

Raman spectra is recorded at 1350 °C for 72 h, where it shows the oxide layer to consist of vitreous SiO_2, as the main phase, in addition to borate units. The analyses are performed at the oxide surface and close to the substrate (points 1 and 2 respectively in Figure 4.10). The 420 cm^{-1} peak is assigned to vitreous SiO_2 [257]. The Raman peak at 527 cm^{-1} may be related to both SiO_2 and B_2O_3 in the borosilicate [258]. According to Hassan [259], the 525 cm^{-1} peak is attributed to vitreous B_2O_3 and becomes more intense with temperature. On the other hand, the 530 cm^{-1} peak is assigned to the vibrations of Si–O–Si in the SiO_4^{4-} network [260]. Furukawa and White [261] noticed a band between 500 and 550 cm^{-1} that intensified with increasing SiO_2/B_2O_3 ratio, which they attributed to Si–O–Si and Si–O–B bonds. Walrafen et al. [262] also assigned the 570 cm^{-1} peak in the profile of molten B_2O_3 at 1152 °C to the motion of BO_3 triangles involved in a random network. The small peak at 640 cm^{-1} may be a distortion of the 630 cm^{-1} peak of the ring-type BO_3 groups [260, 261, 263], while the 770 cm^{-1} peak is assigned to BO_4 units [261, 263, 264]. Finally, the peak at 970 cm^{-1} peak is assigned to BO_3 groups [265]. The Intensity of the Raman peaks decreases for the measurements taken closer to the substrate, indicating less diffusion of oxidising species across the borosilicate layer.

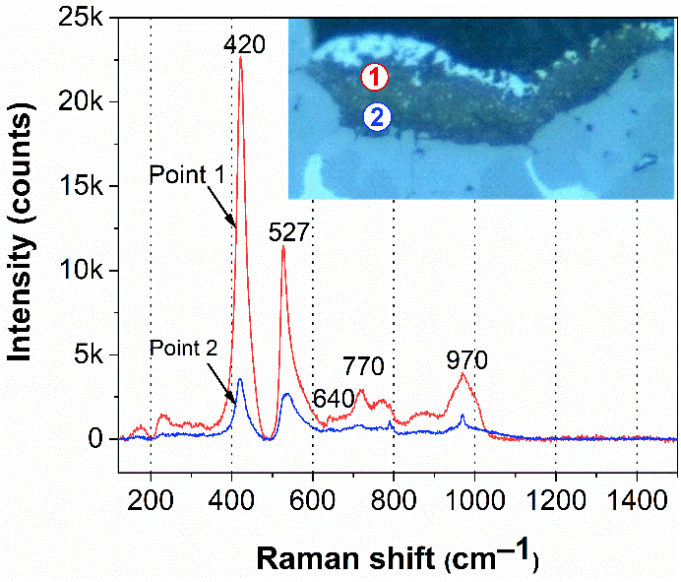


Figure 4.10 Raman spectra of the oxide layer at 1350 °C for 72 h.

The SIMS depth profile (Figure 4.11) shows the distribution of boron across a 4.5 μm oxide depth. The relative amount of boron with respect to Si–O is approximately two orders of magnitude lower (shown in the log counts vs. depth plot in the inset of Figure 4.11), indicating a low content of boron species inside the silica-rich layer. This is confirmed by the low amount of boron detected by TEM and the detection of the SiO_2 peak in the XRD pattern instead of that of borosilicate. The boron content increases gradually and becomes constant when the oxide layer reaches a depth of 1 μm, which shows that the oxide surface is almost SiO_2 dominated. The distribution of boron in the oxide layer is almost constant.

The oxidation kinetics are shown in Figure 4.11b as the normalised weight gain versus the oxidation time. The curves show parabolic behaviour, where weight gain occurs due to Si and SiC oxidation. The percentage increase in the mass gain (Table 4.1) becomes less from 72 to 96 h indicating an enhancement of the protective effect of the oxide, where oxygen diffusion through the oxide layer is hindered. The maximum weight gain is observed at 96 h, as confirmed by the SEM images and XRD results. The weight gain at 1350 °C is higher than that at 1250 °C and 1300 °C reflecting a thicker oxide layer. The parabolic rate constant values are 1.66×10^{-8}, 4.30×10^{-8} and 9.28×10^{-8} $mg^2\ mm^{-4}\ hr^{-1}$ at 1250, 1300 and 1350 °C, respectively. The higher value of k_p at 1350 °C reflects a higher oxidation rate, forming a thicker and denser oxide layer.

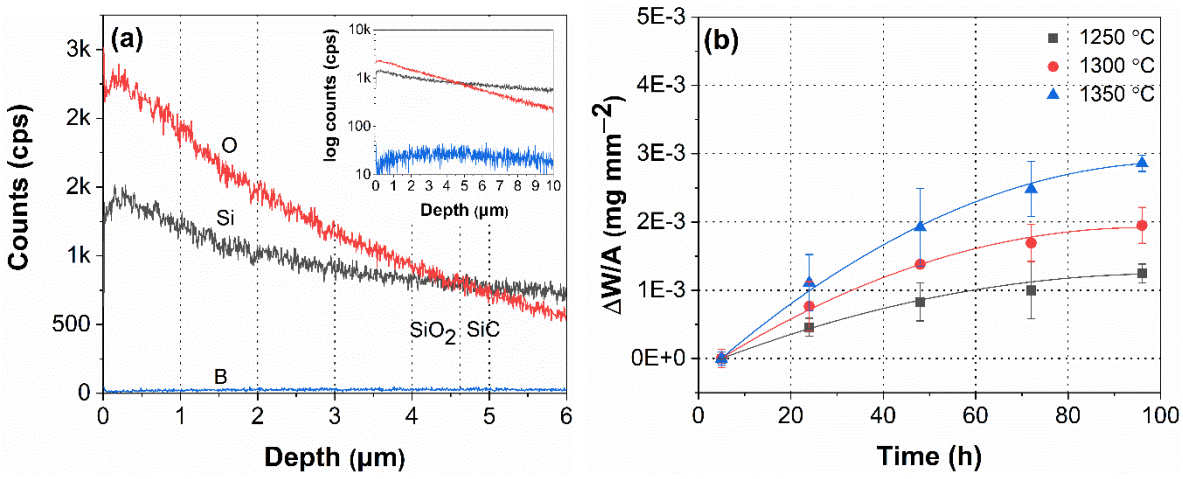


Figure 4.11 (a) SIMS profile for the oxide layer at 1350 °C after 72 h. (b) ΔW plot.

4.4 DISCUSSION

4.4.1 Substrate microstructure

Based on the core-rim structure, it is evident that the dissolution-precipitation mechanism formed SiC grains [16, 30, 36] because the electrochemical reaction between Si and C does not explain the formation of core-rim morphology. During Si infiltration, C in the material dissolves in molten Si raising the local infiltration temperature, which increases C solubility in Si [30]. Consequently, C concentration gradient forms in Si causing dissolved C to diffuse from high solubility regions (reaction regions) to lower solubility ones (non-reaction regions) at the peripheries of the SiC grains (Si/C rim regions). This leads to the formation of SiC solid solution that precipitates as β-SiC. Secondary β-SiC preferentially precipitates at the rims of the existing α-SiC grains to lower their nucleation energy compared to nucleating in the liquid phase, thereby creating a core-rim morphology [16, 36]. The presence of both α-SiC and β-SiC (Figure 4.3a) suggest uncomplete β to α transformation during the exothermic reaction between Si and C, which is arrested once the Si/C solid solution is saturated. The precipitation of β-SiC at the boundaries of B–C–Si–Al results in their entrapment in B–C–Si–Al grains during their growth, where the precipitate form needle-like grains because of the anisotropic nature.

Microhardness test on the B_4C grains confirm the results of EDS analysis and XRD that they contain Si and Al making them $B_4Si_xAl_yC$. The microhardness of $B_4Si_xAl_yC$ grains (39 ± 3 GPa) falls between that of B_4C (33 GPa) and boron carbide-rich $B_{13}(B, C, Si)_3$ phase (46 GPa) [266]. The formation of the B_4C–Si–Al phase is through dissolution-precipitation, where molten silicon dissolves in B_4C grains to form a solid solution of Si in B_4C, and precipitates as boron carbide rich grains containing Si. The presence of Si and SiC increases away from the B_4C core and towards the Si melt pool. The transformation of all B_4C grains to $B_4Si_xAl_yC$ is due to the presence of aluminium. Hayun [267] noticed that the presence of aluminium in the B_4C–Si system enhances the transformation of boron carbide grains to B–C–Si–Al. The dissolution of Si into B_4C (to form B–C–Si) results in the release of C, which reacts with the Si pool to form SiC at its periphery as shown in Figure 4.2 and Eq.(4.3) [251]. This explains the detection of β-SiC Raman peaks at the B–C–Si grains (Figure 4.3), and also account for the precipitation of plate-like β-SiC inside the B–C–Si phase.

$$B_4C + Si \rightarrow SiC + B_xSi_yC_z\ [\boldsymbol{i.e.}, B_{12}(B,C,Si)_3] \quad (4.3)$$

4.4.2 Oxide layer

The analysis revealed the presence of a borosilicate layer. The boron content on the inside of the oxide layer is relatively low (8 mass%), as shown by TEM and SIMS analysis, which indicates that the oxide is a silica-rich borosilicate layer. This is also confirmed by XRD, showing the presence of a SiO_2 peak at the expense of a borosilicate one. The mechanism of borosilicate formation starts with B_4C oxidation to $B_2O_{3(l)}$ at ~700 °C. Silica dissolves in $B_2O_{3(l)}$ to form SiO_2–B_2O_3 until the solubility limit is exceeded and SiO_2 covers the borosilicate layer. This is aided by the evaporation of liquid boria from the borosilicate network at ~1100 °C, which helps to decrease the boron content in the oxide, leaving a rich SiO_2 structure (Figure 4.12). The high (SiC + Si)/B_4C ratio plays a role in forming a silica-rich borosilicate layer, where the slow growth rate of SiO_2 dominates oxide formation, aided by the lower vapour pressure of SiO_2 compared to that of B_2O_3. The slower rate of formation of SiO_2 compared to B_2O_3 [254] makes it the rate limiting step, where the rate of formation of SiO_2 controls the growth rate of borosilicate oxide layer.

The increase in the boron concentration profile at a depth of up to 1 μm indicates that the SiO_2 in the oxide surface originates from the high SiO_2/B_2O_3 ratio. The growth of the oxide scale and the high viscosity of SiO_2 compared to that of B_2O_3 and SiO_2–B_2O_3 impedes oxygen diffusion through the oxide scale and can also supress the evaporation of liquid boria. This is evident from the higher boron concentration with increasing oxide depth compared to that at the surface (≤ 1 μm). The presence of free silicon increases the SiO_2/B_2O_3 ratio by providing short routes for oxygen diffusion, which increases the overall oxidation rate due to the higher oxidation rate of silicon compared to that of SiC [73]. The B_2O_3 consists of boroxol rings attached to the SiO_4^{4-} network. At 1250–1350 °C, the boroxol rings decompose to borate units (BO_3 triangles) that are randomly distributed within the SiO_4^{4-} framework, accounting for the absence of the 806 cm^{-1} Raman band for the borosilicate structure [259], while the 527, 640, and 971 cm^{-1} bands of the BO_3 units and the 770 cm^{-1} of the BO_4 rings are observed instead. Thus, loose BO_3 units are randomly mixed with the SiO_4 network [106], where the extent of mixing increases with temperature and high silicon content [106, 268]. The amorphous oxide does not show clustering or phase separation, which reflects a high degree of mixing in the

borosilicate glass because the SiO_4 and BO_3 groups are neutrally charged. Müller-Warmuth [269] reported high a degree of random mixing in 90 wt% SiO_2–10 wt% B_2O_3. The presence of BO_4 groups is relatively low and could be traced to high-coordination AlO_5 and AlO_6, present in the SiO_2–Al_2O_3 system, which can compensate for the extra negative charge in SiO_4–O–AlO_4 or BO_4–O–AlO_4 bonds [270]. The presence of aluminium oxides in the network decreases the oxidation resistance because the Al–O bond energy is lower than that of the Si–O and B–O bonds. Thus, AlO_6 can stabilize B–O–Al at high temperature.

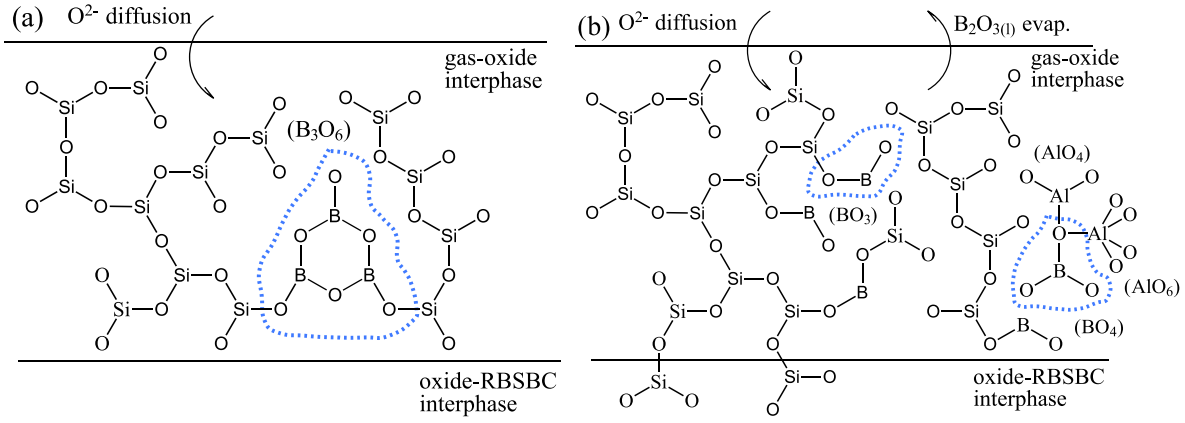


Figure 4.12 2D schematic of the vitreous borosilicate glass. To correspond to 2D representation, Si is shown attached to 3 oxygen atoms instead of 4 and B (in BO_3) is attached to 2 atoms instead of 3.

Previous work [70, 254] recorded a weight loss for B_4C and SiC–B_4C materials upon oxidation. However, the RBSBC is predominantly SiC resulting in weight gain, albeit slow, due to the presence of B_4C, which retards growth of the oxide due to $B_2O_{3(l)}$ evaporation. The low quantity of boria did not negatively affect the oxidation resistance. Boria can be considered an impurity within the silica network that decreases the defect density and thus oxygen diffusion [271]. However, the presence of B_2O_3 exhibits crack-sealing ability up to 1350 °C as a result of the reaction between B_2O_3 and SiC, which would result in the formation of SiO_2 around the surfaces of the SiC cracks. In addition, the formation of lower viscous Si–B–O phase also helps in sealing the cracks at high temperature.

The parabolic rate constant indicates slower oxide growth compared to oxide growth of the silicon carbide materials, as shown in Figure 4.13 and Table 4.2. The oxidation kinetics show parabolic behaviour, where the rate-controlling step for oxide growth is oxygen diffusion

through the borosilicate layer. The activation energy can give an indication on the rate-controlling step of the oxidation reaction. It was calculated to be 353 kJ mol^{-1}, which is in good agreement with the ionic oxygen (O^{2-}) diffusion mechanism in the silica layer. This is expected because SiO_2 is the abundant species in the borosilicate layer, and thus oxygen diffusion through the SiO_4^{4-} network is expected to be rate-controlling. The value of E lies between the value of the activation energy for the permeation of molecular oxygen in vitreous silica (~112–118 kJ mol^{-1}) [47, 65, 272] and the activation enthalpy for Si–O bond breaking (440 kJ mol^{-1}) [47, 65]. However, the E value is closer to the activation energy of the bond-breaking mechanism, suggesting that ionic diffusion dominates the oxygen diffusion process. Because E is not in the range of ~400 kJ mol^{-1}, the formation of network oxygen is most likely aided by the permeation/diffusion mechanism, where O_2 permeation provides interstitial defects for forming network oxygen. Diffusion of ionic oxygen into the silica network can be greatly enhanced by the permeation of molecular oxygen into the network [65]. A permeation mechanism followed by network oxygen diffusion is highly unlikely because the same activation energy prevails across the studied temperature range, indicating that one mechanism controls the oxidation rate. The Arrhenius plot does not deviate between 1250 and 1350 °C, which supports the vitreous nature of the film because any deviation in the parabolic rate behaviour of the oxide layer can result from the difference in the oxygen diffusion rate of the amorphous versus crystalline oxides. The activation energy for oxygen diffusion through the borosilicate layer is close to the values for CVD–SiC and Si–SiC above 1400 °C, as shown in Table 4.2. The oxidation rate of RBSBC is low compared to SiC ceramics. The RBSBC activation energy value that is close to siliconized-SiC above 1400 °C. Finally, the absence of cracks also confirms the vitreous nature of the oxide layer and excludes devitrification occurring on the oxide layer. In addition, the lower CTE of amorphous SiO_2-dominated borosilicate glass (~0.2×10^{-6} $°C^{-1}$ [273]) compared to SiC–B_4C substrate allows it to generate compressive residual stresses in the oxide layer adding to its elastic structure.

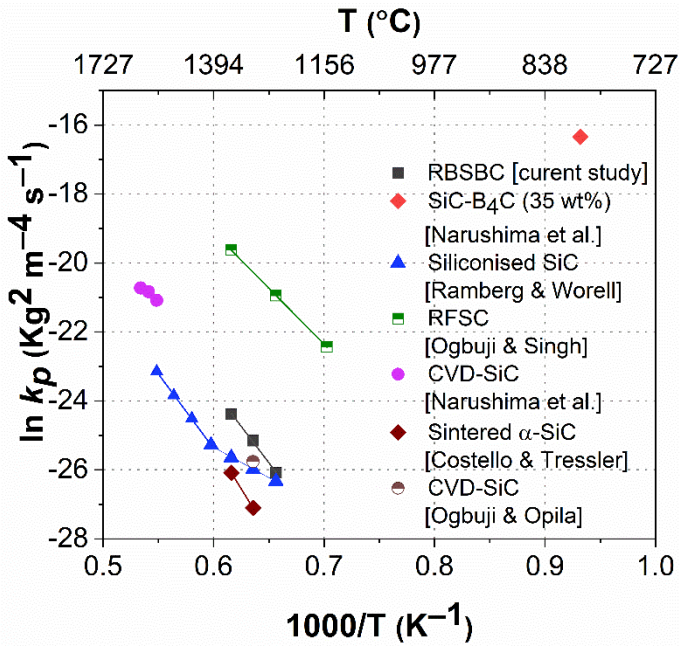


Figure 4.13 Comparison of parabolic rate constants for the oxidation of SiC.

Table 4.2 Oxidation results for SiC and SiC–B_4C materials from previous authors.

Material	Ox. temp. (°C)	Env.	E (kJ mol^{-1})	k_p (Kg^2 m^{-4} s^{-1})	Oxide form	Ref.
RBSBC	1250–1350	Air	353	4.6×10^{-12} (1250 °C) 2.6×10^{-11} (1350 °C)	Amorphous	This study
CVD-SiC	1550–1675	Dry O_2	345 Stg. I 387 Stg. II	7.0×10^{-11} (1550 °C)	Amorphous Crystalline	Narushima et al. [53]
CVD-SiC	1200–1500	Dry O_2 (cyclic)	118	–	Amorphous	Ogbuji & Opila [47]
Sintered α-SiC	1200–1500	Dry O_2	289	–	Amorphous	Costello & Tressler [252]
RFSC	1100–1400	Dry O_2	114	8.0×10^{-10} (1250 °C) 3.0×10^{-9} (1350 °C)	Crystalline	Ogbuji & Singh [73]
Siliconised SiC	1250–1600	Dry O_2	116<1400 361>1400	3.7×10^{-12} (1250 °C) 7.3×10^{-12} (1350 °C)	Amorphous	Ramberg & Worrell [64]
SiC–B_4C (35 wt%)	1000–1500	Dry O_2	–	8.0×10^{-8} (800 °C)	Amorphous	Narushima et al. [70]

4.5 CONCLUSION

The microstructure of RBSBC was composed of SiC and B_4C–Si–Al grains linked by a pool of free Si. The oxidation of RBSBC is studied at 1250, 1300 and 1350 °C in air for 5–96 h. The oxide layer formed at 1350 °C is thicker and offers higher protection than that formed at 1250 and 1300 °C, as evident from SEM images. TEM analysis shows an amorphous oxide with a boron content of ~8 wt%. Raman analysis revealed the presence of BO_3 and BO_4 groups, which were randomly mixed in the SiO_4 framework, resulting in a high degree of intermixing. SIMS analysis also showed a relatively low concentration of boron inside the oxide layer, indicating that the evaporation of liquid boria and the high (SiC + Si)/B_4C ratio results in a SiO_2-rich borosilicate layer. The oxidation kinetics follow parabolic behaviour with low parabolic rate constants and low weight gain, reflecting an oxidation-resistant material. The activation energy of 353 kJ mol^{-1} indicates that the mechanism of oxide growth is dominated by the diffusion of ionic oxygen through the silicate network of the borosilicate layer or a mix of oxygen permeation/ionic oxygen diffusion. The oxide layer behaved like pure silica. RBSBC with 7 wt% B_4C content offers high oxidation resistance comparable to that of silica, but with a lower density. The use of RBSBC will result in a coating system with lower density compared to conventional SiC, while offering similar oxidation resistance.

5 CORROSION BEHAVIOUR OF RARE-EARTH MONOSILICATE-BASED EBCs IN CMAS EXPOSURE

K. El Shafei, "Investigating the mechanism of formation of Ca-rich Ca–Yb apatite that forms from the Yb-silicate–CMAS reaction at 1300 °C," *Materials Characterization*, vol. 210, pp. 113777–113787, 2024.

K. El Shafei, R. Kassem, and N. Al Nasiri, "Diffusion behaviour and corrosion rate of rare earth monosilicate-based EBCs under CMAS exposure," *Ceramics International*, vol. 49, no. 23, Part B, pp. 38544–38555, 2023.

K. El Shafei and N. Al Nasiri, "Corrosion behaviour of rare-earth monosilicates in CMAS exposure," *Corrosion Science*, vol. 202, no. 2, pp. 110312, 2022.

5.1 INTRODUCTION

Most authors studied the corrosion of RE-silicates using spraying techniques such as APS or EB-PVD to produce multi-layered coating architecture, with no focus on dip coating. In addition, most authors also studied the corrosion of RE-monosilicate or RE-disilicate in CMAS environments, with very few studies on RE_2O_3-rich RE-silicates as a CMAS-resistant coat. This chapter studies the corrosion mechanism and morphology of dip-coated EBCs with RE_2SiO_5 bottom coat and RE_2O_3 topcoat processed on reaction-bonded SiC–B_4C substrate, where RE is Yb, Lu or Er, in order to form an economical and efficient CMAS-resistant EBC. The chosen testing conditions is ~8 mg cm^{-2} low-load CMAS at 1300 °C to simulate engine-like conditions. The present coating architecture and chemistry is based on a patent by Al Nasiri et al. [25]. These RE elements (Yb, Lu and Er) are chosen because they have the lowest ionic radius in Lanthanides, and can offer enhanced corrosion resistance and chemical stability. Thus, they can offer enhanced corrosion resistance and chemical stability. Yb has been under study as a potential for EBCs, with less focus on Lu and Er. In addition, RE_2O_3 is specifically chosen as topcoat because, unlike RE-monosilicates and RE-disilicates, it lacks silicon in its structure so that it is more prompt to react with CMAS and consume it faster. Thus, they are more sacrificial compared to monosilicates and silicates and can offer higher resistance against molten CMAS. This chapter also studies the diffusion process of calcium and silicon during

CMAS–EBC reaction, and the corrosion rate of the processed dip coating method. The diffusion coefficient and corrosion rate parameters are used as effective quantitative tools to rank the performance of RE–EBC in a CMAS environment in an attempt to recommend a cost-effective CMAS-resistant EBC architecture. As such, the naturally formed RE_2O_3 topcoat will be assessed as an effective strategy to mitigate CMAS attack on the dense EBC silicate coatings, and improvements on CMAS-resistant RE-silicate coatings is proposed.

5.1.1 EBC–CMAS thermochemical interaction

Stokes et al. [274] studied the CMAS–Yb_2SiO_7 reaction in dry air at 1200 °C for 1–28 h. They observed the formation of grossular garnet $Ca_{1.5}Mg_{1.5}Al_{0.4}Yb_{1.6}(SiO_4)_3$ and Ca–Yb cyclosilicate $Ca_3Yb_2Si_6O_{18}$. They found the disappearance of the phases at temperatures above 1300 °C. Poerschke et al. [275] studied the CMAS reaction with sintered pellets of Hafnate and Zirconate containing Yb_2O_3 in dry air at 1300 °C for 4 h. They found the formation of Ca–Yb garnet at the CMAS–YbHO interface to be beneficial in resisting CMAS attack. They also identified the presence of phases with Yb_2O_3 concentrations that are close to the original Yb_2O_3 starting material, suggesting that some areas of YbHO did not fully dissolve in the penetrated CMAS melt. In their study on silicate deposit degradation, Poerschke et al. [123] noticed that RE-elements with smaller ionic radius form RE_2O_3-rich silicates instead of silicate oxyapatite. They found that Yb_2O_3 will react with CMAS to form Ca–Yb garnet and silicocarnotite $Ca_3RE_2Si_3O_{12}$ at a testing temperature of 1300 °C. Previous authors [276-279] recorded that in the range of 1200–1300 °C, Yb_2O_3 and Yb_2O_3-based EBCs form garnet and silicocarnotite, $Ca_3RE_2Si_3O_{12}$, in addition to apatite. Jiang et al. [120] studied CMAS reaction of Yb_2SiO_5 and Lu_2SiO_5 in dry air at 1200 °C for 4 h and recorded the formation of Ca–RE silicates and garnet phase. They observed slower reaction kinetics for RE-elements with small ionic radius, including Yb and Lu. They recorded the formation of defected-apatite with composition $CaRE_4Si_3O_{13}$, $Ca_3Al_5O_{12}$ garnet and cyclosilicates at the expense of silicate oxyapatite phase.

Tian et al. [143] studied the corrosion behaviour of RE_2SiO_5 (RE = Yb, Lu, Er) under CMAS exposure in dry air at 1300 °C for 50 and 100 h. They found that RE_2SiO_5 resists CMAS attack through the formation of a silicate oxyapatite layer $Ca_2RE_8(SiO_4)_6O_2$ at the CMAS–RE_2SiO_5 interface, which further limits the diffusion of CMAS elements into the coat [280]. They reported higher corrosion rate for Er_2SiO_5 compared to Yb_2SiO_5 and Lu_2SiO_5 due to its higher ionic radius. On the other hand, they observed the same corrosion behaviour and kinetics for

Yb_2SiO_5 and Lu_2SiO_5, because of their relatively small ionic radius leading to better resistance to CMAS attack. They also connected the results with optical basicity (OB). OB is based on the Lewis acid-base concept, where the difference in OB value between CMAS and RE_2O_3 reflects on RE_2O_3 affinity to accept CMAS cations. They found that the OB difference decreases with decreasing RE-element ionic radius and thus the corrosion reactivity decreases. Zhong et al. [281] studied the reaction between CMAS (35 mg cm^{-2} CMAS load) and APS applied Yb-silicate coatings, with various contents of Yb_2O_3, Yb_2SiO_5, and $Yb_2Si_2O_7$ at 1400 °C for 25–50 h. They observed that the CMAS–Yb_2O_3 reaction resulted in garnet precipitation at the CMAS–coat interphase. The Yb-silicate coatings with high Yb_2SiO_5 and $Yb_2Si_2O_7$ contents demonstrated higher surface recession after corrosion compared to Yb_2O_3-rich Yb-silicate coatings, owing to the higher amount of coating dissolved in the reaction layer. Additionally, the presence of SiO_2 in Yb_2SiO_5 and $Yb_2Si_2O_7$-rich coatings decreases Ca diffusivity through the coat which hinders the formation of a dense protective layer and decreases the consumption rate of CMAS. Thus, they concluded that Yb-silicate coatings with high Yb_2O_3 content exhibits better CMAS resistant properties. Poerschke et al. [282] modelled the performance of Y_2O_3 (80 mol%)–ZrO_2 ($Y_{80}Zr_{20}$) thermal barrier coating (TBC) with CMAS. It was observed that higher Y_2O_3 content in the coat increases the dissolution rate because of the high solubility of Y_2O_3 in the coating-CMAS melt. This would be more effective in sealing the channel pores to inhibit further attack and stabilise the corrosion process. They noticed higher performance for $Y_{80}Zr_{20}$ compared to 7YSZ or $Y_4Zr_3O_{12}$. Ptáček et al. [283] studied the SrO–Y_2O_3–SiO_2 system through the preparation and investigation of hexagonal strontium-yttrate-silicate apatite $SrY_4[SiO_4]_3O$. They found that Mg is not incorporated into the crystals of apatite phase but it stays dissolved in the glassy phase.

5.1.2 EBC–CMAS diffusion and infiltration time

Zhu et al. [284] modelled the diffusion-reaction of CMAS with 7 wt% YSZ TBC using Fick's second law and observed a decrease in the concentration profile of CMAS across the infiltration depth. Additionally, Poerschke et al. [285] studied diffusion interaction at the interphase between Yb_2SiO_5/Yb_6HfO_{11} and Yb_2SiO_5/$Yb_4Hf_3O_{12}$ at 1500 °C. They found that the diffusion of SiO_2 species is highly mobile at the first stages of interaction resulting in diffusion along grain boundaries and porosities in the coat. As reaction proceeds, diffusion decreases due to filling of the pores resulting in a direct relation between diffusion and porosity. Iqdari et al.

[286] studied the diffusion of RE elements in natural apatite crystals 900–1150 °C, and concluded that the concentration profile of Nd and Eu diffusion into apatite followed Fick's second law, where the amount of RE atoms diffusing into the apatite crystal was restricted by a maximum saturation value.

Wiesner and Bansal [287] studied the thermal properties of CMAS glass. They estimated the infiltration time of CMAS through a 200 μm EBC at 1300 °C to be 4.3 min for glass with a viscosity of 78.1 Pa s. Sleeper et al. [288] studied the CMAS–$Ca_2Y_8(SiO_4)_6O_2$ apatite interaction in dry air at 1200–1500 °C between 1 and 50 h. They calculated the infiltration time of CMAS through a 3 mm-thick coating and found that the infiltration time decreased from 54 min at 1300 °C to 19 min at 1500 °C. The faster diffusion at 1500 °C resulted in the infiltration of CMAS into the apatite reaction layer through the pores and grain boundaries, which promoted the dissolution of apatite in CMAS and its re-precipitation as apatite needles within the Ca–Y phase. Krämer et al. [289] investigated the thermochemical degradation of EB-PVD applied ZrO_2–7.6%$YO_{1.5}$ (7YSZ) in a CMAS environment with a 40 mg cm^{-2} CMAS load. They reported that the dissolution/precipitation of 7YSZ with CMAS resulted in different reaction compositions depending on the melt chemistry. In addition, CMAS was found to penetrate the open gaps in the coating as soon as melting occurred. The infiltration time of CMAS across a 200 μm coating was found to be less than 1 min, which explained the rapid reaction at the CMAS–TBC interphase.

Gatzen et al. [290] compiled the corrosion rates of RE-based EBCs in water vapour environment by using data from Fritsch and Klemm [158, 291]. They used a methane-fuelled burner rig to test the EBCs between 1200 and 1500 °C at a water vapor partial pressure of 0.24 atm, gas velocity of 100 m s^{-1}, and for 100–350 h. They found that Yb_2SiO_5 offered the best corrosion performance.

5.1.3 EBC–CMAS thermodynamics

Xian et al. [292] prepared lanthanum silicates of the composition $La_9ASi_6O_{27}$, where A = Nd, Sm, Gd and Yb. The microstructure and electrical properties were investigated, where all $La_9ASi_6O_{27}$ compounds were found to be composed of hexagonal apatite-type structure. They found that the activation energy increases with decreasing ionic radius where $La_9YbSi_6O_{27}$ has an activation energy of 100 kJ mol^{-1} compared to 83 kJ mol^{-1} for $La_9GdSi_6O_{27}$. Bonhomme et

al. [293] prepared $Sr_1La_9Si_6O_{26.5}$ apatite SOFCs and studied their formation mechanism under isothermal conditions between 1250–1500 °C. They found that the densification of apatite ceramic is controlled by the Sr diffusion through the grain boundaries of the rare-earth element, La, with an activation energy of 470 kJ mol^{-1}. Strzelecki et al. [294] investigated the thermodynamic properties of a range of Ca RE-silicate oxyapatites, which included $Ca_2Pr_8(SiO_4)_6O_2$, $Ca_2Tb_8(SiO_4)_6O_2$, $Ca_2Ho_8(SiO_4)_6O_2$ and $Ca_2Tm_8(SiO_4)_6O_2$. They found that activation enthalpy ΔH_f for apatite formation is 765.1 ± 22.8, −638.9 ± 20.5, −643.3 ± 10.3 and −403.2 ± 5.1 kJ mol^{-1} respectively. They found a direct relation between the enthalpy of formation of rare-earth silicate oxyapatites and the ionic potential (IP), where the ΔH_f becomes more positive (less exothermic) as IP increases. This means that as the ionic radius decreases from Pr–Tm, so does ΔH_f becomes higher. They also found a direct relation between the volume of $Ca_2RE_8(SiO_4)_6O_2$ versus the ionic potential of RE^{3+}. Zhang et al [142] found that La forms a thicker reprecipitated $La_8Ca_2(SiO_4)_6O_2$ layer compared to Nd and Gd, which indicated that a larger RE cation is easier to crystallize in the melt and form apatite. This is consistent with the enthalpy of formation for RE-apatite, which decreases with the increasing RE cation size (and decreasing ionic potential). The same finding regarding the relation between ΔH_f and ionic radius r and ionic potentials (Z/r, where Z is the ionic charge) were also noticed by several authors including Leu et al. [295], Risbud et al. [296], Liang et al. [297], Costa et al. [298], and Costa and Jacobson [2]. Yoshioka et al. studied the conductivity and defect-structure of Mg-doped $La_{9.33-2x/3}M_xSi_6O_{26}$ SOFC at 800 and 900 °C [299]. This resulted in the formation of $La_{10}Si_{5.8}Mg_{0.2}O_{26.8}$ and $La_{9.8}Si_{5.7}Mg_{0.3}O_{26.4}$, where they noticed an increase in ionic conductivity when doping $La_{9.33-2x/3}M_xSi_6O_{26}$ with Mg, which was attributed to the O^{2-} and Mg^{2+} interstitials in the apatite lattice.

Martínez-González et al. [300] studied ionic conductivity of RE apatite silicate $RE_{10-x}(SiO_4)_6O'_{2+y}$ (RE = La, Nd, Gd and Dy) at 1500 °C for 3 h using electrochemical impedance spectroscopy, where O' is an extra ion responsible for ionic conduction. They found that ionic conductivity decreases with decreasing RE^{3+} ionic radius resulting in higher activation energies for apatite formation with lower RE^{3+} radius. Ardanova et al. [301] studied the solubility limits of RE elements in Ca-hydroxyapatites $Ca_{10-x}RE_x(PO_4)_6(OH)_{2-x}O_x$ ($0 \leq x \leq 2$) at 1100 °C. They found that the solubility limit decreases with decreasing ionic radius. It also correlates with increasing difference in ionic radii between Ca^{2+} and RE^{3+}.

5.1.4 EBC–CMAS structure

Previous authors [144, 145, 302-305] studied the structure of stoichiometric RE lanthanides-silicate oxyapatite, which included $Ca_2Nd_8(SiO_4)_6O_2$ by Fahey et al. [302], $Ca_2La_8(SiO_4)_6O_2$, by Schroeder and Mathew [303], $Ca_2Ce_8(SiO_4)_6O_2$ by Massoni et al. [304], and $Ca_2RE_8(SiO_4)_6O_2$ (RE = La, Nd, Sm, Eu, and Yb) by Crum et al. [305]. Their main focus was to determine lattice parameters and cation ordering with no focus on the formation mechanism.

Wang et al. [306] studied the corrosion behavior of plasma-sprayed RE_2SiO_5 (Gd_2SiO_5, Y_2SiO_5, and Er_2SiO_5) coatings in water vapor environment at 1400 °C. They found from XPS spectra that RE4d (RE = Gd, Er) and Si2p are assigned to RE–O and Si–O bonds respectively. They concluded that the corrosion product, $Gd_{4.67}Si_3O_{13}$ garnet, is a cation-deficient silicate that consists of [SiO_4^{4-}] tetrahedra, and [GdO7] and [GdO9] polyhedrons. The cation-deficient structure results in more defects, which provides extra reactive sites for water vapor corrosion. However, they did not provide experimental evidence using XPS to the existence of cationic vacancies.

Pantiex et al. [307] studied the influence of calcium concentration and anionic vacancies on the electrical properties of $Ca_xLa_{9.33-x}(SiO_4)_6O_{2-x/2}$ ($0 \leq x \leq 1$) between 280–620 °C using electrochemical impedance spectroscopy. They found that higher Ca substitutions (x) resulted in lower conductivities and higher capacitance, which is attributed to lower ionic mobility. This was correlated to stronger interaction between defects in the structure; whereby altering the ionic conductivity of RE silicate oxyapatite can be done by controlling its stoichiometry. Serret et al. [308] studied the diffusion of La^{3+} in Ca-oxyapatites $Ca_{10-x}La_x(PO_4)_6(OH)_y$ ($0 \leq x \leq 2$) at 1450 °C for 120 h. The substitution of Ca^{2+} by La^{3+} of higher valency is compensated by the formation of cationic vacancies, which results in the oxidation of OH^- to O^{2-} ions.

5.2 METHODOLOGY

5.2.1 Rare-earth EBCs slurry

EBC was processed on the thermally grown silica layer obtained by oxidising the sample at 1300 °C for 72 h. Only one RE-oxide was deposited on the silica layer. Thereafter, three separate water-based RE-oxide slurries were prepared using either 30 vol% Yb_2O_3 (abcr, Germany, 4 μm APS), 30 vol% Er_2O_3 (Alfa Aesar, USA, 4 μm APS) or 30 vol% Lu_2O_3 (abcr, Germany, 4 μm APS) [25]. For the preparation of the Yb_2SiO_5 slurry, 0.7 wt% aurintricarboxylic acid (Sigma-Aldrich, USA) dispersant was used with water at pH of 8 [15]. For Lu_2SiO_5 and Er_2SiO_5 slurries, 3.2 wt% dolapix CE64 (Zschimmer and Schwarz, Germany) dispersant was used with water at pH of 9.5 [15]. Polyethylene glycol 10,000 binder (Alfa Aesar, USA) was used to prepare the three slurries. The exact compositions of the mixtures (in g) are provided in Table 5.1. The slurries were homogenously mixed in plastic bottles containing alumina balls (> 99.99% purity, Union Process, USA, 5 mm diameter) and then placed in a tubular shaker (Willy A. Bachofen AG, Switzerland) for 24 h. The oxidised RBSBC substrates were dip coated in the slurry followed by drying for 24 h at room temperature. The dip-coated samples (Figure 5.2b) were sintered in laboratory air at 1400 °C at a heating and cooling rate of 10 °C min^{-1} for 50 h.

Table 5.1 Coatings mixture (gm) for preparing Yb, Lu, and Er-silicate coatings [25].

	Yb_2SiO_5	Er_2SiO_5	Lu_2SiO_5
RE-Oxide	13.755	12.96	14.13
Water	3.5	3.5	3.5
Dispersant	0.0960	0.0238	0.0259
Binder	0.2750	0.2592	0.2826

5.2.2 CMAS pellets preparation

CMAS composition of $33CaO–9MgO–13Al_2O_3–45SiO_2$ (mol%) was selected to simulate the composition of sands sucked into engines during operation [58, 149, 155]. This CMAS composition melts above 1235 °C [309, 310]. Al_2O_3 99.9%, CaO 99.95%, MgO 99.95% (Alfa Aesar, USA) and SiO_2 99.5% (abcr, Germany) were mixed with ethanol in a 1:1 ratio in plastic bottles with alumina balls. The mixture was heated in dry air at 1200 °C for 24 h to facilitate solid-state reaction between the CMAS components [120]. The mixture was then ground into a fine powder using a mortar and pestle (VWR International, USA). A manual hydraulic press

machine (Specac, UK) was used to press the CMAS pellets of φ10 mm diameter) (Figure 5.1a). The pellets were sintered in laboratory air at 1200 °C at a heating and cooling rate of 10 °C min^{-1} for 2 h and subsequently layered on top of each coated sample to cover the sample surface (Figure 5.1b). Corrosion tests were conducted for 1, 6, 12, 24, or 48 h at 1300 °C in laboratory air at a heating and cooling rate of 10 °C min^{-1} [309]. Samples were placed inside zirconia boats, which were placed on high-purity alumina crucibles; the whole setup is placed inside a tube furnace that uses high-purity alumina tube (Figure 5.3 and Figure 5.4).

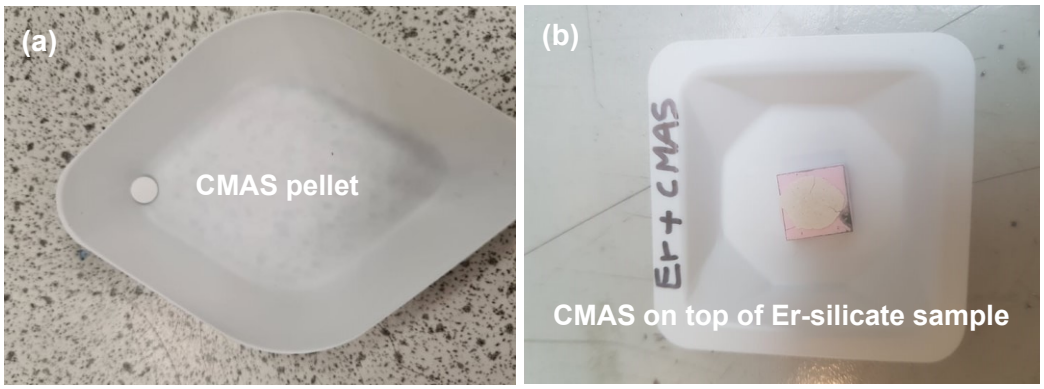


Figure 5.1 (a) CMAS pellet that is ~8 mg with φ5 mm diameter (b) CMAS pellet placed on top of Er-silicate coated sample.

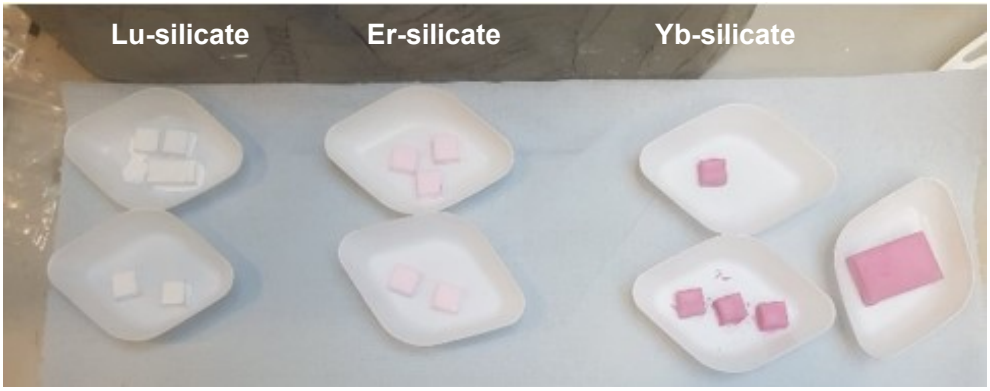


Figure 5.2 Yb, Lu, and Er-silicate coated samples before drying for 24 h.

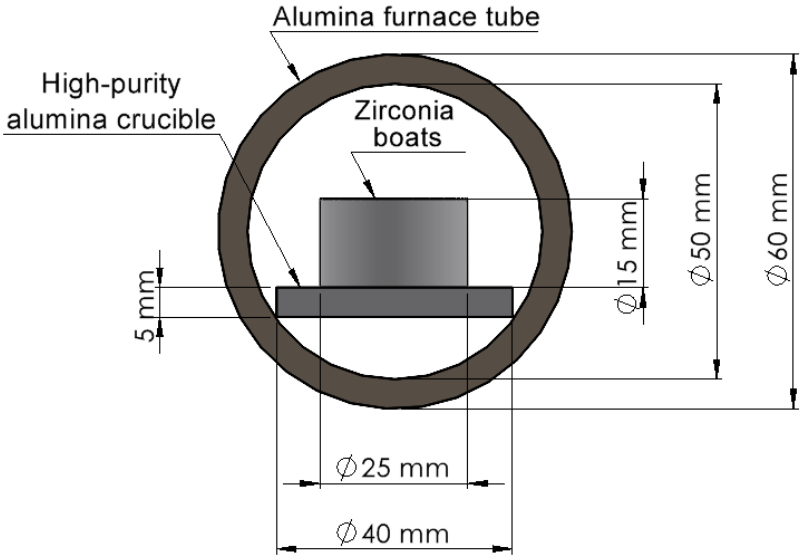


Figure 5.3 Front view of the experimental setup of the CMAS experiments.

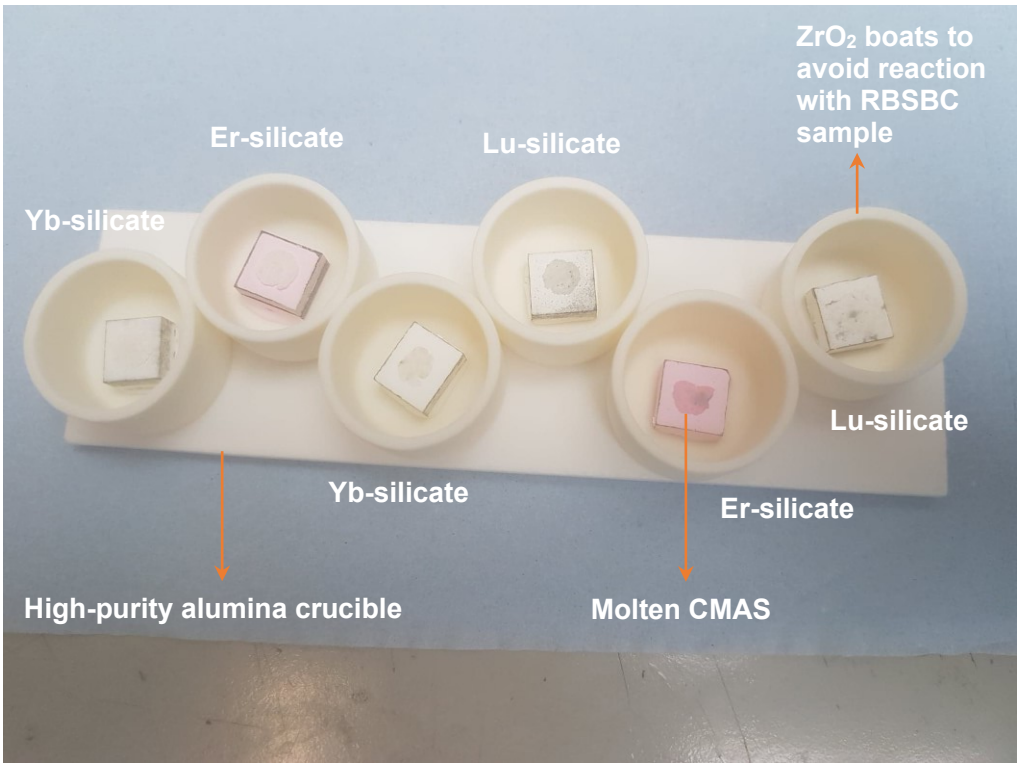


Figure 5.4 Yb, Er, and Lu-silicate samples out of furnace after CMAS corrosion.

5.2.3 Diffusion coefficient and corrosion rate

The diffusion coefficient D_{FSL} ($m^2\ s^{-1}$) of Ca and Si through the penetrated EBC was calculated using Fick's second law for non-steady state diffusion [Eqs. (5.1) and (5.2)], where C_s and C_o are the concentrations of either Ca or Si at the CMAS–EBC interface and the EBC-substrate interface respectively. $C_{(x,t)}$ is the concentration at a penetrated depth X and time t, while erf (z) is the Gaussian error function and it is obtained from the Gaussian error function table [311].

$$\frac{C_{(x,t)} - C_o}{C_s - C_o} = 1 - \text{erf}\left(\frac{X}{2\sqrt{Dt}}\right) = 1 - \text{erf}\,(z) \tag{5.1}$$

$$D_{FSL} = \frac{X^2}{4z^2 t} \tag{5.2}$$

The diffusion coefficient D_{DAN} ($m^2\ s^{-1}$) for the CMAS melt through the coating was calculated using Eq. (5.3) [57]. The equation does not consider the concentration of Ca in the EBC. The obtained values are compared with that calculated from Fick's second law.

$$D_{DAN} = X^2\ t^{-1} \tag{5.3}$$

The infiltration time t_i (min) of CMAS through the EBC coating was calculated according to Eq.(5.4) [287-289] where τ is the tortuosity factor, D_c (μm) is the capillary diameter, ω is the fraction of pores open for CMAS infiltration, L_c is the coating thickness, η (N s m^{-2}) is the viscosity of CMAS glass and σ (J m^{-2}) is the surface tension. D_c was estimated from the average pore size using MIP and ImageJ software, ω was estimated from the volume fraction of pores in the RE_2O_3 topcoat using MIP and ImageJ according to ASTM E2109 [312], while η and σ are obtained from literature [288, 289], and τ is calculated using Eq. (5.5) [313]. The corrosion rate CR (μm min^{-1}) of CMAS across EBC was calculated as a function of EBC thickness and infiltration time [Eq. (5.6)].

$$t_i \sim \left[\frac{\tau}{8D_c}\left(\frac{1-\omega}{\omega}\right)^2 L^2\right]\frac{\eta}{\sigma} \tag{5.4}$$

$$\tau = \sqrt{0.75\omega^{-1.0819}} \tag{5.5}$$

$$CR = L_c\ t^{-1} \tag{5.6}$$

5.3 RESULTS

5.3.1 EBC and CMAS compositions

XRD analysis of CMAS pellet (Figure 5.5) show that the main constituents are anorthite ($CaAl_2Si_2O_8$) and diopside ($CaMgSi_2O_6$). Anorthite is the common reaction product for $33CaO–9MgO–13Al_2O_3–45SiO_2$ CMAS pellets [155]. The presence of Mg is reflected in the diopside and akermanite ($Ca_2MgSi_2O_7$) phases. The composition of CMAS obtained from RIR was 77% anorthite, 18% diopside and 5% akermanite. The as-coated substrates with the three studied coatings are shown in Figure 5.7, where b, d, and f are magnified images of a, c, and e respectively. The coating structure consists of a dense RE_2SiO_5-based bottom coat of ~16 ± 4 μm and RE-oxide topcoat of ~170 ± 20 μm. The RE-silicate bottom coat was formed due to the reaction of RE-oxide with the silica layer from the substrate formed during the oxidation process. The phases present in Yb, Lu and Er-silicates as obtained from the XRD (Figure 5.6a) are: RE-oxide, RE_2SiO_5 and $RE_2Si_2O_7$, where the bottom coat consists of ~85% RE_2SiO_5–15% $RE_2Si_2O_7$ [24]. The measured young's modulus E for Yb_2SiO_5, and CMAS are 119 and 92 GPa respectively, while Poisson's ratio v is 0.27 and 0.28 respectively.

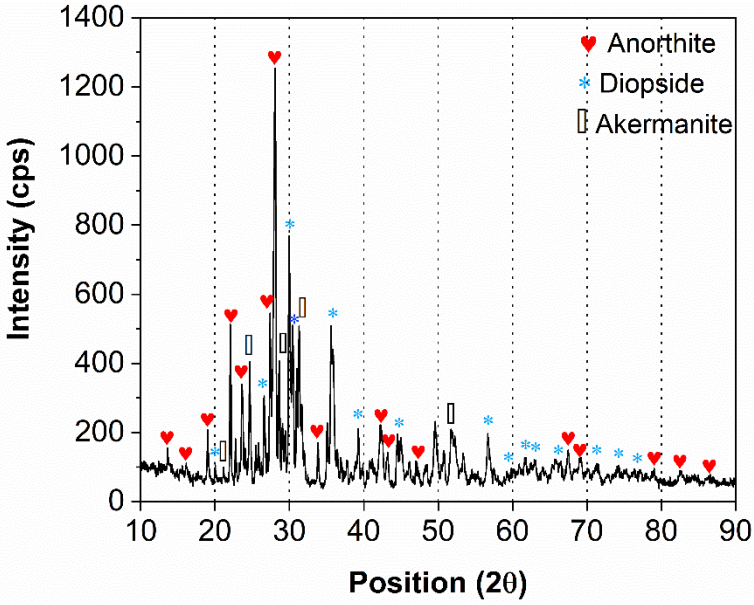


Figure 5.5 XRD of CMAS pellet after heat treatment showing the presence of anorthite, diopside, and akermanite.

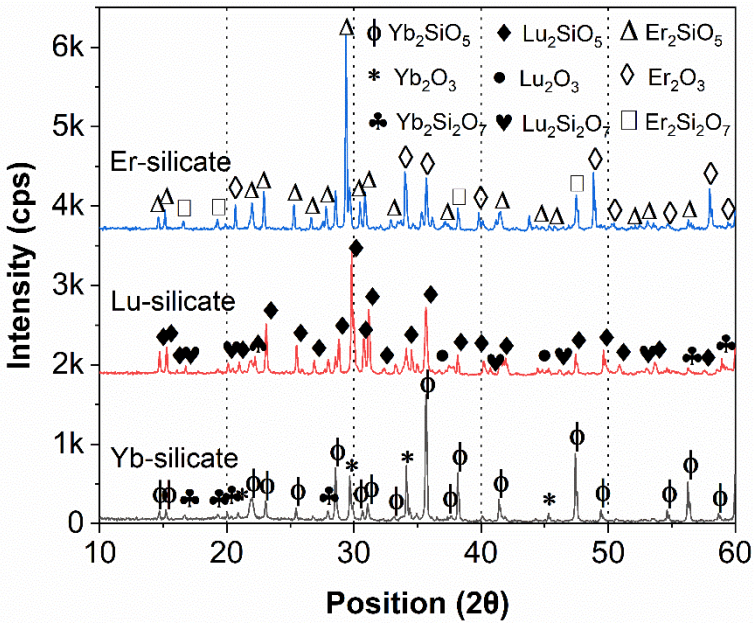


Figure 5.6 XRD of Yb, Lu and Er-silicates showing the presence of RE_2O_3, RE_2SiO_5, and $RE_2Si_2O_7$.

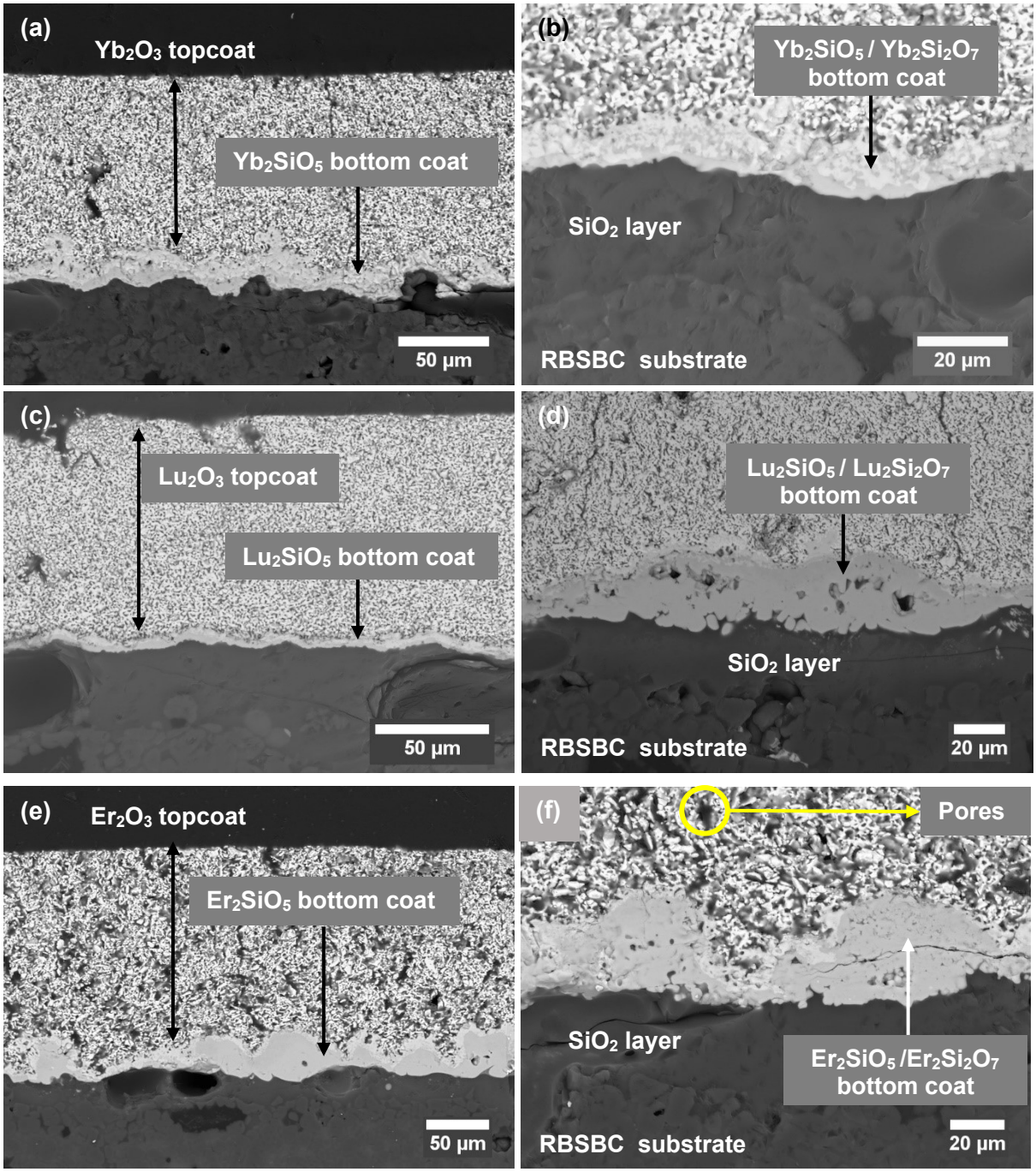


Figure 5.7 (a, b) Yb-silicate (c, d) Lu-silicate (e, f) Er-silicate on RBSBC substrate.

5.3.2 Yb-silicate and CMAS reaction

The cross-section of the CMAS–Yb-silicate at 1300 °C for 1, 6, 12, 24 and 48 h (Figure 5.8a–e respectively) shows a proportional relation between the corrosion duration and the reaction layer thickness (RL) and penetration depth of CMAS into the coat. The penetration depth is measured as the distance between the baseline of the RL and the lowest point in the coat at which CMAS was detected. The RL thickness is 3 µm after 1 h corrosion, and it increases to 6 µm after 6 h where 60% of the coat is penetrated by CMAS. Between 6 and 48 h, the increase in RL thickness and penetration depth occurred at a slower rate. The RL thickness increases to 7 µm after 12 h and 10 µm after 48 h forming a dense reaction layer, while the CMAS penetration depth increases by 71% after 24 h and total penetration (melt reached the bottom coat) after 48 h. The reaction between CMAS and Yb-silicate results in the formation of molten spots that are sporadically distributed in the topcoat. The Ca–Mg–Si–RE reaction layer has the same composition in Lu and Er-silicates.

This reaction forms three melt-like Ca–Mg–Si–Yb garnet phases 1, 2 and 3 (Figure 5.8f). The dark grey BSE contrast area (phase 1) is the reaction layer surrounded by medium grey areas (phase 2), which contains lower Ca and Mg, and higher Yb. The light grey areas (phase 3) consist mostly of Yb_2O_3 with small traces of Ca (~1 wt%), Si, and no Mg. Figure 5.9 show a line scan across phases 1, 2 and 3 at the CMAS–Yb_2O_3 interface after 48 h, where the infiltration of Ca, Mg and Si follows the same trend, and their concentration decreases with decreasing the BSE contrast (phase 1 being the highest). This is confirmed by the EDS mapping (Figure 5.9c) across phases 1, 2 and 3, which shows higher Ca and Si amounts at the darker phases. The compositions of phases obtained from EDS are shown in Table 5.2. Regarding the morphology of the reaction layers, they are amorphous melt-like (Figure 5.8f and Figure 5.9a) and consists of two main features: phase 1 surrounded by phase 2 areas and phase 2 dispersed in the coat matrix (phase 3). The melt penetrated approximately 50% of the bottom coat after 48 h, forming an approximately 2 µm continuous apatite layer (phase V) at the surface of the bottom coat in addition to sporadic apatite areas with slightly lower Ca content compared to phase 2 (Figure 5.10, Figure 5.13a and Table 5.2). Concerning the topcoat, vertical cracks (shown as horizontal white arrows) run along the coating and the CMAS glass, where finer transverse cracks (vertical white arrows) branch from them. Alternatively, the bottom coat

shows the presence of lateral cracks (black arrows) that run close to the interface with the RBSBCS substrate (Figure 5.10b).

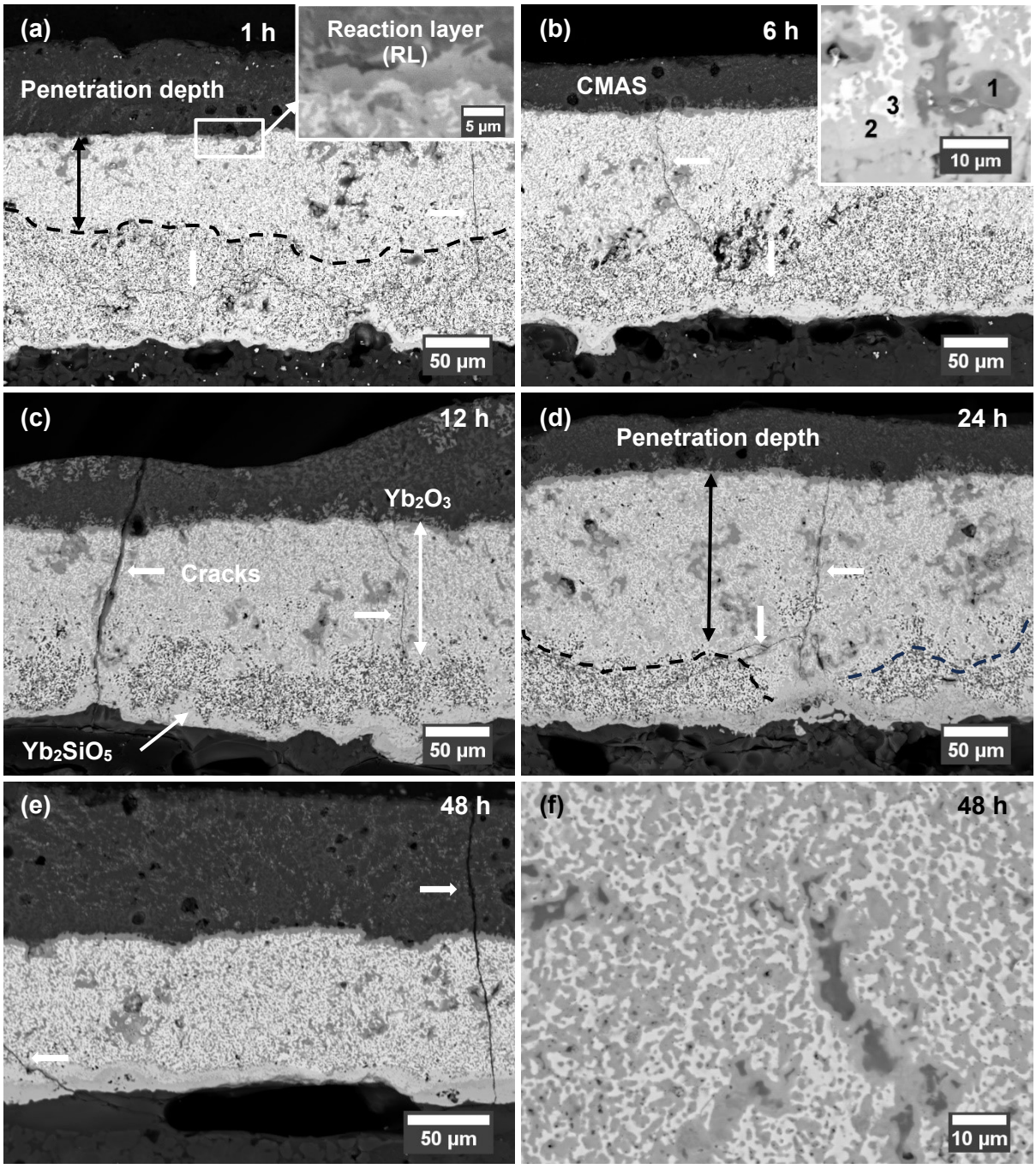


Figure 5.8 CMAS–Yb-silicate at 1300 °C after (a) 1 h (b) 6 h (c) 12 h (d) 24 h and (e) 48 h (f) 48 h showing the coating morphology after CMAS reaction.

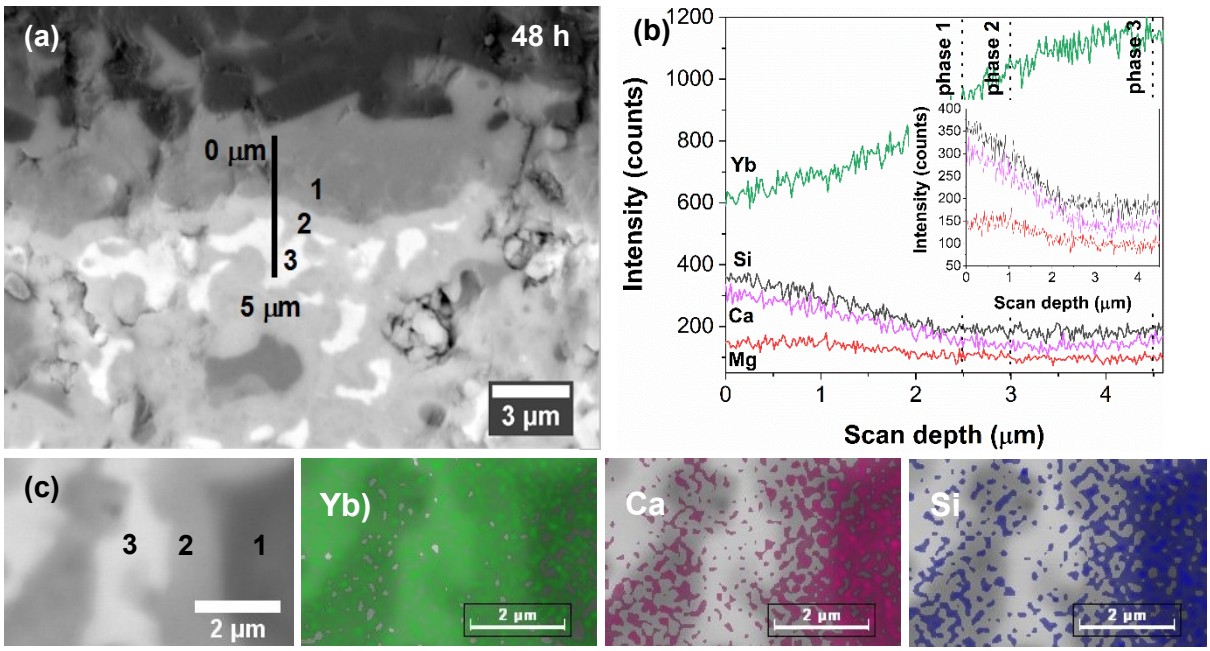


Figure 5.9 (a) CMAS–Yb-silicate after 48 h (b) line scan at the CMAS–Yb_2O_3 interface and (c) EDS mapping at phases 1, 2 and 3.

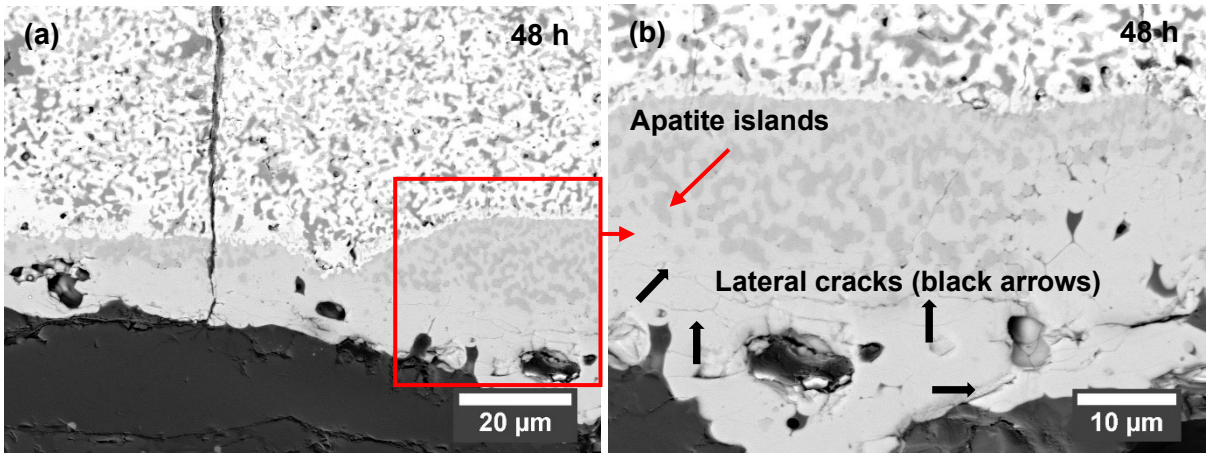


Figure 5.10 (a) CMAS attack Yb_2SiO_5–$Yb_2Si_2O_7$ bottom coat after 48 h (b) magnified image showing the formation of apatite islands within the bottom coat in addition to lateral mud cracks at the substrate-bottom coat interface.

5.3.3 Lu-silicate and CMAS reaction

Figure 5.11a–e shows the cross-section of CMAS–Lu-silicate at 1300 °C between 1 and 48 h. Lu-silicate behaviour to CMAS attack is similar to that observed in Yb-silicate. The RL thickness increases from 5 to 7 μm between 1 and 6 h corrosion, while CMAS penetration depth increases from 50 to 57% of the whole coating. After 24 h corrosion, the RL is 10 μm and the penetration depth is 75%, which increased to full coating penetration after 48 h.

Lu-silicate has the same phases and morphology as Yb-silicate (Figure 5.11e). A line scan across the coat depth of 141 μm at 48 h (Figure 5.12) show the same results for Ca, Mg and Si infiltration as those previously observed in Yb-silicate, where the concentration of Ca, Mg and Si gradually decrease across the coating depth. At the Lu_2SiO_5 bottom coat, the Ca and Mg concentration drops, while Si amount increases. The penetration of the bottom coat formed the same morphology and composition as that of Yb-silicate, but only at approximately 30% melt penetration (Figure 5.13) and ~1 μm apatite reaction layer (Figure 5.13d). As with Yb-silicate, the coat shows vertical and horizontal cracks along with randomly-distributed isolated pores (Figure 5.11f), and lateral cracks at the substrate interface. The mechanisms of crack formation are discussed in section 5.4.4.

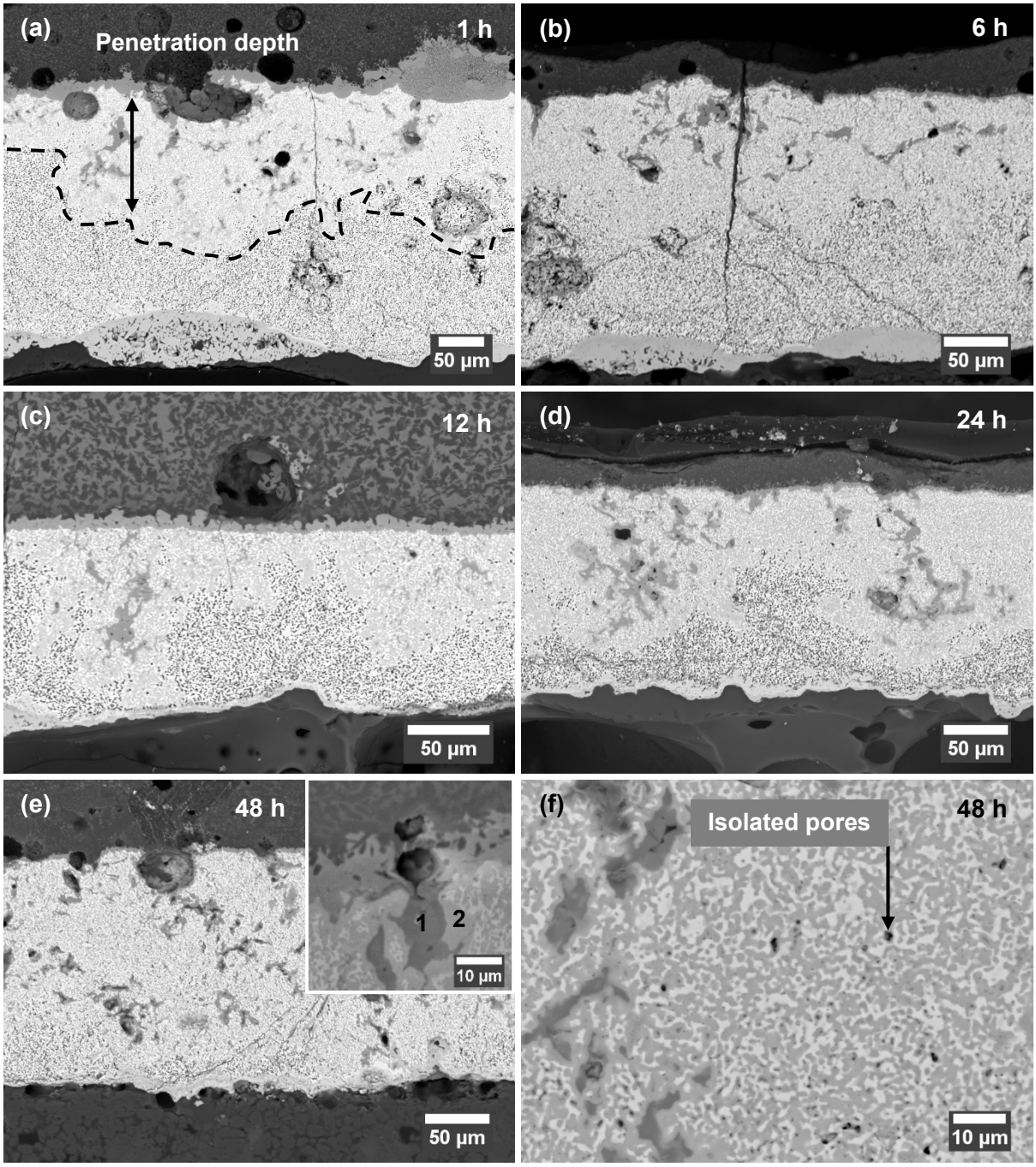


Figure 5.11 CMAS–Lu-silicate at 1300 °C after (a) 1 h (b) 6 h (c) 12 h (d) 24 h (e) 48 h (f) 48 h showing the morphology of the coat after CMAS reaction.

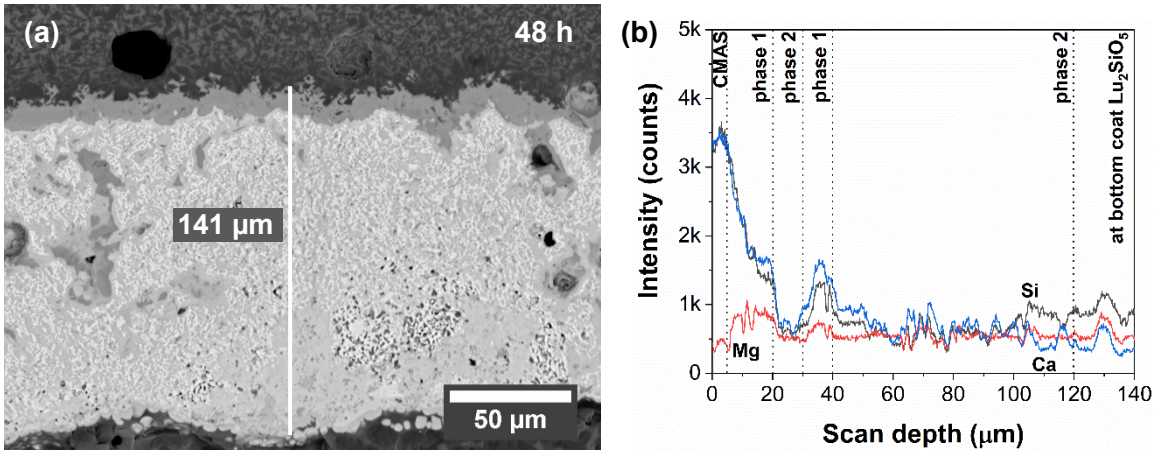


Figure 5.12 (a) CMAS–Lu-silicate at 1300 °C after 48 h (b) line scan.

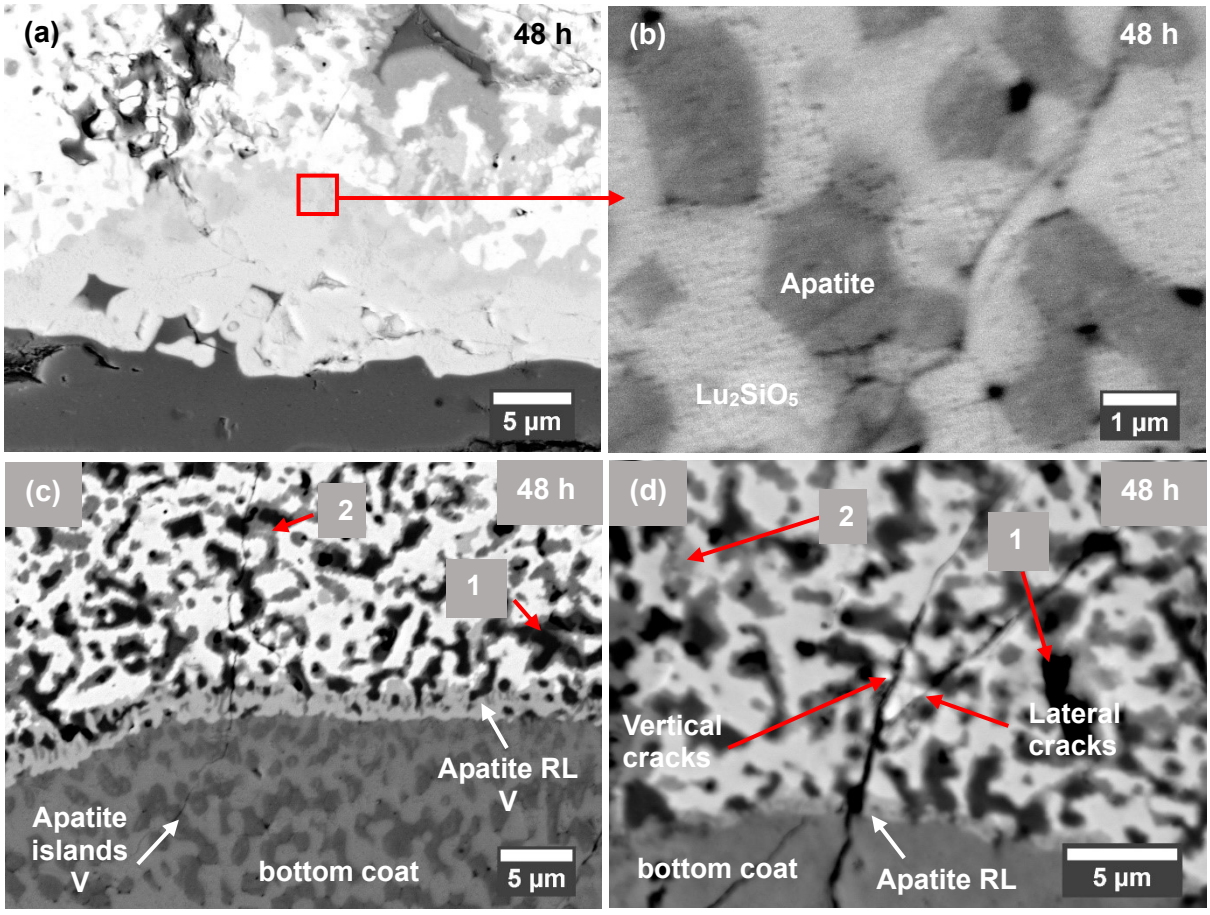
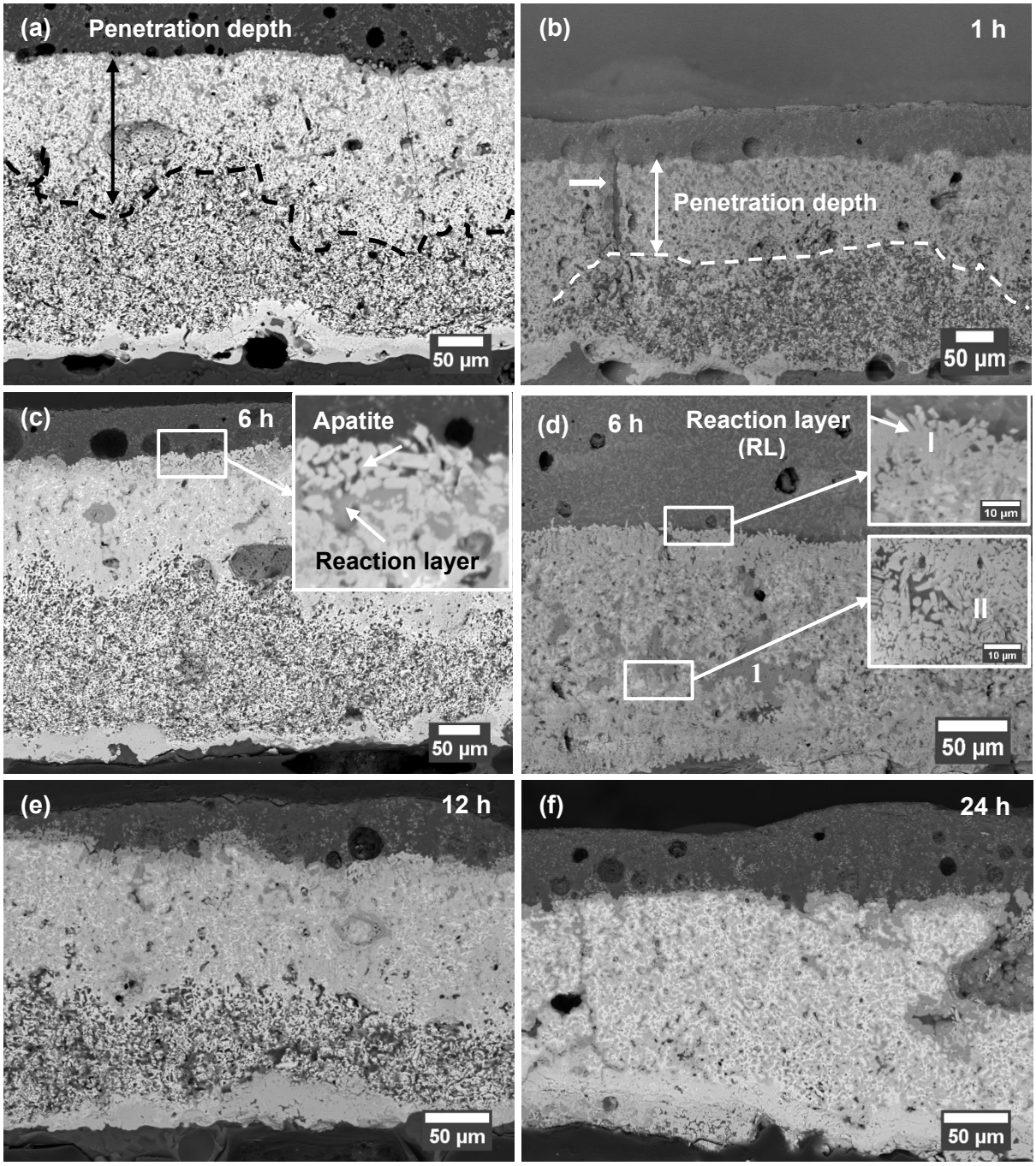


Figure 5.13 (a) CMAS attack Lu_2SiO_5–$Lu_2Si_2O_7$ bottom coat after 48 h (b) magnified image with enhanced contrast (c) formaton of apatite at the surface of the Yb_2SiO_5–$Yb_2Si_2O_7$ bottom coat (d) formaton of apatite at the surface of the Lu_2SiO_5–$Lu_2Si_2O_7$ bottom coat. The figure shows the formation of vertical and laterial mud cracks.

5.3.4 Er-silicate and CMAS reaction

The CMAS–Er-silicate reaction at 1300 °C between 1 and 48 h is shown in Figure 5.14a–e. As with Yb and Lu-silicates, the RL and the penetration depth increase with corrosion duration. The RL thickness (Figure 5.14a–g) increases from 7 to 12 μm between 1 h and 6 h, while the penetration depth increases from 57 to 66%. The RL increases from 18 to 23 μm between 24 and 48 h, while the CMAS penetration depth is 77% at 12 h and full penetration after 24 h.

Er_2O_3 topcoat reaction with CMAS results in the same phases 1, 2 and 3 (Figure 5.14a–e) but with slightly higher Ca content. At 6 h, the RL consists of thick dark grey Ca–Mg–Si–Yb garnet in addition to lighter-contrast equiaxed apatite grains. The penetration of CMAS into the coat also causes the formation of needle-like apatite grains in the Er_2O_3 topcoat and at the Er_2SiO_5 bottom coat (phase II in Figure 5.14d and Figure 5.15a). The volume percent of needle-like phase II increases in the middle of the coat, between 12 and 24 h, with higher amount of CMAS melt penetrating the topcoat (Figure 5.15a). After 48 h, the amount of apatite formed at the CMAS–Er_2O_3 interface increases, associated with growth in apatite grain size, resulting in the detachment of some areas of the RL to form islands within the CMAS melt (phase I in Figure 5.15a). This is correlated with higher melt infiltration (phase IV in Figure 5.15a) till it reaches the bottom of the coat and form equiaxed Ca (~0.25 wt%)–$Er_2Si_2O_7$ grains (phase III in Figure 5.15a). The line scan across the coat depth of 165 μm at 48 h (Figure 5.15) shows that Ca and Si amounts are higher at phases 1 and 2 compared to needle-shaped phase II, while phase III at the bottom of the coat shows a drastic drop in Ca and Mg contents compared to Si. In contrast to Yb and Lu-silicates, a continuous apatite layer was not observed on the bottom coat. Instead, apatite forms sporadically in the bottom coat (Figure 5.15c and d). It is noted that the amount of phase 2 dispersed in phase 3 for Er-silicates are higher than Yb and Lu-silicates as shown in Figure 5.14h.


(a)
Penetration depth
50 µm
(b)
1 h
Penetration depth
50 µm
(c)
6 h
Apatite
Reaction layer
50 µm
(d)
6 h
Reaction layer
(RL)
I
10 µm
II
10 µm
1
50 µm
(e)
12 h
50 µm
(f)
24 h
50 µm

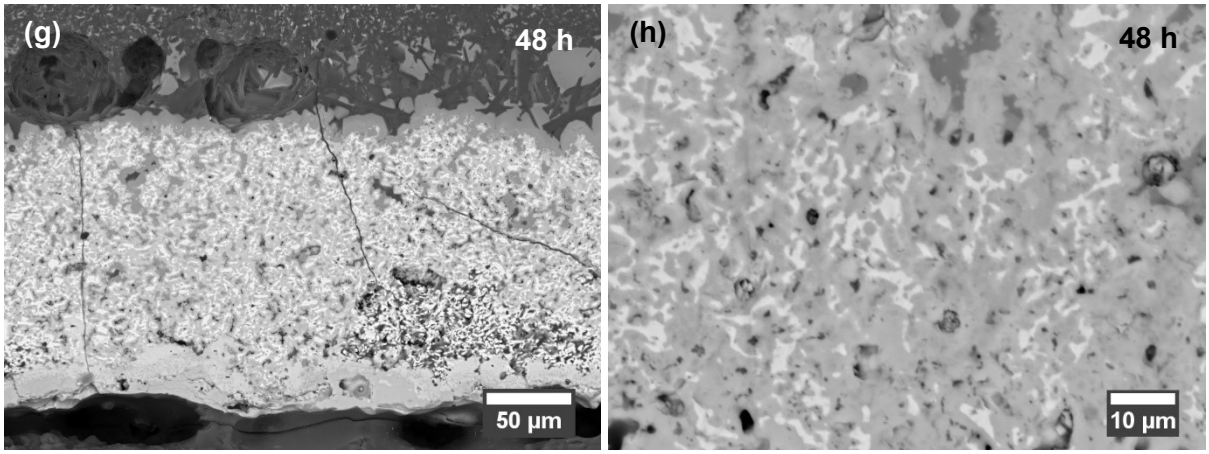


Figure 5.14 CMAS–Er-silicate at 1300 °C after (a, b) 1 h (c, d) 6 h (e) 12 h (f) 24 h (g) 48 h (h) 48 h showing the morphology of the coat after CMAS reaction.

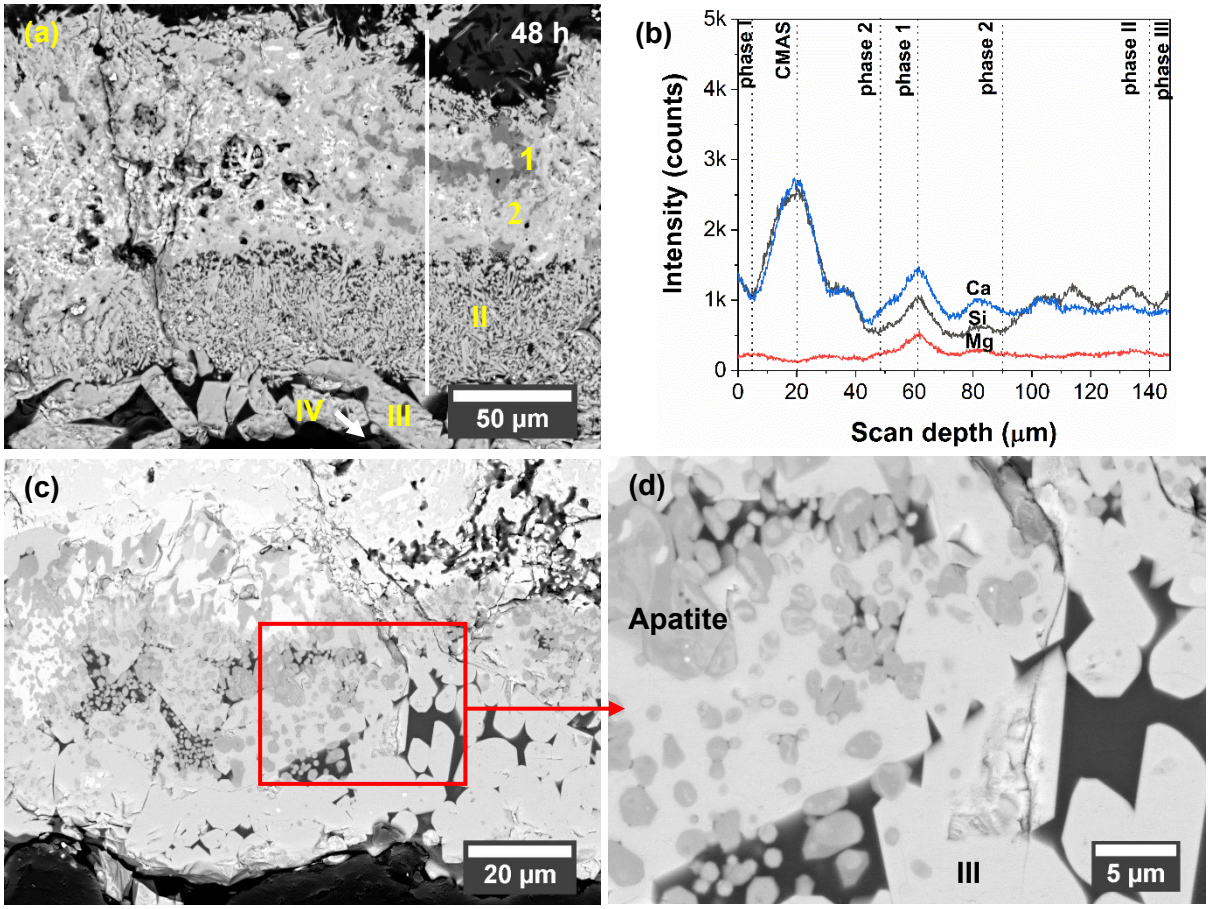


Figure 5.15 (a) CMAS–Er-silicate at 1300 °C after 48 h (b) line scan for Ca, Mg, and Si (c) corrosion of the Er_2SiO_5–$Er_2Si_2O_7$ bottom coat (d) magnified image.

Table 5.2 EDS analysis (at%) for reaction phases of CMAS–RE silicates at 1300 °C.

EBC	Phase	Ca	Mg	Al	Si	O	RE	Phase
Yb-silicate	1	10 ± 3	9 ± 1	-	24 ± 3	43 ± 10	14 ± 3	Ca-Mg-Yb garnet
	2	9 ± 2	1±0.5	-	20 ± 2	32 ± 8	38 ± 4	Ca-Mg-Yb garnet
	3	5 ± 1	-	-	12 ± 6	33 ± 17	50 ± 10	$Ca\text{-}Yb_2O_3$
	V	7 ± 1	-	-	31 ± 4	28 ± 7	36 ± 2	silicate oxyapatite
Lu-silicate	1	10 ± 3	9 ± 2	-	27 ± 3	41 ± 10	13 ± 2	Ca-Mg-Lu garnet
	2	9 ± 2	1 ± 1	-	22 ± 2	32 ± 8	36 ± 3	Ca-Mg-Yb garnet
	3	6 ± 1	-	-	16 ± 3	30 ± 12	48 ± 8	$Ca\text{-}Lu_2O_3$
	V	7 ± 1	-	-	31 ± 4	28 ± 7	36 ± 2	silicate oxyapatite
Er-silicate	1	12 ± 1	9 ± 1	-	26 ± 1	37 ± 6	16 ± 3	Ca-Mg-Er garnet
	2	8 ± 3	2 ± 1	-	19 ± 6	31 ± 20	40 ± 10	Ca-Mg-Er garnet
	I	9 ± 1	-	-	27 ± 4	26 ± 8	38 ± 3	silicate oxyapatite
	II	6 ± 1	-	-	31 ± 4	24 ± 7	39 ± 2	silicate oxyapatite
	III	0.5	-	-	35 ± 1	26 ± 2	39 ± 2	$Ca\text{-}Er_2Si_2O_7$
	IV	9 ± 2	5 ± 2	10±6	44 ± 3	29 ± 10	3 ± 1	Er-CMAS melt

5.3.5 RE-silicate and CMAS microstructure

The TEM images of the CMAS–Yb-silicate reaction phases at 1300 °C for 48 h are shown in Figure 5.17, where the location of the TEM lamella (Figure 5.17a) covers phases 2 and 3. The reaction layer in Figure 5.17b shows phase 2 and 3 (denoted as 2 and 3 respectively), where their placement points indicates the location of diffraction patterns (DP). Phase 2 is analysed because it is the main reaction phase, and the most abundant in the corroded samples. The dark-field mode (where denser region appear brighter) is used to enhance image contrast, which resulted in a lighter contrast for phase 2 compared to phase 3 as opposed to the SEM images. The DP for phase 3 (Figure 5.17c) shows an amorphous structure with minor crystallinity, whilst that of phase 2 is highly crystalline forming hexagonally-shaped grains (Figure 5.17d). The hexagonal shapes of the grains (Figure 5.17b and e) are almost identical to apatite structures that are formed from $Yb_2Si_2O_7$–CMAS reaction [76]. EDS analysis of phase 2 (Figure 5.17e) is taken at the middle and periphery of a single grain (spectrum 6 and 5 respectively). Figure 5.17f shows spectrum 5 at the grain boundary, where the composition in wt% is: 5.9 Si, 5.9 Ca, 1.0 Mg and 87.2 Yb. The composition of spectrum 6 at the middle of the grain is: 6.4 Si, 6.9 Ca, 1.0 Mg and 85.8 Yb.

The TEM images (dark-field mode) for CMAS–Lu-silicate reaction phases 2 and 3 (Figure 5.18a and b) show pentagon-shaped grains, resembling those of Yb-silicate, where the pentagon-shape can be a distortion of the hexagonal grains. Figure 5.18e (bright-field mode) shows that some of the grains have a darker grey core (spectrum 1; surrounded by red dashed

lines) and a light grey rim (spectrum 2; surrounded by dark blue dashed lined), where the EDS analyses (Figure 5.18f) of the core shows higher Ca content compared to the rim. The EDS analysis of phase 3 (Figure 5.18f) shows the highest Lu_2O_3 content. The DP patterns of phases 3 and 2 (Figure 5.18c and d respectively) show the same conclusion as Yb-silicate. Figure 5.16a (dark-field mode) and b (bright-field mode) show TEM line scans for Yb-silicate and Lu-silicate respectively.

The TEM images of the CMAS–Er-silicate apatite reaction product (Figure 5.19) was extracted from the CMAS–RL interface. The morphology shows the existence of three grain shapes: equiaxed pentagonal grains as those formed by Yb and Lu-silicates (Figure 5.19b), vertically-stacked hexagonal finger-like grains (Figure 5.19c), and randomly-oriented wide polygonal elongated grains (Figure 5.19d) that are most-likely hexagonally-elongate. The interface between the finger-like grains are shown at the inset image of Figure 5.19c, where the molten CMAS between the finger grains appear as black lines, and no CMAS-containing grain boundaries for the grains. They are neatly crystallised. The hexagonal wide grains are also surrounded by molten CMAS pool that separates the grains, yet each grain edge does not contain high-Ca melt. Moreover, there aren't any signs of grain boundary interaction with the CMAS melt. Small apatite spherical grains also crystallises within the CMAS melt pool between the above explained grains as shown in Figure 5.19b, c and d.

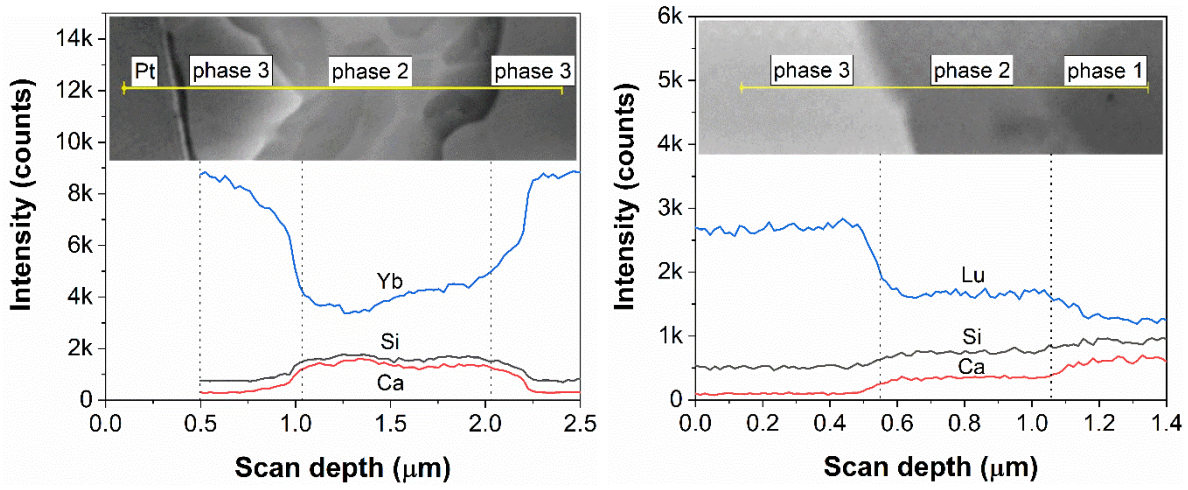


Figure 5.16 TEM line scan at 1300 °C after 48 h for (a) Yb-silicate in Figure 5.17 (b) Lu-silicate in Figure 5.18.

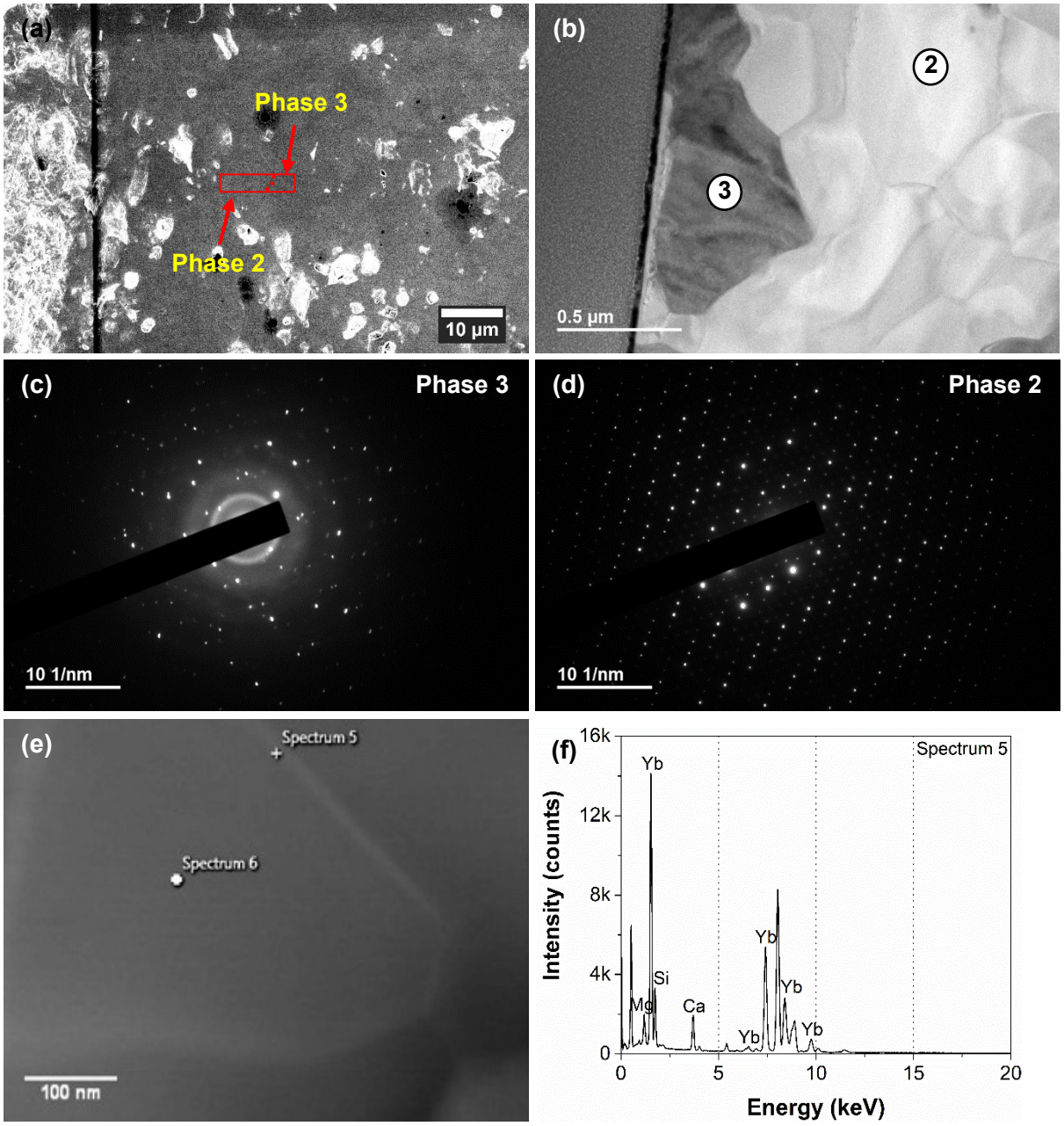


Figure 5.17 TEM image for Yb-silicate at 1300 °C after 48 h (a) FIB lamella location (b) DP locations of (c) phase 3 (d) phase 2 (e) EDS on phase 2 grain (f) EDS analysis.

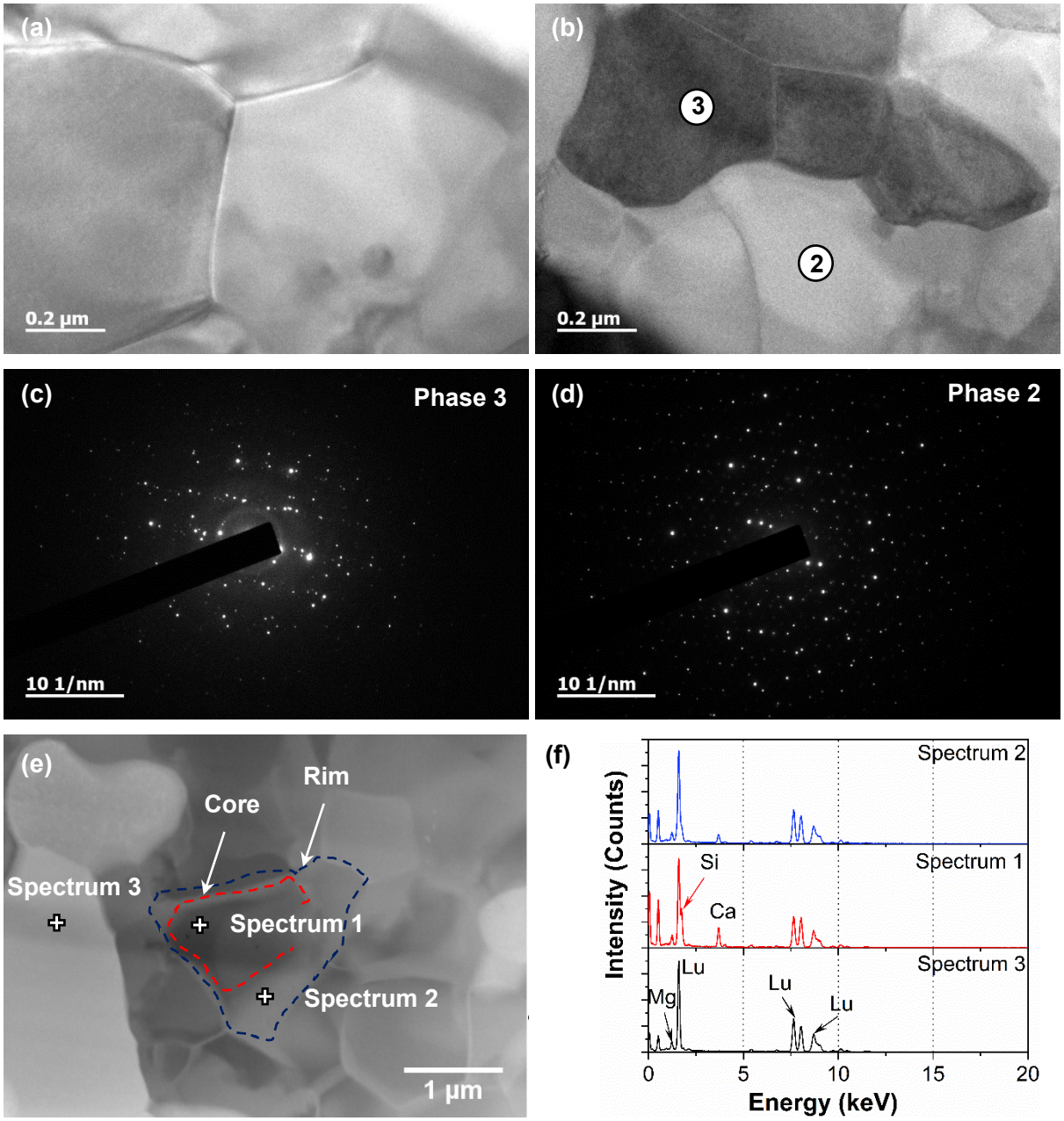


Figure 5.18 TEM image for Lu-silicate at 1300 °C after 48 h (a) phase 2 hexagonal grains (b) DP locations of (c) phase 3 (d) phase 2 (e) EDS on phases 2 and 3 grains (f) EDS analysis.

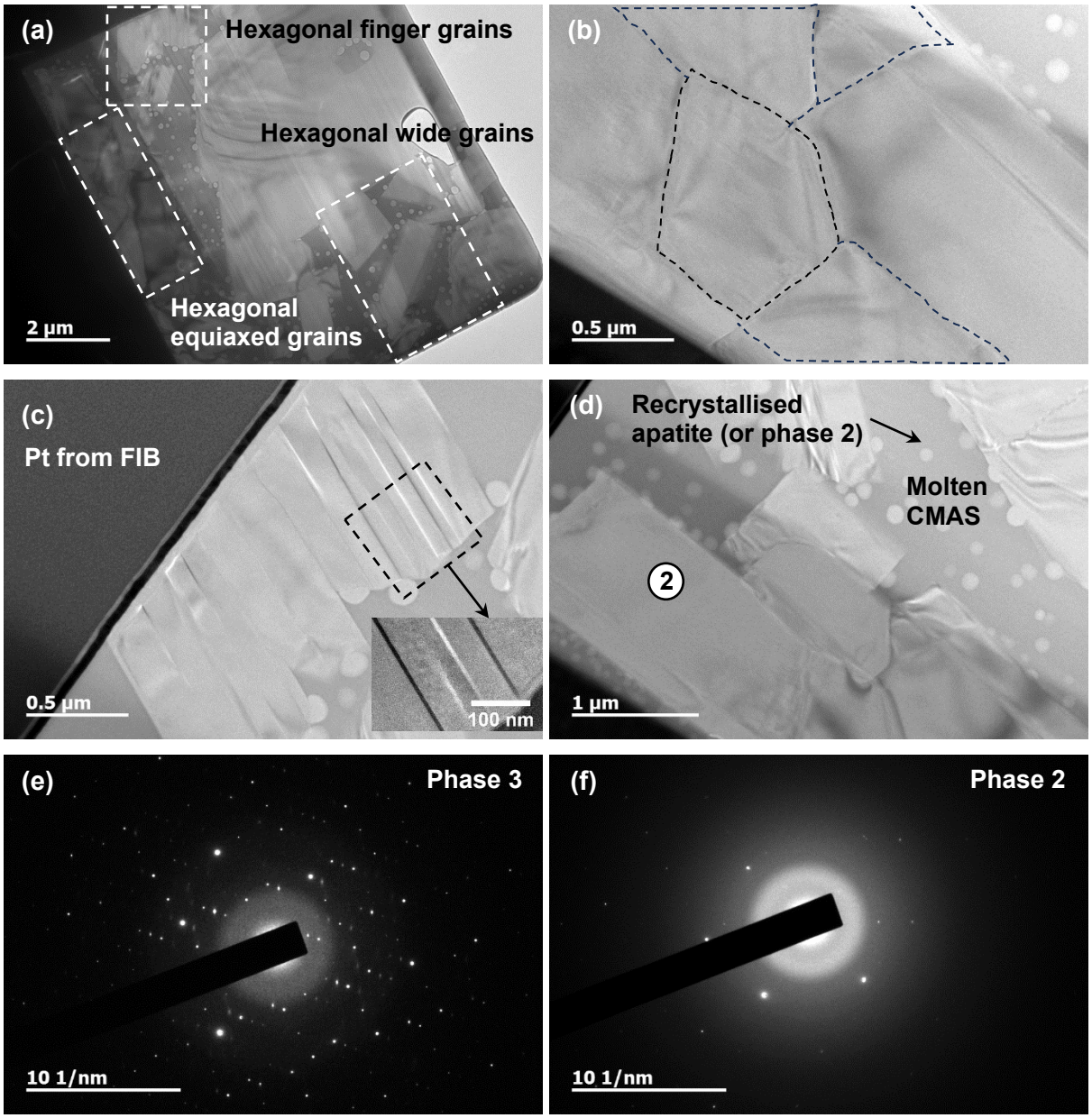


Figure 5.19 TEM image for Er-silicate at 1300 °C after 48 h (a) TEM sample top view (b) hexagonal equiaxed grains (c) hexagonal finger grains (d) hexagonal wide grains (e) phase 2 finger grains (f) molten CMAS.

5.3.6 RE-silicate and CMAS reaction kinetics

The reaction layer thickness versus exposure time (Figure 5.20a) shows that Yb-silicate has the lowest RL thickness followed by Lu-silicate then Er-silicate. The value of the RL thickness of Er-silicate is slightly less than double that of Yb and Lu-silicates. The weight gain ΔW versus exposure time (Figure 5.20b) has the same trend where Yb-silicate has the lowest weight gain and Er-silicate has the highest. The weight gain trend for Yb and Lu-silicates show similar reaction kinetics, which corresponds with the RL thickness and normalised penetration depth plots. The weight gain and RL thickness plots have parabolic behaviour showing a decrease in value with corrosion duration, and the trend for the Yb and Lu-silicates proceed at a slower rate compared to that of Er-silicate.

The normalised penetration depth versus corrosion time (Figure 5.21) is lowest for Lu and highest for Er-silicate. The penetration depth of each measured sample is normalised by dividing it with the measured coating thickness because there is a ~50 μm range variation in thickness between the processed coatings. Both Yb and Lu-silicates have an almost similar values for the penetration depth, that converge after 24 h and both are fully penetrated after 48 h. On the other hand, Er-silicate has a higher rate between 1–24 h, and full penetration by CMAS is achieved after 24 h. The kinetics of the normalised penetration depth plots are linear for Yb, Lu and Er-silicates. Figure 5.21b and Figure 5.22a and b show the weight gain plots for Yb, Lu and Er-silicates respectively at 1250, 1300 and 1350 °C. They show an increased weight gain and higher corrosion with increasing temperature. The corrosion increases by an average of ~85% from 1250 to 1300 °C and ~90% from 1300 to 1350 °C implying a ~100% increase in corrosion for every 50 °C increase in temperature

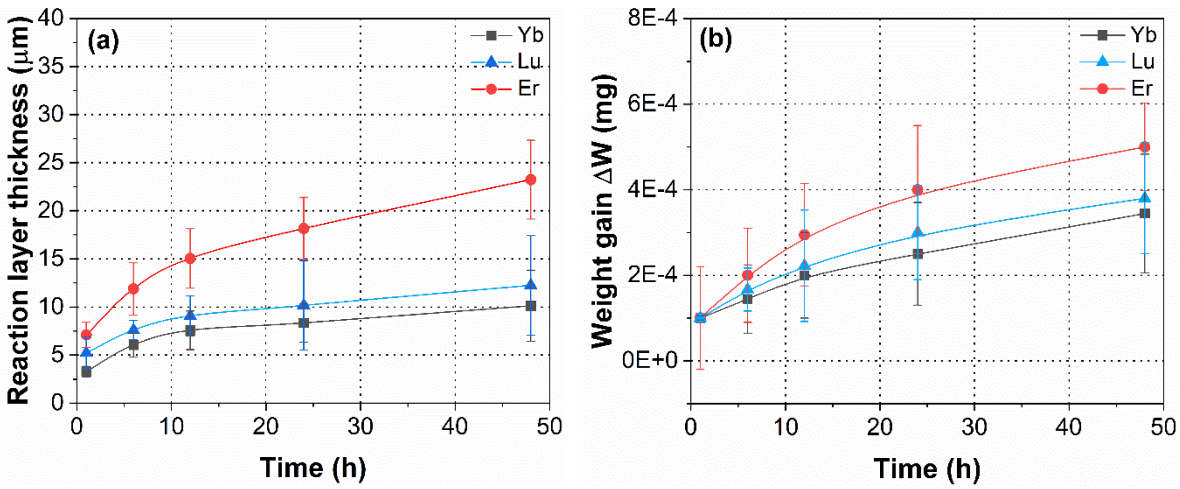


Figure 5.20 (a) Reaction layer thickness (b) ΔW plot of CMAS–EBC reaction at 1300 °C.

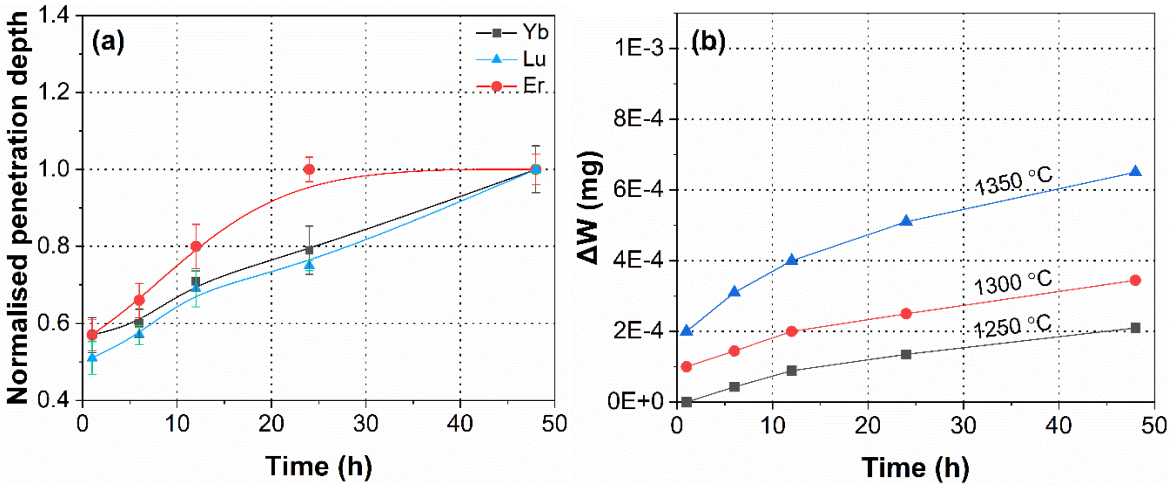


Figure 5.21 (a) Penetration depth of CMAS interaction with Yb, Lu and Er-silicates at 1300 °C (b) ΔW plot of CMAS–Yb-silicate reaction at 1250, 1300, and 1350 °C.

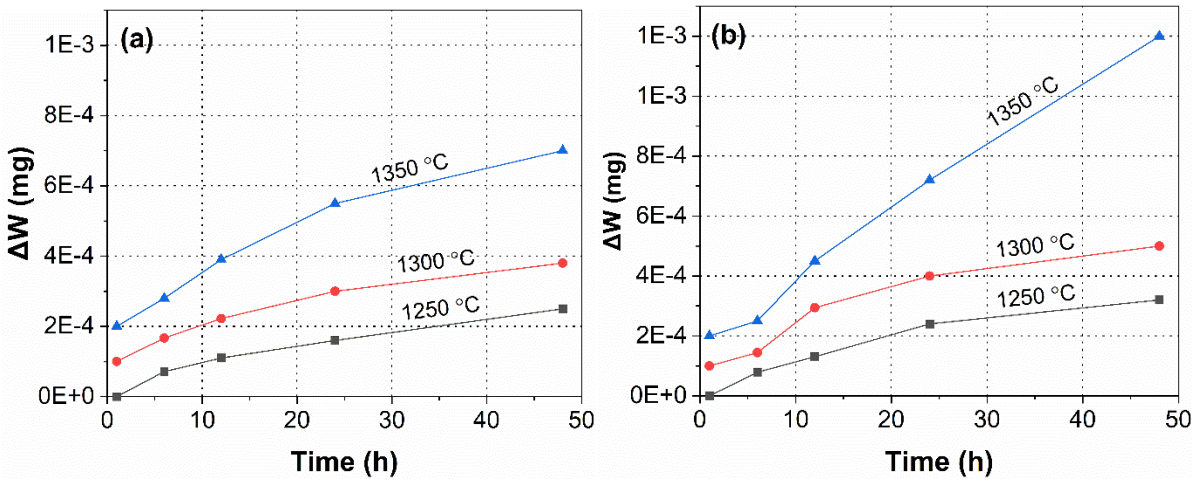


Figure 5.22 ΔW plot of CMAS reaction between 1250, 1300, and 1350 °C for (a) Lu-silicate (b) Er-silicate.

5.3.7 RE-silicate and CMAS diffusion

The diffusion coefficient (based on Fick's second law) D_{FSL} plots for Ca and Si in the penetrated region of the coat are shown in Figure 5.23, while the values are introduced in Table 5.3. Ca concentrations are 10.5 wt% C_s, 7.5 wt% C_o and 9 wt% $C_{(x,t)}$, while Si concentrations are 21.5 wt% C_s, 18 wt% C_o and 19.8 wt% $C_{(x,t)}$. The concentration values at each of the above mentioned C parameters are considered as the average of 20 EDS points. The values of $C_{(x,t)}$ are obtained from phase 2 because they are the most-abundant reaction phase. The D_{FSL} values for Yb and Lu-silicates are almost the same, while Er-silicate is higher than both by ~32%. The plot shows an exponential behaviour where D_{FSL} decreases with increasing corrosion duration. The diffusion coefficient drops suddenly between 1–6 h, then decreases linearly until 48 h. Alternatively, D_{DAN} is calculated based on the CMAS penetration depth and corrosion duration only without taking into consideration the concentration profiles of Ca or Si along the penetrated depth. Hence, it is considered as the mean square displacement in the diffusion process, which estimates the distance moved by the melt from its initial position over a time interval. It reflects the diffusive behavior of the species in the melt including Ca and Si but is also influenced by the coating processes. The results show that for Ca at penetration depth X and corrosion time t, D_{DAN} is lower than D_{FSL} by 6.55% for Yb-silicate and ~10% for Lu and Er-silicates. The diffusion of Si is higher than Ca by 10.27% for Yb-silicate and 7% for Lu and Er-silicates.

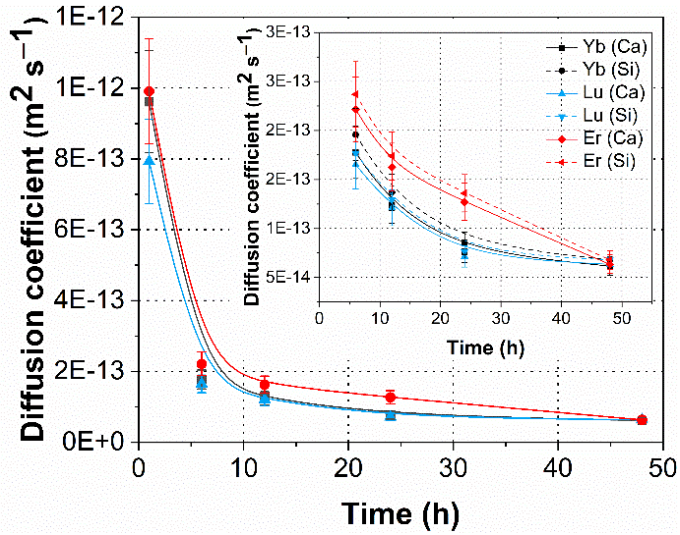


Figure 5.23 D_{FSL} **of Ca in Yb, Lu and Er-silicates after CMAS corrosion between 1–48 h at 1300 °C. Inset:** D_{FSL} **of Ca and Si (shown as dashed lines).**

Table 5.3 D_{FSL} **and** D_{DAN} **of Ca and Si in Yb, Lu and Er-silicates.**

EBC coat	Time (h)	X (μm)	$D_{FSL, Ca}$ (m^2 sec^{-1})	$D_{FSL, Si}$ (m^2 sec^{-1})	D_{DAN} (m^2 sec^{-1})
Yb-silicate	1	57	9.61×10^{-13}	1.06×10^{-12}	9.02×10^{-13}
	6	60	1.77×10^{-13}	1.95×10^{-13}	1.66×10^{-13}
	12	71	1.24×10^{-13}	1.37×10^{-13}	1.16×10^{-13}
	24	79	8.70×10^{-13}	8.48×10^{-14}	7.22×10^{-14}
	48	100	6.16×10^{-14}	6.79×10^{-14}	5.78×10^{-14}
Lu-silicate	1	51	7.93×10^{-13}	8.41×10^{-13}	7.93×10^{-13}
	6	57	1.65×10^{-13}	1.76×10^{-13}	1.65×10^{-13}
	12	69	1.20×10^{-13}	1.29×10^{-13}	1.20×10^{-13}
	24	75	7.93×10^{-14}	7.64×10^{-14}	7.14×10^{-14}
	48	100	6.35×10^{-14}	6.79×10^{-14}	6.35×10^{-14}
Er-silicate	1	57	9.90×10^{-13}	9.90×10^{-13}	9.02×10^{-13}
	6	66	2.21×10^{-13}	2.21×10^{-13}	2.01×10^{-13}
	12	77	1.62×10^{-13}	1.62×10^{-13}	1.37×10^{-13}
	24	100	1.27×10^{-13}	1.27×10^{-13}	1.15×10^{-13}
	48	100	6.35×10^{-14}	6.35×10^{-14}	5.78×10^{-14}

5.3.8 RE-silicate and CMAS structure

The XPS analysis were obtained close to the CMAS–RE_2O_3 interface, as shown in Figure 5.24a, Figure 5.26a and Figure 5.28a. The purpose of the XPS is to obtain the binding energies (BE), oxidation states, and atomic weight for Si2p, O1s, Ca2p, Yb4d, Lu4d, and Er4d as detailed in Table 5.4.

The wide spectra shown in Figure 5.24b is assigned to Si2p, O1s, Ca2p and Yb4d. The fitting of the Si2p peak resulted in 4 main peaks, 2 doublets each, as shown in Figure 5.25a. The first doublet is at 102.1 and 102.6 eV, which is related to SiO_2 [314-316]. The second doublet peak at 103.4 and 104.0 eV concerns Si–O_4 units, which is attributed to silicate SiO_4^{4-} units [314, 317-319]. It is noted that the BEs of SiO_4^{4-} and SiO_2 are the same, where Si has the same oxidation state [314, 320]. The peak at 102.6 eV can also be linked to Si–O_3 [321] because the lower BE indicates lower oxidation state compared to the SiO_2 at 103.4 and 104 eV [314]. Regarding Lu-silicate (Figure 5.26 and Figure 5.27a), the BE at 102.8 and 103.5 eV is linked either to SiO_4^{4-} and SiO_2 [314, 320], whilst the 101.3 and 101.9 eV peaks are related to SiO_2 [314, 322]. They are almost similar to the BEs of 102.6 and 103.4 eV for Yb-silicate. As to Er-silicate (Figure 5.28 and Figure 5.29a), the peak at 99.50 eV represents either Si [314], SiO_2 [314, 323, 324], or SiO_x [314, 325], while the 100 eV peak reflects the presence of Si [314, 326]. The peak at 102.3 eV is assigned to silicates in calcium apatite structures as $Ca_6(Si_6O_{17})(OH)_2$ and $Ca_{10}(PO_4)_{4.4}(SiO_4)_{1.24}$ [314, 327].

The O1s binding energy is commonly linked to oxides as shown in Figure 5.25b. There is discrepancy in literature when assigning O1s peaks for oxygen vacancies. Some authors [328, 329] assign oxygen vacancies between 531–532 eV, while others [330, 331] assign it at the lower binding energy of 529–530 eV. Assigning a peak for oxygen vacancy is not reliable and will be disregarded from the current XPS analysis. Regarding O^{2-} in CaO, it is assigned at 530.6 eV [332-335], while 532 eV is assigned to bridging oxygens in silicates [332, 334, 336]. The O1s BE for an oxygen atom in CaO is 2 eV lower than that for SiO_2 because of the stronger Si–O covalent bond compared to the Ca–O ionic bond [337-339]. The peak at 530.6 is also close to the 531 eV peak assigned for Yb_2O_3 [314]. Regarding Lu-silicate (Figure 5.27b), the BE at 530.5 eV is related to O^{2-} in CaO [332-335], which is synonymous with the Yb-silicate peak at 530.6 eV. The BE of 531.8 eV is also synonymous with that obtained for Yb-silicate at 532 eV, and it can also relate to bridging oxygens in SiO_2 [340-342]. Concerning Er-silicate

(Figure 5.29b), the peak at 531.3 eV is related to O^{2-} in the CaO [314, 343], while the peak at 533 eV is related to O^{2-} in SiO_2 [344] or oxygen in Er-silicate structures $Er_2(SO_4)_3$ [345].

The BEs for Ca–O bond are between 347–350.9 eV [314, 333, 346, 347]. The doublet peaks at 347.3 and 350.9 eV (Figure 5.25c) are assigned to chlorapatite $Ca_5(PO_4)_3Cl$ [348] and hydroxyapatite $Ca_{10}(PO_4)_6(OH)_2$ [314, 349] respectively, where both belong to the apatite family minerals. This indicates that these peaks are for CaO reaction linked to the tetrahedral PO_4 group; which is synonymous with the SiO_4 interaction in case of silicate oxyapatites. The doublet peaks at 344.3 and 347.6 eV relate to Ca–O bond [318]. However, the peak at 347.6 eV can also be assigned to $Ca_{10}(PO_4)_6F_2$ [314]. Regarding Lu-silicate (Figure 5.27c), the BE peaks of 347.5 and 351.2 eV are synonymous with the Yb-silicate peaks at 347.3 and 350.9 eV. The peak at 348.3 concern the presence of Ca^{2+} [314], while that of 352 eV concern Ca–O bond [314, 350]. Regarding Er-silicate (Figure 5.29c), the peak at 348 eV is related to Ca^{2+} as indicated before in Lu-silicates or to Ca–SiO_4 bond [351], which is related to calcium polyhedron linked to silicates in apatites structures. The peaks at 351.4 and 351.6 eV are also related to Ca–SiO_4 bond, which is synonymous with the 351.2 eV peak of Lu-silicates.

The $Yb4d_{5/2}$ peak at 185.4 eV (Figure 5.25d) is assigned to Yb–O in apatite structures [314]. Regarding Lu-silicate (Figure 5.27d), the $Lu4d_{5/2}$ peak is at 196.7 eV [314, 352]. The peak at 198.5 eV relates to $Lu_2(SO_4)_3$; Lu-silicates (Lu–SiO_x) in apatite structure [314, 345]. The peak at 107 eV on the other hand, concerns Lu–O [314]. The BE of 169 eV is for the presence of Er or Er_2O_3 as shown in Figure 5.29d [314, 317].

Table 5.4 Fitting parameters from the XPS spectra for Si2p, O1s, Ca2p and RE4d.

Element	BE (eV)	Structure (oxidation state)	At (%)	References
Yb-silicate–CMAS corrosion				
Si2p	102.1	Si–O_2 (Si^{4+})	36.5	[314, 315]
	102.6	Si–O_2 (Si^{4+}) or Si–O_3 (Si^{3+})	36.5	[314, 316]
	103.4	Si–O_4 (Si^{4+})	13.5	[314, 317-319]
	104.0	Si–O_4 (Si^{4+})	13.5	
O1s	530.6	O–Ca (O^{2-})	36.1	[314, 332-336]
	532.0	O_4–Si (O^{2-})	64.0	[332, 334, 336]
Ca2p	347.3	Ca–SiO_4 in apatite (Ca^{2+})	43.2	[314, 333, 346-349]
	350.9	Ca–SiO_4 in apatite (Ca^{2+})	43.0	
	344.3	Ca–O (Ca^{2+})	6.90	[314, 317, 318]
	347.6	Ca–O (Ca^{2+})	6.86	
Yb4d	185.4	Yb–O_3 (Yb^{3+})	100	[314]
Lu-silicate–CMAS corrosion				
Si2p	101.3	Si–O_2 (Si^{4+})	11.0	[314, 322]
	101.9	Si–O_2 (Si^{4+})	11.0	
	102.8	Si–O_4 (Si^{4+}) or Si–O_3 (Si^{3+})	39.1	[314, 320, 321]
	103.5	Si–O_4 (Si^{4+})	39.1	[314, 317-319]
O1s	530.5	O–Ca (O^{2-})	3.75	[332-335]
	531.8	O_4–Si (O^{2-})	81.2	[332, 334, 336]
	532.4	O_4–Si (O^{2-})	15.0	[314, 340-342]
Ca2p	347.5	Ca–SiO_4 in apatite (Ca^{2+})	39.7	[314, 333, 346-349]
	351.2	Ca–SiO_4 in apatite (Ca^{2+})	39.7	
	348.3	Ca (Ca^{2+})	10.2	[314]
	352.0	Ca–O (Ca^{2+})	10.2	[314, 350]
Lu4d	194.2	Lu–O_3 (Lu^{3+})	8.40	[314]
	196.7	Lu–O_3 (Lu^{3+})	42.0	[314, 352]
	198.5	Lu–O in apatite (Lu^{3+})	10.1	[314, 345]
	207.0	Lu–O_3 (Lu^{3+})	39.6	[314]
Er-silicate–CMAS corrosion				
Si2p	99.50	Si or Si–O_2 (Si^{4+}) or Si–O_x	10.7	[314, 323-325]
	100.0	Si	10.7	[314, 326]
	102.3	Si–O_4 (Si^{4+}) in apatite	39.2	[314, 327]
	102.8	Si–O_4 (Si^{4+}) or Si–O_3 (Si^{3+})	39.2	[314, 320, 321]
O1s	531.3	O–Ca (O^{2-})	52.0	[314, 343]
	532.2	O_4–Si (O^{2-})	35.1	[314, 340-342]
	533.0	O_2–Si (O^{2-}) or O^{2-} in Er-silicates	18.0	[344, 345]
Ca2p	348.0	Ca (Ca^{2+}) or Ca–SiO_4 in apatite (Ca^{2+})	45.0	[314, 351]
	351.6	Ca–SiO_4 in apatite (Ca^{2+})	5.01	[314, 333, 346-349]
	351.4	Ca–SiO_4 in apatite (Ca^{2+})	45.0	
	355.3	Ca–SiO_4 in apatite (Ca^{2+})	5.01	[314]
Er4d	169.0	Er or Er–O_3 (Er^{3+})	100	[314, 317]

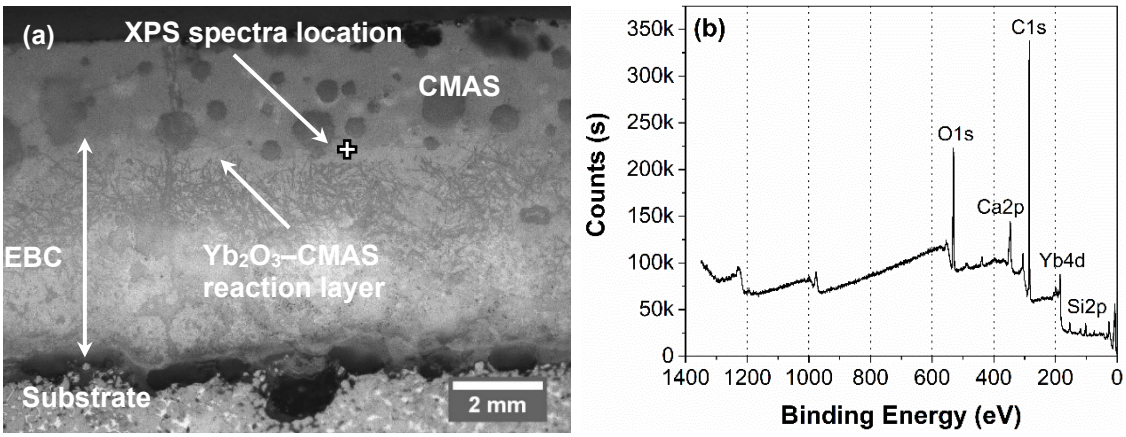


Figure 5.24 (a) optical image showing the location of XPS scans Ca–Yb apatite (b) XPS wide scan.

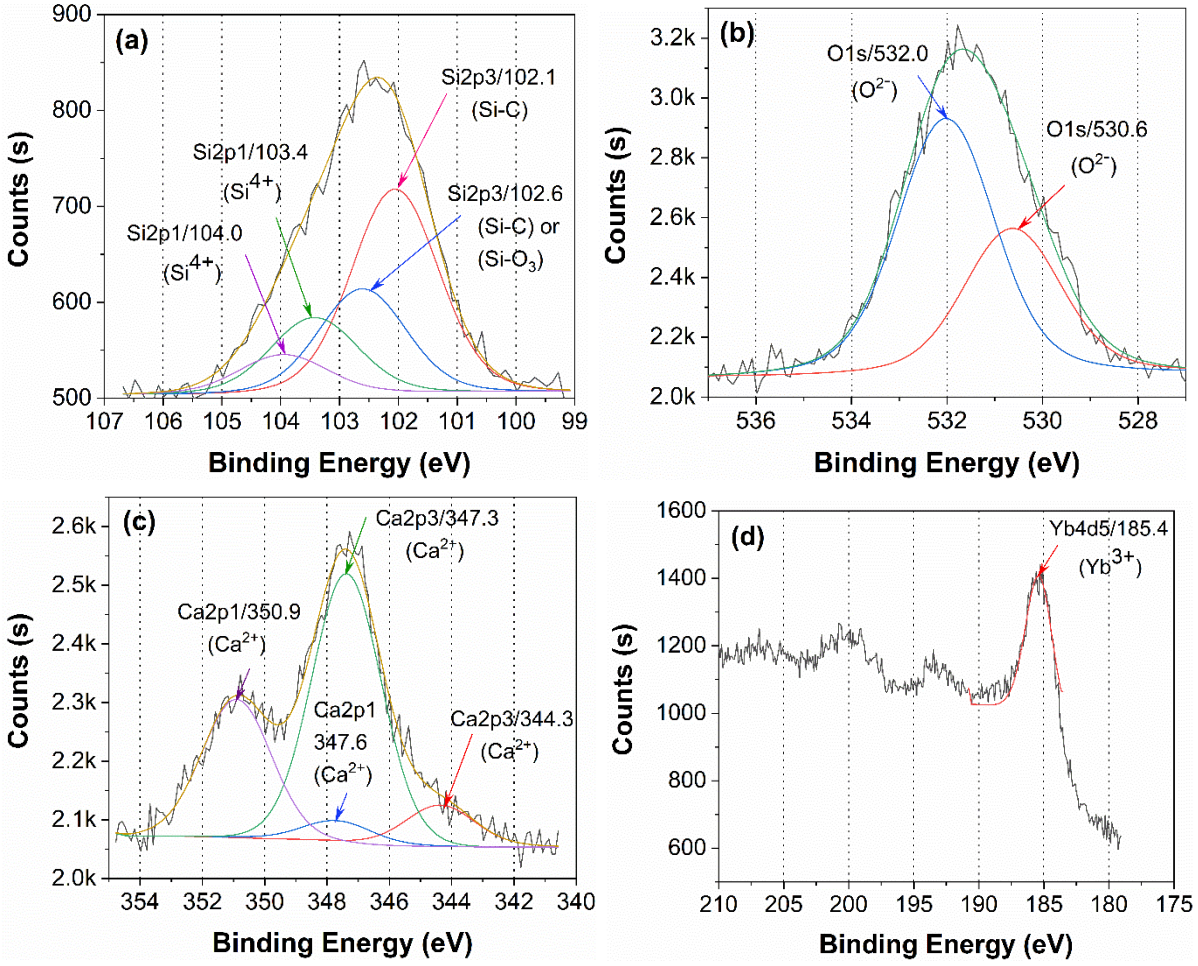


Figure 5.25 XPS scans on phase 2 Ca–Yb apatite for (a) Silicon Si2p (b) oxygen O1s (c) Calcium Ca2p (d) Ytterbium Yb4d.

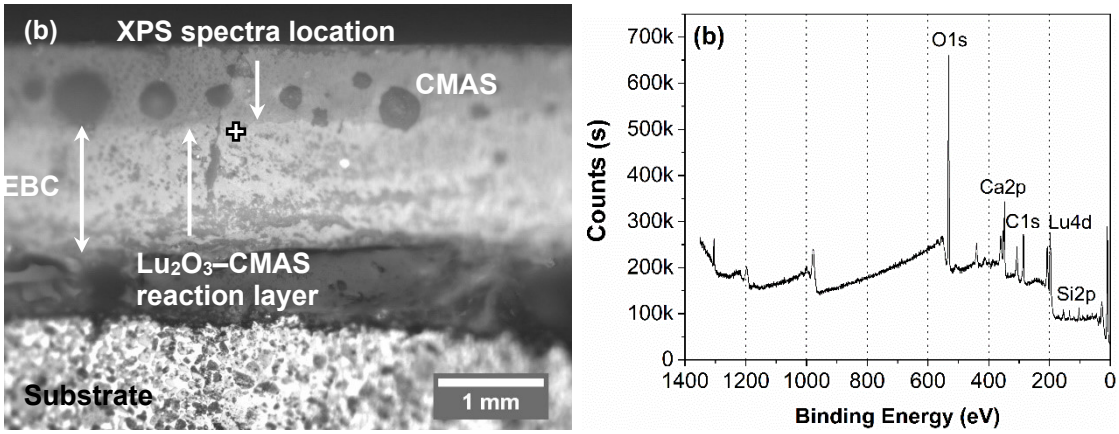


Figure 5.26 (a) optical image showing the location of XPS scans Ca–Lu apatite (b) XPS wide scan.

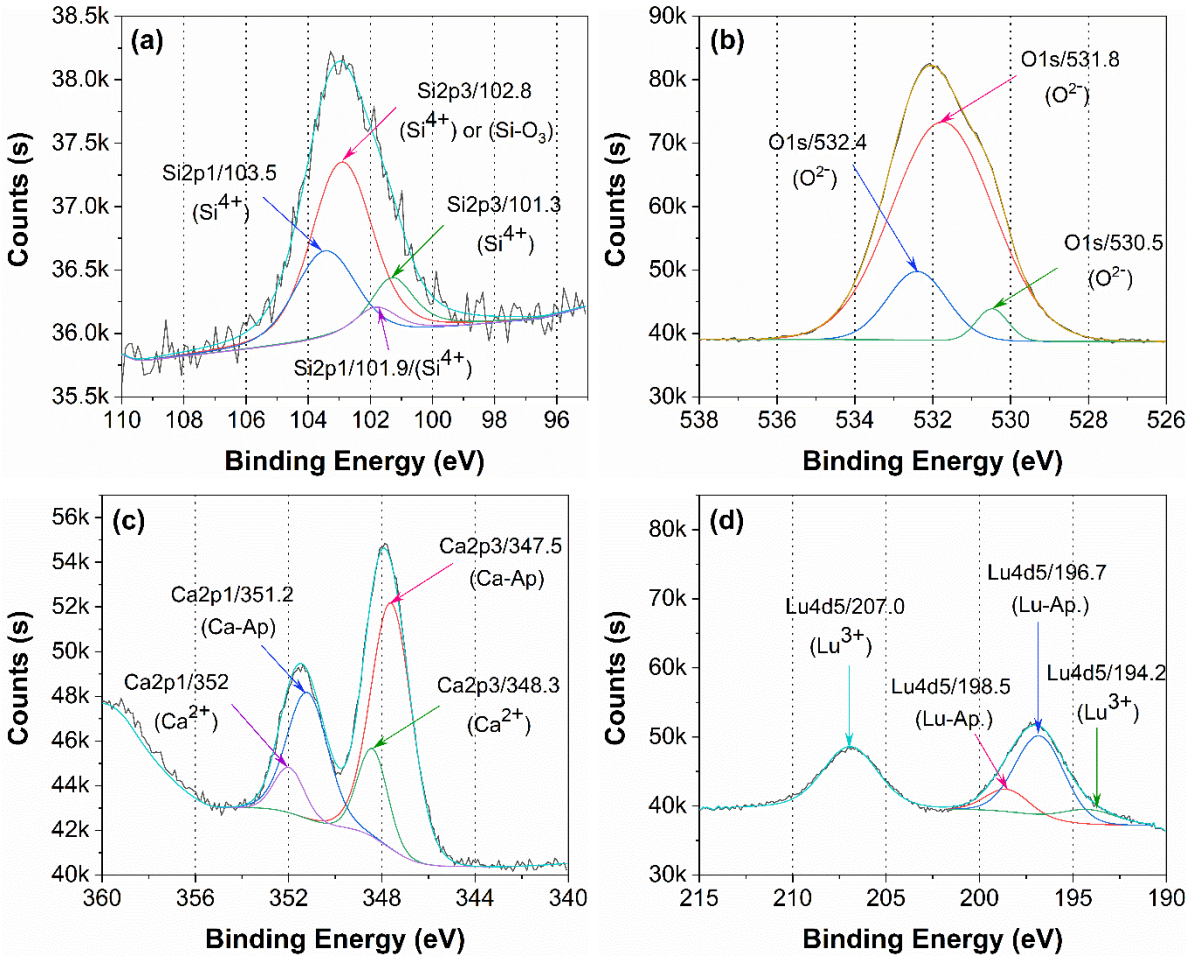


Figure 5.27 XPS scans on phase 2 Ca–Lu apatite for (a) Silicon Si2p (b) oxygen O1s (c) Calcium Ca2p (d) Lutetium Lu4d.

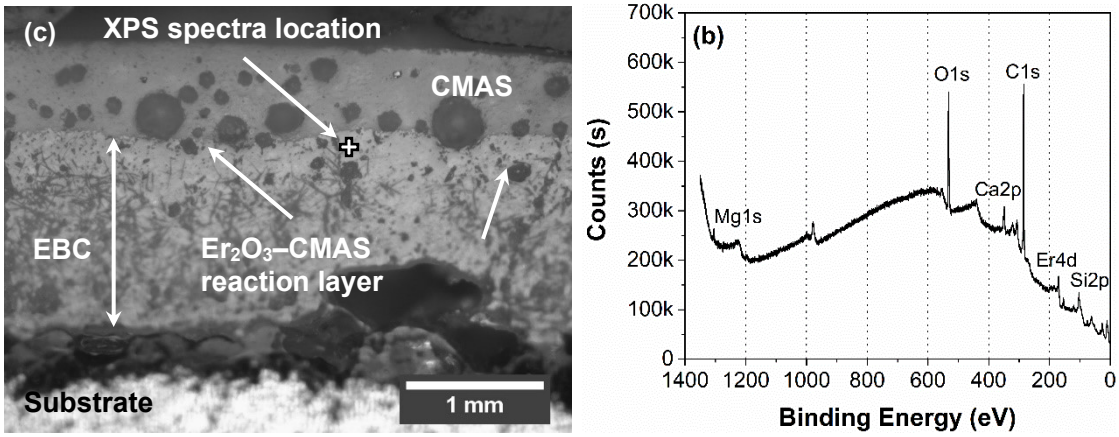


Figure 5.28 (a) optical image showing the location of XPS scans for Ca–Er apatite (b) XPS wide scan.

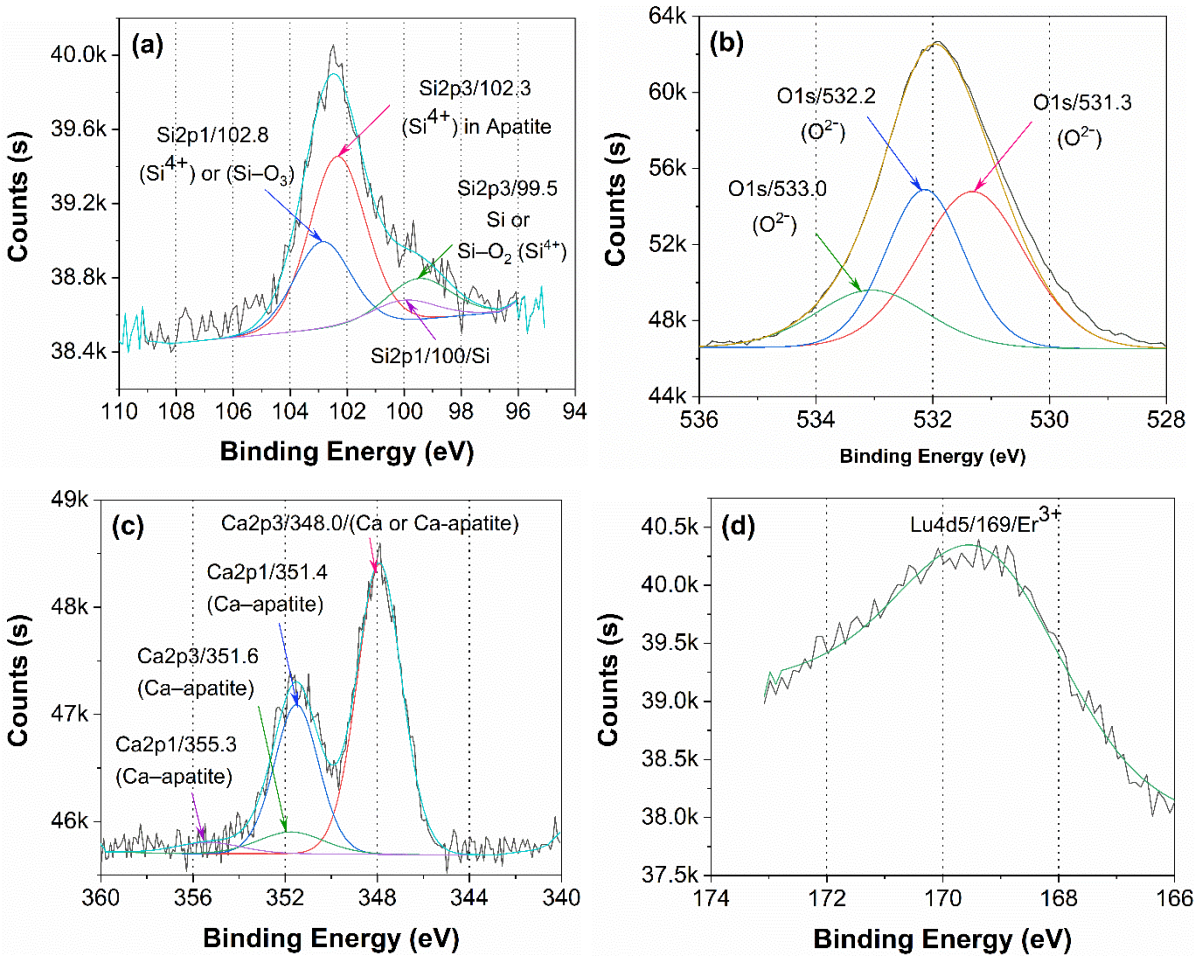


Figure 5.29 XPS scans on phase 2 Ca–Er apatite for (a) Silicon Si2p (b) oxygen O1s (c) Calcium Ca2p (d) Erbium Er4d.

5.4 DISCUSSION

5.4.1 Corrosion composition

The corrosion of coating passes through five main stages as shown in Figure 5.30. First, CMAS particles from the environment deposit on the coating. Second, the particles melt at approximately 1250 °C and starts reaction with the coating surface. Third, the melt gradually infiltrates the coating, where corrosion occurs in the middle of the coating at the fourth step. Infiltration and reaction occurs simultaneously until full penetration occurs. Fifth and finally, during cooling, cracking occurs. This section will examine the composition of corrosion products followed by the corrosion mechanism and the corrosion process.

The corrosion behaviour and microstructure morphology of Yb_2O_3 and Lu_2O_3 under CMAS attack are similar. The composition of the reaction layers formed by Yb_2O_3 and Lu_2O_3, at the CMAS–RE_2O_3 interface, falls between that of grossular garnet $Ca_{1.5}Mg_{1.5}Yb_{1.6}(SiO_4)_3$ and Ca–RE cyclosilicate $Ca_3Yb_2Si_6O_{18}$. Regarding RL phase 1, the CMAS reaction with RE_2O_3 differs from that of RE_2SiO_5 and $RE_2Si_2O_7$ due to the presence of Mg and high amounts of alkaline earth oxides (AEO) at the expense of RE_2O_3 as shown by the solid lines in Figure 5.31. The formation of Ca–Mg–Si–RE garnet phase 2 in Yb_2O_3 and Lu_2O_3 topcoats instead of silicate oxyapatite agrees with previous authors [123, 276-279]. Phase 2 for Yb and Lu-silicates has Mg content ~0.5–3 wt% and a Ca:RE ratio that ranges between 0.24 (for stoichiometric apatite) and 0.65; the Ca–Mg–Si–RE composition is dominated by AEO and SiO_2 and slightly deviates from silicate oxyapatite (dashed lines in Figure 5.31). The compositional range of phase 2 (Figure 5.31) is $Ca_{10-x}Yb_x(SiO_4)_6O_y$ ($y = ½x–2$; $6 \leq x \leq 8$), which agrees with previous authors [120, 274, 281] who recorded that the corrosion of Yb_2SiO_5 and Yb_2SiO_7 with high Yb_2O_3 content in CMAS environment results in the formation of non-stoichiometric apatite $CaRE_4Si_3O_{13}$ [120], grossular garnet $Ca_{1.5}Mg_{1.5}Al_{0.4}Yb_{1.6}(SiO_4)_3$ [274, 281] or cyclosilicate $Ca_3Yb_2Si_6O_{18}$ [120, 274]. The reaction for phases 1 and 2 deviates from stoichiometric apatite because they did not start with RE_2SiO_5 or $RE_2Si_2O_7$ but with RE_2O_3, which may not have formed stoichiometric silicates as a mid-way reaction to apatite.

Concerning Er_2O_3, the reaction product consists of Ca–Mg–Si–Er garnet in addition to stoichiometric apatite ($Ca_2Er_8(SiO_4)_6O_2$) that has a Ca:RE ratio of ~0.24 [123, 147, 152]. As with Yb and Lu-silicates, the Ca:RE ratio does not change with corrosion duration; for example, phase 2 at 6 h has the same composition as that of 24 h. The Ca:RE ratio decreases away from the RL, where phase II needle-like grains in the middle of the coat has slightly higher Er content (and Ca:Er ratio of ~0.2) compared to the coarse apatite grains. The silica released from the apatite formation reacts further with the available Er_2O_3 to form new apatite grains; the ongoing reaction continues until Er_2O_3 is consumed. Thus, Er_2O_3 reaction with CMAS is more vigorous compared to Yb_2O_3 and Lu_2O_3. This explains why CMAS melt has penetrated to the Er_2SiO_5 bottom coat after short duration of 6 to 12 h. The high rate of product-formation for Er-silicate compared to Yb and Lu-silicates conforms with its high weight gain plot, where weight gain reflects the quantity of products formed. The weight gain over time can also be translated to the rate of reaction formation (mg h^{-1}). In addition, the stoichiometric apatite RL forms more rapidly than the garnet formed by Yb and Lu-silicates, making it less stable in comparison. The stoichiometric appetite formed is proceeded by the formation of Er_2SiO_5 and $Er_2Si_2O_7$ or by metastable $Er_{9.33}(SiO_4)_6O_2$ apatite, which requires Ca^{2+} cations to stabilise it [147], explaining the formation of Er-silicate oxyapatite as the dominant reaction layer.

The equations for the phases 1 (RL) and 2 (main corrosion product) are described by Eqs. (5.7) and (5.8) respectively. The compliment of the CMAS formula unit for Eq. (5.7) is Al_{13} and for Eq. (5.8) is Mg_9Al_{13}, which are excluded because they are not significantly incorporated in the reaction product. The reaction of the melt with RE_2O_3 to produce the RL [Eq. (5.7)] results in a Ca–RE residue that further reacts with RE_2O_3 increasing its consumption rate. The reaction equation of phase 2 garnet [Eq.(5.8)] assumes that half the melt amount reacts with RE_2O_3 because by the time the melt reaches the reaction front (RE_2O_3), it becomes partially consumed from the infiltration process [353, 354]. This results in lower Ca and Si amounts at the middle of the coat compared to the top areas close to the melt, and also lower Ca and Si amounts for phase 2 garnet compared to phase 1. The reaction of the diluted melt with RE_2O_3 to form phase 2 [Eq. (5.8)] results in a $Ca_{11.5}RE_{92}$ byproduct (phase 3).

$$Ca_{33}Mg_9Si_{45} + 2RE_{50} \rightarrow Ca_{33}Mg_9RE_{10}Si_{45}\ (phase\ 1\ RL) + Ca_3RE_{90} \quad (5.7)$$

$$0.5Ca_{16.5}Si_{22.5} + 2RE_{50} \rightarrow Ca_5RE_8Si_{22.5}\ (phase\ 2) + Ca_{11.5}RE_{92}\ (phase\ 3) \quad (5.8)$$

The stoichiometry of the product and the stability of apatite precipitates are functions of RE^{3+} cation size. The ionic radius (IR) of RE^{3+} affects the reaction kinetics and RE_2O_3 resistance to CMAS. The formation of Ca–RE-silicate oxyapatite increases with increasing RE^{3+} because of the increase in cation to oxygen bond length, which will result in higher affinity for CaO [143, 149, 355]. In addition, Stokes et al. [148] found that during RE_2O_3–SiO_2 reaction, the formation of $RE_{9.33}(SiO_4)_6O_2$ is more stable than RE_2SiO_5 and $RE_2Si_2O_7$ at larger IR. The current finding confirms with Poerschke et al. [282] who observed that larger RE cations tend to stabilise apatite, while smaller ones stabilise garnet phase. This relates to the higher degree of distortion in the polydehra of larger radius RE elements and longer RE–O bond length [120]. Apatite is also promoted when the RE^{3+} IR is closer to that of Ca^{2+} as it would favour the substitution of RE^{3+} by Ca^{2+} into the RE_2O_3 and RE_2SiO_5 phases. The Er^{3+} IR (0.88 Å) is larger than that of Yb^{3+} (0.86 Å) and Lu^{3+} (0.85 Å), and the closest to Ca^{2+} (~1 Å) [121, 301], which is the reason Er-silicate forms apatite while Yb and Lu-silicates do not.

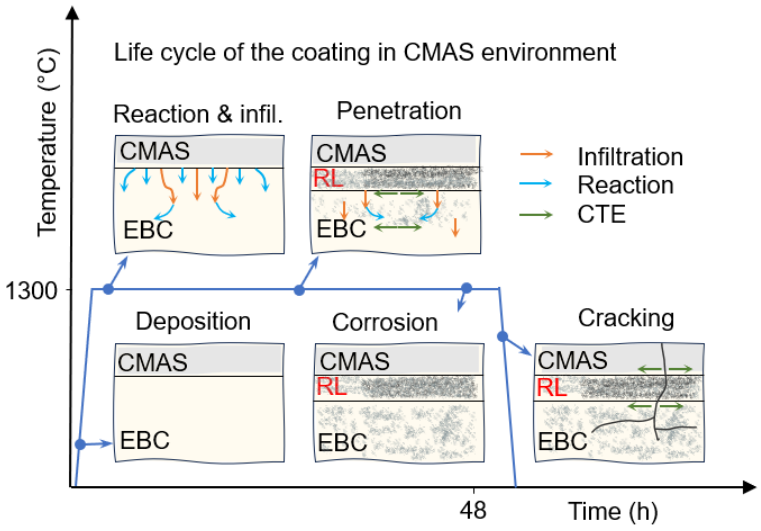


Figure 5.30 Coating failure sequence due to EBC–CMAS interaction at 1300 °C.

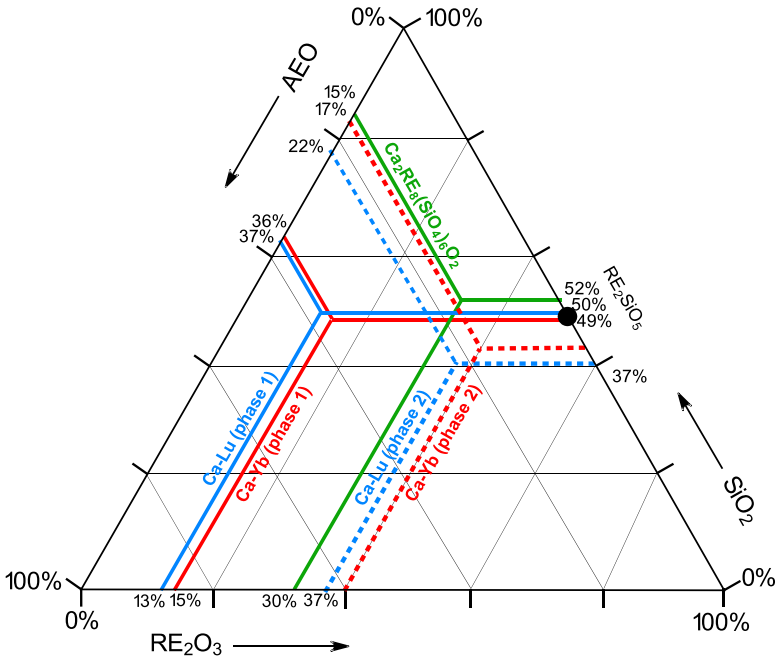


Figure 5.31 Redrawn ternary phase diagram [136] for the CMAS–RE_2O_3 reaction phases.

Figure 5.32a shows the range of ionic radii for the elements involved in the corrosion reaction (Ca, Mg, Si and RE cations) and the ionic potential (IP) of their oxides. where the IR is inversely proportional to IP. The increase in RL thickness and penetration depth (Figure 5.32b) with IR shows that the lower IP of Er_2O_3 compared to Yb and Lu-oxides makes it more readily reactive with the melt, which confirms with the low parabolic rate constant k_p of Yb and Lu-silicates compared to Er-silicate reflecting a faster reaction kinetics for Er-silicate as shown in Figure 5.33a.

The lower activation energy E for Er-silicate (450 ± 4 kJ mol^{-1}) compared to Yb and Lu-silicates (474 ± 6 and 500 ± 3 kJ mol^{-1} respectively), in Figure 5.33b, confirms that Er-silicate reacts with the melt more readily because its larger radius results in lower lattice energy compared to Yb^{3+} and Lu^{3+}, and thus a lower IP. In addition, the RE^{3+}–O bond length decreases with decreasing ionic radius and therefore, apatites form with lower RE^{3+} IR may require higher energy to accommodate distortions in their lattice that are associated with apatite formation. This confirms with the lowest BE of RE4d that decreases with increasing IR (BE of Er4d < Yb4d < Lu4d), and also agrees with the findings of Martínez-González et al. [300] and Ardanova et al. [301] regarding an inverse connection between RE^{3+} IR and activation energy for apatite formation. The formation of both stoichiometric apatite and garnet for Er-silicate

can be the reason behind the low activation energy. Apatite can be more thermodynamically favourable in Er-silicate compared to garnet, which explains its formation at the reaction front in contact with the melt. This also confirms with the presence of higher amount of apatites in the XPS scans of Er-silicate compared to Yb and Lu-silicates. The activation energy E for the formation of phase 2 is close to the activation energy values obtained for the formation of Sr apatite $Sr_1La_9Si_6O_{26.5}$ (470 kJ mol^{-1}) [293] and Nd apatite $Ca_2Nd_8Si_6O_{26}$ at 1400 °C (~423 kJ mol^{-1}) [356]. Moreover, stoichiometric apatites form with lower Ca content compared to Ca-rich phase 2 apatites and thus, they form at a faster rate and with lower E.

Optical basicity also links the coat's reactivity with the melt and its recession. A smaller difference in OB between the coat and the melt is preferable for a milder reaction because RE base compounds with larger ionic radius tend to react more readily with the AEO cations in the melt. Thus, the OB difference between CMAS and RE_2O_3 increases with increasing ionic radius: $OB_{(CMAS-Er_2O_3)}$ is 0.299 compared to 0.263 for $OB_{(CMAS-Yb_2O_3)}$ and 0.256 for $OB_{(CMAS-Lu_2O_3)}$. This is consistent with the enthalpy of formation ΔH_f of RE-monosilicates and oxyapatites, which decreases (becomes more exothermic) with increasing RE IR and increasing OB [2, 142, 296, 297]. However, the enthalpic stability of a compound also depends on other parameters in addition to IR and IP, such as bonding character, crystal structural parameters (**e.g.**, coordination with oxygen) and the size of the dopant compared to RE^{3+}.

The CaO amount in the RL of Yb and Lu-silicates is close to that of apatite, but the AEO (CaO + MgO) amount is close to that of SiO_2, which reflects higher Si amount in the reaction layer compared to Ca. This can indicate higher silicon diffusion through the coat compared to calcium. In phase 2, the SiO_2 content decreases while RE_2O_3 increases, demonstrating lower silicon diffusion across the reaction depth. In the corrosion phases, the AEO amount is inversely proportional to the RE amount; RE_2O_3 concentration increases from phase 1–3, while Ca and Si concentrations drop. The RE:Ca ratio in phase 2 is ~4 compared to ~1.3 for phase 1 showing higher RE_2O_3 content. The high AEO in phase 1, compared to phase 2, makes it at equilibrium with CMAS. Thus, it acts as first line of defence. The protective nature of Yb and Lu-silicates RL compared to Er-silicate is manifested in the amount of Ca in the Ca–$RE_2Si_2O_7$ bottom coat for Yb and Lu-silicates (~0.1 wt%), which is almost half that of Er-silicate (~0.25 wt%) as shown in the EDS line scans (Figure 5.9b, Figure 5.12b and Figure 5.15b).

The absence of Al in the EDS spectrum indicates that anorthite does not react with the coat at 1300°C, but rather $CaSiO_3$, $MgSiO_3$, CaO or MgO that were formed during the melting of CMAS [155], which confirms that Ca and Si are the main corrosive elements and Mg to lesser extent. This agrees with the line scans that shows lower Mg counts compared to Ca and Si.

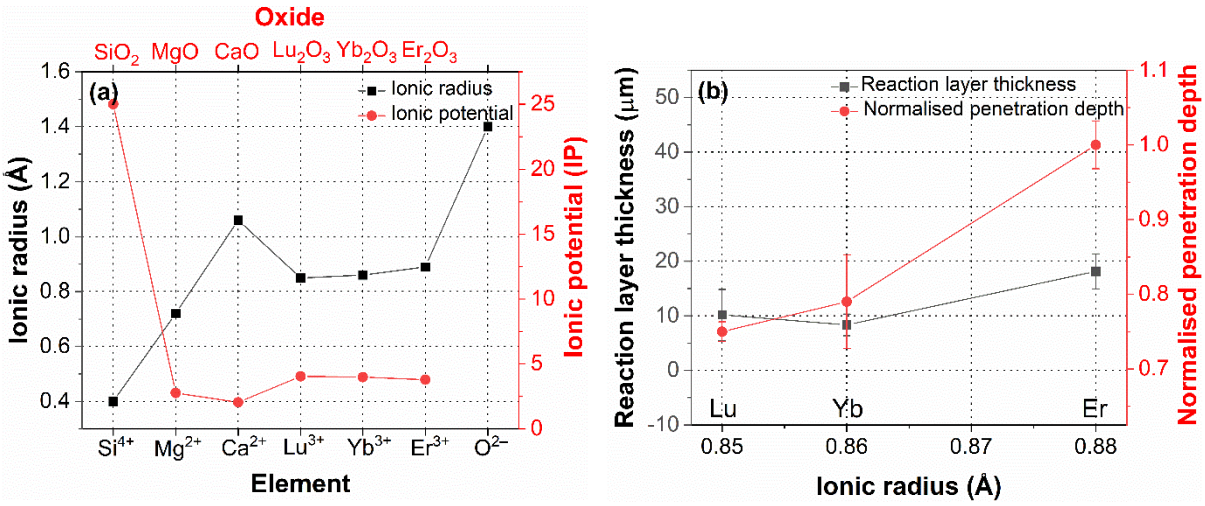


Figure 5.32 (a) IR and IP of ions and oxides involved in CMAS–EBC reaction (b) Ionic radius vs. RL thickness and normalised penetration depth at 48 h.

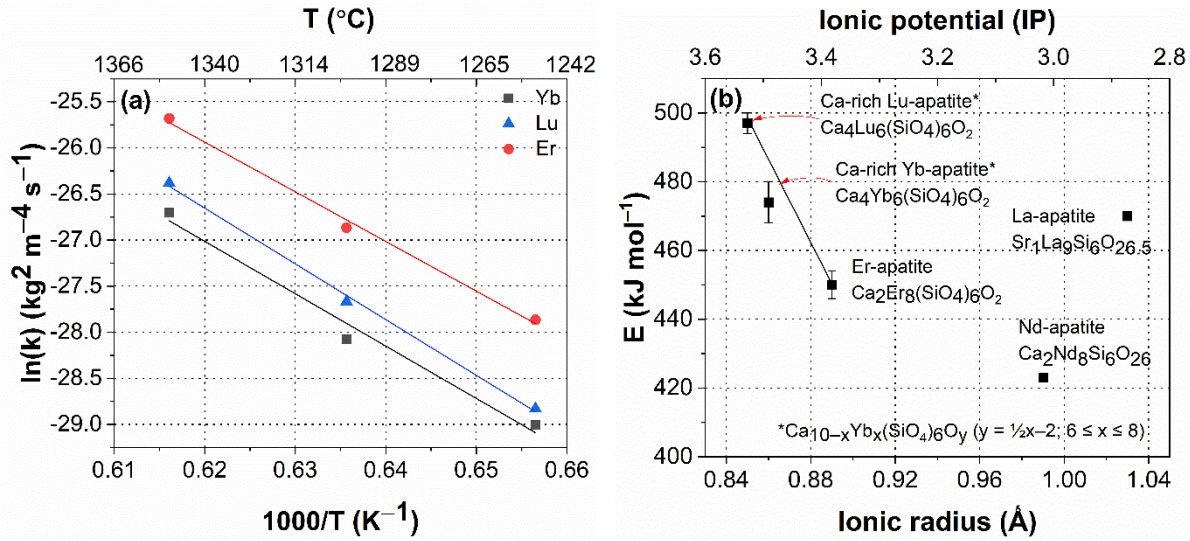


Figure 5.33 (a) Arrhenius plot for the CMAS–EBC reaction at 1250, 1300, and 1350 °C (b) E values with respect RE-element ionic radius and IP.

5.4.2 Corrosion mechanism

The incorporation of AEO and Si into RE_2O_3 structure to form Ca–Mg–Si–RE garnet, and the amorphous and uniformly continuous morphology for phases 1 and 2 are synonymous with those of reaction products formed by dissolution/precipitation. Previous studies mentioned dissolution/precipitation model as the mechanism of CMAS reaction with RE_2SiO_5 and $RE_2Si_2O_7$ to produce apatite and/or garnet [120, 143, 151, 353]. The dissolution process is governed by the diffusion of Ca, Mg, and Si with RE_2O_3 to form Ca–RE garnet in the case of Yb and Lu-silicates, and apatite and garnet in the case of Er-silicate (Figure 5.34). This is accompanied by the diffusion of RE^{3+} into the CMAS outer layer to form islands of reaction products incorporating fractions of components from both the coatings and the melt. The same cation coordination of CaO and RE_2O_3, being linked to 6 O atoms forming octahedra, renders the substitution of Ca^{2+} in place of RE^{3+} in its lattice positions convenient.

Phase 2 garnet forms in the middle of the coat over the following steps. First, CMAS melt infiltrates the open pores and cracks in the coat (Figure 5.35b) where they settle in them to form clusters of phase 1 that act as local reaction spots. This step is function of the coating defects such as pore size and distribution, and vertical channel cracks. Afterwards, the melt dissolves in the surrounding RE_2O_3 (blue hue surrounding phase 1 local reaction spots in Figure 5.25c), in which dissolution occurs owing to the lack of chemical equilibrium at the interface between infiltrated melt and local RE_2O_3 reaction spots. The reaction occurs around the rims of phase 1 regions, where it precipitates phase 2 garnet around these rims, and generates a morphology that comprise phase 2 precipitates at the periphery of phase 1 nucleus (Figure 5.34a and Figure 5.35c). The reaction then proceeds inwards until most phase 1 nucleus is consumed. The formed phase 2 links together forming a network as shown in Figure 5.35d and Figure 5.8f, Figure 5.11f and Figure 5.14h. The consumption of phase 1 local spots inside the coat indicates that the dissolution/precipitation rate at the reaction front is higher than the melt infiltration rate to these spots. However, in cracked and porous areas, the melt infiltration rate becomes higher than the dissolution/precipitation at the reaction front resulting in trapped regions of phase 1 within the phase 2 network.

Er-silicate oxyapatite forms by the gradual dissolution of Er_2O_3 in the CMAS melt to precipitate silicate oxyapatite grains. The continuous dissolution of Er_2O_3 in CMAS melt at the RL is evident from the increase in apatite grain size with corrosion time, creating gapes between the

apatite grains at the melt interface, which widens over time, and their detachment from the reaction layer to form islands in the CMAS melt (Figure 5.34b). These effects result in an unprotective RL, that facilitates the infiltration of the melt through the coat in considerable amount, which eventually form a pool of infiltrated CMAS melt at the middle of the coat that precipitates of needle-like apatite grains (Figure 5.34b). The abundance of melt between the formed apatite grains forces the grains to crystallise annisotropically forming elongated grains that are constrained by melt. Additionally, the substitution of Ca^{2+} at the expense of Er^{3+} occurs parallel to the c-axis, which results in a directionally oriented precipitation. The needle-like grains are particular to the middle of the coat, where melt pool forms, nevertheless, towards the bottom of the coat, lower amount of melt is observed, associated with the formation of Ca–$Er_2Si_2O_7$ equiaxed grains, which reflects total dissolution of the coat after 6 and 12 h. It is noted that the infiltrated melt surrounding the apatite grains have a similar composition to the CMAS glass pellet, which means that most of the infiltrated melt did not undergo reaction with the surrounding $Er_2Si_2O_5$ bottom coat, otherwise they will be diluted resulting in lower Ca and Si amounts; only the melt at the periphery of the apatite grains have lower Ca and Si amounts. The seeping of melt in excessive quantities is not related to vertical cracks and pores but to the unprotective nature of the RL and the apatite grains.

The reaction of the melt with the RE_2SiO_5-based bottom coat formed a continuous apatite reaction layer, inhibiting further reaction of the bottom coat. During the 48-hour corrosion, the melt penetrated only half of the Yb-silicate bottom coat and a third of the Lu-silicate. The formation of apatite islands within the bottom coat is attributed to CMAS reaction the RE_2SiO_5–$RE_2Si_2O_7$ mixed-phase bottom coat. Webster and Opila [357] observed a similar dispersed apatite attack in CMAS corrosion of $Yb_2Si_2O_7$–30 vol% Yb_2SiO_5 EBC at 1300 °C.

CMAS penetration depth into the coat indicates the amount of RE_2O_3 consumed; the volume percentage of phase 1 is 10 ± 2% between 1–12 h and increases to 18 ± 4% after 48 h. Increasing corrosion time induces cracks, which increases the volume percentage of phase 1 by creating new pathways for melt infiltration. The fraction of phase 1 in the middle of the coat is similar for Yb and Lu-silicates because the volume fraction of pores are the same. Alternatively, the volume percentage of phase 2 spots is higher for Er-silicate and cover larger areas, which indicates stronger reaction with CMAS compared to Yb and Lu-silicates. This corresponds with the higher Ca^{2+} and Si^{4+} diffusion coefficient for Er-silicate compared to Yb and Lu-silicates.

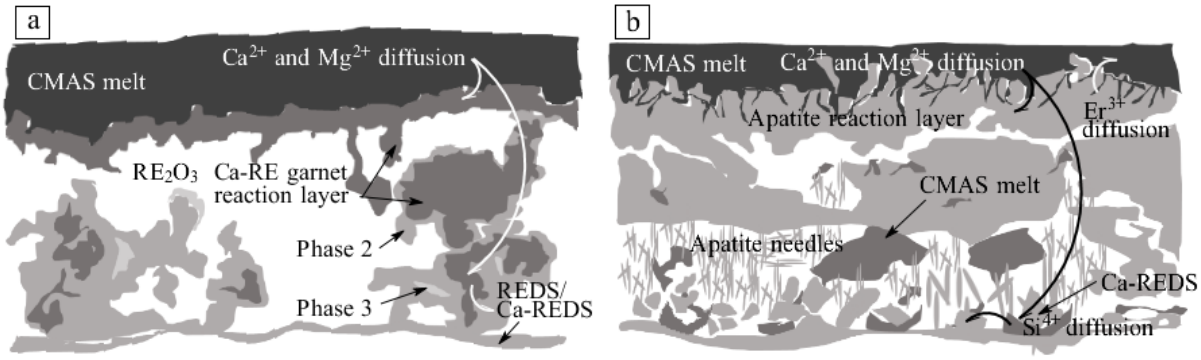


Figure 5.34 The CMAS–RE_2O_3 reaction products (a) Yb and Lu-silicates (b) Er-silicate.

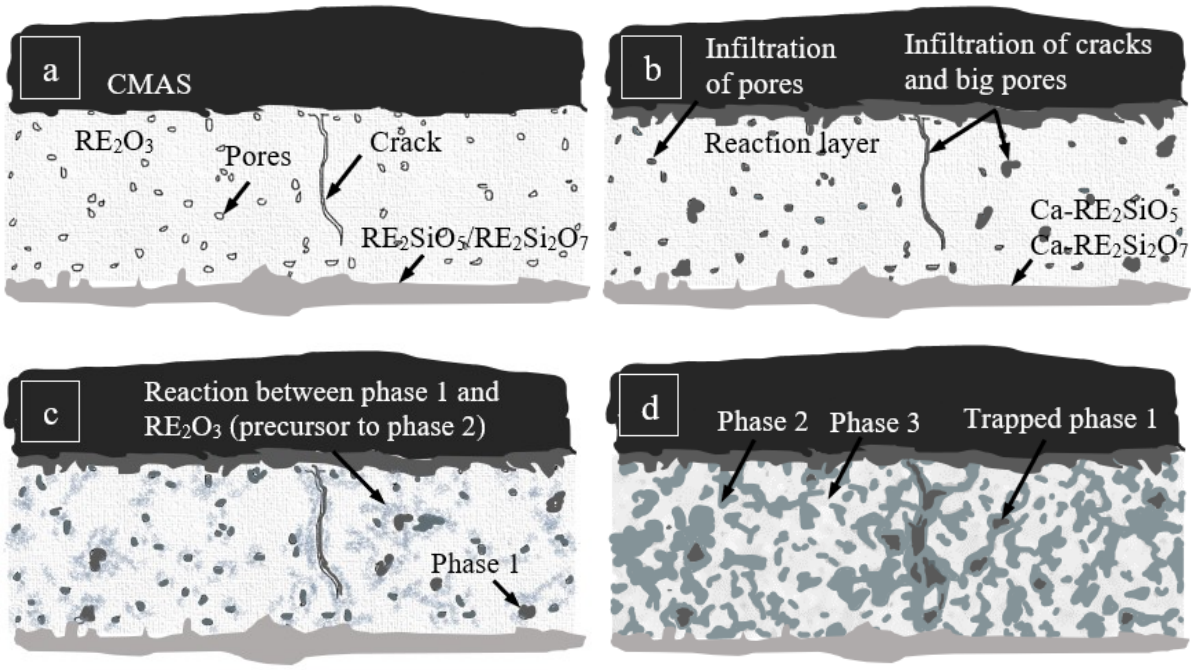


Figure 5.35 The CMAS–RE_2O_3 rection mechanism (a) coating morphology (b) infiltration (c) dissolution (d) precipitation of the dissolved CMAS–RE_2O_3.

5.4.3 CMAS diffusion into RE-silicate

The parabolic time dependence of weight gain plot, accompanied by the exponential decrease in the diffusion rate, with corrosion duration, reflect a diffusion-controlled mechanism. The diffusion coefficient values of Ca^{2+} and Si^{4+} in RE_2O_3-rich EBCs under CMAS increase with increasing the ionic radius of RE^{3+} (Figure 5.36). This relates to higher Er_2O_3 corrosion because of the lower polarisation power of Er^{3+} compared to Yb^{3+} and Lu^{3+}, as explained earlier, which renders it more feasible for Ca^{2+} to replace Er^{3+} and form CaO–Er_2O_3-based garnet (phase 2). Diffusion coefficient also increases with OB showing that Er_2O_3 is more susceptible to react with CaO in the melt [353], where the diffusion coefficient values of Er-silicate are higher than those of Yb and Lu-silicates (Figure 5.37) because of the larger amount of coating dissolved in the reaction layer. The dissolution process of RE_2O_3 in the melt is derived by the diffusion of Ca^{2+} cations and silicate spicies into the RE_2O_3 crystal structure, which depends on the concentration of the diffusing species.

The Ca and Si concentration values C_s, C_o, $C_{(x,t)}$ are constant for Yb, Lu and Er-silicates phase 2. The value of $C_{(x,t)}$ is constant because it is the maximum concentration of Ca and Si incorporation in the Yb, Lu and Er-oxide structure. This results in small variation between D_{FSL} and D_{DAN} because the deciding factor becomes the penetration depth. Thus, for the diffusion calculations, it would be more convenient to use D_{DAN} because of its simple approach. Diffusion coefficient decreases with increasing penetration depth and oxidation time because the melt and phase 2 garnet clogs the pores and cracks thus hindering further melt infiltration and increasing the tortuosity factor of the coat. Additionally, the formation of phase 2 network lowers the concentration difference to drive the dissolution process. Hence, it acts as a protective barrier against further corrosion of the coat. Alternatively, the diffusion of divalent cations is two orders of magnitude higher than the diffusion of RE trivalent cations in apatite structures [126, 358], which explains the fast growth of the reaction layer and phase 2 by the inwards diffusion of cations compared to the outward diffusion of RE^{3+} into the CMAS glass.

The diffusion coefficient of Si is higher than that of Ca because Si concentration in the CMAS glass is higher, and so the flux of Si^{4+} diffusing through the EBC is higher. Additionally, Si^{4+} has a smaller ionic radii (0.40 Å) compared to Ca^{2+} (~1 Å) [359], and thus the bond energy, in solid state, for Si–O formation (421 kJ mol^{-1}) is lower than that for Ca–O (487 kJ mol^{-1}) [360],

rendering it more attractive for reacting with O^{2-}. This is in agreement with Zhao et al. [76] who concluded that CMAS reaction with ~15 vol.% Yb_2O_3 EBC consumed Si at a relatively faster rate than Ca. This contradicts previous work [145, 301] that mentioned the diffusion coefficient of 'binding' cations as Ca^{2+} and Mg^{2+} are greater than that of Si^{4+} in orthosilicates. This was explained by the proposition that the number of vacancies of binding cations is higher than the vacancies at the Si^{4+} sites. In addition, Ardanova et al. [301] concluded that a diffusing atom with closer radii to its substituent results in faster and diffusion with higher concentration. Ptáček [144, 145] mentioned that Si diffusion is slower and rate limiting compared to Ca^{2+} by one order of magnitude because SiO_2 diffuse as SiO_4^{4-} units (the process does not involve dissociation of SiO_2 into Si^{4+} and O^{2-}, and the recombining of Si^{4+} with oxygens to reform SiO_4^{4-} units within the apatite lattice because Si^{4+} presence in RE_2O_3 lattice is unstable) which is larger in size compared to CaO and thus, slower to diffuse. The similar diffusion coefficient values of Ca and Si, and the discrepancy in literature regarding which is rate-limiting, reflects that this area requires further study.

The D_{FSL} values for dip-coating are between 10^{-13} and 10^{-14}, which are similar to those obtained by Watson, Harrison, and Ryerson (10^{-13} and 10^{-14}) for Sm, Sr, and Pb in fluorapatite between 900–1250 °C [361]. These values are in close proximity with the diffusion coefficients D_{DAN} for Yb, Lu and Er-silicates that were calculated from the penetration depths obtained from literature (Figure 5.36 and Table 5.5). Diffusion is mainly controlled by the Ca–O bond because if it is controlled by both Ca–O and Si–O bonds, then there would be a difference in the diffusion coefficient values between RE_2SiO_5 and RE_2O_3 because of the extra SiO_2 present in RE_2SiO_5, which is expected to further lower the diffusion coefficient values; which is not observed in Table 5.5. The same can be said for Yb_2SiO_5 and $Yb_2Si_2O_7$. Therefore, since the reaction kinetics of CaO during the formation of garnet or apatite is slower than SiO_4^{4-}, it is most-likely the rate controlling step, as the slowest reaction controls the kinetics of the process in corrosion. As a result, the diffusion coefficient for Ca is the indicator for coating performance. D_{DAN} values indicate slower formation rates for Yb_2O_3-rich–Yb_2SiO_5 compared to single-phase Yb_2SiO_5, and even slower for $Yb_2Si_2O_7$. This is attributed to increased Ca and Si diffusion through Yb_2O_3, leading to a more protective garnet formation. Yb_2O_3 enhances sacrificial properties, boosting CMAS resistance in Yb_2SiO_5, and similarly, Yb_2SiO_5 enhances CMAS resistance in $Yb_2Si_2O_7$ because of its higher Yb_2O_3 activity.

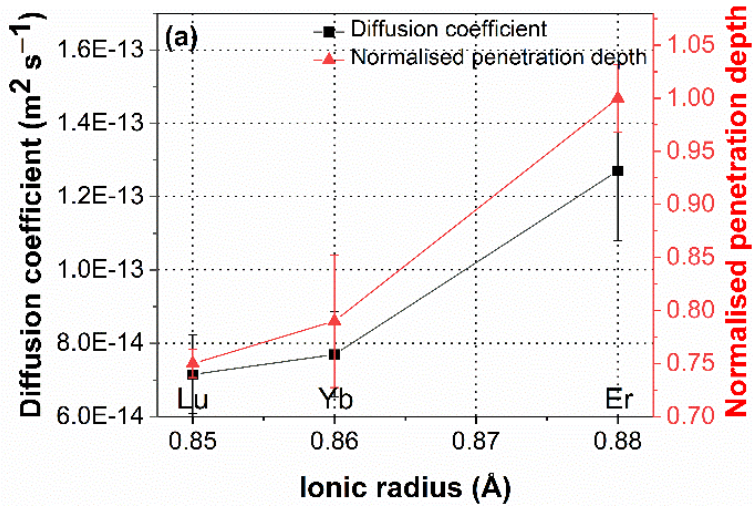


Figure 5.36 Calculated D_{DAN} of Ca in RE-silicates under CMAS environment at 24 h.

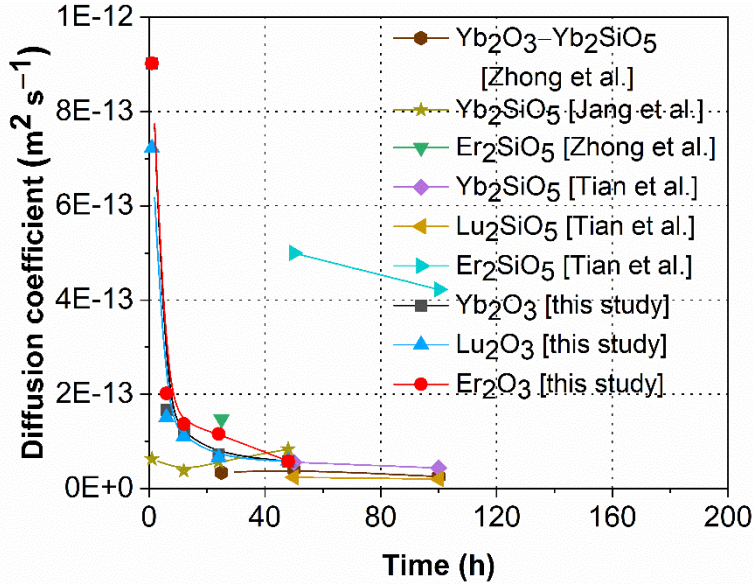


Figure 5.37 Calculated D_{FSL} of Ca and Si in RE-silicates under CMAS environment.

Table 5.5 D_{DAN} for CMAS–RE_2SiO_5 corrosion in air; obtained from previous authors.

Coating type	Application method	CMAS (mol%)	T (°C)	t (h)	X (μm)	D_{DAN} ($m^2\ sec^{-1}$)	References
Yb_2O_3–rich Yb_2SiO_5	APS	$C_{33}M_9Al_{13}S_{45}$	1400	25 50 100	55 85 95	3.36×10^{-14} 4.01×10^{-14} 2.50×10^{-14}	Zhong et al. [281]
Yb_2SiO_5	SPS	$C_{33}M_9Al_{13}S_{45}$	1400	1 12 24 48	15 40 70 120	6.25×10^{-14} 3.70×10^{-14} 5.67×10^{-14} 8.33×10^{-14}	Jang et al. [58]
Yb_2SiO_5	SPS	$C_{33}M_9Al_{13}S_{45}$	1300	4 24 96	50 55 125	1.73×10^{-13} 3.50×10^{-14} 4.52×10^{-14}	Webster and Opila [357]
$Yb_2Si_5O_7$	SPS	$C_{33}M_9Al_{13}S_{45}$	1300	1 4 24	50 370 710	6.94×10^{-13} 9.50×10^{-12} 5.83×10^{-12}	Webster and Opila [357]
$Yb_2Si_5O_7$–20 vol% Yb_2SiO_5	SPS	$C_{33}M_9Al_{13}S_{45}$	1300	4 24 96	160 325 355	1.77×10^{-12} 1.22×10^{-12} 3.64×10^{-13}	Webster and Opila [357]
$Yb_2Si_5O_7$–30 vol% Yb_2SiO5	SPS	$C_{33}M_9Al_{13}S_{45}$	1300	4 24 96	210 305 305	3.06×10^{-12} 1.07×10^{-12} 2.69×10^{-13}	Webster and Opila [357]
Er_2SiO_5	APS	$C_{33}M_9Al_{13}S_{45}$	1400	25	115	1.46×10^{-13}	Zhong et al. [362]
Yb_2SiO_5	Hot press pellets	$C_{33}M_9Al_{13}S_{45}$	1300	50 100	100 125	5.55×10^{-14} 4.34×10^{-14}	Tian et al. [156]
Lu_2SiO_5	Hot press pellets	$C_{33}M_9Al_{13}S_{45}$	1300	50 100	65 80	2.34×10^{-14} 1.77×10^{-14}	Tian et al. [156]
Er_2SiO_5	Hot press pellets	$C_{33}M_9Al_{13}S_{45}$	1300	50 100	300 390	5.00×10^{-13} 4.22×10^{-13}	Tian et al. [156]

The Ca–Mg–Si–RE phase 2 garnet is comprised of hexagonal precipitates. As the crystal morphology is often related to its crystal structure [150], this phase most-likely possesses a hexagonal crystal structure consistent with silicate oxyapatite. The reaction garnet grains have no amorphous layer between them which indicates no melt infiltration occurs through the grain boundaries. The grain boundaries are sharp and preferentially oriented, implying that phase 2 did not evolve through grain boundary diffusion. This is confirmed by the low Ca content at the grain boundaries compared to the middle of grains. Yb_2O_3 has low degree of crystallinity and low packing of atoms, which allows for the diffusion of Ca^{2+} and Si^{4+} through the lattice to form highly-ordered crystalline apatite-like garnet that further crystallises upon cooling

(Figure 5.38). Thus, lattice diffusion is the dominant mechanism by which cations from the melt are transferred to the reaction front. This does not imply that grain boundary diffusion does not occur, but to much less effect. The crystalline nature of the garnet indicates that grain boundaries play a role in transporting cationic species to the lattice. The lattice diffusion mechanism and grain boundary-to-lattice diffusion affects the way crystals grow forming crystals with longer width than height and aspect ratio of 1.3. This aspect ratio does not affect the packing efficiency because there are no voids between grains, but their coarsening results in an increase in volume fraction (Figure 5.38). Thus, garnet grain size increases with corrosion time at a rate controlled by Ca^{2+} diffusion into the grains. The RL phase 1 also Ca^{2+} and SiO_4^{4-} lattice diffusion into the RE_2O_3 structure.

The diffusion coefficient is directly proportional to the total porosity [$D = \omega D_o$], where D_o is the diffusion coefficient at zero porosity [363]. This is because porosities facilitate the diffusion of elements through the coating. The calculated D is at ω ~0.08, which indicates that decreasing the volume of porosity will result in lower diffusion coefficient across the coat.

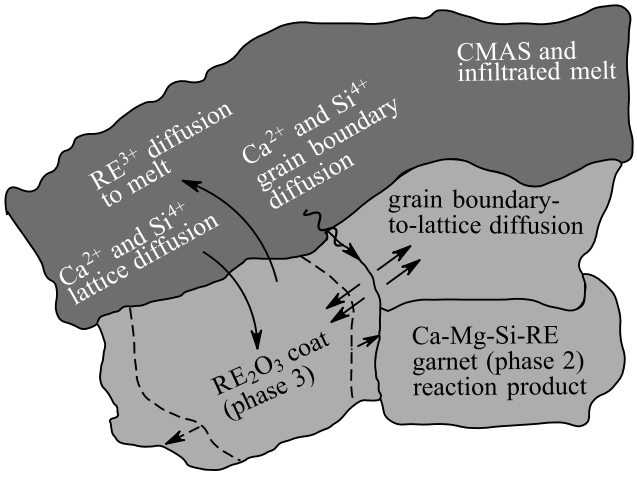


Figure 5.38 Diffusion of Ca^{2+} and Si^{4+} from the melt to the RE_2O_3 grains.

5.4.4 Infiltration time and corrosion rate

To compare the current coating with previous studies, the infiltration time t was considered for a coating thickness of 200 μm at 1300 °C, where higher t indicates improved performance. The equation is function of the geometry of coating (the average pore diameter D_c, tortuosity factor τ, fraction of pores ω, and coating thickness L) and the CMAS melt properties (viscosity of η and surface tension σ). It does not consider the type of diffusing species or the material of the coating. As a result, it cannot be used to compare RE-based EBCs based on their element type.

The following parameters were used for calculating infiltration time; D_c is ~2 μm, τ is calculated to be 3, ω is ~0.08, η is ~23.7 N s m^{-2} and σ is 0.40 J m^{-2}. For a 200 μm thickness, CMAS infiltrates the coating in less than 1 min, which is consistent with the infiltration time recorded for hot-pressed EBC pellets of the same thickness (Table 5.6). The value of infiltration time implies instantaneous CMAS reaction with the coating, facilitated by the constant presence of melt at the reaction front. The value obtained for t is not in line with that obtained from the SEM images that showed full melt penetration of Yb and Lu-silicates after 48 h and Er-silicate after 24 h. This is because the equation considers the coat as one big pore; without considering microstructural variation due to the formation of phase 2, which serves a protective function by decreasing melt infiltration and inhibiting Ca diffusion across the coat.

Table 5.6 Infiltration time and CR of different EBCs and TBCs in CMAS environment.

Coating type	Application method	CMAS comp. (mol%)	t (min)	CR/100 (μm min^{-1})	References
RE_2O_3 topcoat / RE_2SiO_5 bottom coat	Dip coating	$C_{33}M_9A_{13}S_{45}$	0.60	2.04	This study
ZrO_2–7.6%$YO_{1.5}$ (7YSZ) TBC	EB-PVD	$C_{33}M_9A_{13}S_{45}$	0.90	2.20	Krämer et al. [289]
ZrO_2–8%$YO_{1.5}$ (YPSZ) TBC	APS	$C_{33}M_9A_{13}S_{45}$	1.20	1.67	Kang et al. [364]
Apatite coat $Ca_2Y_8(SiO_4)_6O_2$	Hot pressed pellets	$C_{23.3}M_{6.4}A_{3.1}S_{62.5}N_{4.1}K_{0.5}F_{0.04}$	0.24	8.35	Sleeper et al. [288]
No coating used. Only CMAS pellets	Hot pressed pellets	$C_{23.3}M_{6.4}A_{3.1}S_{62.5}N_{4.1}K_{0.5}F_{0.04}$	1.01	1.97	Wiesner and Bansal [287]

The channel cracks formed in the coating are attributed to the released stresses during cooling, which arise from the thermal expansion mismatch between CMAS and RE_2O_3 [365], because these channel cracks were observed to run vertically through the CMAS–RE_2O_3 topcoat, so probably they originated at the interface. The high CTE of RE_2O_3 compared to RE-silicates plays a role in the heavy presence of cracks. Additionally, the incorporation of Ca, Mg and Si into the RE_2O_3 crystal results in lattice expansion; the volume cell of phase 2 Yb garnet is expected to be close to that of Yb-silicate oxyapatite, which is 129.72 $cm^3\ mol^{-1}$ compared to 100.50 for Yb_2SiO_5 and 39.50 $cm^3\ mol^{-1}$ for Yb_2O_3. Lattice expansion in the CMAS penetrated regions with respect to unpenetrated regions result in the buildup of tensile stresses in the affected region, and the formation of blister cracks. In addition, the presence of a glassy and brittle oxyapatite phase also results in loss of strain tolerance because Ca–silicate rare earth oxyapatite is more brittle compared to RE oxide due to the presence of weak bonds such as Ca–O. The lateral cracks near the substrate suggest that they result from the difference in CTE between monosilicate and RBSBC. Other than microcracks, randomly distributed macropores were formed in the RE_2O_3 topcoat during the coating process due to entrapped gasses or lack of fusion between particles.

The pores are likely formed as a result of thermal diffusion process during the coating sintering process. They are linked through channelled network, where the melt seeps through them. This is evidenced from the even distribution of phase 2 garnet in the corroded samples. Some pores are isolated with no open channels through them, where CMAS melt did not reach them as seen in Figure 5.11f and Figure 5.14h. Porosities lead to higher strain tolerance but lower corrosion resistance. Thus, highly dense coatings are advantageous for corrosion-resistance, but can compromise stress compliance under thermal cyclic conditions and thermal conductivity [96]. Therefore, careful balance between the coat's resistance to corrosion and thermal stresses should be considered.

Corrosion rate CR quantifies the speed at which the coating corrodes based on infiltration time, in order to predict the performance of coatings in real conditions; where lower CR suggests a longer coating lifetime. The corrosion rate of dip-coating is 2.04 $\mu m\ min^{-1}$ which is higher than APS coatings and hot-pressed pellets. The reason for the lower CR of APS compared to dip coating relates to its microstructure, which affects the infiltration kinetics. Even though defects comprise randomly distributed void, as in dip coating, they are entrapped between flattened

splats that are randomly layered on top of each other, which render it difficult for CMAS melt to reach the pores and increases its tortuosity path. Additionally, APS results in a denser coat with lower porosity percentage and finer pores compared to the current dip coating method. Alternatively, EB-PVD CR is higher than that of dip coating by 7%. It comprises columnar microstructure with free-space inter-columnar gaps that act as cannels for CMAS melt infiltration. The vertical orientation of the gaps allows for faster melt flow through gravitational and capillary actions, leading to a low tortuous path for the melt as opposed to the randomly formed channel paths, and pores of dip coating and APS. Naraparaju et al. [366] calculated a tortuosity factor of 1.25–2.31 for EB-PVD, which is lower than that estimated by Kang et al. [364] for APS, which is 3. Accordingly, melt infiltration and tortuosity is more arduous in APS and dip coating compared to EB-PVD. The effect of these microdefects are observed in the irregular profile of the penetration depth observed earlier by SEM images [367].

To sum up, corrosion rate is concerned with predicting coating performance based on its geometry and application technique. On the other hand, diffusion coefficient can be used to rank coating performance based on RE element. The dip-coating technique is promising from a corrosion perspective, and it offers an economical and convenient coating technique, particularly for complex structures. Nevertheless, further studies are required to increase the efficiency of the slurry and the dip-coating process to generate a coating with lower porosity and finer pores with diameters less than 1 μm. The investigated coating is sacrificial; they rapidly dissolve into the molten CMAS and precipitate as a reaction phase that prevent further melt infiltration while consuming CMAS. A coating that inhibits reaction with CMAS, then generate a protective product afterwards upon corroding, would be more durable in sand-corrosion environment.

5.4.5 Real-life conditions versus CMAS pellets

Using CMAS pellets to study EBC corrosion is a common approach in literature because it is simple and cost-effective, though it doesn't fully reflect real-life conditions. In practice, molten CMAS droplets impact the coating at high speeds and temperatures, forming splats in which their shape and formation are dependent on the in-flight particle properties along with the surface conditions of the EBC [128]. The splat distribution affect the CMAS infiltration properties (i.e. if the CMAS splats are distributed randomly on the coat, then CMAS infiltration amount will decrease, and the coat will not undergo uniform corrosion). In addition, high-

velocity particles impact the coat and leads to erosion or erosion-corrosion, where an accelerated corrosion occurs due to the tear-away of the coat from the erosion effect. CMAS droplets would also arrive to the coating surface at high temperature and will not sit on the coat till it becomes hot. This will affect the deposition rate and the adhesion properties of the CMAS [128, 176]. Additionally, the real-life scenario involves CMAS arriving with fuel residue, creating a complex corrosion process. To accurately simulate these conditions, a burner-rig or microturbine experiment would be needed. However, this research could not include such experiments due to financial constraints and safety issues related to turbine exhaust gases.

5.4.6 Role of defects in CMAS diffusion

The formation of RL garnet and apatite-structures proceeds by the reaction of Yb_2O_3 with SiO_2, to form Yb-silicate or metastable Yb-apatite [$Yb_{9.33}(SiO_4)_6O_2$] [Eq. (5.9)], which react with Ca to generate Ca–Yb-silicate oxyapatites [Eq. (5.9)]. Further substitution of Yb^{3+} by Ca^{2+} [Eq. (5.10)] leads to Ca-rich apatite structures [144, 368]. Metastable apatite requires Ca to stabilise [147], which explains the rapid corrosion of the coatings and the widespread distribution of the reaction product phase 2.

$$5Yb_2O_3 \xrightarrow{6SiO_2} Yb_{10}(SiO_4)_6O_3 \xrightarrow{Ca^{2+}} Yb_9Ca_1(SiO_4)_6O_{2.5} \xrightarrow{Ca^{2+}} Yb_8Ca_2(SiO_4)_6O_2 \quad (5.9)$$

$$Yb - apatite_{(ss)} + Ca^{2+} \longrightarrow Ca - apatite_{(ss)} + Yb^{3+} \quad (5.10)$$

Ion exchange through lattice defects, which occur upon EBC–melt contact at the reaction front, is expressed using the Wagner-Hauffe rule and the Kröger-Vink notation [369, 370]. Figure 5.39 presents three main images: kinetics, mechanics, and equations. The kinetics image shows that the reaction layer grows parabolically as mentioned previously. The mechanics show schematically the diffusion process when CMAS melt is in contact with the Yb_2O_3 topcoat. The orange squares at the bottom show the effect of temperature on the Yb_2O_3 lattice, where the Yb_2O_3 dissociates to divalent and trivalent ytterbium oxides in addition to oxygen, which in turn forms oxygen vacancies. The dissociation process also results in the formation of cationic vacancies. On the other hand, and at the CMAS–Yb_2O_3 interface, the high concentration of vacancies, shown in blue squares, are the result of high temperature dissociation in addition to Yb_2O_3 lattice reaction with Ca and Si from the CMAS melt (shown in white). The blue arrows indicate the migration of vacancies and defects from the interface to the inside of the Yb_2O_3

lattice, while the yellow arrow shows the opposite (migration of Yb_2O_3 lattice defects from lattice interior towards the interface); in which vacancies and defects destroy each other. They are divided by an imaginary dashed line for illustration. The parabolic rate of formation for the corrosion product reflects a parabolic trend in vacancy formation, where it increases rapidly at the start of the reaction until they destroy each other, and the lattice at the Yb_2O_3–CMAS interface (above the dashed line) becomes saturated such that that vacancy formation decreases to negligible amounts. That is when the reaction reaches a plateau. Equation section is explained in conjunction with Figure 5.40, which visually represents the Kröger-Vink equations, and the movement of defects within the Yb_2O_3 lattice during substitutional diffusion.

Each lattice is represented as a square cell, where each cell represents the lattice position of an ion (shown as a letter and a number in Figure 5.40d); for example, $L^1_{O^{2-}}$ is O^{2-} ion in lattice position 1, and $L^2_{Ca^{2+}}$ is Ca^{2+} in lattice position 2. The stoichiometry of molecules in Figure 5.40 were taken into consideration, where three O^{2-} ions are available for each two Yb^{3+} ions, and one O^{2-} for each Ca^{2+}. The bottom left corner of the cell shows the type of point defect taking place within the cell (blue colour), while the top right corner of the cell shows the valence of the lattice position after the formation of the point defect (green colour). Figure 5.40a shows the Yb_2O_3 lattice during heating, where the cream cells are the Yb_2O_3 lattice and the grey cells are the melt lattice containing CaO. Figure 5.40b and c show Yb_2O_3–CMAS interaction, where the cream cells represent phase 2 apatite consisting of Yb–Ca–O. Each equation or section of the equation in Figure 5.40 is coloured with the same colour as that of the arrows in the lattice above that equation. This is to explain the physical behaviour of each equation and link the equation with the diffusion process in the lattice.

At high temperatures, vacancies are formed due to the excitation of atoms from their lattice position. As shown in Figure 5.40a black arrows, oxygen atom from air $O_{2_{(g)}}$ adsorbs to the surface as O^o_{ads}. This prompts some oxygen from the inner lattice (shown as dashed square $L^6_{O^{2-}}$ in Figure 5.40a) to donate its electrons $2e^{\prime}$ for the adsorbed oxygen to ionise it to O^{2-}, and sits in a lattice position O^x_o at the surface of the lattice (shown in cell $L^9_{O^{2-}}$). This is to maintain charge neutrality. In the process, the oxygen atom that lost its electrons moves to the surface as $^1/_2\, O_{2_{(g)}}$ and leaves behind a positively charged vacancy ($V_o^{\bullet\bullet}$ shown in cell $L^6_{O^{2-}}$). This process is expressed by Eq. (5.11) in Figure 5.39, where the right hand side shows the

reactants ($V_o^{\bullet\bullet}$, $2e^{\prime}$ and $^1/_2\, O_{2_{(g)}}$) while the left hand side shows the final product which is oxygen sitting in a new lattice position O_o^x. Oxygen vacancy can be thought of as a positively charged void in the lattice, and it has a larger volume than that of the negatively charged oxygen ion [371]. Thus, a surface layer grows at the expense of vacancies in the lattice.

It is noted that determining defects/vacancies in the apatite structure by defining oxygen vacancies based on the O1s peaks in XPS is not reliable or consistent in literature, though it has been used by previous authors. The assignment of shifts in the O1s BE to oxygen vacancies is based on the assumption that the presence of vacancies changes the electrostatic potential for the oxygen anions in the system [329]. However, to obtain an O1s BE, and oxygen atom in the lattice is needed. If this oxygen atom has been removed, then there are no electrons to be analysed. Tian et al. [372] in his study of CMAS–RE_2SiO_5 (RE = La, Nd, Sm, Eu, and Gd) corrosion in dry air at 1300 °C recorded oxygen vacancy in the calcium silicate oxyapatite $Ca_2RE_8(SiO_4)_6O_2$ reaction layer using XPS. However, if oxygen vacancies are present then the oxyapatite reaction layer formed is not stoichiometric (defect-free). In addition, their results were not evidentially supportive of oxygen vacancy. Other authors as Morgan [373] states that the O1s shift between 531–532 eV is linked to hydroxyl formation instead. This conclusion is not accurate because many corrosion experiments [331, 353, 354, 371, 374, 375] were prepared in a controlled environment to prevent water ingress or reaction.

Cationic vacancies also form in high temperature as shown in Figure 5.40a blue arrows. When oxygen ions from the melt (**i.e.** resulting from the dissolution of $Ca^{2+}O^{2-}$) sit at a surface position in lattice, it prompts Yb^{3+} to hop to a lattice position close to O^{2-} and leave its position vacant $V_{Yb}^{|||}$ with extra three negative charges as shown in $L^3_{Yb^{3+}}$. To achieve charge neutrality, an oxygen site close to the recently-formed Yb vacancy must be vacant. This happens by O^{2-} (shown in cell $L^5_{O^{2-}}$) donating an electron $2e^{\prime}$ to Yb^{3+} to reduce it to Yb^{2+} ($Yb^{\prime}_{Yb}$) which results in an extra negative charge (cell $L^4_{Yb^{3+}}$). Another electron can go to a chemisorbed oxygen $O^-_{(chem)}$, and transfer it to O^{2-} in a lattice position at the surface O_o^x as shown in $L^8_{O^{2-}}$. The Ca^{2+} substitution of Yb^{3+} is equated as: $Ca^{2+} \leftrightarrow RE^{3+} + O^-$. Creating a vacancy in the lattice requires breaking more bonds than joining the Yb^{3+} to the surface, which is linked to the activation energy E required for forming an apatite-structure at the Yb_2O_3–CMAS melt

front. The above process is expressed by Eq. (5.12) in Figure 5.39, where the right hand side shows the products of Yb_2O_3 dissociation ($Yb_{Yb}^{\cdot}$, O_o^x, $V_{Yb}^{'''}$, $V_o^{\bullet\bullet}$ and $2h^{\bullet}$ which is equivalent to $2e^{'}$ at the left hand side). The XPS doublet peaks 347.3 and 350.9 eV (Figure 5.25c) that represent Ca–SiO_4^{4-} apatite-structure, are where Ca^{2+} substitutes Yb^{3+}.

Silica reacts with Yb_2O_3 in the form of SiO_4^{4-} tetrahedra that bonds with the Yb_2O_3 octahedra and fit between the Yb_2O_3 spaces, which balances the charge of SiO_4^{4-} as each oxygen is shared between two sites. The introduction of silica strengthens the structure because the Si–O bonds are covalent, and thus, the structure of SiO_2 tetrahedron is more stable and harder to break than the Yb_2O_3 octahedra. Additionally, the Si–O bond length in the SiO_4^{4-} tetrahedra (1.62 Å) [376, 377] is shorter than the Yb–O bonds (~2.30 Å) [378-380] in monosilicates and disilicates [125, 381]; the Yb–O bonds are the weakest links in the structure. The prospect of SiO_3 presence highlights the presence of oxygen vacancies in the Si–O structure because the reduction of metal ion leads to the expulsion of oxygen out of the lattice sites to neutralise the extra negative charge gained from the reduction process. Additionally, the reduction of Yb^{3+} to Yb^{2+} also leads to the creation of oxygen vacancies in order to compensate for the loss of positive charge.

Introducing Ca^{2+} to Yb^{3+} atomic positions (brown lines in Figure 5.40b) decreases the number of cationic vacancies in the Yb_2O_3 lattice [144, 368], but it creates new oxygen vacancies at their expense, as shown in Eqs. (5.13) and (5.14) in Figure 5.39, and in Figure 5.40. Two Ca^{2+} ions substitute two Yb^{3+} ions in their lattice positions ($2Ca_{Yb}^{'}$ at $L_{Ca^{2+}}^{3}$ and $L_{Ca^{2+}}^{4}$ cells) creating two negative charges; –1 for each substitution. The extra negative charges are balanced by 2 electron holes ($h^{\bullet}$ resulting from an electron abandoning its natural position leaving behind a positive charge), which are created from an oxygen ion abandoning its lattice position leaving behind a positively charged vacancy $V_o^{\bullet\bullet}$ as shown in cell $L_{O^{2-}}^{5}$. The rest of the equation describes the existing Yb^{3+} in their respective lattice positions $2Yb_{Yb}^{x}$ and oxygen in their respective lattice positions $3O_o^x$, where they form Yb_2O_3. The stoichiometry of the reaction is 3CaO for each $2Yb_2O_3$ because oxygen vacancies form in pairs. It is expected that when Ca^{2+} replaces Yb^{3+}, oxygen vacancies will form along the $Yb_{(2)}$ sites, where Ca and Yb share 9 oxygen anions, to maintain charge balance and compensate for the extra negative charge as shown in Figure 5.41. Thus, garnet stability depends on the cations linked to the $Yb_{(2)}$ sites.

Unlike silicon, calcium is a network modifier, which means that Ca^{2+} does not bond directly to the network. When Ca^{2+} substitute Yb^{3+}, the structure becomes less rigid because of the formation of weaker bonds with oxygen. The substitution of a modifier oxide with another relates to the ionization potential (IP) because it explains the preference of a network-modifying cation in bonding with oxygen, which is factor of the cross-linking density and the strength of the crosslinks between cations and oxygen ions. CaO has lower IP (0.97) compared to Yb_2O_3 (1.30) because of the smaller Ca–O bond length of 2.06 Å [377] compared to that 2.30 Å for Yb–O [378-380]. In addition, ions with greater charge have higher lattice energy than ions with smaller charge. Thus, the substitution of Yb^{3+} with Ca^{2+}, and the reduction of Yb^{3+} to Yb^{2+} lowers the stability of the apatite products. This is reflected in the enthalpy of formation ΔH_f for Ca–Yb silicate oxyapatite which is approximately –403.2 kJ mol^{-1} [294] compared to –1809 kJ mol^{-1} for Yb_2O_3 [2] and –2774 kJ mol^{-1} for Yb_2SiO_5 [297]. The less exothermic value of apatite indicates a less stable product compared to Yb_2O_3 and Yb_2SiO_5. The effect of Mg^{2+} is the same as Ca^{2+} where it falls in the same sites and acts as network modifier but the small amount of MgO compared to CaO in the original CMAS makes its effect not noticeable, and they are almost not present in phase 2. The variation in phase composition is significant because modifiers such as CaO are extremely relevant in the crystallization of phases from the melt, which is a pathway for CMAS mitigation [131]. The Ca–O and Yb–O interactions are associated with Ca–apatite structures, as indicated by the BEs observed in Ca2s and Yb4d (Figure 5.25c and d).

Ca^{2+} ionic radius (1 Å) is close to the ionic radius of Yb^{3+} (0.86 Å) compared to Si^{4+} (0.4 Å) [121, 359], which makes Ca^{2+} more thermodynamically favoured to substitute Yb^{3+} in its $4f$ position compared to Si^{4+}. Thus, Si^{4+} does not compete with Ca^{2+} on its position but involved as SiO_4^{4-} units linking the CaO9 and the YbO6 polyhedrons. However, the increased concentration of oxygen from the SiO_4^{4-} structures plays an important role in cationic diffusion because the SiO_4^{4-} tetrahedra acts as a link connecting CaO9 and YbO6 polyhedrons forming open channels between them, which can be attractive sites for diffusion. Additionally, SiO_4^{4-} tetrahedra acts as a catalyst for substitutional diffusion by increasing oxygen content in the system which allows for the formation of anionic vacancies that facilitate inward diffusion of Ca^{2+} into the Yb_2O_3 lattice to achieve electroneutrality.

The high Ca-rich composition of Ca:Yb at ~0.6 means that there are more Ca per Yb sites compared to stoichiometric silicate oxyapatites, which results in higher number of O^{2-} vacancies that leads to higher amount of Ca^{2+} diffusion. Substitutional diffusion occurs through the movement of point defects, particularly the formation and destruction of vacancies and electron holes. Thus, to control and decrease the diffusion of Ca^{2+} (deleterious element in RE silicate oxyapatite formation [353, 354]) through the coating structure, it is beneficial to saturate the EBC structure with CaO and SiO_2 to the point where the formation of vacancies is unfavourable. As vacancies occurs, ions keep hopping and exchanging locations relentlessly, which is a function of the number of vacancies available. Accordingly, Ca^{2+} cannot create new vacancies, and the reaction would cease because the diffusion coefficient is directly proportional to the number of vacancies. The incorporation of Ca in the Yb-apatite establishes an equilibrium condition with the melt concerning Ca concentration, which prevents further inward diffusion of Ca through the coat. Moreover, the substituted Ca atoms are tied to the CaO9 polyhedra at the 4*f* Wyckoff position (¼, ¼, 2), which will require higher E to release them from their position and form anionic vacancies required for the diffusion process.

Higher apatite content in Er-silicate, compared to Yb and Lu-silicates, relates to the higher amount of stoichiometric apatite formed. As the ionic radius of RE^{3+} decreases, the RE^{3+}(6*h*)–O(2*a*) bond length shortens, which leads to the decrease in the coordination number of cation positions 6h and 4f [300]. This results in more lattice defects and the formation of defected apatite. The formation of a lattice structure with immobile defect clusters will effectively reduce the mobility and concentration of defects, which in turn will suppress atomic mobility and mass transport. Therefore, diffusion decreases with increasing the formation of phase 2. It is also noted that the incorporation of modifier oxides, such as CaO and MgO, into the melt increases the melt viscosity, which leads to lower infiltration depth and lower corrosion rates.

This can be a premise to the formation of a Ca–Yb silicate oxyapatite CMAS-resistant coating, with higher activation energy of formation, that decreases the prospect of ionic conduction within the apatite lattice. The purpose of the coat would be to slow the infiltration kinetics of the salicaceous melt, and afterwards upon eventual reaction with the melt, the reaction phases formed within the coat would be protective to prevent further consumption of the coat. However, it is worth noting that Ca reacts readily with water, and so an apatite coating with Ca content may not be stable in water vapour environment.

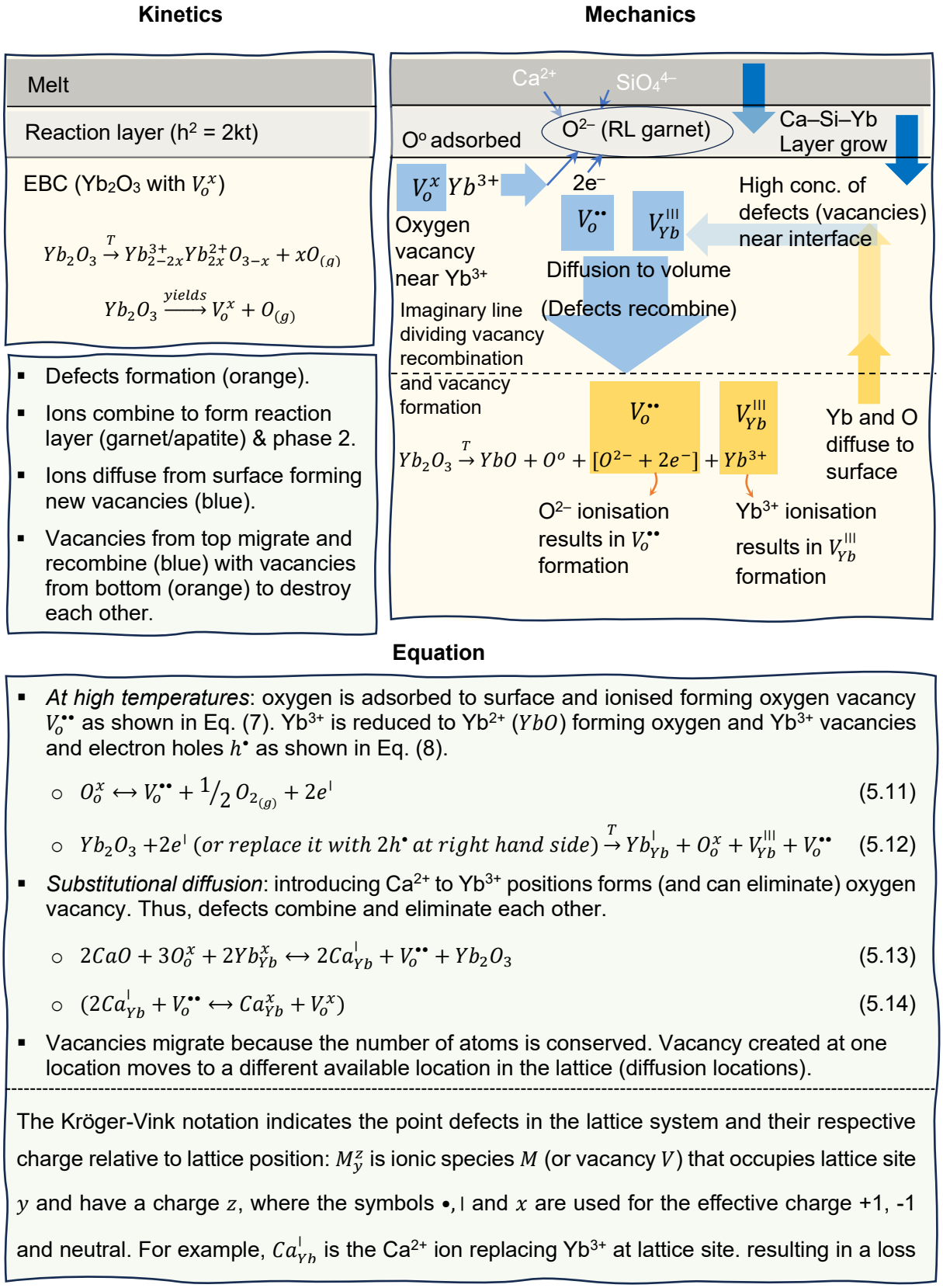
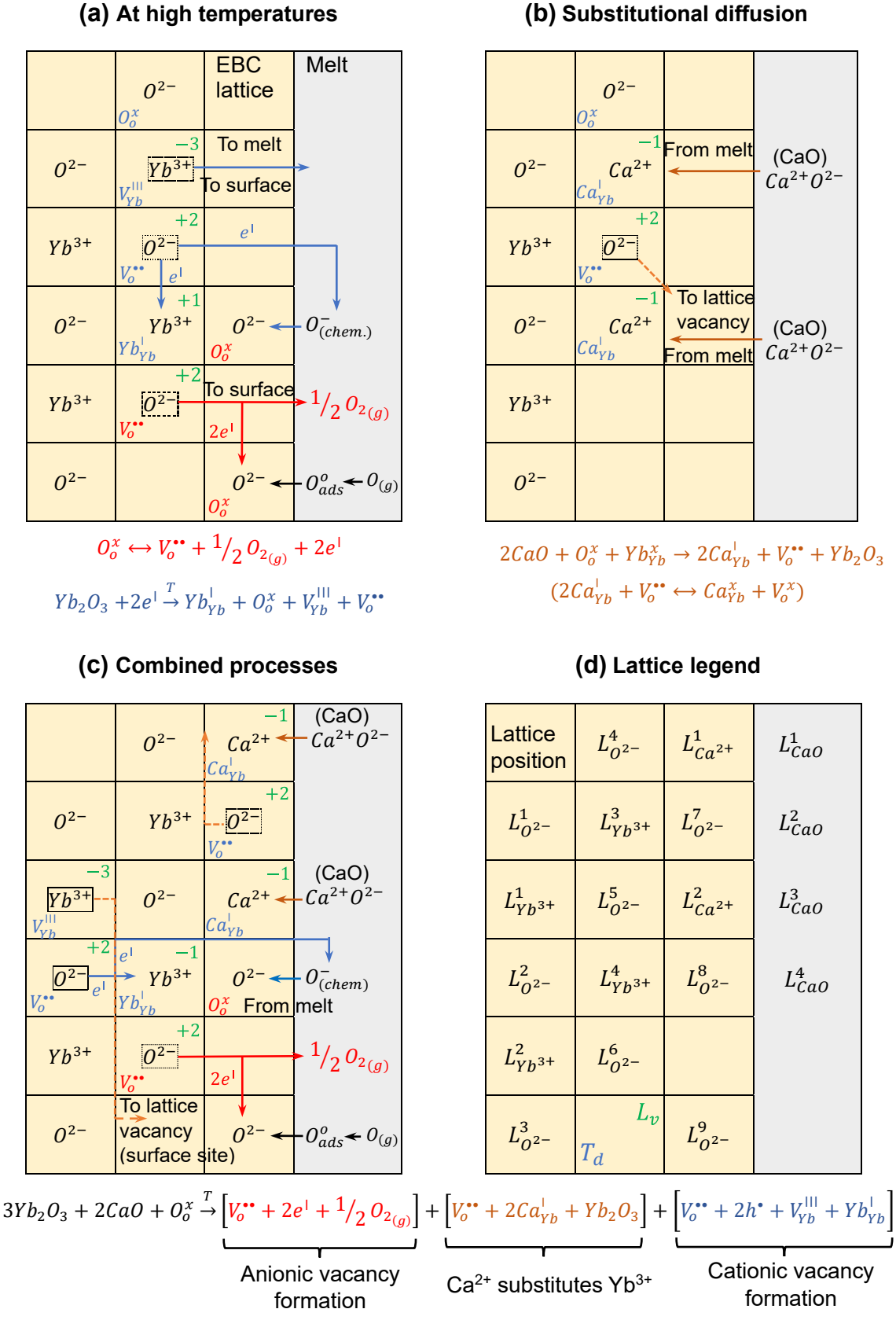


Figure 5.39 The CMAS–Yb-silicate corrosion sequence from a point defect perspective showing the kinetics of corrosion-layer formation, the mechanics of defects (courtesy of Petr Ptáček), and the equations governing the mechanics of corrosion.



$$O_o^x \leftrightarrow V_o^{\bullet\bullet} + {}^1/_2\, O_{2(g)} + 2e^{\prime}$$

$$Yb_2O_3 + 2e^{\prime} \xrightarrow{T} Yb_{Yb}^{\prime} + O_o^x + V_{Yb}^{\prime\prime\prime} + V_o^{\bullet\bullet}$$

$$2CaO + O_o^x + Yb_{Yb}^x \rightarrow 2Ca_{Yb}^{\prime} + V_o^{\bullet\bullet} + Yb_2O_3$$

$$(2Ca_{Yb}^{\prime} + V_o^{\bullet\bullet} \leftrightarrow Ca_{Yb}^x + V_o^x)$$

$$3Yb_2O_3 + 2CaO + O_o^x \xrightarrow{T} \underbrace{\left[V_o^{\bullet\bullet} + 2e^{\prime} + {}^1/_2\, O_{2(g)}\right]}_{\text{Anionic vacancy formation}} + \underbrace{\left[V_o^{\bullet\bullet} + 2Ca_{Yb}^{\prime} + Yb_2O_3\right]}_{Ca^{2+}\text{ substitutes }Yb^{3+}} + \underbrace{\left[V_o^{\bullet\bullet} + 2h^{\bullet} + V_{Yb}^{\prime\prime\prime} + Yb_{Yb}^{\prime}\right]}_{\text{Cationic vacancy formation}}$$

Figure 5.40 Pictorial translation of the Kröger-Vink equations in Figure 5.39. (a) during heating (b) substitutional diffusion (c) combined processes (d) lattice legend.

Formation of Ca–Yb silicate oxyapatite reaction layer

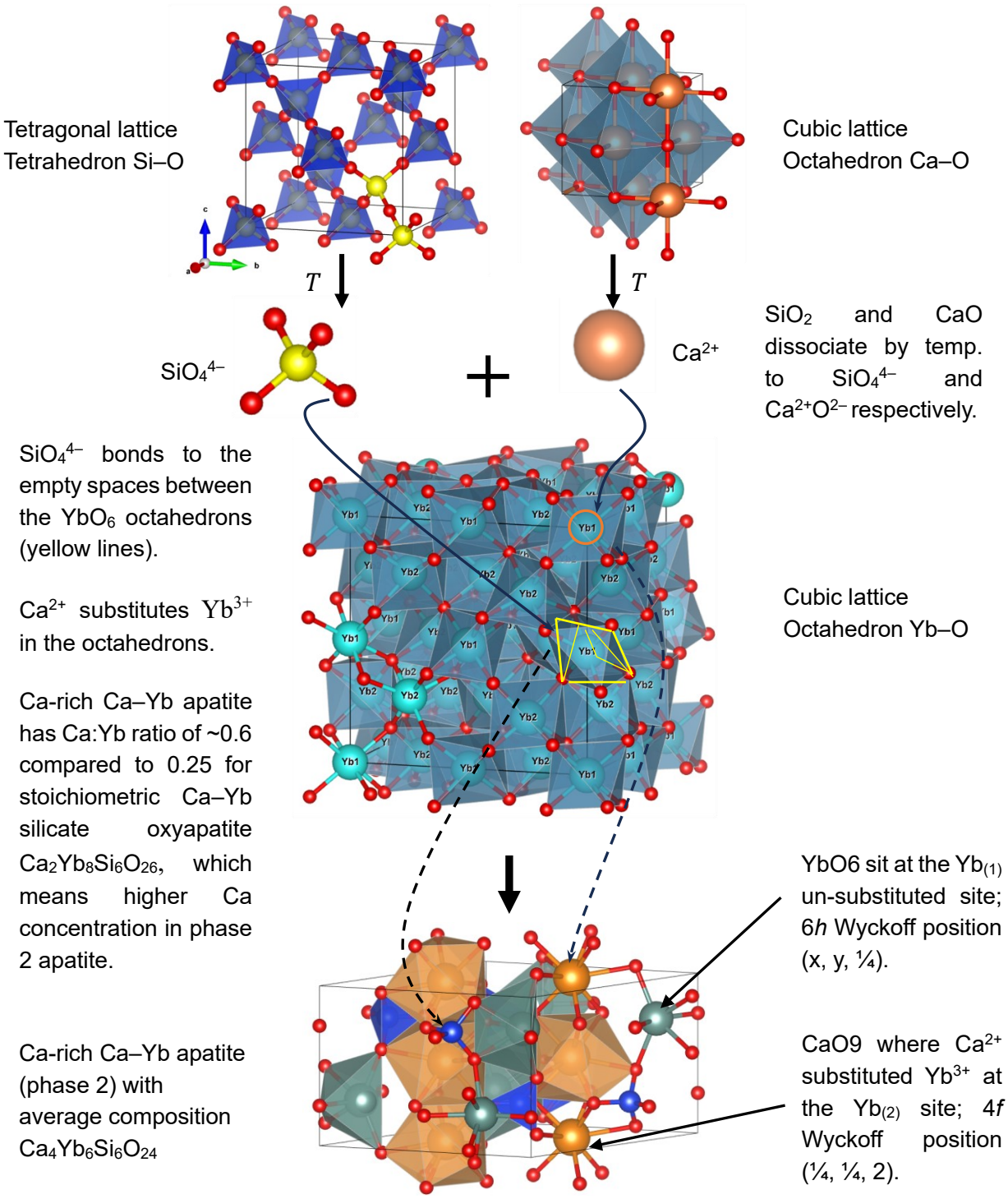


Figure 5.41 The chemical reaction resulting in Ca-rich apatite phase.

5.5 CONCLUSION

The CMAS–EBC corrosion tests can be thought of as analogous to the crucible tests of refractory materials, where molten CMAS corrosion of ceramic-based coatings can be compared to molten slag corrosion of ceramic-based refractories. CMAS corrosion occurs through dissolution/precipitation. It starts with CMAS melt infiltrating the open pores and cracks in the coat and fill them. This transports calcium and silicon to the reaction front, where the melt dissolves with the neighbouring coat, and Ca^{2+} and Si^{4+} diffuses into the RE_2O_3 lattice to precipitate a Ca-rich Ca–Mg–Si–RE garnet. Er_2O_3 forms stoichiometric apatite phase in addition to garnet. This is because ionic radius affects the composition of the reaction layer, where lower RE ionic radius (such as those of Yb and Lu) have the tendency to form garnets, while larger ionic radius (Er^{3+}) stabilises the formation of apatite. The reaction process is thus function of coating properties and the properties of the diffusing species. The continuous dissolution with corrosion time increases the reaction layer thickness and the penetration depth. This is aided by deleterious element diffusion through coat porosities and melt infiltration through cracks. Diffusion occurs by substitutional replacement of RE^{3+} with Ca^{2+} in addition to the involvement of SiO_4^{4-} tetrahedral units. The mechanism proceeds through anionic and cationic defects in the crystal lattice.

The diffusion coefficient of Ca^{2+} and Silicates in RE_2O_3 are calculated based on Fick's second law, where Er-silicates has the highest D and Yb and Lu-silicate are the lowest respectively. The diffusion coefficient is directly proportional to the ionic radius of RE material. The corrosion rate of the coating is calculated based on the infiltration time, which takes into consideration coating application defects. Dip coated RE-silicate coating shows corrosion rate lower than APS coatings. As a result, D can be used to assess EBC resistance to CMAS from corrosion perspective, while CR can be used to assess EBC resistance to CMAS from coating application perspective. The benefit of using RE_2O_3 topcoat is to offer a better resistance for the main RE_2SiO_5 bottom coat and act as a more effective sacrificial layer compared to RE-monosilicates and RE-disilicates. Yb and Lu-silicates display better CMAS corrosion resistance compared to Er-silicate. The fact that Yb-silicate is cheaper to produce compared to Lu-silicate, makes it a strong candidate for a coating structure consisting of Yb_2SiO_5–Yb_2O_3 dip coated on silicon based substrates. Dip coating method is also a promising application technique that can offer an economically affordable corrosion resistant EBC.

6 FRACTURE BEHAVIOUR OF REACTION-BONDED SILICON CARBIDE-BORON-CARBIDE USING DIGITAL IMAGE CORRELATION

K. El Shafei, Reem Kassem, Philip Holloway, Ashraf Nayel, John P. Dear, and David Nowell "Fracture Behaviour of Reaction-Bonded Silicon Carbide–Boron Carbide Using Digital Image Correlation," *Engineering Fracture Mechanics*, Submitted, 2024.

6.1 INTRODUCTION

The fracture behaviour of silicon carbide ceramics have been extensively reported in literature, while much less so for the R-curve analysis. However, there are a scarcity of research on the fracture and crack resistance of reaction-bonded silicon carbide-boron carbide (RBSBC). This study involves the use of DIC aided with high speed camera to understand the kinetics of crack propagation and evaluate the R-curve behavior of RBSBC, which has not been studied before. The purpose of the study is to evaluate the mechanical behaviour of RBSBC with low B_4C content (~7 wt%) in order to examine its suitability in load-bearing applications.

6.1.1 Fractography of brittle materials

SiC-based ceramics are becoming attractive to use in the hot section part of gas turbines because of their high specific tensile strength and ability to operate 200 °C higher than conventional superalloy metallics [382]. When SiC ceramics are used, their structural integrity is compromised because cracking is the dominant failure mechanism. Due to the highly crystalline nature of SiC–B_4C material, the fracture behavior is strongly related to its microstructure. Thus, understanding the fracture behaviour and crack resistance of reaction bonded silicon carbide-boron carbide (RBSBC) ceramics are essential for the successful development of its use in mechanical applications. For these tasks, a high speed camera in combination with Digital Image Correlation (DIC) was employed. High speed camera images reveal the crack development, whilst DIC measures the displacement and strain in materials under external load. These techniques have been used extensively in the aerospace sector [383, 384]. The specimen is coated with a fine distribution of random speckle dots and the DIC analysis software divides the viewing area into facets. The coordinates of each facet are characterised by random speckle dots and are tracked as load is applied. This allows the

dynamic displacement to be correlated with crack development during the fracture process. Hsu et al. [385] studied the SiC/Si interfacial tensile strength in reaction-bonded silicon carbide ceramic (RBSC) using micro-sized dog-bone tensile samples (20 μm × 2 μm) and in-situ tensile testing within field emission scanning electron microscope, where the specimens were prepared by focused ion beam milling. They found that the tensile fracture of SiC/Si interface occurred on the Si side because it is the weakest link. The crack starts elastically at the Si side until brittle fracture occurs. Zhang and Zhang [386] modelled the development of primary and secondary cracks of a single-flaw brittle specimen based on the bonded-particle model, which consists of particles that are bonded together to create a material with a bulk behaviour, where crack occurs by the failure or breakage of bonds between the particles [387]. They found that primary cracks consists solely of micro-tensile cracks, while secondary cracks majorly consists of micro-tensile cracks in addition to the presence of few micro-shear cracks. Wong and Einstein [388] studied the cracking behaviour of Carrara marble. They concluded that only high speed camera can capture the cracking processes of single-flawed brittle material. Eberhardt et al. [389] studied the relation between crack process and grain size in rocks and ceramics. They found that grain size plays no role in transgranular crack initiation and propagation. However, grain size does affect intergranular cracks, where larger grains can offer paths of weakness for cracks to propagate along.

6.1.2 Crack velocity

Whitlow et al. [390] observed the cracking behavior of SiC/SiC ceramic matrix composite using DIC. They noticed that the final failure location coincided at ~1–2 mm deviation with the damage initiation point, and that porosities do not play a role in the tensile failure. Crack velocity reflects the dynamics of fracture as a function of load. Ngo et al. [391] found that the crack velocity of ultra-high performance concrete matrix ranges from 8.01 m s^{-1} under static loading conditions to 738.82 m s^{-1} under high strain rate. They related an increase in cracking velocity with increasing strain rates. Zhang et al. [392] also found that the crack velocity increased with increasing the static loading rate. They noticed that low loading rates between 10^{-4}–10^{1} mm s^{-1} resulted in significant differences in cracking velocity. Regarding the resistance of SiC–B_4C to crack propagation, Pittari III et al. [393] studied the fracture behaviour of reaction bonded SiC–B_4C under static four-point bend tensile load. They found that SiC–B_4C composites exhibited strain hardening behaviour [393, 394]. They also recorded an

increase in fracture toughness with increasing silicon content. At Si-content higher than 30%, the fracture toughness values approached that of pure polycrystalline Si. Multiple authors [395-397] have used DIC to measure crack propagation speeds in concrete testing. They used high speed camera shots to obtain the temporal position of the crack tip during brittle fracture, in combination with displacement field analysis using DIC software.

6.1.3 Crack-resistance plots

The single-value linear-elastic parameter K_{IC} has traditionally been used to quantify fracture toughness. However, they represent resistance to fracture at the crack initiation point and cannot capture the multiple length-scale toughening that acts on the materials [398, 399]. This results in an underestimation of the actual toughness of the material during fracture [398]. In addition, the value of K_{IC} may not be a direct indication of the materials toughness because the microstructural features that improves crack resistance may result in non-uniform microstructural flaws. For example, Quinn [400] mentioned that yttrium-stabilized tetragonal zirconia Y-TZP with a K_{IC} of 5–6 MPa $m^{1/2}$ is stronger than magnesium partially stabilised zirconia Mg–PSZ, which has a K_{IC} of 10–20 MPa $m^{1/2}$ because Y-TZP has a uniform submicron grain size, while Mg-PSZ microstructure is coarse-grained with grain-boundary defects and micropores. Evaluating the actual toughness of a material requires an R-curve analysis to characterize the toughness K_I associated with crack growth including sub critical cracks. That is because the stress field at the moving crack tip in linear elastic brittle solids can be expressed by the stress intensity factor K_I where the crack-tip region is subjected to near-plane strain conditions [401-406]. Thus, the conditions for crack propagation are created by stress intensity at the crack tip region [406]. The R-curve measures the material's resistance to stable crack extension, and prior to catastrophic fracture at K_{IC}. For a complete R-curve characterization, the values of K_I or J are calculated ahead of the crack tip across a number of crack-length values between the initial and final crack lengths [402]. The shape and slope of the R-curve reflects the crack-resistance of the ceramic.

DIC has also been used to either calculate or measure the crack tip opening displacement (CTOD), δ, along the crack length based on successive frame shots [191, 395]. This is usually done by measuring δ between the two surfaces of the opening crack just before the crack tip. It is one of the three fracture toughness parameters, along with stress intensity factor K_I and

the strain energy release rate J, where they are commonly used in defect assessment procedures particularly Fitness-For-Service FFS in the oil and gas industry. This allows for evaluating the fitness of a structure or equipment for operational purposes [407]. Measurement of the displacement near the crack tip can provide a direct characterization of the crack-tip stress intensity and deformation fields [402]. Bu et al. [395] verified the reliability of DIC measurements with the results recorded from the clip-on-extensometer during tensile bending test, and found the DIC to be an accurate method for measuring δ. Khor [408] calculated δ for different elastic materials and found that a δ with a value less than 0.2 mm is highly affected by the elastic behaviour of the material and usually a function of high tensile ratio (yield stress σ_Y/ultimate tensile stress σ_{UTS}) materials.

6.2 METHODOLOGY

The Reaction-Bonded Silicon Carbide-Boron Carbide (SiC–B_4C) ceramic (RBSBC) were supplied by M-Cubed Technologies (USA). They were cut to dimensions (mm) of 45 (length) l × 4 (width) B × 10 (height) W, as shown in Figure 6.1, where the proportions ($1 \leq W/B \leq 4$) follow ASME E1820–20 [409]. The sample was prepared according to the single-edge-V-notch beam method [232], where an 0.8 mm notch was introduced at the sample centre along the 3 mm face by an 0.3 mm diamond blade [230]. This is to ensure that a sharp crack initiates from the notch tip without the need for a precrack. A sharpening machine was used in which a razor blade slides back and forth over a pre-notch while being lubricated with a 1 μm diamond suspension (Buehler MetaDi). The notch radius is ~20–30 μm. The notch crack length after sharpening is ~2 ± 0.5 mm. Vickers hardness HV indentation was performed with a 2 N load using a Wilson VH1102 microhardness tester (Buehler, Germany) according to ASTM C1327-15 [410]. The hardness value obtained was the average of five measurements. The microstructures of the fractured sample was investigated using SEM (TESCAN MIRA, Czech Republic) equipped with Energy-Dispersive Spectrometry (EDS).

For the DIC analysis, the specimen was speckled with a white and black paint respectively to generate a binary speckle pattern which enhances DIC resolution as seen in Figure 6.2 inset. The specimen was then loaded under tension in a 3-point bending test (Instron 3366, USA) at ambient temperature with 16 mm supporting span and displacement-controlled (quasistatic) at 0.01 mm min^{-1} displacement rate. The DIC system measured 2D displacement using a 12-bit monochrome camera (Photron FASTCAM NOVA S16, Japan), which captures images at a

frame rate of 137,500 fps using a shutter speed of 1/500,000 s and a resolution of 256 × 272 pixels. The camera is coupled with a 100 mm lens (Nikkon F, Japan) that is placed at 1.5 m from the tensile rig configuration to achieve the desired magnification at a zoom ratio of 273.7%. Two LED lighting sets (LTMAX+, Photron), each is 24,000 lm, provided contrast between light and dark speckles. The actual camera and test rig setup is shown in Figure 6.2. Image acquisition was triggered manually once the sample broke, and the camera captured the last ~2–3 ms before the crack occurred. The image series was record successively with an interval of ~0.007 ms between each image. The DIC analysis and data were performed using both LaVision DaVis (Germany), MATLAB, and Ncorr (Georgia Institute of Technology, USA) [411, 412].

The load-displacement was obtained from the testing machine, while the fracture strength σ and fracture strain ε were obtained according to Eqs. (6.1) and (6.2) respectively [413], where P is the maximum load at fracture, S_o is the clamp span (16 mm), B is sample width, W is sample height, D_{flex} is the flexural displacement, and D_{comp} is the machine compliance displacement.

$$\sigma = \frac{3PS_o}{2BW^2} \tag{6.1}$$

$$\varepsilon = \frac{6(D_{flex} - D_{comp})W}{S_o^2} \tag{6.2}$$

The residual stresses inside the substrate was calculated according to Eq. (6.3) taking into consideration that the ceramic material consists of particles p surrounded by a semi-infinite matrix pool m. The factors of the equation are: Δc is the thermal expansion mismatch between particle and matrix ($\Delta c_p - \Delta c_m$), ΔT is the temperature difference between processing and room temperature, ν_m and ν_p and the Poisson's ratios of the matrix and the particles respectively, E is the Young's modulus, and f_p is the volume fraction of the particle phase. The Young's modulus was calculated from the rule of mixtures using the composition of RBSBC (82% SiC, 7% $B_4Si_xAl_yC$, 10% Si, and 1% Al) [414].

$$\sigma_{m-p} = -\frac{\Delta c.\Delta T}{\left[\frac{0.5(1+\upsilon_m)+f_p(1-2\upsilon_m)}{E_m(1-f_p)}+\frac{1-2\upsilon_p}{E_p}\right]} \tag{6.3}$$

The crack velocity, V, (m s^{-1}) was calculated from Eq. (6.4) [391, 415], where a_1 and a_1 are the crack lengths (mm) at times t_1 and t_2, respectively.

$$V = \frac{da}{dt} = \frac{a_2 - a_1}{t_2 - t_1} \tag{6.4}$$

The stress intensity at the crack tip K_I is a displacement-related parameter, where the experimental value of K_I (MPa m$^{1/2}$) was calculated based on Eqs. (6.7) to (6.8) [191]. The value of displacement points at the crack tip is related to the fracture toughness at that crack tip using the plane stress solution for an elastic crack as shown below, where r and θ are the polar coordinates at the crack tip signifying the distance away from crack tip and the angle between the axis extending from the crack tip and the stress plane, and ν is Poisson's ratio. By monitoring only points at the crack flanks, where $\theta = \pi$, Eq. (6.5) can be written as shown in Eq. (6.6), where the plus-minus sign refer to the positive and negative displacements at the opposite sides of the crack face. Therefore, the relative displacement ΔU between the two opposite points at both sides of the crack flanks can be expressed as in Eq. (6.7). The relative displacement ΔU was measured using virtual extensometers on the DIC images with respect to its position from the crack tip r. The value of K_I was calculated from the slope m of the ΔU versus $\sqrt{r}$ plot based on Eqs. (6.7) and (6.8).

$$U = 2\frac{K}{E}\sqrt{\frac{r}{2\pi}}sin\frac{\theta}{2}\left(1 + sin^2\frac{\theta}{2} - \nu cos^2\frac{\theta}{2}\right) \tag{6.5}$$

$$U = \pm\frac{4K_I}{E}\sqrt{\frac{r}{2\pi}} \tag{6.6}$$

$$\Delta U = \frac{8K_I}{E}\sqrt{\frac{r}{2\pi}} \tag{6.7}$$

$$K_I = \frac{mE\sqrt{2\pi}}{8} \tag{6.8}$$

The quasistatic value for K_I was calculated from Eqs. (6.9) and (6.10) using linear elastic fracture mechanics (LEFM) single-edge notch bend (SENB) according to ASTM E1820–20 [409], where P and B are explained above, α is the ratio of crack length to specimen height a/W, which represents geometrical deviation from the actual solution [402]. The crack tip was identified visually from the DIC images, while the crack length Δa was measured from the DIC images using Photron FASTCAM Viewer 4 image processing software. A manual calibration was used to convert pixel measurements to real world distance in mm. This was done by measuring the distance between two known points on the DIC image (the two points with known distance are taken at the top and bottom of the specimen since the sample height Whas a known length of 10 mm), and dividing it by the pixel counts across that distance, which resulted in a scale factor that corelates the pixels count to a known dimension (0.07427 mm/px). Afterwards, the crack length was measured in mm from the DIC image. The camera frame rate records the time at which crack propagates between each frame. The equation assumes that the test material is linear-elastic, isotropic and homogeneous. Measuring the crack length using DIC images results in uncertainty in pinpointing the exact crack tip location due to the low image resolution caused by the camera's high frame rate.

$$K_I = \left[\frac{P}{BW^{3/2}}\right]\left[\frac{3(\alpha)^{1/2}}{2(1-\alpha)^{3/2}}\right] f(a/W) \tag{6.9}$$

$$f(a/W) = \frac{1.99 - [\alpha][1-\alpha][2.15 - 3.93[\alpha] + 2.7[\alpha]^2]}{1 + 2[\alpha]} \tag{6.10}$$

The J-integral (kJ m^{-2}) was calculated using the quasistatic K_I, as in Eq. (6.11), and according to ASTM E1820–20 [409]. The crack tip opening displacement δ (mm) was calculated using the calculated quasistatic K_I, as shown in Eq. (6.12), and according to BS 7448 [416, 417] and WES 1108 [417, 418], where v is Poisson's ratio, and σ_Y is the yield tensile stress.

$$J = \frac{K_I^2(1-v^2)}{E} \tag{6.11}$$

$$\delta = \frac{K_I^2(1-v^2)}{2\sigma_Y E} \tag{6.12}$$

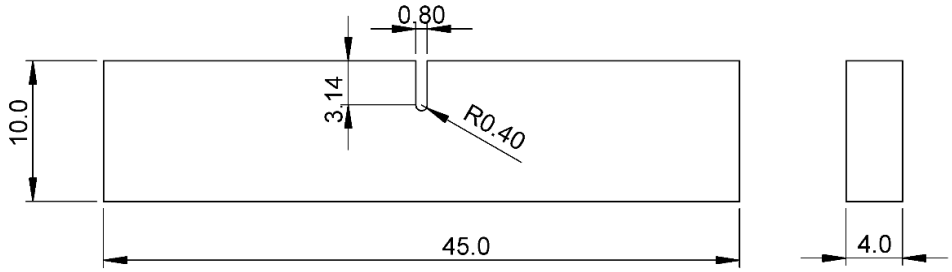


Figure 6.1 The dimension of the three-point bend sample with notch size.



Figure 6.2 Experimental setup of the bending test with DIC configuration using Photron Nova camera. The inset images show the three-point bend test, and the speckled sample.

6.3 RESULTS AND DISCUSSION

6.3.1 Fracture behaviour

The three-point bending test until fracture was captured by the DIC camera as shown in Figure 6.3a–d. The load-displacement plot in Figure 6.4a shows a linear behavior until fracture and fracture instability resulting in an unstable crack growth, where the material popped-in at fracture [409]. The bending strength is 110.53 MPa, which is on the low end of the reaction-bonded silicon carbide value because of the presence of high Si amount [419-422]. The fracture strain (calculated at the surface of the sample) is 0.00169, which is much lower than the 0.07 value obtained by Hsu et al. [385] for reaction-bonded SiC–Si. The reason Hsu et al. fracture strain value is lower than that measured for RBSBC by an order of magnitude relates to two main reasons. First, Hsu et al. measured the strain for RBSC which has higher ductility compared to RBSBC that owes its brittleness to the presence of B_4C, and thus RBSC fractures at higher strain levels. In addition, the amount of Si in Hsu et al. samples is almost 20 wt% compared to 7 wt% for the RBSBC. Second, the difference in testing method and environmental conditions result in different fracture strain values. Tensile test results in higher fracture strain compared to bending because the material is only subjected to uniaxial tensile stress.

After unloading, the fractured section of the specimen was imaged by SEM to observe the effect of microstructure on the cracking behavior. Figure 6.4b shows the crack propagation shape, which consists of a primary crack and secondary cracks that branch from it. Figure 6.5a shows the widefield view of the fractured surface, while Figure 6.5b is magnified and shows the location of SiC, Si and $B_4Si_xAl_yC$ grains. The primary crack has a width of ~7 ± 2 μm, while secondary cracks that stem from the main median crack have a width of ~1.3 ± 0.3 μm. The median or secondary cracks do not increase in width along the propagation depth. The random orientation and distribution of SiC grains in a pool of Si (Figure 6.5b) induces a tortuous path for crack propagation. The main crack is formed under tension, while secondary crack morphology is close to that of the main crack indicating that it is mainly formed under tensile effects as well. The cracking density of ~10 cracks/mm indicates an abundance of secondary cracks, which is in good agreement with Morscher [423] who studied 5HSW SiC/BN/SiC CMC. The secondary microcracks probably resulted from the low loading rate, where the fracture path tends to be more tortuous, and it allows time for the fracture tip to

develop secondary microcracks. This phenomenon has been previously noted in concrete and rock-like materials [424-428].

The RBSBC fracture morphology can be explained by the bonded-particle model, where two solid grains are bonded by lower stiffness material that acts as a spring effect between these two grains under tension. The Si pool acts as a bond substance to the individual SiC grains resisting their shear or rotational movement as shown in Figure 6.6. The crack propagation from the notch tip occurs when the tensile force exerted exceeds the normal strength of the Si bond pool. The presence of Si induces desired stresses in the material that can increase its resistance to cracking. That is because when cooling the sample after oxidation, the B–C–Si grains contract because of their higher CTE compared to Si, which results in residual compressive micro-stresses in the grains. The Si–B_4C residual compressive stresses, calculated according to Table 6.1 [393, 429-432], is ~540 MPa, which is close to the value obtained by Jannotti et al. [429]. On the other hand, silicon has lower fracture toughness compared to SiC and B–C–Si [433], which means it will fail prematurely and at lower stresses. In addition, since brittle crack tips are atomically sharp and propagate by breaking the interatomic bonds at each point of the moving crack front [434, 435], the crack is expected to occur at the Si–Si bonds first. That is because the Si–Si bond dissociation energy (327 kJ mol^{-1}) is lower than that of Si–O (798 kJ mol^{-1}) or B–O (806 kJ mol^{-1}) bonds [436].

Table 6.1 Si, SiC and B_4C selected properties for residual stress calculation [429, 437].

	Si	SiC	B_4C
CTE (10^{-6} °C^{-1})	3.6	4.6	6.0
Elastic modulus (GPa)	149	423	426
Poisson's ratio	0.22	0.15	0.17

Regarding the SiC grains, the tensile force is exerted on the β-SiC rims, which have higher hardness and tensile strength compared to α-SiC because of their cubic structure [438]. In addition, the smaller thickness of β-SiC rims acts as a thin film with higher tensile strength compared to the core α-SiC grains. Thus, once they break, the crack moves transgranularly (see Figure 6.5c) and cleaves through the grains by following the preferred cleavage planes (see Figure 6.5a and d). Under tension, the SiC grains that are in contact can rotate around each

contributing shear effect to the tensile forces. This can be noted from the spalled areas embedded within the fractured path as noticed on secondary cracks in Figure 6.5d. The SiC grains are not faceted but are oriented randomly where the edges of some grains are pressed against their neighboring grains resulting in point loads and internal stresses at the β-SiC rims as shown by red circles in Figure 6.6. The transgranular nature of crack propagation indicates that crack initiation/propagation is not a function of grain size but of SiC strength. The crack behaviour is almost like Hexoloy-SA SiC, which showed a transgranular crack path with no indication of crack deflection or bridging [439].

Figure 6.5d shows crack deflection around the $B_4Si_xAl_yC$ grains. The microhardness of the $B_4Si_xAl_yC$ grains is 39 ± 3 GPa compared to that of SiC grains which is 23 ± 2 GPa. The inclusion of B_4C contributes to the toughening mechanism of RBSBC as the cracks navigate around the ceramic grain rather than through them. The transition from transgranular fracture in the SiC grains to intergranular fracture is seen when the crack opens trenches around the $B_4Si_xAl_yC$ grains as shown in Figure 6.5d. This phenomenon contributes to increased toughness. In addition, the presence of secondary phase B_4C-based grains has the positive effect of raising the residual compressive stresses in the material as explained above.

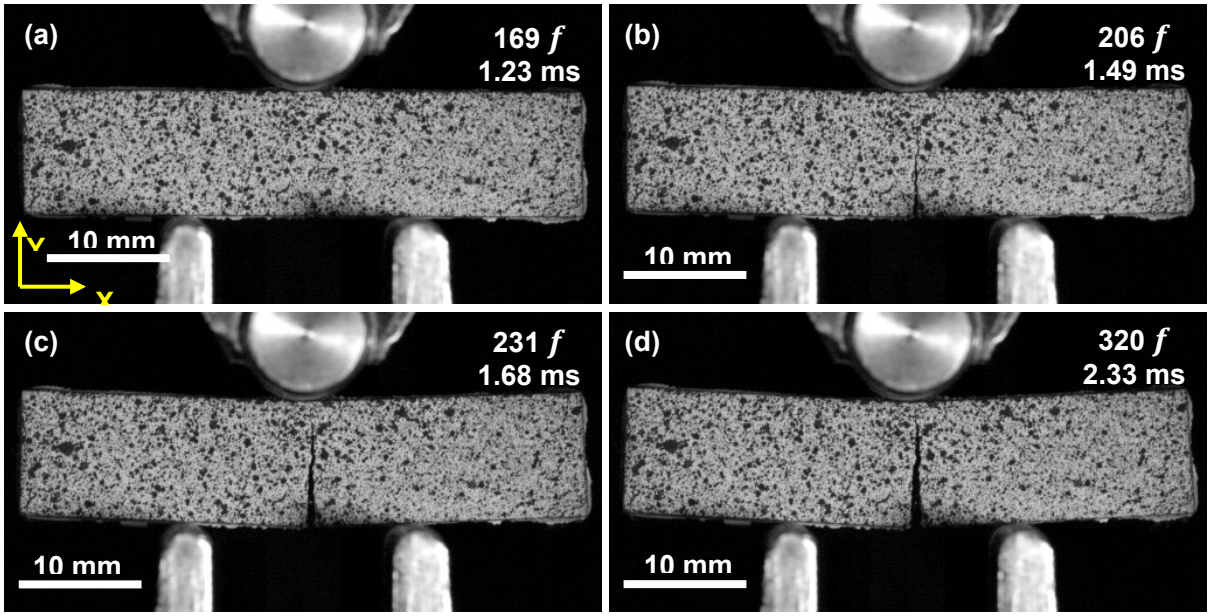


Figure 6.3 Three-point bend behaviour of RBSBC until final fracture. The image was recorded by the Photron Nova HS camera at a framing rate of 137,500 fps.

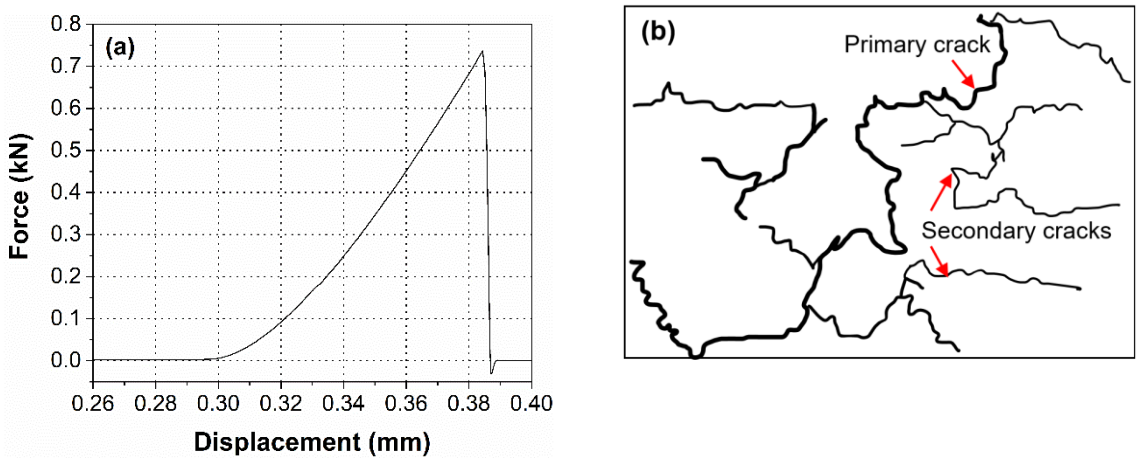


Figure 6.4 Loading response: (a) load-displacement plot for RBSBC (b) schematic of the crack propagation shape.

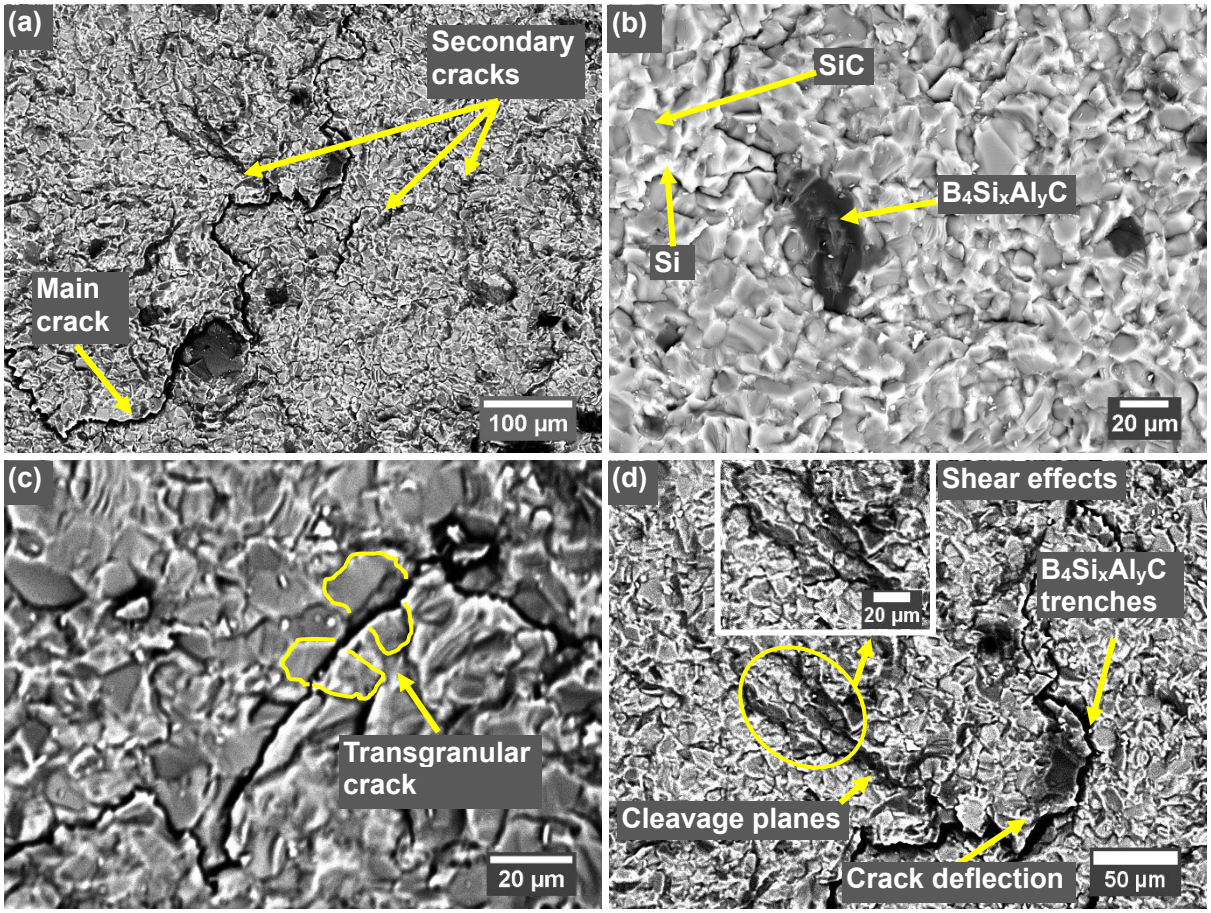


Figure 6.5 Fracture surface morphology: (a) widefield image of the fractured specimen (b) magnified image of the fractured surface (c) SiC transgranular crack (d) crack deflection through the $B_4Si_xAl_yC$ grains.

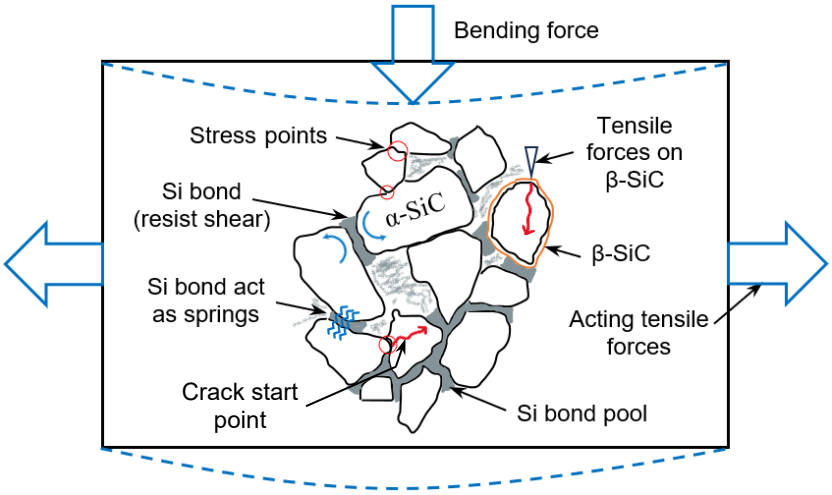


Figure 6.6 Schematic of the RBSBC morphology under tension, where Si acts as bonds between individual SiC grains according to the bond-particle model [386].

6.3.2 DIC analysis

High-speed camera DIC pictures the crack extension process in slow motion, which provide full-field displacement at the crack surface of the specimen, and along successive crack extensions. The Photron camera captures the last 2.66 ms before the crack propagates, which is beyond the Instron testing machine recording range of 10 ms between each reading. The captured images are an expanded result of the fracture point over 366 frames between an inter-frame time of 0–2.66 ms. This covers the range of loading including crack initiation from 0 frame f and 0 ms to near fracture at 366 f and 2.66 ms. During loading, the crack is vertical along the axis of the loading head, which indicates that it is driven by the lateral component of displacement at the notch tip [405]. Therefore, the lateral strain is recorded at the crack flanks.

The strain mapping is shown in Figure 6.7. The strain values are in the order of 10^{-3}, which is the same value reported by Hayun for infiltrated B_4C–Si composites under static loading. There is a scarcity of sources on the fracture strain behaviour of RBSBC under static loading. However, previous authors [440-443] who studied the dynamic behavior of hot-pressed boron carbide-based materials, recorded strain-rates between 10^{-3} and 10^{-6}. The minimum strain in the x-direction ε_{xx} is 0.001, which can be considered the crack initiation strain that occurs at Δa~0.2 mm. This corresponds to 173 f at 1.26 ms (Figure 6.7a). As the load increases, the crack opens up and propagates further, resulting in higher strain with increasing f. At fracture

(Figure 6.7d), the strain reaches its maximum value at 0.004 ± 0.0005. The calculated ε_{xx} is ~56% higher than the value calculated from the load-displacement plot (0.00169), which relates to the inaccuracy of calculating strain from bending tests.

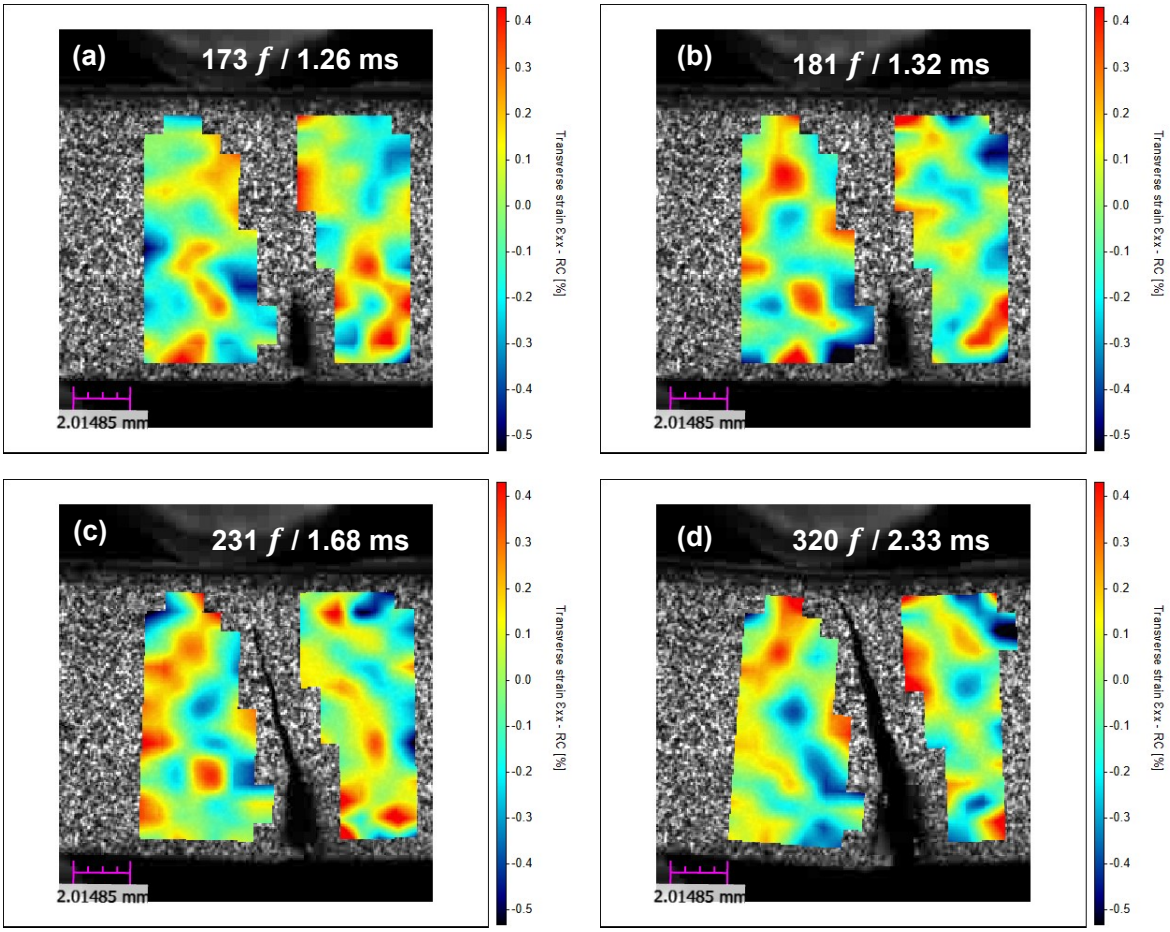


Figure 6.7 Strain mapping ε_{xx} for (a) 173 f and 1.26 ms (b) 181 f and 1.32 ms (c) 231 f and 1.68 ms (d) 320 f and 2.33 ms (there are 366 frames covering the time period 0–2.66 ms - top right gives frame number and time in ms).

The displacement in the x-direction U at the onset of crack extension (Δa~0.2 mm) is shown in Figure 6.8, where the crack path is along the orange-coloured arrow. Figure 6.9a–f shows the displacement mapping around the crack from its onset till fracture, while Figure 6.10 shows the plot of U versus r, where r is the distance away from the crack tip till the notch tip (shown as white arrow on Figure 6.9b). The value of r is zero at the crack tip, and maximum at the notch tip. The minimum and maximum displacements at 173 f (1.26 ms) are 0.0125 and 0.0155 respectively. As the crack length Δa (shown in mm in Figure 6.9a–f) and r increases slightly

to 0.92 mm at 181 f (1.32 ms), the value of U at the crack tip and crack mouth becomes 0.0378 and 0.0490 mm respectively. When Δa and r jumps to 4.60 mm (Figure 6.9c), the value of U at crack tip (0.072 mm) increased by 476%, which then drops after 196 f, where Δa reaches almost half the sample height at 4.60 mm. When Δa reaches 6.06 mm, the value of U at the crack tip (0.120 mm) increases by only 66%. The plot in Figure 6.10 shows the U versus r plot of the frames represented in Figure 6.9a–f. The slope of the displacement increases with increasing f or crack extension Δa, which means that the percent increase in displacement in the material becomes higher with crack extension. In other words, the displacement value becomes more sensitive to the change in crack extension. This is because the substrate is subjected to higher bending with increasing load and frame rate, which results in an increase in Δa and subsequently displacement in the x-direction as well.

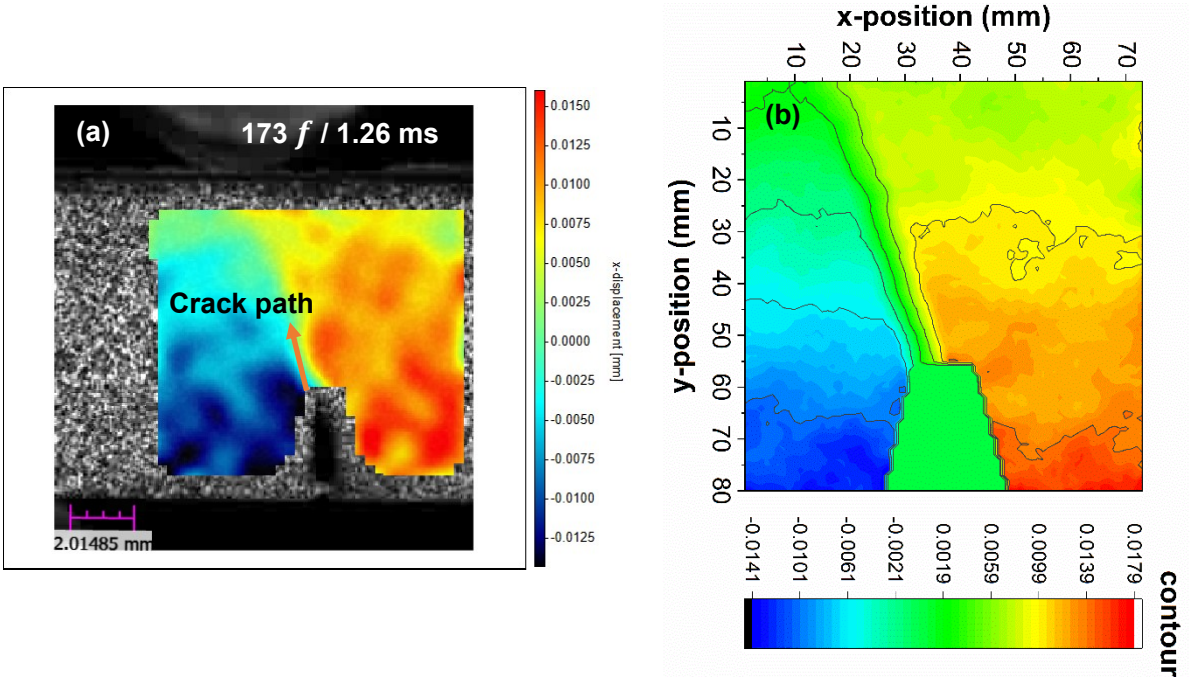


Figure 6.8 Displacement in x-direction U at the onset of crack (Δa~0.2 mm) at 173 f and 1.26 ms: (a) displacement map by DIC software DaVis (b) contour map plot. (there are 366 frames covering the time period 0–2.66 ms - top right gives frame number and time in ms).

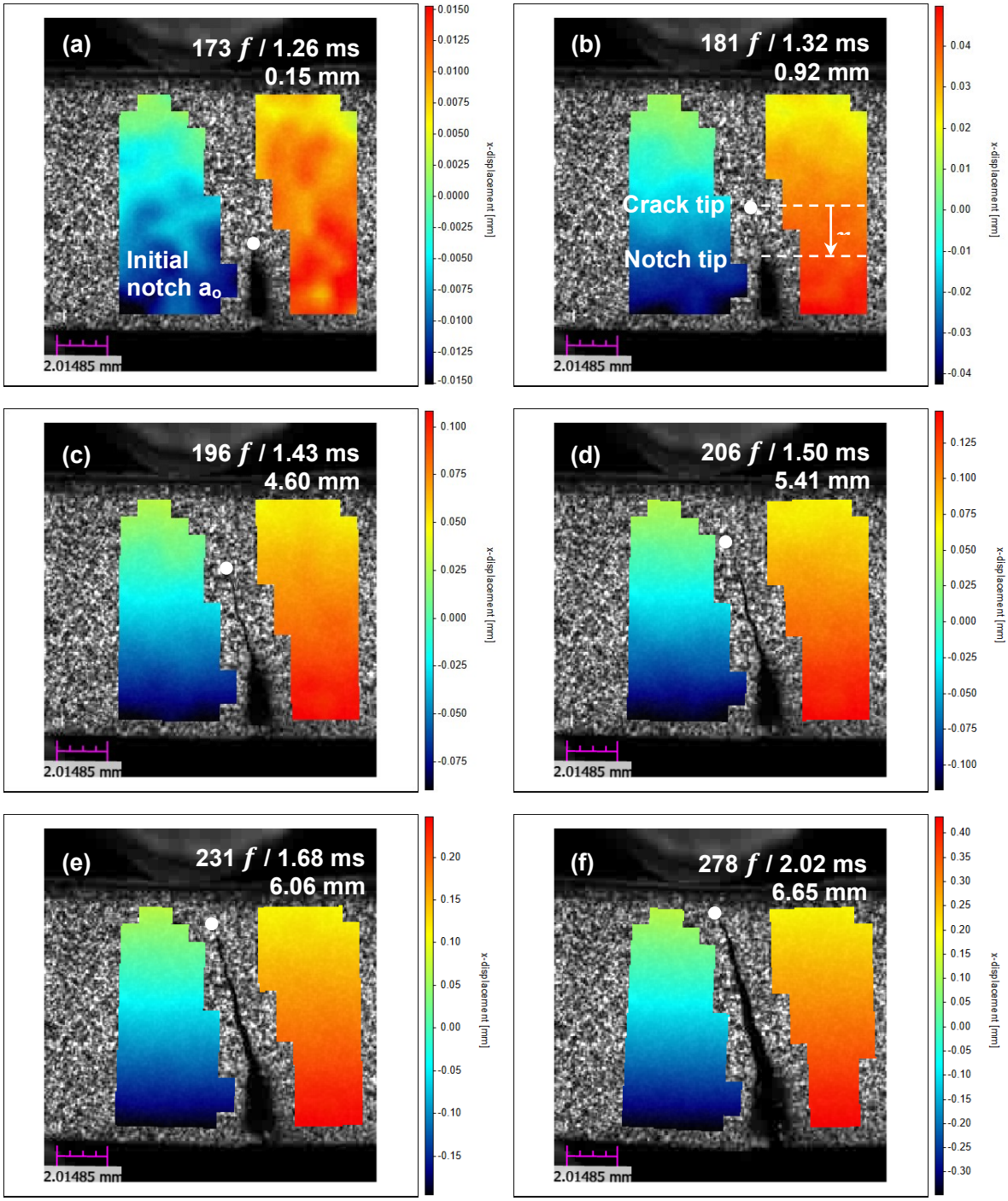


Figure 6.9 (a–f) show the U displacement maps between 173–278 f (1.26–2.02 ms), where the white circle shows the extent of the crack tip. (there are 366 frames covering the time period 0–2.66 ms - top right gives frame number and time in ms).

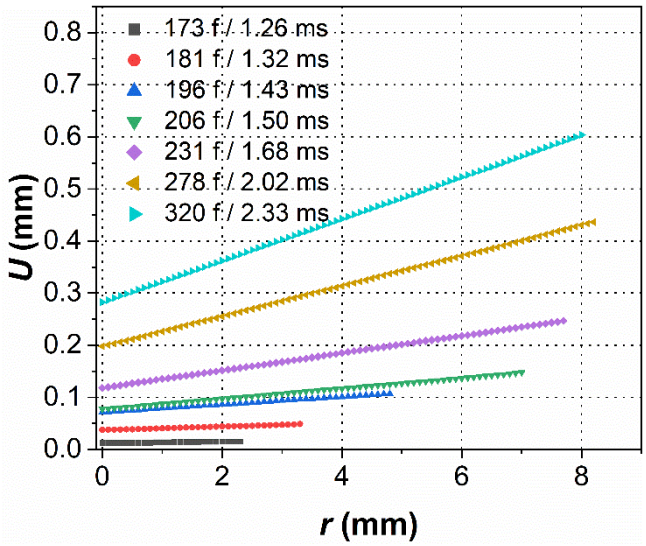


Figure 6.10 Plot of the compiled U versus r for the frames shown in Figure 6.9.

6.3.3 Crack velocity

The crack velocity V refers to the speed at which the crack tip will propagate, and it signifies the bond-breaking velocity [444]. The crack velocity was calculated from the images, between 1.20–1.80 ms, by measuring the crack extension Δa against recorded time t (ms) until the point of failure. The crack length-time plot has two main stages as shown by the blue arrows in Figure 6.11a. In the first stage, the crack velocity increases very rapidly. The crack length Δa increased linearly from 0.36 to 2.87 mm between 1.28–1.35 ms (~700% increase). It then increased approximately from 2.87 to 4.6 mm between 1.35 and 1.42 ms at a ~60%. This region accounts for an average of 10 frames. Afterwards, the slope of the crack extension shown in Figure 6.11a became flatter, where the percentage increase in Δa from 4.6–5 mm between 1.42 and 1.49 ms, was only 6%. The cracks measured are considered long cracks because their lengths exceed 0.4 mm and falls between ~3–10 mm [439].

Figure 6.11b shows the plot of V versus Δa, where it takes the form of a normal curve. The velocity increases steeply from 5 to 20 m s^{-1} between 1.28 and 1.31 ms, and then re-increases instantaneously from ~20 to 54 m s^{-1} in a single step (~63% increase) between 1.31 and 1.35 ms, where Δa reaches midway of the sample width. This behavior is related to the acceleration region in the Δa versus t plot. The increase in crack velocity signifies an increased frequency in the bond-breaking events [435]. The low density of the material and strong elastic bonding

(high E) participate in transmitting elastic waves faster, which results in cracks running faster. This can explain the sudden increase in velocity. The velocity then decreases in the deceleration region until it reaches ~6 m s^{-1} at the end of the experiment. The presence of B–C–Si grains act as a microstructural irregularity that result in deviation at the crack-front, which decreases the velocity of fast-moving cracks. However, the sudden drop of velocity after almost half the crack length Δa is related to machine-sample contact and not to strain hardening of the sample.

Regarding machine-sample contact, the loss of contact occurs when the sample bends before fracture, and so the loading head, which moves slowly at 0.01 mm min^{-1}, loses contact with the sample resulting in a sudden drop of load. The decrease in load results in a decrease in V and Δa. This phenomenon started at almost half the sample height, which is equivalent to the last 1.33 ms. This is below the machine data-reading-interval, which is the reason this drop is not reflected in the load-displacement plot. Strain hardening is not the case because the high tensile ratio (σ_Y/σ_{UTS}) of ~1 indicates the absence of yield and plasticity. Regarding strain hardening, the lower load allows time for stress relaxation to occur, which increases the internal stiffness of the material. In addition, the B_4C grains can aid in the hardening process by presenting interlocks to the movement of atoms, which would raise their potential energy and would result in a higher crack-tip energy required to continue the propagation of crack. However, even though the substrate may exhibit all of the above-mentioned hardening effects, it is not sufficient to be a strain hardening behavior because of the faster bond breaking effect compared to the increasing internal stresses in the remaining ligament.

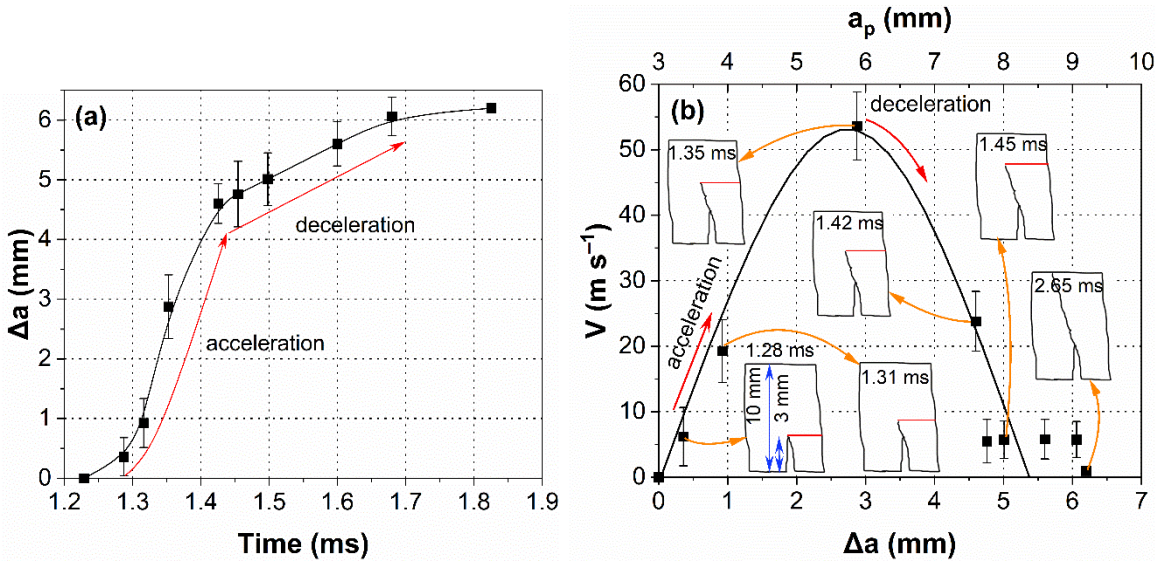


Figure 6.11 (a) crack length versus cracking time (b) cracking velocity versus crack length. Inset pictures show the crack propagation in relative scale until fracture.

6.3.4 Crack resistance behaviour

Experimental K_I and J-integral

The stress intensity at the crack tip was calculated experimentally using a series of DIC images that track the progress of crack extension. Virtual extensometers were drawn (using LaVision DaVis software) across the crack opening as shown in Figure 6.12 and Figure 6.13, where the difference in displacement across the crack flanks ΔU ($U_{right} - U_{left}$) was determined with respect to its position from the crack tip r. The experimental $K_{I,exp}$ was calculated along each frame rate, which corresponds to a single crack extension, resulting in a single value of $K_{I,ext}$ for each crack extension. This results in a plot of $K_{I,ext}$ versus Δa, which is compared with the quasistatic $K_{I,a}$ that is obtained based on specimen load and crack geometry.

The purpose of the K_I versus Δa plot is to determine the materials resistance to crack propagation. Figure 6.12 shows a schematic illustrating the process of calculating $K_{I,ext}$ experimentally as explained in Eqs. (6.7) and (6.8). Figure 6.13 shows the placement of a total of 67 equidistant extensometers (distance between each extensometer is 0.1 mm) between the crack tip at fracture till the notch tip. The value of the slope m that is used to calculate $K_{I,ext}$ according to Eq. (6.8), was obtained from the first few millimeters (~0.1–0.3) of the crack tip (equivalent to first three extensometers from the crack tip), as shown in Figure 6.14a, because

this is the crack extension area that is most affected by stress intensity. As r increases away from the crack path, the values of U and r will not be directly linked to K_I. This is represented in Figure 6.14a, where the ΔU versus $\sqrt{r}$ plot deviates from linearity when $\sqrt{r}$ > ~0.9. Figure 6.14b shows the variation of ΔU with respect to f across six equidistant locations that span across the crack length, where r = 0 at sample top and r = 6 at notch tip. This shows that the displacement increases with f as the crack opening width increases due to the increased bending process.

Figure 6.15 shows the plot of experimentally-obtained $K_{I,ext}$ versus Δa. The values at the first three frames 173 f (1.26 ms), 177 f (1.26 ms) and 181 f (1.32 ms) at Δa of 0.15, 0.36, and 0.92 mm were 1.42, 2.09 and 3.66 MPa $m^{1/2}$ respectively. However, once the crack jumps to 2.87 mm at 186 *f*, the stress intensity increases to 14.33 MPa $m^{1/2}$ and the values of $K_{I,ext}$ keeps increasing rapidly with increasing Δa because the remaining ligament and the crack-tip comes into close proximity to the sample back surface. Thus, the first three frames forms the linear region that represents the subcritical crack growth, where $K_{IC,ext}$ is at 3.66 MPa $m^{1/2}$. Fracture occurs when K_I reaches K_{IC}, and the rate of fracture toughness increase becomes higher than the rate of toughness at the onset of crack tip. Thus, the values outside the K_{IC} range do not accurate describe the relation between ΔU and K_I at the crack tip. Hence, the limit Δa_{max} for obtaining $K_{I,ext}$ for the current case is only for the first three points till Δa_{max}= 1 mm, where they have a slope of ~2.8 ± 0.08 (Figure 6.15). The experimentally-obtained $K_{I,ext}$ from the displacement data around the crack tip produces a reasonable elastic model for SiC-based materials, but only at a limited range before the crack extension becomes evident, and this is due to the unstable crack growth. It is worth noting that the experimental determination of stress intensity for brittle SiC-materials can be subject to inaccuracy. This relates to the challenge of determining the crack tip location for brittle materials, which in-turn makes it difficult to associate the crack tip r with its corresponding displacement readings. In addition, a small change in the ΔU value at the crack tip can result in a considerable change in $K_{I,ext}$. Thus, to experimentally calculate $K_{I,ext}$ accurately, an in-situ bend test with a DIC setup can be used to monitor crack propagation on a micron scale. However, this may prove to be challenging for the highly-brittle RBSBC ceramic.

The J-integral is an alternative method to quantify fracture toughness. The J–Δa plot was used to calculate the energy required to drive the crack tip by a certain displacement Δa. In solids that behave elastically, whether linear or non-linear, the J-integral is equal to the crack extension force G [409]. According to ASTM E1820–20 [409], the maximum J-integral capacity is the smaller of the following: $J_{max} = b\,\sigma_Y/10$ or $J_{max} = B\,\sigma_Y/10$. The J–Δa curve is therefore defined as the data bounded by the J_{max} and Δa_{max} limits. Thus, the maximum measurement capacity is at J_{max}= 44 kJ m^{-2}. To ensure that the J-integral represents valid fracture toughness values and that the plane-strain conditions are met, the thickness and remaining ligament should be large enough according to ASTM E1820–20 condition; $b\ and\ B\ \geq 25\ (J_C/\sigma_Y)$, where J_C measures the maximum fracture toughness of a material at the onset of fracture instability before significant crack extension that causes the measurement to become geometry-dependent [398, 409, 445]. The value of σ_Y was used in calculation since the strain-rate sensitivity of fracture depends mainly on σ_Y [446, 447]. The value of J_C (0.035 kJ m^{-2}), which is equivalent to K_{IC} of 3.2 MPa m$^{1/2}$, is considered at Δa_{max} of 1 mm in accordance with the crack extension limit of the $K_{I,ext}$–Δa plot, which would be prior to the unstable crack extension at 186 f (1.35 ms) and Δa ≈2.87 mm. This is also the end of the linear region as shown in Figure 6.15b inset. The experimental J_{ext}–Δa plot is linear and flat for the first three points at 173 f (1.26 ms), 177 f (1.26 ms) and 181 f (1.32 ms) as with the $K_{I,ext}$–Δa curve. The value of J is 0.0052 kJ m^{-2} at the start of crack growth Δa = 0.15 mm, which then increased to 0.011 then 0.035 kJ m^{-2} at Δa of 0.36 and 0.92 mm respectively.

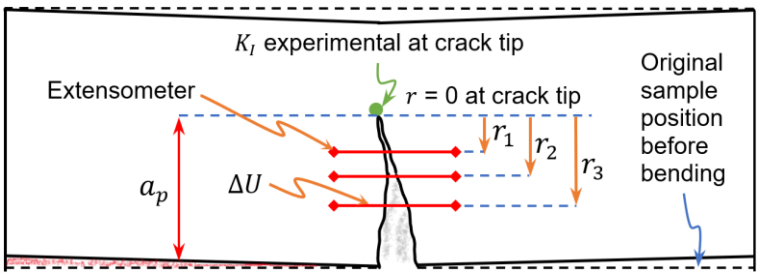


Figure 6.12 Schematic of obtaining experimental K_I from the change of U across r.

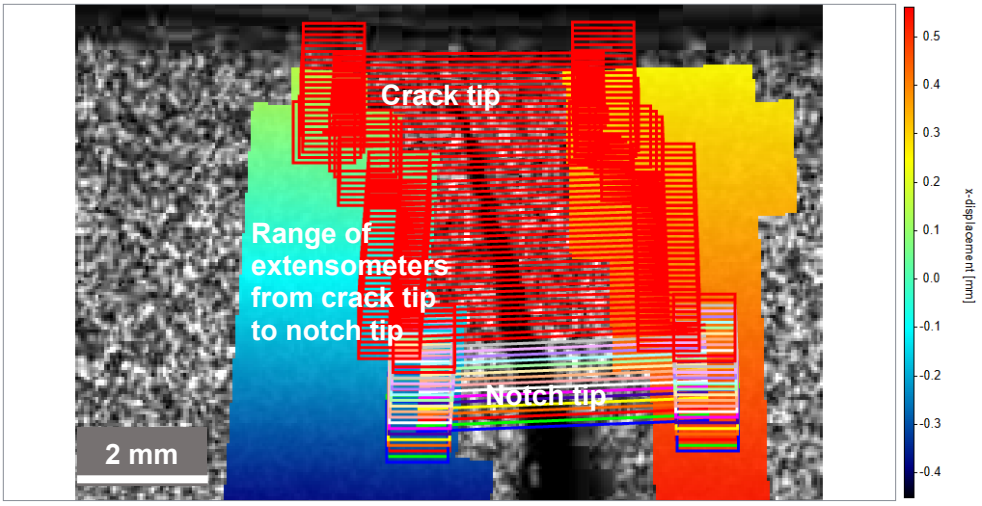


Figure 6.13 Image of the crack at 278 f (2.01 ms) showing the grid of 67 extensometers placed at 0.1 mm equidistance along the crack flanks, where ΔU was measured.

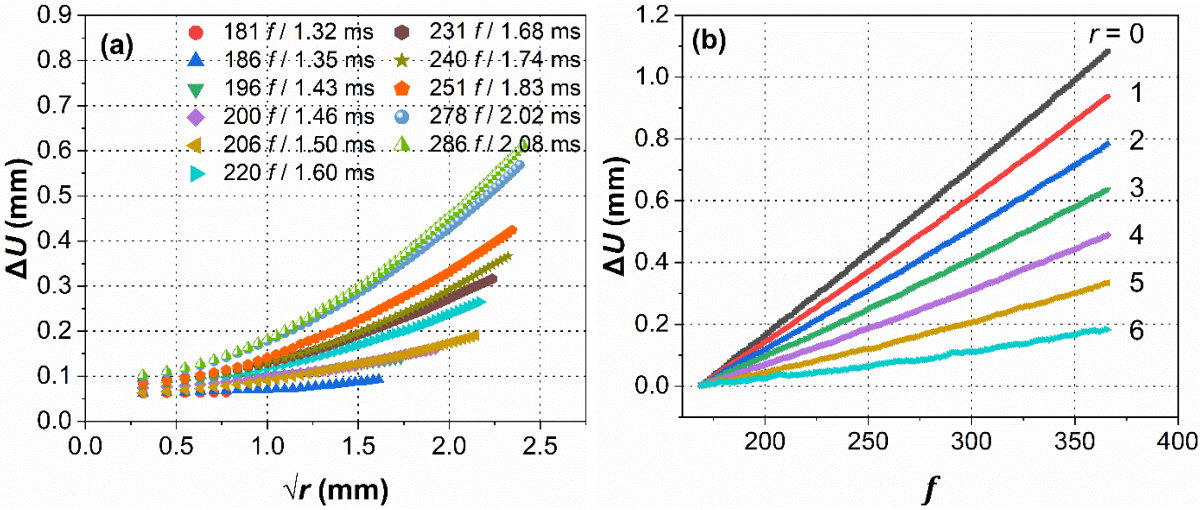


Figure 6.14 Plots: (a) ΔU versus $\sqrt{r}$ for various frame rates (b) ΔU versus f for six equidistant extensometers, where r is 0 at the top of the sample, and 6 at the notch tip.

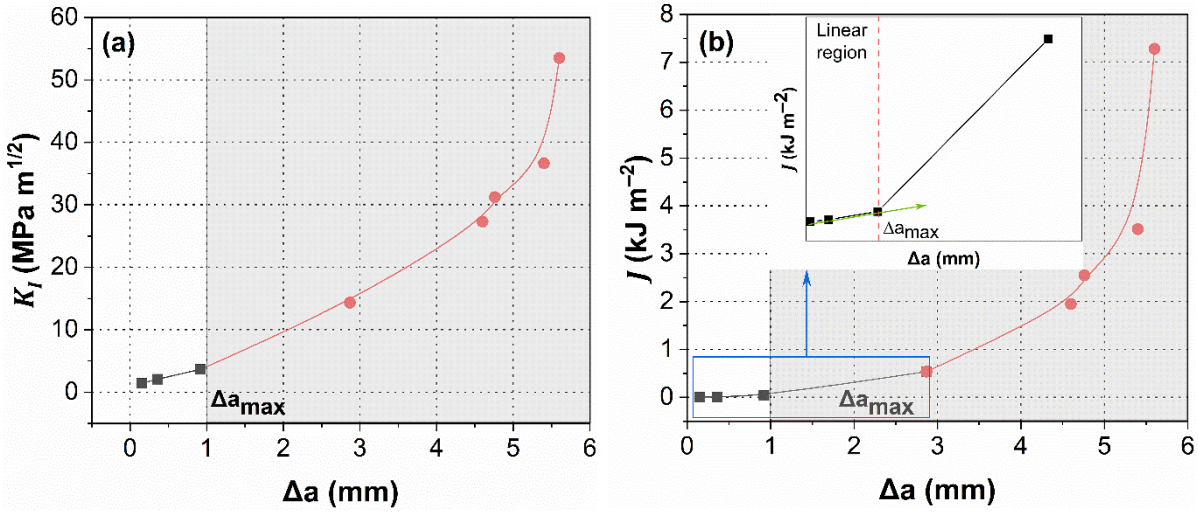


Figure 6.15 Plots of experimentally-obtained (measured using virtual extensometers form the DIC images): (a) K_I versus Δa (b) J versus Δa.

Quasistatic K_I and J-integral

The quasistatic $K_{I,a}$ is function of the sample's geometry and load according to the LEFM SENB theory, where a single value of $K_{I,a}$ is obtained for each crack extension Δa as shown in Figure 6.16 to produce a plot of $K_{I,a}$ versus Δa. The computed $K_{I,a}$ values also disregards the potential effects of residual stress or crack closure.

At Δa equals to 0.15, the value of $K_{I,a}$ is 1.05 MPa m$^{1/2}$, which increases to 1.59 and 2.41 MPa m$^{1/2}$ at Δa of 0.36 and 0.92 mm respectively. These values are below the critical stress intensity factor K_{IC} of 3.2 MPa m$^{1/2}$, where the sudden crack occurs when the value of K_{IC} is exceeded. Afterwards, the value of $K_{I,a}$ increased linearly with Δa at a rate of 80 ± 20% till it reached ~9 MPa m$^{1/2}$ at 110 MPa when a/W = 0.56 as shown in Figure 6.17a. This value is close to the values obtained for SiC50/PMMA and SiC40/PMMA [SiC with Al_2O_3 and Y_2O_3 sintering aids and infiltrated with polymethyl methacrylate (PMMA)] which showed ~9 MPa m$^{1/2}$ at 108–125 MPa tensile strength respectively [448]. The value of $K_{I,a}$ was calculated before the start of crack initiation to determine the point at which $K_{I,a}$ exceeded K_{IC}, and the rate of K_I change. However, ASTM E1820–20 [409] defines the maximum crack extension capacity for a specimen under bending as $\Delta a_{max} = 0.25b$, where b is the original remaining ligament ($W - a_o$ = 7 mm). This sets the limit for $K_{IC,a}$ at Δa_{max} of 1.75 mm, which is equal to ~3.40 MPa

$m^{1/2}$. This value deviates from the $K_{IC,ext}$ by ~8%, and both values are almost similar to the K_{IC} (3.2 MPa $m^{1/2}$) obtained from the 3-point bend test.

The Δa_{max} limit is set at 1.75 mm instead of 1 mm because the linear region extends till crack length is 2.87. Beyond this value, the crack propagation may be affected by the ligament geometry at a much higher degree than by the stress intensity at the crack tip, which is reflected in the deviation from linearity in the $K_{I,QS}$ versus Δa in Figure 6.17a. This is because when the crack becomes large compared to the component size, like Δa reaching half-way through the substrate thickness W, K_I becomes no longer proportional to Δa [400]. The relation between $K_{I,a}$ and Δa till Δa_{max} is a straight line with a slope of ~1.7 ± 0.24, which has the same trend as $K_{I,ext}$. The linear relations of $K_{I,ext}$ and $K_{I,a}$ are synonymous with the linear behaviour of V at Δa between 0.15 and 2.87 mm. The slopes exhibited by the plots reflect no plasticity constraint at the crack tip, and therefore no strain hardening effect would be expected to occur. This reflects a low resistance to crack propagation as expected for monolithic ceramics.

The quasistatic J_a–Δa R-curve has the same behavior as that of the experimental J_{ext}, with an almost flat slope as shown in Figure 6.17b. The value of J is 0.0029 kJ m^{-2} at Δa = 0.15 mm, which then increased to 0.0065 and 0.015 kJ m^{-2} at Δa of 0.36 and 0.92 mm respectively. As with J_{ext}, the deviation from linearity occurs at Δa_{max} of ~1.75 mm as shown in Figure 6.17b, where the value of J_C is ~0.032 kJ m^{-2}. The percentage increase from J to J_C is ~130%, which is close to the percentage increase value of J_{ext}. The value of J_C is at the low end of the range for ceramics, and the onset of significant crack extension occurs at a small Δa, which indicates that RBSBC is at the high end of brittle materials. The low values of J and the low rate of energy increase proves that the material does not exhibit strain hardening, where in that case more energy would be required for crack extension Δa compared to the energy required for crack opening, and the plot will be exponential and not a straight line.

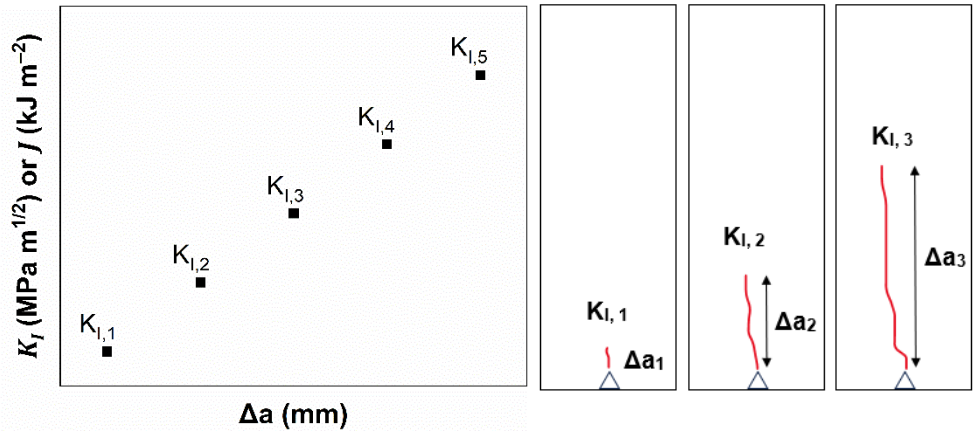


Figure 6.16 Crack extension measurement and the formation of the R-curve [399].

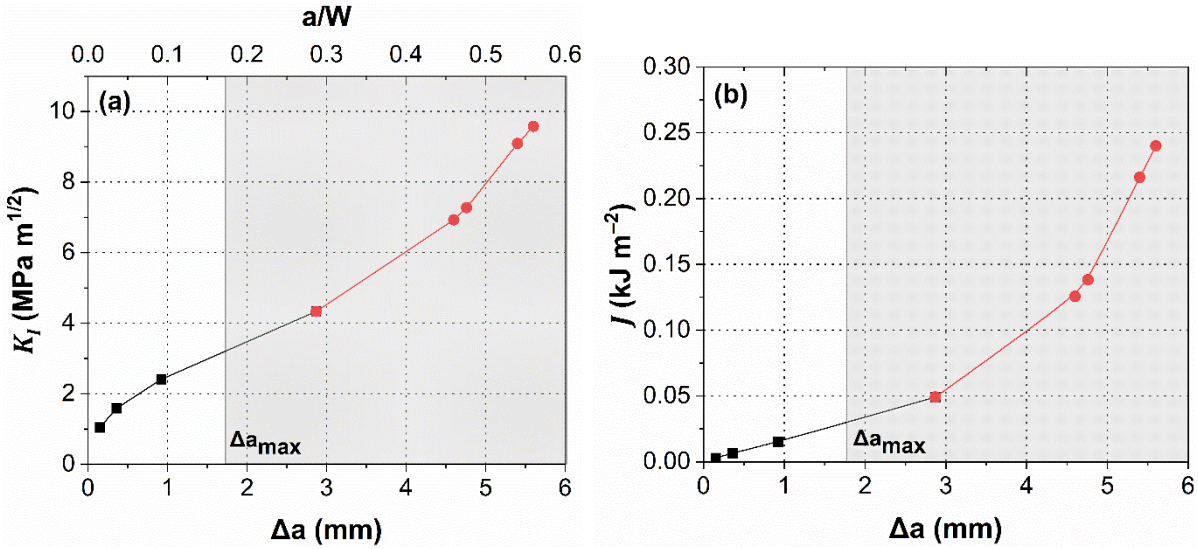


Figure 6.17 Plots of quasistatic calculation (according to LEFM SENB) for: (a) K_I versus Δa (b) J versus Δa.

CMOD and CTOD

The crack width was calculated from the Crack Mouth Opening Displacement (CMOD) instead of being calculated at the crack tip (CTOD) δ because the small and subsurface nature of δ makes direct measurement from DIC images difficult. Figure 6.18 shows the schematic of crack dimensions that is used for measuring CMOD and calculating δ.

Figure 6.19a shows the plot of CMOD versus Δa, where it starts at Δa of 4.60 mm because below that value, the CMOD is constant and cannot be measured visually. However, at Δa of

4.60 mm, the a/W ratio is 0.46, which indicates a deeply cracked specimen [417]. This shows that at the linear region of subcritical crack growth, the increase in CMOD with crack length is negligibly small, which confirms with the low values of strain and U displacement that are in the order of 10^{-3} mm. In ceramics, where the material fails in brittle/cleavage fracture without plastic deformation at the crack tip or stable ductile tearing, the elastic component of δ is the main contributor to the total δ since the value of the δ elastic component can be 1340% times that of the plastic component [417]. In addition, if plastic deformation at the crack tip is confined to a very small area, it will not disturb linear elasticity and will lead to negligible deviation from the linearity of the test record. The sharp crack tip indicates that elastic deformation took place, and that is because inelastic deformation results in a wide (mm-scale) distribution of damage around the crack tip due plasticity [398]. The calculated values of δ were smaller than what may appear at the crack tip visually by the naked eye because locating the crack tip is imprecise owing to the related low resolution of the captured image. In addition, the crack tip position in reality is ahead of what is visually identified in the DIC images [191].

The values of δ_{ext} (Figure 6.20a) were calculated from $K_{I,ext}$ using Eqs. (6.8) and (6.12), while δ_a (Figure 6.20b) was calculated from $K_{I,a}$. The values of δ_{exp} are greater than those of δ_a by ~95%, however, both plots have the same trend. The change of δ with respect to Δa is influenced by the crack shape, length and crack conditions. The small change in δ across crack length indicates that the crack progresses in an unstable behavior. The relation between the measured CMOD and the calculated δ is almost linear (Figure 6.19b). It can be assumed that with brittle ceramics where the plastic component of δ is negligible, the incremental increase of δ at the leading edge is linearly related to the widening of the CMOD and the increase in θ due to out-of-plane bending (see Figure 6.18). This however, does not agree with the experimental results of Khor [417], who found that δ does not increase proportionally with CMOD when the value of δ is less than 0.2 mm. The difference in behavior can be related to the difference in the tested material and geometry, and testing conditions. Even though direct relation between CMOD and δ indicates that CMOD can be used to represent the crack tip in ceramics, the limitations concerning CMOD measurements at subcritical cracks and small Δa makes it unreliable compared to δ, which is directly calculated from the stress intensity and thus it can properly reflect the conditions during the subcritical crack growth.

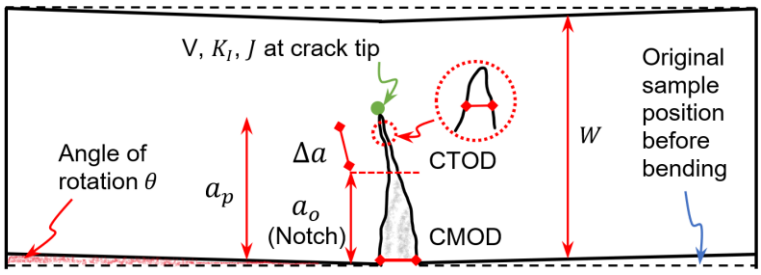


Figure 6.18 Schematic of the crack and its related dimensions and properties.

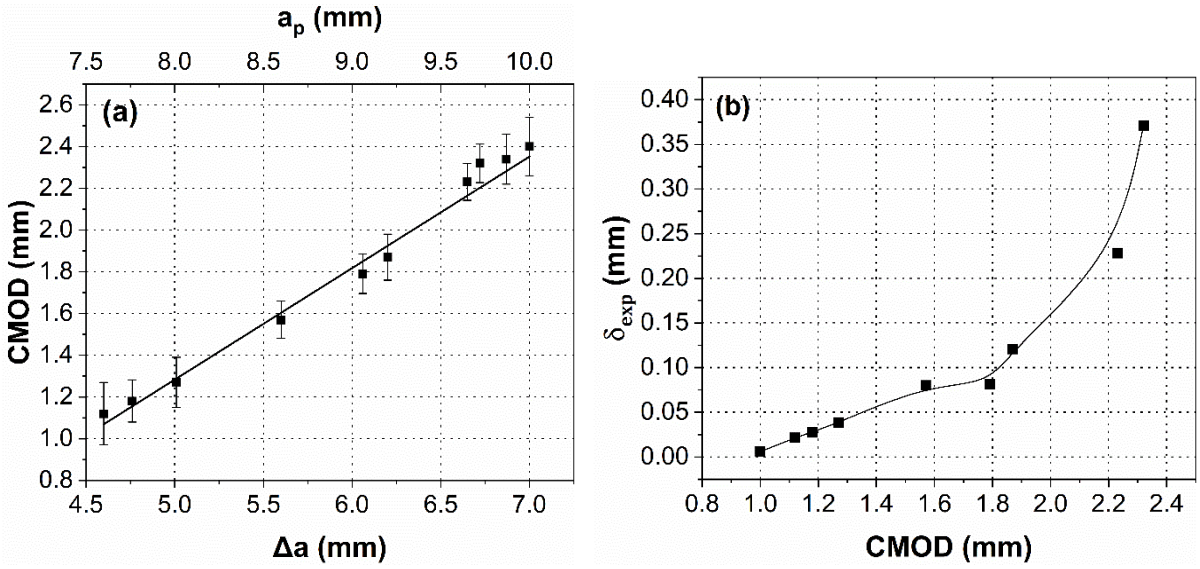


Figure 6.19 Plots of: (a) CMOD versus Δa (b) CMOD versus δ_{ext}.

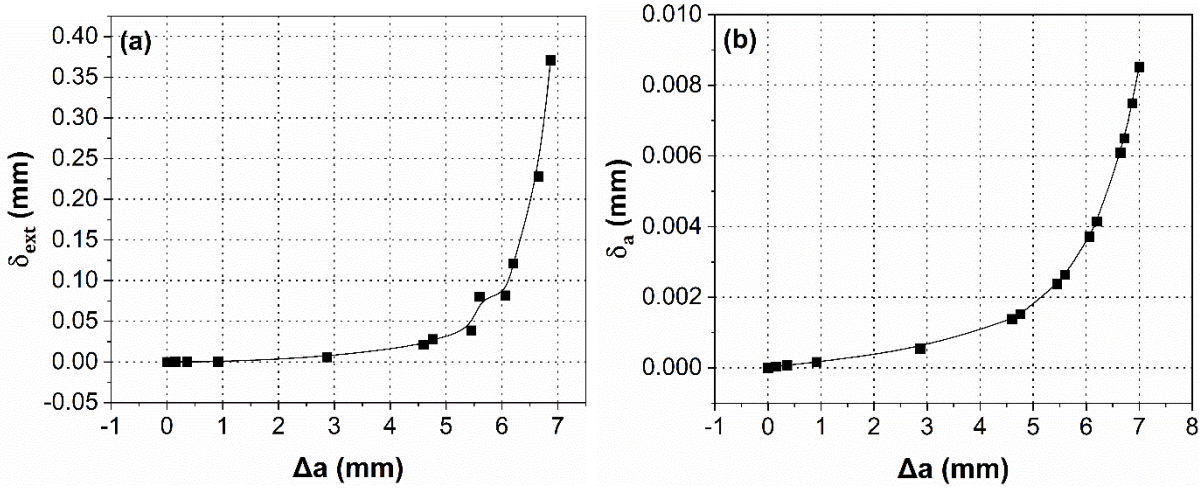


Figure 6.20 Plots of δ versus Δa for: (a) experimental (virtual extensometer) (b) quasistatic (LEFM SENB).

Table 6.2 The values of V, δ, K_I and J at the measured Δa and CMOD within the captured recorded time and frame rate.

	f	Time ms	Δa mm	a_p mm	V m s^{-1}	$\frac{a}{W}$	CMOD mm	m x 10^{-3}	$K_{I,exp}$ MPa m$^{1/2}$	$K_{I,QS}$ MPa m$^{1/2}$	δ_{exp} x 10^{-3} mm	δ_{QS} x 10^{-3} mm	J_{exp} kJ m^{-2}	J_{QS} kJ m^{-2}
Frame count 366 f (fracture between 169–365 f)	169	1.229	0.00	3.00	0.00	0.00	1.00	0.00	0.00	0.00	0.000	0.000	0.000	0.000
	173	1.258	0.15	3.15	5.17	0.02	1.00	0.38	1.42	1.05	0.058	0.032	0.005	0.003
	177	1.287	0.36	3.36	7.19	0.04	1.00	0.57	2.09	1.59	0.126	0.072	0.011	0.006
	181	1.316	0.92	3.92	19.25	0.09	1.00	1.00	3.66	2.41	0.385	0.166	0.035	0.015
	186	1.353	2.87	5.87	53.62	0.29	1.00	3.91	14.33	4.33	5.902	0.540	0.537	0.049
	196	1.425	4.60	7.60	23.79	0.46	1.12	7.45	27.30	6.93	21.42	1.380	1.949	0.125
	200	1.455	4.76	7.76	5.50	0.48	1.18	8.52	31.22	7.27	28.01	1.520	2.549	0.138
	206	1.498	5.01	8.01	5.73	0.55	1.27	10.0	36.65	9.09	38.60	2.375	3.512	0.216
	220	1.600	5.60	8.60	5.79	0.56	1.57	14.4	52.77	9.58	80.03	2.636	7.282	0.239
Record time (1.2–2.6 ms)	231	1.680	6.06	9.06	5.75	0.61	1.79	14.6	53.51	11.36	81.68	3.710	7.432	0.337
	251	1.825	6.20	9.20	0.96	0.62	1.87	17.7	64.87	12.01	120.9	4.146	11.01	0.377
	278	2.020	6.65	9.65	2.29	0.67	2.23	24.3	89.06	14.56	227.9	6.093	20.74	0.554
	310	2.260	6.72	9.72	0.95	0.69	2.32	31.0	113.6	16.14	370.9	7.491	33.75	0.681
	320	2.330	6.87	9.87	2.06	0.67	2.34	–	–	15.04	–	6.497	–	0.591
	365	2.661	7.00	9.90	0.86	0.70	2.40	–	–	17.22	–	8.520	–	0.775

6.3.5 Testing conditions of K_I and J-integral

The experimentally-obtained K_I and J values (Table 6.2) were higher than the quasistatic values by ~30 and 50% respectively during the linear region as in Figure 6.21a and Figure 6.22a. Regarding δ, the experimental values are higher than the quasistatic ones by ~50% as shown in Figure 6.23a. The higher experimental values of K_I, J and δ compared to the quasistatic ones indicates that there is no crack closure present because crack closure will result in lower stress intensity values than those dependent on load and crack geometry alone (quasistatic). The slope of the linear region of $K_{I,ext}$ and J_{ext} are higher than that of $K_{I,a}$ and J_a by ~65 and 150% respectively as shown in Figure 6.21b and Figure 6.22b. Following the same trend, the slope of δ_{ext} is higher than that of δ_a by 60% as shown in Figure 6.23b. The lower values for the quasistatic plot relate to the difference in the estimation of stress intensity at the crack tip between the experimental DIC measurements using virtual extensometers and the displacement-controlled (quasistatic) conditions using LEFM SENB. The virtual extensometer can be considered as a local measurement of K_I at the crack tip as obtained directly from the lateral displacement measurements around the crack tip. Thus, experimental measurement accurately represents the actual condition of K_I at the crack tip. On the other hand, the displacement-controlled bend test can be thought of as a global measurement, where the K_I value depends on the fracture force P obtained from the bend test in addition to specimen size.

The $K_{I,a}$ is quasistatic, where the load is applied very slowly with respect to the response of the material, which means that the load acts in a manner that results in no substantial variation of the substrate response with time. This results in the neglection of time-dependent forces as inertial force $m\ddot{X}(t)$, where m is the mass of the sample and $\ddot{X}$ is the acceleration. Thus, the load P of the quasistatic analysis will be function of the elastic component $kU(t)$ only, where k is the material stiffness (Figure 6.24). This will result in a lower estimation for P, and lower value of $K_{I,a}$. However, the development of crack with time in the DIC images indicate that the analysis conditions of $K_{I,a}$, J_a, and δ_a are not purely quasistatic but somewhere between the quasistatic and fully dynamic (load-controlled). On the other hand, the $K_{I,ext}$, J_{ext}, and δ_{ext} were directly measured from the DIC images, where they reflect the actual conditions at the crack tip and the true material behavior. Thus, DIC offers a tool to accurately determine the stress intensity and J-integral at the crack tip without underestimation of the R-curve. Kolednik [449] found that for a given crack extension, the value of J in the R-curve for a load-controlled

test is always higher than that of the displacement-controlled test. In addition, the slope of load-displacement J for the linear part ($\Delta a_{max} \approx 1\ mm$) is higher than displacement-controlled J by 19%. Additionally, the presence of secondary non-through-thickness microcracks around the crack tip also plays a role in the increased K_I and J with crack length [450, 451]. The difference in the slope between K_I and J relates to Eq. (6.11), where $K_I\ \alpha\ \sqrt{J}$ ($K = \sqrt{EG}$). It should be noted that the aforementioned results and following discussions only pertain to cracking that occurs on the surface of the composite. Cracking behavior and patterns may change in the composite interior due to different and more complex three-dimensional stress states.

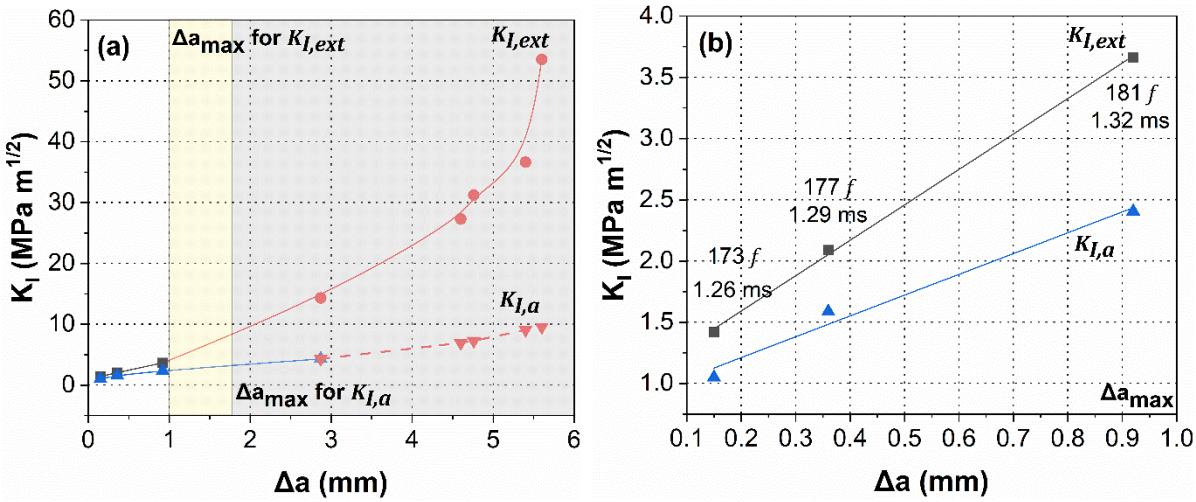


Figure 6.21 Plots of experimental (virtual extensometer) and quasistatic (LEFM SENB) analyses for: (a) K_I versus Δa (b) the linear region for the two K_I curves.

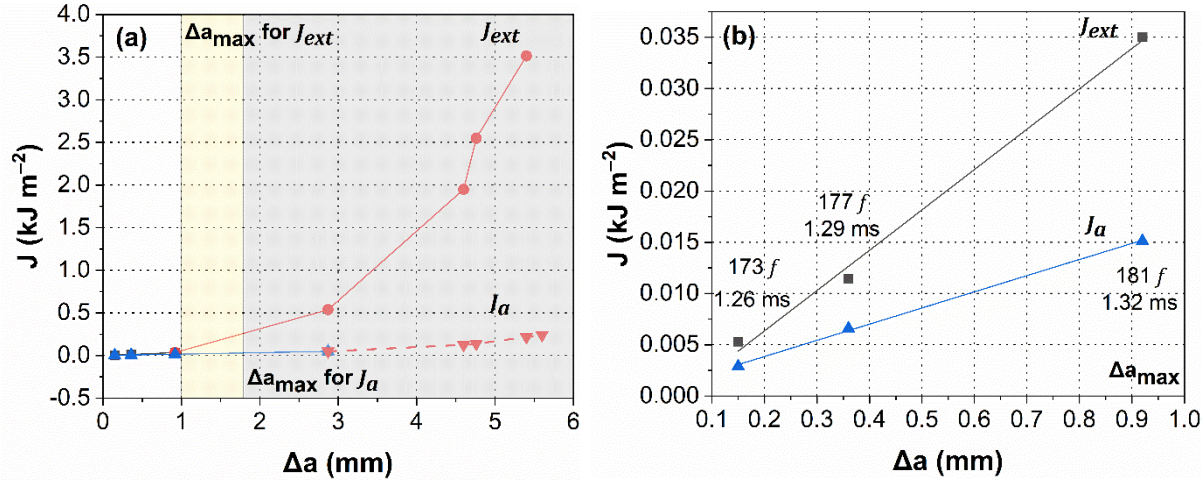


Figure 6.22 Plots of experimental (virtual extensometer) and quasistatic (LEFM SENB) analyses for: (a) J versus Δa (b) the linear region for the two J curves.

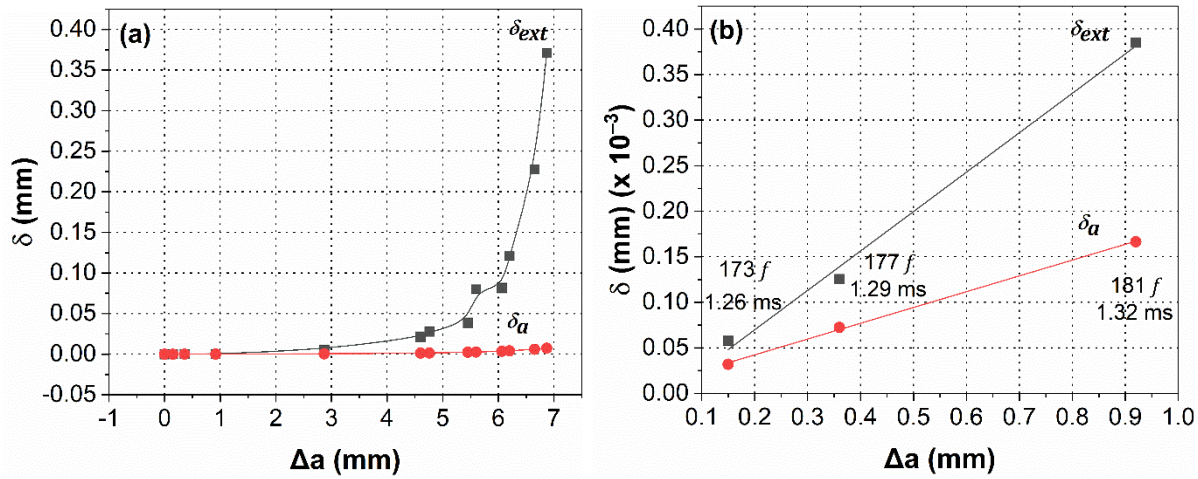


Figure 6.23 Plots of experimental (virtual extensometer) and quasistatic (LEFM SENB) analysis for (a) δ versus Δa (b) the linear region (from the K_I and J plots) for the two δ curves.

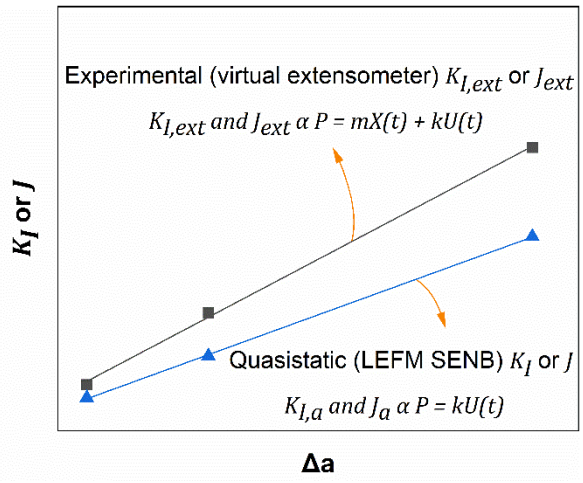


Figure 6.24 Difference in values and slopes between the experimental (virtual extensometer) and the quasistatic (LEFM SENB) K_I and J for the linear region.

Most SiC-based materials have an R-curve slope within the range of 1×10^{-3} or 1×10^{-2} like commercial Hexoloy-SA, as shown in Table 6.3 and Figure 6.25, which is much flatter than the SiC–B_4C composite in this study or SiC50/PMMA. The flatter R-curve slope indicates that the plain strain regions of these materials are more highly constraint resulting in lower toughness and lower resistance to crack. In these cases, the stress intensity K_I is constant and equal to plain-strain fracture toughness K_{IC}, where the fracture toughness is independent of crack extension Δa. The higher slope of RBSBC shows that resistance to crack propagation is

dependent to subcritical crack extension Δa ($\Delta a < \Delta a_{max}$). This can be related to the microstructure of RBSBC and the presence of coarse B_4C grains that are dispersed randomly within the structure in addition to the α and β-SiC grains randomly distributed in a Si pool. There is a scarcity in data regarding the crack-resistance behaviour of SiC–B_4C composites and reaction bonded SiC-based ceramics. In addition, comparing R-curves in the current research is for referencing purpose because there are many factors that affect the resistance profile including but not limited to: material composition and microstructure, manufacturing method, porosity and internal defects, initial crack size and shape, mode of loading, and the methods of calculating the stress intensity.

Table 6.3 Comparing R-curve for various SiC-based materials.

Material	Processing	K_{IC} (MPa m$^{1/2}$)	R-curve slope	References
SiC–B_4C	Reaction-bonded	3.2	1.5	This study
Coarse α-SiC	Hot pressing	~3	0.0011	Al Nasiri [198]
ABC-SiC (SiC–0.6B–3Al–3C)	Hot pressing	–	0.0064	Gilbert et al. [452]
ABC-SiC (SiC–0.6B–3Al)	Hot pressing	–	0.0027	Gilbert and Ritchie [453]
Fine SiC–$6Al_2O_3$–$4Y_2O_3$	Hot pressing	–	0.0048	Lee et al. [198, 454]
Hexoloy-SA SiC	Pressureless-sintered	~2.5	0.05	Gilbert et al. [439]
SiC50/PMMA	Freeze casting	–	0.9	Naglieri et al. [448]
SiC40/PMMA	Freeze casting	–	2.3	Naglieri et al. [448]

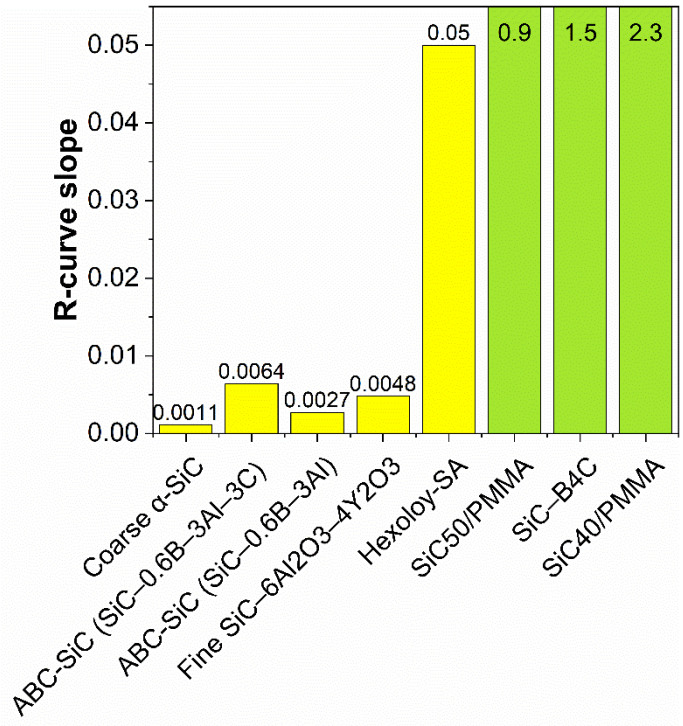


Figure 6.25 Bar chart showing the slope of R-curves for various SiC-based materials.

6.4 CONCLUSION

The fracture behaviour and resistance to crack propagation of reaction-bonded SiC–B_4C ceramic was studied under flexural three-point bending at ambient temperature using a DIC setup. The high-speed camera allowed the capture of crack propagation at the fracture point, where 366 frames were produced across a time interval of 2.66 ms. This resulted in successive images showing the crack extension from the initiation point till fracture. The fracture toughness and strain energy calculated at the crack tip showed a steep curve with low crack resistance as would be typical for brittle ceramics. However, the slope of the resistance curve is higher than for commercially available conventional SiC-based ceramics, which showed that the presence of B_4C in SiC–B_4C ceramics results in higher crack resistance than monolithic SiC-only ceramics, and lower fracture strain. Two methods were used to determine the crack-resistance plots from the stress intensity at crack tip: experimentally determined $K_{I,exp}$, which is based on displacement measurements around the crack tip, and the quasistatic $K_{I,QS}$, which is based on the geometry of the crack. DIC is very useful in determining the R-curve because it based on the measurement of crack-tip displacement so it reflects the actual conditions of the crack propagation, and because the quasistatic or dynamic testing may not accurately represent

the actual cracking conditions, which can result in lower estimation of K_I and J by as much as 30 to 50%.

For future work, the values of δ can be measured using an extensometer clip gauge, which can be compared with the calculated δ to determine the accuracy of DIC in determining δ for ceramic materials. Additionally, the camera lens cannot capture short crack-growth, where crack length is below the SiC grain size of 15–20 μm. The shortest crack captured at the current study is ~150 μm. Studying short cracks is important to understand the effect of RBSBC morphology on crack resistance since R-curve behaves differently between short and long cracks. For that purpose, an in-situ bending test bed equipped with DIC setup will facilitate such a study. The current setup cannot acquire images for the coating because the coating thickness is ~200 μm opposed to a 10 mm substrate thickness, and therefore the mechanical behaviour of the coating would be significantly affected by that of the substrate.

Recommendations to improve the substrate include adjusting the chemical composition and controlling the reaction bonded process to achieve the following:

- Decrease the grain size of B–C–Si grains and disperse them more evenly among the matrix to increase the tortuosity of crack propagation path.
- Increase the B_4C percentage in the RBSBC, which will lead to an increase in bending strength.
- Increase the thickness of the β-SiC rim around the main α-SiC grains, which will offer higher resistance to crack initiation on the main α-SiC grains.
- Decrease the amount of Si between the α-SiC grains to nm level so that the Si can act as springs/glue to the SiC grains without being thick enough to compromise the integrity of the structure.
- Changing the structure of the material can also increases its fracture toughness. Previous authors [398, 448] proposed a brick-and-mortar structure that offered higher fracture toughness and strength.

7 CONCLUSIONS

The chapter summarises the key findings presented in the current research. The conclusion of the thesis sums up the understanding and durability of ceramic-based coatings in high-temperature sand environment. Two main aspects were studied: the oxidation resistance of reaction-bonded silicon carbide-boron carbide (RBSBC) ceramics, and the corrosion resistance of dip coated rare-earth silicate environmental barrier coatings in calcium–magnesium–alumino–silicate (CMAS) environment; which is a salicaceous sand.

The findings of the oxidation study (Chapter 4) shows the high oxidation resistance of RBSBC, which owes its behaviour to the formation of a SiO_2-rich borosilicate layer during high temperature (higher than 1300 °C) exposure. The protective layer is characterised by its thickness and composition. The B_4C addition of less than 8 wt.% does not change the oxide layer properties or growth mechanism. The formed oxide has a high SiC/B_4C ratio, where the rate-limiting step of oxide growth is ionic oxygen diffusion through SiO_2 layer. Thus, the RBSBC substrate offers a lightweight alternative to conventional monolithic SiC ceramics, where the presence of B_4C in low percentage contributes to a lower density yet oxidation-resistant substrate. Understanding the oxide layer is essential because the dip coated rare-earth (Yb, Lu, or Er) EBCs were processed on the RBSBC samples after being oxidised so that he oxidation layer reacts with the dip coating and form a double layered coat.

The corrosion mechanism of RE coatings in the CMAS environment was studied. The investigation highlighted the role of coating microstructure, composition, and application technique in resisting CMAS infiltration and subsequent damage. The corrosion resulted in the formation of a protective uniform garnet layer at the EBS–CMAS interface, and an apatite-like phases within the coating matrix. The CMAS melt infiltrates the pores and cracks of the coatings, where it reached to the reaction front and reacted with the RE_2O_3 through dissolution/precipitation mechanism. The gradual dissolution of the melt in the coating structure resulted in the formation of three phases that forms successively; where the distinct between them is in the Ca and Si content which is represented in grey contrasts - higher Ca and Si results in a darker grey contrast.

The RE element ionic radius plays a part in the corrosion product, where Er-silicate tends to form unprotective apatite at the interface because the ionic radius of Er^{3+} is close to Ca^{2+}. The reaction kinetics showed that Yb and Lu-silicates have higher melt-resistance compared to Er-silicates. Two quantification methods were proposed to assess EBC performance in CMAS melt: (1) diffusion coefficient as a method to rank the coating performance based on its RE element type, and (2) corrosion rate to assess the coating performance based on its defects and application method. The diffusion coefficient of Ca and Si from the melt into the coat is function of the ionic radius and RE material polarising power, where Yb and Lu-silicates had the lowest values compared to Er-silicates. On the other hand, the corrosion rate is function of coating defects as total porosity, pore diameter and melt viscosity. In that area, the performance of dip coating is lower than other established methods as APS, which results in dense coatings. The formation of Ca–RE–Si phase occurred by Ca^{2+} substituting RE^{3+} on their lattice sites. The process is governed by the vacancy formation and defect movement until no newer defects can be formed. Thus, it is concluded that increasing the amount of CaO and SiO_2 into the RE_2O_3 lattice may decrease vacancy formation and thus the diffusion of Ca^{2+} and Si^{2+} into the coat. Thus in turn, can inhibit melt infiltration and increase the durability of the coat in sand environments. As a result, Ca–Yb apatite coat is potentially proposed as a CMAS-resistant coating that can inhibit melt infiltration through its structure.

The final chapter examined how RBSBC ceramic responded to bending stresses under normal temperature using a DIC setup equipped with a high-speed camera to record the crack growth till the fracture point; capturing 366 frames over 2.66 ms. The fractography showed that the presence of B_4C grains offered a tortuous path for crack propagation, which aids in increased toughness, while the Si pool between the main α-SiC grains has the double effect of weakening the overall fracture toughness of the material, while inducing compressive residual stresses in the structure. However, the overall effect of high-silicon content is negative. The crack-resistance analysis at the crack-tip was determined using experimental $K_{I,ext}$ and J_{ext}, and quasistatic $K_{I,a}$ and J_a. The experimental determination of the stress intensity at the crack tip relies on measuring the crack-tip displacement from the DIC images, which allows the construction of a crack-resistance plot based on actual conditions. The analysis showed a steep curve for the stress intensity and the strain energy, indicating low crack resistance typical of brittle ceramics. However, the slope of the resistance curve was higher than that of standard SiC ceramics, suggesting greater crack resistance in SiC–B_4C ceramic.

8 FUTURE WORK

8.1 INTRODUCTION

Some topics could not be investigated either due to time constraint or being outside the scope of the current research focus. This section highlights the areas that would be of significant value in the evaluation of EBCs that are processed using dip coating. These include examining the dip coating processes and mechanical response of the coating architecture.

8.2 DIP COATING

In this study, the dip coating of RE-silicates was performed manually. This resulted in variations in the coating thickness. Although dip coating is a promising application method, studies on dip coating as an application technique for RE-silicate EBCs have not been conducted before. For this reason, our group bought a Nadetech ND-DC 150 precision dip coater (Nadetech Innovations, Spain) (Figure 8.1a and b). The sample is placed the sample in the moving arm of the dip coater and dipped in a beaker filled with the RE-silicate slurry. The dip coater facilitates the analysis of the effects of coating properties, such as compositions, viscosity, and wettability, on the thickness and microstructure of the coat, which will allow the formulation of an optimum Yb-silicate slurry for dip coating. It will also enable the investigation of the influence of dip-coating parameters as immersion speed, immersion time, withdrawal speed, stirring speed, and number of dip-coating cycles, on the thickness and properties of the finalised coat. Additionally, a cost study can be performed to determine the cost of dip coating a batch of RE-silicate samples. Based on this study, the outcomes of dip-coating can be compared with those of thermal spraying and vapour deposition, particularly APS and EB-PVD. The objectives of dip-coating include but not limited to coatability with SiC substrate and no spallation, high density, low defects such as pores and vertical cracks, high thickness coat up to 1000 μm, ability to uniformly coat intricate parts, low cost, and short processing time. Furthermore, dip coating can be performed to form a thick two-layered Yb_2SiO_5–$Yb_2Si_2O_7$/Yb_2O_3 architecture, where the corrosion rates of dip-coated Yb_2SiO_5 and $Yb_2Si_2O_7$ topcoats can be compared with that obtained for the Yb_2O_3 topcoat in the current research to determine the best CMAS-resistant topcoat.

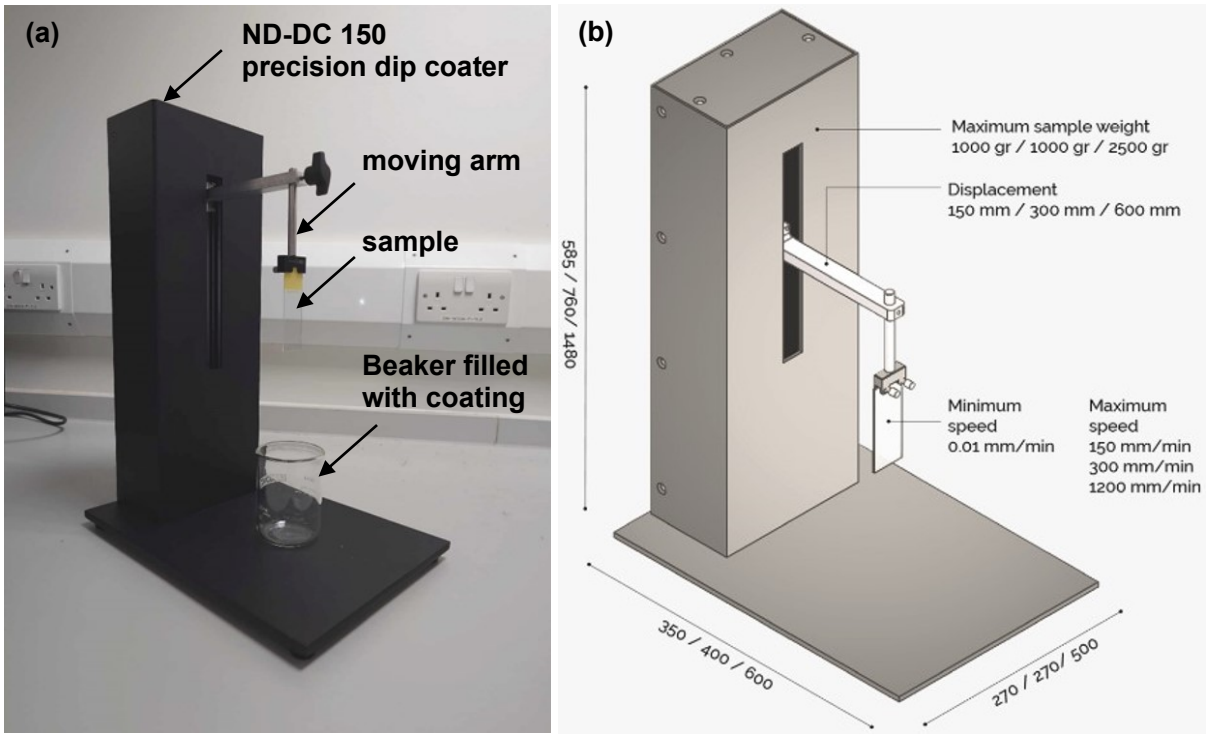


Figure 8.1 (a) Nadetech precision dip coater (b) dashes between specification numbers above show the ND-DC 150 / ND-DC 300 / ND-DC 600 dip coaters [455].

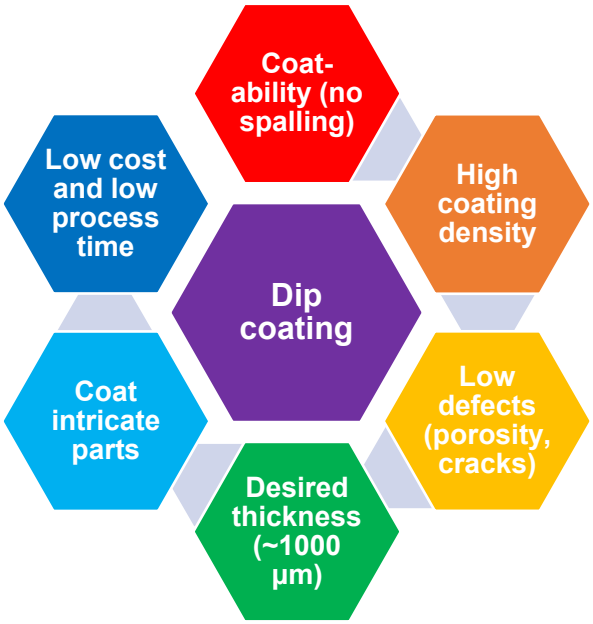


Figure 8.2 Main objectives of dip coating method to produce corrosion-resistant EBCs.

8.3 DIC ON Yb_2SiO_5–Yb_2O_3/SiC WAFERS

The coating thickness (~190 μm) is very small compared to substrate thickness (10 mm), which presents a challenge to experimentally test the mechanical behaviour of the coating because it would be significantly affected by that of the substrate. Fracture behaviour of the coating can be examined using an ultra-high-speed camera (**i.e.** Photron or Phantom) equipped with a high-magnification telescopic lens that can focus on the coating and coat/substrate interface to monitor the fracture behaviour of coating/substrate system. This solution is expensive, and the equipment is difficult to acquire. Another option would be to combine DIC with in-situ mechanical bending in a cheaper setup. The group bought Si wafers with 5 μm SiO_2 layers on the top (Siegert Wafer GmbH, Germany) to have the exact thickness of the oxide layer formed by the RBSBC (refer to Chapter 4) (Figure 8.3a). The Si wafers were cut, using a dicing saw (Inseto, UK) to the same dimensions as those of three-point bending DIC samples (45 mm length × 4 mm width) but with different thicknesses of 675 ± 20 μm. The Si wafers were coated with Yb-silicate (Figure 8.3b). Coated wafers are shown in Figure 8.3b. Coating composition and thickness (~190 μm) were the same as those explained earlier in Chapter 5. The coating-to-substrate thickness ratio was 1:3.5, compared to 1:52.6 for the EBC–RBSBC system. Thus, the contribution of the substrate to the mechanical testing results decreased, allowing the testing procedure to focus on the EBC layer rather than the substrate. Si was chosen as the wafer material instead of SiC owing to its higher ductility because if the substrate fracture toughness is lower than that of the coating, the entire substrate-EBC material will break under bending, which will be reflective of the mechanical properties of the coating. Testing is required to determine the K_{IC} of Yb-silicate coating and compare it with RBSBC (3.2 MPa $m^{1/2}$) and Si (~1–1.5 MPa $m^{1/2}$ [456, 457]). Afterwards, the coated wafers were placed in an in-situ micro-tensile bending stage for SEM (Deben MT300, UK) (Figure 8.3b). The coated Si wafer appear shorter than the uncoated one on its left due to breakage during coating, though their intended length is 40 mm long. Coated Si wafer was placed at the Deben tensile stage with a maximum load of 300 N, where four-point bending test was conducted at a loading rate of 0.1 mm min^{-1} in order to test the set-up. A DIC setup equipped with an ultra-high-speed camera is to be focused on the scanning electron microscope (SEM) monitor. The use of a tensile stage inside the SEM also allows high-resolution images for accurate COD. If possible, the crack and its propagation path throughout the loading profile can be imaged at the same location to ensure consistent COD measurements. Therefore, the mechanical failure and crack resistance of the

coating can be appropriately investigated. Additionally, the CMAS effect on the mechanical response of the coating can be examined by placing the CMAS powder on the coated wafer and corroding it in a furnace at 1350 °C for 1–48 h. Afterwards, the DIC in-situ setup can compare the results with the failure of the coating-substrate alone. Thermomechanical analysis of the coating layers, such as delamination and energy release rate, can be calculated via LayerSlayer based on the mechanics of thin films [458-460].

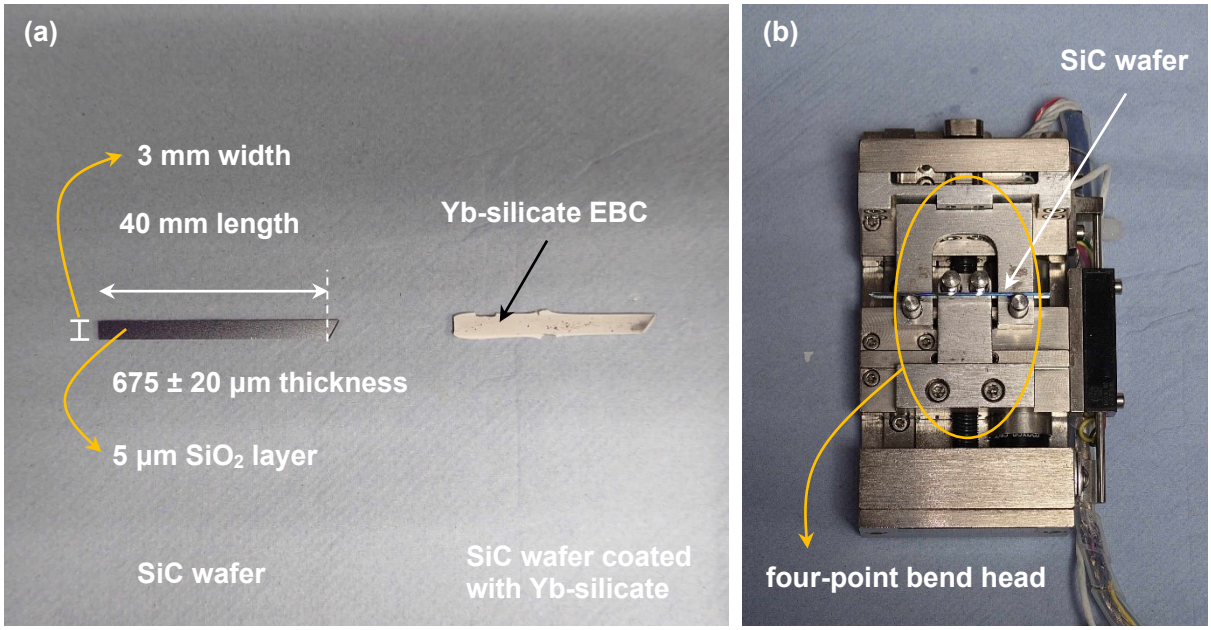


Figure 8.3 (a) Uncoated SiC wafer on the left, and SiC wafer coated with Yb-silicate on the right (part of the wafer broke; therefore, it is shorter) (b) Deben four-point bend stage.

Another option worth studying is spraying SiO_2 on the RBSBC substrate at a thickness of 1000 µm, and then preparing the Yb-monosilicate on the thick oxide layer according to the method mentioned in this study. This will produce a single-layer-thick dip-coated Yb_2SiO_5, which may demonstrate the advantage of decreasing the possibility of thermally induced stresses and stresses arising from various corrosion phases formed due to the reaction of CMAS melt with different layers of the coat. The aim is to produce a corrosion-resistant single-layer dense coat that lead to a more corrosion-resistant reaction phase upon reacting with the CMAS melt. Thus, the coating can initially act as a preventive coat, hindering melt infiltration, and then become reactive by hindering further reactions with the CMAS melt. However, further mechanical studies are required to ensure that the coating retains its mechanical integrity.

REFERENCES

[1] N. S. Jacobson, "Silica Activity Measurements in the Y_2O_3–SiO_2 System and Applications to Modeling of Coating Volatility," *Journal of the American Ceramic Society,* vol. 97, no. 6, pp. 1959-1965, 2014.

[2] G. C. C. Costa and N. S. Jacobson, "Mass spectrometric measurements of the silica activity in the Yb2O3-SiO2 system and implications to assess the degradation of silicate-based coatings in combustion environments," *Journal of the European Ceramic Society,* vol. 35, pp. 4259-4267, 2015.

[3] N. A. Nasiri, N. Patra, D. Horlait, D. D. Jayaseelan, and W. E. Lee, "Thermal Properties of Rare-Earth Monosilicates for EBC on Si-Based Ceramic Composites," *Journal of American Ceramic Society,* vol. 99, no. 2, 2016.

[4] K. N. Lee, D. S. Fox, and N. P. Bansal, "Rare earth silicate environmental barrier coatings for SiC/SiC composites and Si3N4 ceramics," *Journal of the European Ceramic Society,* vol. 25, no. 10, pp. 1705-1715, 2005, doi: 10.1016/j.jeurceramsoc.2004.12.013.

[5] A. J. Fernández-Carrión, M. Allix, and A. I. Becerro, "Thermal Expansion of Rare-Earth Pyrosilicates," *Journal of the American Ceramic Society,* vol. 96, no. 7, pp. 2298-2305, 2013.

[6] Y. Gao, H. Shen, J. Cao, D. Li, and D. Yang, "Control of the formation and luminescent properties of polymorphic erbium silicates on silicon," *Optical Material Express,* vol. 9, no. 4, pp. 1716-1727, 2019.

[7] D. Tejero-Martin, C. Bennett, and T. Hussain, "A review on environmental barrier coatings: History, current state of the art and future developments," *Journal of the European Ceramic Society,* vol. 41, pp. 1747-1768, 2021.

[8] N. P. Bansal and S. R. Choi, "Properties of CMAS glass from desert sand," *Ceramics International,* vol. 41, pp. 3901-3909, 2015.

[9] K. N. Lee, "Environmental Barrier Coatings with Reduced Bond Coat Oxidation Rates Via Chemical Modifications for Long Life," *Journal of American Ceramic Society,* vol. 102, no. 3, pp. 1507–1521, 2019.

[10] B. T. Richards, K. A. Young, F. d. Franqueville, S. Sehr, M. R. Begley, and H. N. G. Wadley, "Response of Ytterbium Disilicate-Silicon Environmental Barrier Coatings to Thermal Cycling in Water Vapor," *Acta Materialia,* vol. 106, pp. 1–14, 2016.

[11] T. A. S. o. M. E. (ASME), "Basic Gas Turbine Engine Technology," ed. USA, 2023.

[12] M. Suzuki, M. Shahien, K. Shinoda, and J. Akedo, "The Current Status of Environmental Barrier Coatings and Future Direction of Thermal Spray Process," *Materials Transactions,* vol. 63, no. 8, pp. 1101-1111, 2022, doi: http://doi:10.2320/matertrans.MT-T2021003.

[13] D. Zhu, "Aerospace Ceramic Materials: Thermal, Environmental Barrier Coatings and SiC/SiC Ceramic Matrix Composites For Turbine Engine Applications," NASA, Ohio, USA, NASA/TM—2018-219884, 2018.

[14] S. Subha, N. Benny, and D. Singh, "Thermo-mechanical behavior of SiC-based composites for gas turbine engines," *MaterialsToday:Proceedings,* vol. 68, pp. 2301–2309, 2022, doi: https://doi.org/10.1016/j.matpr.2022.08.554.

[15] N. A. Nasiri, N. Patra, M. Pezoldt, J. Colasc, and W. E. Lee, "Investigation of a single-layer EBC deposited on SiC/SiC CMCs: Processing and corrosion behaviour in high-temperature steam," *Journal of the European Ceramic Society,* vol. 39, p. 9, 2019.

[16] T. Wang, Y. Zhang, P. Karandikar, and C. Ni, "Structural evolution in reaction-bonded silicon carbide and boron carbide composites (RBSBC)," *Ceramics International,* vol. 44, no. 2, pp. 2593-2598, 2018, doi: 10.1016/j.ceramint.2017.10.131.

[17] Y. Zhou, D. Ni, Y. Kan, P. He, S. Dong, and X. Zhang, "Microstructure and mechanical properties of reaction bonded B4C-SiC composites: The effect of polycarbosilane addition," *Ceramics International,* vol. 43, no. 8, pp. 5887-5895, 2017, doi: 10.1016/j.ceramint.2017.01.066.

[18] S. M. Salamone, M. K. Aghajanian, S. E. Horner, and J. Q. Zheng, "Effect of SiC:B4C ratio on the properties of Si-Cu/SiC/B4C composites," *Ceramic Engineering and Science Proceedings,* vol. 35, no. 2, pp. 83-90, 2014.

[19] J. Pete Meltzer. "Ceramic Matrix Composite seals proving reliable for jet engine nozzles." Wright-Patterson Air Force Base, AFRL Materials & Manufacturing Directorate. https://www.wpafb.af.mil/News/Article-Display/Article/400832/ceramic-matrix-composite-seals-proving-reliable-for-jet-engine-nozzles/ (accessed 2023).

[20] E. P. Bouillon *et al.*, "Characterization and Nozzle Test Experience of a Self Sealing Ceramic Matrix Composite for Gas Turbine Applications," in *Proceedings of ASME Turbo Expo 2002*, Amsterdam, The Netherlands, 2002: American Society of Mechanical Engineers (ASME), pp. 1-8.

[21] Y. Uesaka. "SiC fibers find their way into aircraft engines." Nikkei Asia. https://asia.nikkei.com/Business/SiC-fibers-find-their-way-into-aircraft-engines (accessed 2023).

[22] J. Steibel, "Ceramic matrix composites taking flight at GE Aviation " *American Ceramic Society Bulletin,* vol. 98, no. 3, pp. 30-33, 2019.

[23] D. Zhu and B. Harder, "Development Status and Performance Comparisons of Environmental Barrier Coating Systems for SiC/SiC Ceramic Matrix Composites," in *40th International Conference and Expo on Advanced Ceramics and Composites*, Florida, 2016: NASA John H. Glenn Research Center, pp. 1-25.

[24] N. A. Nasiri, N. Patra, D. Horlait, D. D. Jayaseelan, and W. E. Lee, "Thermal Properties of Rare-Earth Monosilicates for EBC on Si-Based Ceramic Composites," *Journal of American Ceramic Society,* vol. 99, no. 2, p. 8, 2016.

[25] S. E. L. Nasrin Al Nasiri, Adam Lee Chamberlain, William Edward Lee "Slurry-Based Reaction Bonded Environmental Barrier Coatings," United States, 2017.

[26] M. Fraga and R. Pessoa, "Progresses in Synthesis and Application of SiC Films: From CVD to ALD and from MEMS to NEMS," *Micromachines (Basel),* vol. 11, no. 9, pp. 799-822, 2020.

[27] A. Materials. "Sintered Silicon Carbide (SiC) Properties and Applications." https://www.azom.com/article.aspx?ArticleID=15 (accessed 2023).

[28] M. K. Aghajanian, B. N. Morgan, J. R. Singh, J. Mears, and R. A.Wolffe, "A New Family of Reaction-Bonded Ceramics for Armour Applications," in *Ceramic Armor Materials by Design*, United States, 2012, vol. 134: Ceramic Armor Materials by Design.

[29] A. Materials. "Reaction Bonded Silicon Carbide (RBSC)." https://www.azom.com/article.aspx?ArticleID=147 (accessed 2023).

[30] T. F. P. J. N. Ness, "Microstructural evolution in reaction-bonded silicon carbide," *Journal of Materials Science,* vol. 21, p. 20, 1986.

[31] S. G. A. R. o. I. Theses. "Chapter 2: Processing Methods of Silicon Carbide Composites." Information and Library Service Network https://shodhganga.inflibnet.ac.in/bitstream/10603/75128/10/10_chapter%202.pdf (accessed 28 Januaryt, 202).

[32] P. G. Karandikar and M. J. Aghajanian, "Microwave Assisted (Mass) Processing of Metal-Ceramic and Reaction-Bonded Composites," *Ceramic Engineering and Science Proceedings,* vol. 27, no. 2, pp. 435-446, 2007.

[33] R. S. Evans, D. L. Bourell, J. J. Beaman, and M. I. Campbell, "Reaction Bonded Silicon Carbide: SFF, Process Refinement and Applications," in *Proceedings of 14th Solid Freeform Fabrication Symposium*, 2003, pp. 414-422.

[34] L. M. Jérôme Magnant, René Pailler, Jean-Christophe Ichard, Alain Guette, Francis Rebillat, Eric Philippe, "Carbon fiber /reaction-bonded carbide matrix for composite materials -Manufacture and characterization," *journal of European Ceramic Society,* vol. 32, no. 16, p. 8, 2012.

[35] J. Wang, A. McDannald, P. Karandikar, and M. Aghajanian, "Fabrication of reaction bonded TiB2/Si/SiC composites for thermal applications," *International Journal of Ceramic Engineering & Science,* vol. 2, pp. 264-270, 2020.

[36] T. Wang, C. Ni, and P. Karandikar, "Microstructural Characteristics of Reaction-Bonded B4C/SiC Composite," in *Characterization of Minerals, Metals, and Materials*, 2016, pp. 279-286.

[37] S. Hayun, N. Frage, and M. P. Dariel, "The morphology of ceramic phases in BxC–SiC–Si infiltrated composites," *Journal of Solid State Chemistry,* vol. 179, no. 9, pp. 2875-2879, 2006, doi: 10.1016/j.jssc.2006.01.031.

[38] R. N. S. Hong Zhou, "Kinetics Model for the Growth of Silicon Carbide by the Reaction of Liquid Silicon with Carbon," *Journal of American Ceramic Society,* vol. 78, no. 9, p. 6, 1995.

[39] W. Zhang, "Recent progress in B_4C–SiC composite ceramics: processing, microstructure, and mechanical properties," *Materials Advances,* vol. 4, pp. 3140-3191, 2023, doi: http://10.1039/d3ma00143a.

[40] C. Zhang *et al.*, "Coarsening of boron carbide grains during the infiltration of porous boron carbide preforms by molten silicon," *Ceramics International,* vol. 42, no. 16, pp. 18681-18691, 2016, doi: 10.1016/j.ceramint.2016.09.006.

[41] I. Solodkyi *et al.*, "Addition of carbon fibers into B4C infiltrated with molten silicon," *Ceramics International,* vol. 45, no. 1, pp. 168-174, 2019, doi: 10.1016/j.ceramint.2018.09.148.

[42] M. M. Balakrishnarajan, P. D. Pancharatna, and R. Hoffmann, "Structure and Bonding in boron carbide: the invincibility of imperfections," *New Journal of Chemistry,* vol. 31, no. 4, pp. 473-485, 2007.

[43] D. Gosset and M. Colin, "Boron carbides of various compositions: An improved method for X-rays characterisation " *Journal of Nuclear Materials,* vol. 183, no. 3, pp. 161-173, 1991.

[44] S. Suyama, T. Kameda, and Y. Itoh, "Development of high-strength reaction-sintered silicon carbide," *Diamond and Related Materials,* vol. 12, no. 3-7, pp. 1201-1204, 2003, doi: 10.1016/s0925-9635(03)00066-9.

[45] C. S. A. Sayano, S. Suyama, Y. Itoh, S. Nakagawa, "Development of a reaction-sintered silicon carbide matrix composite," *Journal of Nuclear Materials,* vol. 271&272, p. 4, 1999.

[46] W. J. Miller, "High Temperature Oxidation of Silicon Carbide," Master of Science, Faculty of the School of Engineering, Air Force Institute of Technology, Wright-Paterson Air Force Base, Ohio, 1972.

[47] L. U. J. T. Ogbuji and E. J. Opila, "A Comparison of the Oxidation Kinetics of SiC and Si3N4," *Journal of Electrochemical Society,* vol. 142, no. 3, pp. 925-930, 1995.

[48] B. E. Deal and A. S. Grove, "General Relationship for the Thermal Oxidation of Silicon," *Journal of Applied Physics,* vol. 36, no. 12, pp. 3770-3778, 1965, doi: 10.1063/1.1713945.

[49] C. Hollauer, "Modeling of Thermal Oxidation and Stress Effects," PhD, Faculty of Electrical Engineering and Information Technology, Technischen Universität Wien, Wien, Austria, 2007. [Online]. Available: https://www.iue.tuwien.ac.at/phd/hollauer/node12.html

[50] W. W. Pultz and W. Hertl, "SiO2+SiC Reaction at Elevated Temperatures. Part 1.—Kinetics and Mechanism," Research and Development Laboratories, Corning Glass Works, New York, United States, 1966.

[51] C. Wagner, "Passivity during the Oxidation of Silicon at Elevated Temperatures," *Journal of Applied Physics,* vol. 29, pp. 1295-1297, 1958.

[52] N. A. Nasiri, N. Patra, N. Ni, D. D. Jayaseelan, and W. E. Lee, "Oxidation behaviour of SiC/SiC ceramic matrix composites in air," *Journal of the European Ceramic Society,* vol. 36, no. 14, pp. 3293-3302, 2016, doi: 10.1016/j.jeurceramsoc.2016.05.051.

[53] T. Narushima, T. Goto, and T. Hirai, "High-Temperature Passive Oxidation of Chemically Vapor Deposited Silicon Carbide," *Journal American Ceramic Society,* vol. 72, no. 8, pp. 1386-1390, 1989.

[54] S. Alekseev *et al.*, "Size and Surface Chemistry Tuning of Silicon Carbide Nanoparticles," *Langmuir,* vol. 33, pp. 13561-13571, 2017.

[55] N. S. Jacobson, D. S. Fox, and E. J. Opila, "High temperature oxidation of ceramic matrix composites," *Pure and Applied Chemistry,* vol. 7, no. 2, pp. 493-500, 1998.

[56] R. Kassem and N. A. Nasiri, "A comprehensive study on the mechanical properties of Yb2SiO5 as a potential environmental barrier coating," *Surface & Coatings Technology,* vol. 426, 2021.

[57] E. N. Dayi and N. Al Nasiri, "Diffusion study of rare-earth oxides into silica layer for environmental barrier coating applications," *Journal of the European Ceramic Society,* vol. 39, no. 14, pp. 4216-4222, 2019.

[58] B.-K. Jang *et al.*, "Corrosion behavior of volcanic ash and calcium magnesium aluminosilicate on Yb_2SiO_5 environmental barrier coatings," *Journal of the Ceramic Society of Japan,* vol. 125, no. 4, pp. 326-332, 2017.

[59] X. Zhang *et al.*, "CMAS corrosion and thermal cycle of Al-modified PS-PVD environmental barrier coating," *Ceramics International,* vol. 44, pp. 15959–15964, 2018, doi: https://doi.org/10.1016/j.ceramint.2018.06.019.

[60] E. J. Opila and R. E. H. Jr., "Paralinear Oxidation of CVD SiC in Water Vapor," *Journal of the American Ceramic Society,* vol. 80, no. 1, pp. 197-205, 1997.

[61] M. Steinbrueck, M. Grosse, U. Stegmaier, J. Braun, and C. Lorrette, "Oxidation of Silicon Carbide Composites for Nuclear Applications at Very High Temperatures in Steam," *Coatings,* vol. 12, pp. 875-894, 2022.

[62] E. J. Opila, "Variation of the oxidation rate of silicon carbide with water-vapor pressure," *Journal of American Ceramic Society,* vol. 82, pp. 625-636, 1999.

[63] N. S. Jacobson, J. Smialek, D. S. Fox, and E. Opila, "Durability of Silica-Protected Ceramics in Combustion Atmospheres," NASA Lewis Research Center, 1995.

[64] C. E. Ramberg and W. L. Worrell, "Oxygen Transport in Silica at High Temperatures: Implications of Oxidation Kinetics," *Journal American Ceramic Society,* vol. 84, no. 11, pp. 2607-2616, 2001.

[65] M. A. Lamkin, F. L. Riley, and R. J. Fordham, "Oxygen Mobility in Silicon Dioxide and Silicate Glasses: a Review," *Journal of the European Ceramic Society,* vol. 10, pp. 347-367, 1992.

[66] E. O. E. Wuchina, M. Opeka, W. Fahrenholtz, I. Talmy, "UHTCs: Ultra-High Temperature Ceramic Materials for Extreme Environment Applications," The Electrochemical Society, 2007.

[67] D.-H. Riu, R. Choi, H.-E. Kim, and E.-S. Kang, "Oxidation behaviour and strength of B4C-30 wt% SiC composite materials," *Journal of Materials Science,* vol. 30, pp. 3897-3902, 1995.

[68] Y. G. Gogotsi, V. P. Yaroshenko, and F. Porz, "Oxidation resistance of boron carbide-based ceramics," *Journal of Materials Science Letters,* vol. 11, pp. 308-310, 1992.

[69] T. N. Nazarchuk and L. N. Mekhanoshina, "The oxidation of Boron Carbide," *Poroshkovaya Metallurgiya,* vol. 2, no. 20, pp. 46-50, 1964.

[70] T. Narushima, T. Goto, M. Maruyama, H. Arashi, and Y. Iguchi, "Oxidation of Boron Carbide-Silicon Carbide composite at 1073 to 1773 K," vol. 44, no. 3, pp. 401-406, 2003.

[71] M. Xu, L. Guo, and H. Wang, "Crack Evolution and Oxidation Failure Mechanism of a SiC-Ceramic Coating Reactively Sintered on Carbon/Carbon Composites," *Materials,* vol. 14, pp. 7780-7791, 2021, doi: https://doi.org/10.3390/ma14247780.

[72] H. Hatta, T. Sohtome, Y. Sawada, and A. Shida, "High temperature crack sealant based on SiO_2-B_2O_3 for SiC coating on carbon–carbon composites," *Advanced Composite Materials,* vol. 12, no. 2-3, pp. 93-106, 2003.

[73] L. U. J. T. Ogbuji and M. Singh, "High-temperature oxidation behavior of reaction-formed silicon carbide ceramics," *Journal of Materials Research,* vol. 10, no. 12, pp. 3232-3240, 2011, doi: 10.1557/jmr.1995.3232.

[74] N. P. Padture, M. Gell, and E. H. Jordan, "Thermal Barrier Coatings for Gas-Turbine Engine Applications," *Science,* vol. 296, no. 5566, pp. 280-284, 2022.

[75] K. N. Le, R. A. Miller, and N. S. Jacobson, "New generation of plasma-sprayed mullite coatings on silicon carbide," *Journal of American Ceramic Society,* vol. 78, pp. 705-710, 1995.

[76] H. Zhao, B. T. Richards, C. G. Levi, and H. N. G. Wadley, "Molten silicate reactions with plasma sprayed ytterbium silicate coatings," *Surface and Coatings Technology,* vol. 288, pp. 151-162, 2016, doi: 10.1016/j.surfcoat.2015.12.053.

[77] D. Zhu *et al.*, "Advanced Environmental Barrier Coating Development for SiC-SiC Ceramic Matrix Composite Components," in *12th Pacific Rim Conference on Ceramic and Glass Technology (PACRIM 12)*, Waikoloa, Hawaii, 2017: NASA John H. Glenn Research Center, p. 28.

[78] L. Sun *et al.*, "High temperature corrosion of $(Er_{0.25}Tm_{0.25}Yb_{0.25}Lu_{0.25})_2Si_2O_7$ environmental barrier coating material subjected to water vapor and molten calcium–magnesium–aluminosilicate (CMAS)," *Corrosion Science,* vol. 175, pp. 1-9, 2020.

[79] B. T. Richards, "Ytterbium Silicate Environmental Barrier Coatings," Doctor of Philosophy, School of Engineering and Applied Sciences, University of Virginia, USA, 2015.

[80] B. T. Richards and H. N. G. Wadley, "Plasma spray deposition of tri-layer environmental barrier coatings," *Journal of the European Ceramic Society,* vol. 34, no. 12, pp. 3069-3083, 2014, doi: https://doi.org/10.1016/j.jeurceramsoc.2014.04.027.

[81] K. N. Lee, "Key Durability Issues With Mullite-Based Environmental Barrier Coatings for Si-Based Ceramics," *Journal of Engineering for Gas Turbines and Power,* vol. 122, pp. 632-636, 2000.

[82] K. N. Lee *et al.*, "Upper Temperature Limit of Environmental Barrier Coatings Based on Mullite and BSAS," *Journal of American Ceramic Society,* vol. 86, no. 8, pp. 1299-1306, 2003.

[83] V. L. Wiesner, B. J. Harder, A. Garg, and N. P. Bansal, "Molten calcium-magnesium-aluminosilicate interactions with ytterbium disilicate environmental barrier coating," *Journal of Materials Research,* vol. 35, no. 17, pp. 2346-2357, 2020.

[84] R. Vaßen, E. Bakan, C. Gatzen, Seongwong Kim, D. E. Mack, and O. Guillon, "Environmental Barrier Coatings Made by Different Thermal Spray Technologies," *Coatings,* vol. 9, no. 12, pp. 784-806, 2019, doi: http://doi:10.3390/coatings9120784.

[85] C. V. Cojocaru, D. Lévesque, C. Moreau, and R. S. Lima, "Performance of thermally sprayed Si/mullite/BSAS environmental barrier coatings exposed to thermal cycling in water vapor environment," *Surface and Coatings Technology,* vol. 216, pp. 215-223, 2013, doi: https://doi.org/10.1016/j.surfcoat.2012.11.043.

[86] E. Bakan, D. Marcano, D. Zhou, Y. J. Sohn, G. Mauer, and R. Vaßen, "$Yb_2Si_2O_7$ Environmental Barrier Coatings Deposited by Various Thermal Spray Techniques: A Preliminary Comparative Study," *Journal of Thermal Spray Technology,* vol. 26, pp. 1011–1024, 2017.

[87] S. Tsukada, S. Kuroda, M. Nishijima, H. Araki, A. Yumoto, and M. Watanabe, "Effects of amorphous phase on hot corrosion behavior of plasma-sprayed LaMgAl11O19 coating," *Surface and Coatings Technology,* vol. 363, pp. 95-105, 2019, doi: https://doi.org/10.1016/j.surfcoat.2019.01.097.

[88] K. N. Lee, D. Zhu, and R. S. Lima, "Perspectives on Environmental Barrier Coatings (EBCs) Manufactured via Air Plasma Spray (APS) on Ceramic Matrix Composites (CMCs): A Tutorial Paper," *Journal of Thermal Spray Technology,* vol. 30, pp. 40–58, 2021, doi: https://doi.org/10.1007/s11666-021-01168-0.

[89] P. Fauchais, V. Rat, C. Delbos, J. F. Coudert, T. Chartier, and L. Bianchi, "Understanding of suspension DC plasma spraying of finely structured coatings for SOFC," *IEEE Transactions on Plasma Science,* vol. 33, no. 2, pp. 920-930, 2005, doi: http://10.1109/TPS.2005.845094.

[90] N. Curry, K. VanEvery, T. Snyder, N. Markocsan, and N. Markocsan, "Thermal Conductivity Analysis and Lifetime Testing of Suspension Plasma-Sprayed Thermal Barrier Coatings," *Coatings,* vol. 4, no. 3, pp. 630-650, 2014, doi: https://doi.org/10.3390/coatings4030630.

[91] J. Xu, V. K. Sarin, S. Dixit, and S. N. Basu, "Stability of interfaces in hybrid EBC/TBC coatings for Si-based ceramics in corrosive environments," *International Journal of Refractory Metals and Hard Materials,* vol. 49, pp. 339-349, 2015, doi: https://doi.org/10.1016/j.ijrmhm.2014.08.013.

[92] A. Ito, J. Endo, T. Kimura, and T. Goto, "High-speed deposition of Y–Si–O films by laser chemical vapor deposition using Nd:YAG laser," *Surface and Coatings Technology,* vol. 204, no. 23, pp. 3846-3850, 2010, doi: https://doi.org/10.1016/j.surfcoat.2010.04.066.

[93] R. Naraparaju, M. Hüttermann, U. Schulz, and P. Mechnich, "Tailoring the EB-PVD columnar microstructure to mitigate the infiltration of CMAS in 7YSZ thermal barrier coatings," *Journal of the European Ceramic Society,* vol. 37, pp. 261-270, 2017, doi: http://dx.doi.org/10.1016/j.jeurceramsoc.2016.07.027.

[94] C. Mikulla, L. Steinberg, P. Niemeyer, U. Schulz, and R. Naraparaju, "Microstructure Refinement of EB-PVD Gadolinium Zirconate Thermal Barrier Coatings to Improve Their CMAS Resistance," *Coatings,* vol. 13, no. 905, pp. 2-23, 2023, doi: http://10.3390/coatings13050905.

[95] M. R. Kabir, A. K. Sirigiri, R. Naraparaju, and U. Schulz, "Flow Kinetics of Molten Silicates through Thermal Barrier Coating: A Numerical Study," *Coatings,* vol. 9, no. 5, pp. 332-356, 2019, doi: https://doi.org/10.3390/coatings9050332.

[96] T. Yokoi *et al.*, "Preparation of a dense ytterbium disilicate layer via dual electron beam physical vapor deposition at high temperature," *Materials Letters,* vol. 193, pp. 176-178, 2017, doi: https://doi.org/10.1016/j.matlet.2017.01.085.

[97] Z. Gao *et al.*, "Strain tolerance evolution of EB-PVD TBCs after thermal exposure or CMAS attack," *Journal of the European Ceramic Society,* vol. 44, no. 1, 2024, doi: https://doi.org/10.1016/j.jeurceramsoc.2023.08.047.

[98] F. Shao *et al.*, "Dense yttria-stabilized zirconia coatings fabricated by plasma spray-physical vapor deposition," *Ceramics International,* vol. 43, no. 2, pp. 2305-2313, 2017, doi: https://doi.org/10.1016/j.ceramint.2016.11.014.

[99] B. Zhang, W. Song, and H. Guo, "Wetting, infiltration and interaction behavior of CMAS towards columnar YSZ coatings deposited by plasma spray physical vapor," *Journal of the European Ceramic Society,* vol. 38, no. 10, pp. 3564-3572, 2018, doi: https://doi.org/10.1016/j.jeurceramsoc.2018.04.013.

[100] B. J. Harder and D. Zhu, "Plasma Spray-Physical Vapor Deposition (PS-PVD) of Ceramics for Protective Coatings " in *Ceramic Engineering and Science Proceedings*, 2011, vol. 32, no. 3, pp. 73-84, doi: http://10.1002/9781118095232.ch7.

[101] Sulzer. "Atmospheric plasma spraying APS." https://www.sulzer.com/en/shared/services/atmospheric-plasma-spraying-aps# (accessed 2023).

[102] B. T. Richards, M. R. Begley, and H. N. G. Wadley, "Mechanisms of Ytterbium Monosilicate/Mullite/Silicon Coating Failure During Thermal Cycling in Water Vapor," *Journal of American Ceramic Society,* vol. 98, no. 12, pp. 4066-4075, 2015.

[103] B. Richards, S. Sehr, F. d. Franqueville, M. R. .Begley, and H. N. G. Wadley, "Fracture mechanisms of ytterbium monosilicate environmental barrier coatings during cyclic thermal exposure," *Acta Materialia,* vol. 103, pp. 448–460, 2016, doi: https://doi.org/10.1016/j.actamat.2015.10.019.

[104] E. Garcia, H. F. Garces, L. R. Turcer, H. Bale, N. P. Padture, and S. Sampath, "Crystallization behavior of air-plasma-sprayed ytterbium-silicate-based environmental barrier coatings " *Journal of the European Ceramic Society,* vol. 41, pp. 3696–3705, 2021. [Online]. Available: https://doi.org/10.1016/j.jeurceramsoc.2020.12.051.

[105] A. H. Paksoy and P. Xiao, "Review of processing and design methodologies of environmental barrier coatings for next generation gas turbine applications," *Advances in Applied Ceramics,* vol. 122:1, no. 1, pp. 36-56, 2023, doi: 10.1080/17436753.2023.2193783.

[106] S. K. Lee and J. F. Stebbins, "Extent of intermixing among framework units in silicate glasses and melts," *Geochimica et Cosmochimica Acta,* vol. 66, no. 2, pp. 303-309, 2002.

[107] E. H. Jordan, C. Jiang, and M. Gell, "The Solution Precursor Plasma Spray (SPPS) Process: A Review with Energy Considerations," *Journal of Thermal Spray Technology,* vol. 24, no. 7, 2015, doi: 10.1007/s11666-015-0272-9.

[108] E. Bakan, G. Mauer, Y. J. Sohn, D. Koch, and R. Vaßen, "Application of high velocity oxygen-fuel (HVOF) spraying to the fabrication of Yb-silicate environmental barrier coatings," *Coatings,* vol. 7, no. 55, pp. 1–12, 2017, doi: doi:10.3390/coatings7040055.

[109] A. Ito, M. Sekiyama, T. Hara, and T. Goto, "Self-oriented growth of β-Yb2Si2O7 and X1/X2-Yb2SiO5 coatings using laser chemical vapor deposition," *Ceramics*

International, vol. 46, pp. 9548–9553, 2020, doi: https://doi.org/10.1016/j.ceramint.2019.12.217.

[110] H. Guo, Y. Guo, Z. Xue, S. Gong, and H. Xu, "Overview of thermal barrier coatings for advanced gas turbine engine," in *Thermal Barrier Coatings*, H. Guo Ed., no. Metals and Surface Engineering): Woodhead Publishing, 2023, pp. 1-20.

[111] W. Chen, J. He, D. Zhou, and H. Guo, "13 - Advanced thermal and environmental barrier coatings for ceramic matrix composites," in *Thermal Barrier Coatings*, H. Guo Ed., no. Metals and Surface Engineering): Woodhead Publishing, 2023, pp. 433-465.

[112] M. Northam, "Investigation of PS-PVD and EB-PVD Thermal Barrier Coatings Over Lifetime Using Synchrotron X-ray Diffraction," Master of Science, DepartmentofMechanicalandAerospaceEngineering, University of Central Florida University of Central Florida USA, 2019.

[113] R. Vaßen, "Chapter 19 - High-Temperature Behaviour of Thermal Barrier and Bond Coatings in Oxidizing and Corrosive Atmospheres," in *Materials Surface Processing by Directed Energy Techniques*, Y. Pauleau Ed., no. European Materials Research Society Series): Elsevier Science, 2006, pp. 629-657.

[114] N. A. Nasiri, N. Patra, M. Pezold, J. Colasc, and W. E. Lee, "Investigation of a single-layer EBC deposited on SiC/SiC CMCs: Processing and corrosion behaviour in high-temperature steam," *Journal of the European Ceramic Society,* vol. 39, pp. 2703-2711, 2019.

[115] S. Ramasamy, S. N. Tewari, K. N. Lee, R. T. Bhatt, and D. S. Fox, "Slurry based multi layer environmental barrier coatings for silicon carbide and silicon nitride ceramics—I. Processing," *Surface & Coatings Technology,* vol. 205, pp. 258–265, 2010, doi: doi:10.1016/j.surfcoat.2010.06.029.

[116] S. Ramasamy, S. N. Tewari, K. N. Lee, R. T. Bhatt, and D. S. Fox, "Slurry based multi layer environmental barrier coatings for silicon carbide and silicon nitride ceramics—II. Oxidation resistance," *Surface & Coatings Technology,* vol. 205, pp. 266–270, 2010, doi: doi:10.1016/j.surfcoat.2010.07.048.

[117] K. N. Lee *et al.*, "Development of oxide-based High temperature environmental barrier coatings for ceramic matrix composites via the slurry process," *Journal of the European Ceramic Society,* vol. 41, no. 2, pp. 1639-1653, 2021, doi: https://doi.org/10.1016/j.jeurceramsoc.2020.10.012.

[118] D. Zhu, B. Harder, and D. S. Fox, "Advanced Processing and Environmental Barrier Coating System Development for SiC/SiC Ceramic Matrix Composites," in *Materials Science & Technology*, Columbus, Ohio, USA, 2011, p. 27.

[119] J. A. Deijkers, M. R. Begley, and H. N. G. Wadley, "Failure mechanisms in model thermal and environmental barrier coating systems," *Journal of the European Ceramic Society,* vol. 42, pp. 5129–5144, 2022, doi: https://doi.org/10.1016/j.jeurceramsoc.2022.04.046.

[120] F. Jiang, L. Cheng, and Y. Wang, "Hot corrosion of RE_2SiO_5 with different cation substitution under calcium–magnesium–aluminosilicate attack," *Ceramics International,* vol. 43, no. 12, pp. 9019-9023, 2017.

[121] D. L. Poerschke, D. D. Hass, S. Eustis, G. G. E. Seward, J. S. V. Sluytman, and C. G. Levi, "Stability and CMAS Resistance of Ytterbium-Silicate/Hafnate EBCs/TBC for SiC Composites," *Journal of American Ceramic Society,* vol. 98, no. 1, p. 9, 2015.

[122] N. P. Padture, "Environmental degradation of high-temperature protective coatings for ceramic-matrix composites in gas-turbine engines," *npj Materials Degradation,* vol. 3, no. 1, 2019, doi: 10.1038/s41529-019-0075-4.

[123] D. L. Poerschke, R. W. Jackson, and C. G. Levi, "Silicate Deposit Degradation of Engineered Coatings in Gas Turbines: Progress Toward Models and Materials Solutions," *Annual Review of Materials Research,* vol. 47, pp. 297–330, 2017.

[124] C. M. Toohey, "Novel Environmental Barrier Coatings for Resistance Against Degradation by Molten Glassy Deposits in the Presence of Water Vapour," Master of Science, Department of Materials Science and Engineering, Ohio State University, Ohio, United States, 2011.

[125] G. Cao *et al.*, "CMAS hot corrosion behavior of rare-earth silicates for environmental barrier coatings applications: a comprehensive review," *Heat Treatment and Surface Engineering,* vol. 3, no. 1, pp. 9-28, 2021.

[126] T. M. Letcher, J. L. Scott, and L. Peter, *Materials for a Sustainable Future*. United Kingdom: Royal Society of Chemistry, 2012.

[127] G. T. Seaborg, J. J. Katz, and L. R. Morss, *The Chemistry of the Actinide Elements*. Springer Science & Business Media, 2012.

[128] W. Song *et al.*, "Impact interaction of in-flight high-energy molten volcanic ash droplets with jet engines," *Acta Materialia,* vol. 171, pp. 119-131, 2019, doi: https://doi.org/10.1016/j.actamat.2019.04.011.

[129] A. Nieto, R. Agrawal, L. Bravo, C. Hofmeister-Mock, M. Pepi, and A. Ghoshal, "Calcia–magnesia–alumina–silicate (CMAS) attack mechanisms and roadmap towards Sandphobic thermal and environmental barrier coatings," *International Materials Reviews,* pp. 1-42, 2020.

[130] J. L. Smialek, "The Chemistry of Saudi Arabian Sand: A Deposition Problem on Helicopter Turbine Airfoils," NASA, USA, NASA TM–105234, 1991.

[131] J. L. Stokes, B. J. Harder, V. L. Wiesner, and D. E. Wolfe, "Melting and Crystallization Behavior of CaO-MgO-Al_2O_3-SiO_2 Silicates Relevant to Turbine Engine Applications," NASA USA, NASA/TM-20210020388, 2021.

[132] T. J. Grindle and J. Frank W. Burcham, "Engine Damage to a NASA DC-8-72 Airplane From a High-Altitude Encounter With a Diffuse Volcanic Ash Cloud," NASA Dryden Flight Research Center, Edwards, California, USA, NASA/TM-2003-212030, 2003.

[133] J. Kim, M. G. Dunn, A. J. Baran, D. P. Wade, and E. L. Tremba, "Deposition of Volcanic Materials in the Hot Sections of Two Gas Turbine Engines," *Journal of Engineering for Gas Turbines and Power,* vol. 115, pp. 641-651, 1993.

[134] W. Song, Y. Lavallée, K.-U. Hess, U. Kueppers, C. Cimarelli, and D. B. Dingwell, "Volcanic ash melting under conditions relevant to ash turbine interactions," *Nature Communications,* vol. 7, pp. 1-10, 2016.

[135] W. Song *et al.*, "Fusion Characteristics of Volcanic Ash Relevant to Aviation Hazards," *Geophysical Research Letters,* vol. 41, no. 7, pp. 2326–2333, 2014.

[136] N. L. Ahlborg and D. Zhu, "Calcium–magnesium–aluminosilicate (CMAS) reactions and degradation mechanisms of advanced environmental barrier coatings," *Surface and Coatings Technology,* vol. 237, pp. 79-87, 2013, doi: 10.1016/j.surfcoat.2013.08.036.

[137] C. G. Levi, J. W. Hutchinson, M.-H. Vidal-Sétif, and C. A. Johnson, "Environmental degradation of thermal barrier coatings by molten deposits," *MRS Bulletin,* vol. 37, pp. 932-941, 2012.

[138] U. Kueppers, C. Cimarelli, K.-U. Hess, J. Taddeucci, F. B. Wadsworth, and D. B. Dingwell, "The thermal stability of Eyjafjallajökull ash versus turbine ingestion test sands," *Jounral of Applied Volcanology,* vol. 3, no. 1, pp. 4-14, 2014.

[139] A. N. d. A. C. (ANAC). "Volcanic ash." Ministério de Portos e Aeroportos. https://www.gov.br/anac/en/topics/safety/aeronautical-meteorology/conditions/volcanic-ash (accessed 2024).

[140] M. R. Radcliff and K. Elkins. "Tracking Volcanic Ash With Satellites." NASA Scientific Visualization Studio: . https://svs.gsfc.nasa.gov/12221/ (accessed 2024).

[141] J. Descloitres. "Visible earth: a catalog of NASA images and animations of our home planet." NASA. https://visibleearth.nasa.gov/view.php?id=73342 (accessed 2023).

[142] H. Zhang *et al.*, "A promising molten silicate resistant material: Rare-earth oxy-apatite $RE_{9.33}(SiO_4)_6O_2$ (RE = Gd, Nd or La)," *Journal of European Ceramic Society,* vol. 40, pp. 4101-4110, 2020.

[143] Z. Tiana *et al.*, "General trend on the phase stability and corrosion resistance of rare earth monosilicates to molten calcium–magnesium–aluminosilicate at 1300 oC," *Corrosion Science,* vol. 148, p. 12, 2019.

[144] P. Ptáček, "Rare-earth Element-bearing Apatites and Oxyapatites," in *Apatites and their Synthetic Analogues - Synthesis, Structure, Properties and Applications*: Intech Open, 2016, ch. 5, pp. 245-288.

[145] P. Ptáček, "Substituents and Dopants in the Structure of Apatite," in *Apatites and their Synthetic Analogues - Synthesis, Structure, Properties and Applications*: Intech Open, 2016, ch. 6, pp. 289-334.

[146] E. Valsami-Jones, *Phosphorus in Environmental Technologies: Principles and Applications* London: IWA Publishing, 2004.

[147] J. L. Stokes, B. J. Harder, V. L. Wiesner, and D. E. Wolfe, "High-Temperature thermochemical interactions of molten silicates with Yb2Si2O7 and Y2Si2O7 environmental barrier coating materials," *Journal of the European Ceramic Society,* vol. 31, pp. 5059-5067, 2019.

[148] J. L. Stokes, B. J. Harder, V. L. Wiesner, and D. E. Wolfe, "Effects of crystal structure and cation size on molten silicate reactivity with environmental barrier coating materials," *Journal of American Ceramic Society,* vol. 103, pp. 622-634, 2020.

[149] K. M. Grant, S. Krämer, G. G. E. Seward, and C. G. Levi, "Calcium-Magnesium Alumino-Silicate Interaction with Yttrium Monosilicate Environmental Barrier Coatings," *Journal of the American Ceramic Society,* vol. 93, no. 10, pp. 3504-3511, 2010.

[150] F. Stolzenburg, M. T. Johnson, K. N. Lee, N. S. Jacobson, and K. T. Faber, "The interaction of calcium–magnesium–aluminosilicate with ytterbium silicate

environmental barrier materials," *Surface and Coatings Technology,* vol. 284, pp. 44-50, 2015, doi: 10.1016/j.surfcoat.2015.08.069.

[151] L. R. Turcer, A. R. Krause, H. F. Garces, L. Zhang, and N. P. Padture, "Environmental-barrier coating ceramics for resistance against attack by molten calcia-magnesia-aluminosilicate (CMAS) glass: Part II, β-Yb2Si2O7 and β-Sc2Si2O7," *Journal of the European Ceramic Society,* vol. 38, no. 11, pp. 3914-3924, 2018, doi: 10.1016/j.jeurceramsoc.2018.03.010.

[152] D. L. Poerschke and C. G. Levi, "Effects of cation substitution and temperature on the interaction between thermal barrier oxides and molten CMAS," *Journal of the European Ceramic Society,* vol. 35, pp. 681-691, 2015.

[153] W. D. Summers, D. L. Poerschke, D. Park, J. H. Shaw, F. W. Zok, and C. G. Levi, "Roles of composition and temperature in silicate deposit-induced recession of yttrium disilicate," *Acta Materialia,* vol. 160, pp. 34-46, 2018.

[154] V. L. Wiesner, B. J. Harder, and N. P. Bansal, "High-temperature interactions of desert sand CMAS glass with yttrium disilicate environmental barrier coating material," *Ceramics International,* vol. 44, pp. 22738–22743, 2018.

[155] J. Liu, L. Zhang, Q. Liu, L. Cheng, and Y. Wang, "Calcium–magnesium–aluminosilicate corrosion behaviors of rare-earth disilicates at 1400 ◦C," *Journal of the European Ceramic Society,* vol. 33, p. 10, 2013.

[156] Z. Tian *et al.*, "General trend on the phase stability and corrosion resistance of rare earth monosilicates to molten calcium–magnesium–aluminosilicate at 1300 °C," *Corrosion Science,* vol. 148, pp. 281–292, 2019.

[157] M. Wolf, D. E. Mack, O. Guillon, and R. Vaßen, "Resistance of pure and mixed rare earth silicates against calcium-magnesium-aluminosilicate (CMAS): A comparative study," *Journal of American Ceramic Society,* vol. 103, p. 16, 2020, doi: 0.1111/jace.17328.

[158] M. Fritsch and H. Klemm, "The water vapor hot gas corrosion behavior of Al_2O_3-Y_2O_3 materials, Y_2SiO_5 and $Y_3Al_5O_{12}$-coated alumina in a combustion environment " in *Advanced Ceramic Coatings and Interfaces: Ceramic Engineering and Science Proceedings*, Cocoa Beach, Forida, USA, 2008, vol. 27, no. 3, pp. 148-159, doi: http://10.1002/9780470291320.ch14.

[159] R. A. Golden, K. Mueller, and E. J. Opila, "Thermochemical Stability of $Y_2Si_2O_7$ in High-Temperature Water Vapor," *Journal of American Ceramic Society,* vol. 103, no. 8, pp. 4517–4535, 2020.

[160] N. A. Nasiri, N. Patra, D. D. Jayaseelan, and W. E. Lee, "Water vapour corrosion of rare earth monosilicates for environmental barrier coating application," *Ceramics International,* vol. 43, pp. 7393-7400, 2017, doi: http://dx.doi.org/10.1016/j.ceramint.2017.02.123.

[161] M. G. Dunn, A. J. Baran, and J. Miatech, "Operation of Gas Turbine Engines in Volcanic Ash Clouds," *Transactions of the ASME,* vol. 118, pp. 724-732, 1996.

[162] L. F. Aprigliano, "Burner-Rig Simulation of Low-Temperature Hot Corrosion," David W. Taylor Naval Ship Research & Development Center (DTNSRDC), USA, 1977.

[163] N. S. Jacobson, C. A. Stearns, and J. L. Smialek, "Burner Rig Corrosion of SiC at 1000 °C," NASA, Cincinnati, Ohio, USA, NASA-TM-8706, 1985.

[164] D. Baxter, A. Bellosi, and F. Monteverde, "Oxidation and burner rig corrosion of liquid phase sintered SiC," *Journal of the European Ceramic Society,* vol. 20, pp. 367-382, 2000.

[165] D. S. Fox, R. A. Miller, D. Zhu, M. Perez, M. D. Cuy, and R. C. Robinson, "Mach 0.3 Burner Rig Facility at the NASA Glenn Materials Research Laboratory," NASA Glenn Research Center Cleveland, Ohio, USA, NASA/TM—2011-216986, 2011.

[166] E. Bakan, D. E. Mack, S. Lobe, D. Koch, and R. Vaßen, "An investigation on burner rig testing of environmental barrier coatings for aerospace applications," *Journal of the European Ceramic Society,* vol. 40, pp. 6236–6240, 2020, doi: https://doi.org/10.1016/j.jeurceramsoc.2020.06.016.

[167] D. Zhu, D. S. Fox, and R. T. Pastel, "High Pressure Burner Rig Testing of Advanced Environmental Barrier Coatings for Si3N4 Turbine Components," in *The 31st International Cocoa Beach Conference & Exposition on Advanced Ceramics & Composites*, Daytona Beach, Florida, USA, 2007, p. 12.

[168] J.-P. Immarigeon *et al.*, "Evaluation of Thermal Barrier Coatings from Burner Rig Tests," National Research Council of Canada, Institute for Aerospace Research, Ottawa, Ontario, Canada, 1997.

[169] R. A. Miller and M. A. Kuczmarski, "Burner Rig for Small Particle Erosion Testing of Thermal Barrier Coatings," *Journal of Testing and Evaluation,* vol. 42, no. 3, 2014, doi: http://10.1520/JTE20120303.

[170] M. Negami, K. Kyuma, T. Oda, Y. Takada, M. Kobayashi, and M. Azuma, "Durability investigation of burner rig of Yb_2SiO_5 environmental barrier coatings," presented at the Ceramic Matrix Composites II: Science and Technology of Materials, Design, Applications, Performance and Integration, 2022.

[171] M. J. Presby *et al.*, "The Development and Use of a Natural Gas/Oxygen Burner Rig for Environmental Barrier Coating and Ceramic Matrix Composite Technology Maturation," *Journal of Engineering for Gas Turbines and Power,* vol. 146, no. 1, pp. 011012-011023, 2024, doi: https://doi.org/10.1115/1.4063386.

[172] T. Steinke, D. Sebold, D. E. Mack, R. Vaßen, and D. Stöver, "A novel test approach for plasma-sprayed coatings tested simultaneously under CMAS and thermal gradient cycling conditions," *Surface & Coatings Technology,* vol. 205, pp. 2287–2295, 2010, doi: http://doi:10.1016/j.surfcoat.2010.09.008.

[173] D. S. Fox and J. L. Smialek, "Burner Rig Hot Corrosion of Silicon Carbide and Silicon Nitride," *Journal of American Ceramic Society,* vol. 73, no. 2, pp. 303-311, 1990.

[174] M. Shinozaki, K. A. Roberts, B. v. d. Goor, and T. W. Clyne, "Deposition of Ingested Volcanic Ash on Surfaces in the Turbine of a Small Jet Engine," *Advanced Engineering Materials,* vol. 15, no. 10, pp. 986-995, 2013, doi: http://10.1002/adem.201200357.

[175] R. Naraparaju *et al.*, "Integrated testing approach using a customized micro turbine for a volcanic ash and CMAS related degradation study of thermal barrier coatings," *Surface & Coatings Technology,* vol. 337, pp. 198-208, 2018, doi: https://doi.org/10.1016/j.surfcoat.2018.01.030.

[176] C. Giehl, R. A. Brooker, H. Marxer, and M. Nowak, "An experimental simulation of volcanic ash deposition in gas turbines and implications for jet engine safety," *Chemical Geology,* vol. 461, pp. 160–170, 2017, doi: http://dx.doi.org/10.1016/j.chemgeo.2016.11.024.

[177] K. N. Lee, J. I. Eldridge, and R. C. Robinson, "Residual Stresses and Their Effects on the Durability of Environmental Barrier Coatings for SiC Ceramics," *Journal of American Ceramic Society,* vol. 88, no. 12, pp. 3483–3488, 2005.

[178] A. Abdul-Aziz, S. Mustapha, and A. Fakha, "Analytical and experimental verification of environmental barrier coating (EBC) covering crack propagation, failure mechanisms, and life modeling," in *Proceedings of SPIE*, 2021, vol. 11592, pp. 1-9.

[179] A. Abdul-Aziz, D. J. Roth, R. Cotton, G. F. Studor, E. Christiansen, and P. C. Young, "Composite Material Characterization using Microfocus X-ray Computed Tomography Image-based Finite Element Modeling," *Materials Evaluation,* pp. 167-175, 2013.

[180] A. Abdul-Aziz, F. Abdi, R. T. Bhatt, and J. E. Grady, "Durability Modeling of Environmental Barrier Coating (EBC) Using Finite Element Based Progressive Failure Analysis," *Journal of Ceramics,* p. 10, doi: http://dx.doi.org/10.1155/2014/874034.

[181] A. Abdul-Aziz, J. Arias, F. Abdi, R. Bhatt, J. Grady, and D. Zhu, "Environmental barrier coating (EBC) durability modeling using a progressive failure analysis approach part II," in *Proceedings of SPIE*, San Diego, California, USA, 2013, p. 16.

[182] A. Abdul-Aziz, A. Najafi, F. Abdi, R. Bhatt, and J. Grady, "Test validation of environmental barrier coating (EBC) durability and damage tolerance modeling approach," in *Proceedings of SPIE*, San Diego, California, USA, 2014, pp. 1-12, doi: http://10.1117/12.2045914.

[183] J. Alqallaf and J. A. Teixeira, "Numerical study of effects of solid particle erosion on compressor and engine performance," *Results in Engineering,* vol. 15, no. 1, 2022, doi: http://10.1016/j.rineng.2022.100462.

[184] A. S. f. T. a. M. (ASTM), "ASTM G76-18 − Standard Test Method for Conducting Erosion Tests by Solid Particle Impingement Using Gas Jets," p. 6, 2018.

[185] M. Schrade and S. Staudacher, "Hight-Speed Test Rig For the Investigation of Erosion Damage of Axial Compressor Blades," University of Stuttgart, Stuttgart, Germany, 2014.

[186] D. Zhu, D. S. Fox, L. Ghosn, J. L. Smialek, and R. A. Miller, "Environmental Barrier Coatings for Turbine Engines: A Design and Performance Perspective," in *The 33rd International Conference on Advanced Ceramics & Composites*, Daytona Beach, Florida, USA, 2009, p. 17.

[187] W. LePage. "A practical guide to DIC." The Advanced Materials Design Group, Department of Mechanical Engineering, The University of Tulsa. https://digitalimagecorrelation.org/ (accessed 2024).

[188] C. Solutions, "Speckle Pattern Fundamentals," USA, 2021. [Online]. Available: https://correlated.kayako.com/article/38-speckle-pattern-fundamentals

[189] N. Lovaas. "Subset, Step Size and Strain Filter Selection." Correlated Solutions. https://correlated.kayako.com/article/44-subset-step-size-and-strain-filter-selection (accessed 2024).

[190] H. Schreier, J.-J. Orteu, and M. A. Sutton, *Image Correlation for Shape, Motion and Deformation Measurements: Basic Concepts, Theory and Applications*. New York, USA: Springer, 2009.

[191] S. O'Connor, "Plasticity-Induced Fatigue Crack Closure: An Investigation Using Digital Image Correlation," MSc by Research, Engineering Department, University of Oxford, Oxford, Uniuted Kingdom, 2015.

[192] P. Caporossi, P. Mazzanti, and F. Bozzano, "Digital Image Correlation (DIC) Analysis of the 3 December 2013 Montescaglioso Landslide (Basilicata, Southern Italy): Results from a Multi-Dataset Investigation," *International Journal of Geo-Information,* vol. 7, pp. 372-397, 2018, doi: http://doi:10.3390/ijgi7090372.

[193] C. Lim, Y. Jeong, S. Limkantanyu, and M. Kwon, "Strain Measuring of Composite Grid Using Digital Image Correlation," *Advances in Materials Science and Engineering,* vol. 2022, pp. 1-12, 2022, doi: https://doi.org/10.1155/2022/6041887.

[194] M. A. Sutton, J. H. Yan, V. Tiwari, H. W. Schreier, and J. J. Orteu, "The effect of out-of-plane motion on 2D and 3D digital image correlation measurements," *Optics and Lasers in Engineering,* vol. 46, pp. 746–757, 2008.

[195] W. S. LePage, S. H. Daly, and J. A. Shaw, "Cross Polarization for Improved Digital Image Correlation," *Experimental Mechanics,* vol. 56, pp. 969-985, 2016.

[196] I. D. I. C. S. (iDICs), "A Good Practices Guide for Digital Image Correlation: Standardization, Good Practices, and Uncertainty Quantification Committee," 2018. [Online]. Available: www.idics.org

[197] *ASTM C830 - 00(2016) - Standard Test Methods for Apparent Porosity, Liquid Absorption, Apparent Specific Gravity, and Bulk Density of Refractory Shapes by Vacuum Pressure*, A. S. f. T. a. M. (ASTM), United States, 2016.

[198] N. A. Nasiri, "Effect of Grain Boundary Chemistry and Grain Morphology on the Mechanical Behaviour of Silicon Carbide," Doctor of Philosophy (PhD), Department of Mechanical Engineering, Imperial College London, London, UK, 2014.

[199] M. A. Materials. "Microstructure." https://www.morgantechnicalceramics.com/en-gb/ceramics-101/mechanical-properties-of-ceramics/microstructure (accessed 2023).

[200] X. Li *et al.*, "Automation of intercept method for grain size measurement: A topological skeleton approach," *Materials & Design,* vol. 224, pp. 111358-111370, 2022.

[201] *BS EN 623-3:2001 - Advanced technical ceramics – Monolithic ceramics – General and textural properties – Part 3: Determination of grain size and size distribution (characterized by the linear intercept method)*, B. Standard, 2001.

[202] M. I. Mendelson, "Average Grain Size in Polycrystalline Ceramics," presented at the The American Ceramic Society, Palo Alto, United States, 1969.

[203] *ASTM E112-13 - Standard Test Methods for Determining Average Grain Size*, A. S. f. T. a. M. (ASTM), United States, 2013.

[204] A. Thorvaldsen, "The intercept method—2. Determination of spatial grain size," *Acta Metallurgica Inc.,* vol. 45, no. 2, p. 6, 1997.

[205] M. I. Corporation. *Mercury Intrusion Porosimetry Theory*. Georgia, USA. [Online]. Available: chrome-

extension://efaidnbmnnnibpcajpcglclefindmkaj/https://www.micromeritics.com/Repository/Files/Mercury_Porosimetry_Theory_poster.pdf

[206] F. Rodríguez-Reinoso and A. Sepúlveda-Escribano, "Chapter 9 - Porous Carbons in Adsorption and Catalysis," in *Handbook of Surfaces and Interfaces of Materials*, vol. 5, H. S. Nalwa Ed.: Academic Press, 2001, pp. 309-355.

[207] P. T. L. (ptl). "Mercury Intrusion Porosimetry." Particle Technology Labs (ptl). https://particletechlabs.com/analytical-testing/mercury-intrusion-porosimetry/ (accessed.

[208] C. Giannini, M. Ladisa, D. Altamura, D. Siliqi, T. Sibillano, and L. D. Caro, "X-ray Diffraction: A Powerful Technique for the Multiple-Length-Scale Structural Analysis of Nanomaterials," *Crystals,* vol. 6, no. 8, 2016, doi: 10.3390/cryst6080087.

[209] U. o. Cambridge. "X-ray Diffraction Techniques." University of Cambridge. https://www.doitpoms.ac.uk/tlplib/xray-diffraction/index.php (accessed 22 January, 2020).

[210] J. Epp, "X-ray diffraction (XRD) techniques for materials characterization," in *Materials Characterization Using Nanodestructive Evaluation (NDE) Methods*, G. Hubschen, I. Altpeter, R. Tschuncky, and H.-G. Herrmann Eds.: Woodhead Publishing Series in Electronic and Optical Materials: Number 88, 2016, pp. 81-124.

[211] A. F. R. Stephen T. Thornton, *Modern physics for scientists and engineers*. London: Saunder's College Publishing, 1993.

[212] R. R. S. Camden R. Hubbard, "RIR - Measurement and Use in Quantitative XRD," *Powder Diffraction,* vol. 3, no. 2, 1988.

[213] I. C. f. D. D. (ICDD), "Quantitative Analysis: Reference Intensity Ratio (RIR)." [Online]. Available: https://www.icdd.com/

[214] J. I. Goldstein, D. E. Newbury, J. R. Michael, N. W. M. Ritchie, J. H. J. Scott, and D. C. Joy, "Quantitative Analysis: From k-ratio to Composition," in *Scanning Electron Microscopy and X-Ray Microanalysis*: Springer, 2017, pp. 289–307.

[215] P. Simon, V. G. Baldovino-Medrano, and R. Wojcieszak, "X-Ray Photoelectron Spectroscopy (XPS): Principles and Application for the Analysis of Photoactive Materials," in *Springer Handbook fo Inorganic Photochemistry*, D. W. Bahnemann and A. O. T. Patrocinio Eds. Switzerland: Springer, 2020.

[216] T. F. Scientific. "X-Ray Photoelectron Spectroscopy." Thermo Fischer Scientific. (accessed 2023).

[217] S. Massahi, "Industrialization of the mirror plate coatings for the ATHENA mission," PhD, Astrophysics and Atmospheric Physics department, Technical University of Denmark, Denmark, 2019.

[218] M. Biesinger. "X-ray Photoelectron Spectroscopy (XPS) Reference Pages." The University of Western Ontario. https://www.xpsfitting.com/2012/08/spin-orbit-splitting.html (accessed December, 2023).

[219] D. o. C. a. B. Grimmgroup, Worcester Polytechnic Institute. "XPS and UPS Background." Worcester Polytechnic Institute. (accessed 2023).

[220] N. Marturi, "Vision and Visual Servoing for Nanomanipulation and Nanocharacterization using Scanning Electron Microscope," Grade de Docteur, Université de Franche-Comté, Université de Franche-Comté, 2013.

[221] J. Ltd., "SEM - Scanning Electron Microscope A To Z - Basic Knowledge For Using the SEM " JEOL Ltd. , Tokyo, Japan.

[222] I. S. U.-M. S. a. Engineering. "Backscattered Electrons." Iowa State University of Science and Technology. https://www.mse.iastate.edu/research/sem/microscopy/how-does-the-sem-work/high-school/how-the-sem-works/backscattered-electrons/ (accessed 23 January, 202).

[223] B. J. Inkson, "Scaning electron microscopy (SEM) and transmission electron microscopy (TEM) for materials characterization," in *Materials Characterization Using Nondestructive Evaluation (NDE) Methods*, G. Hubschen, I. Altpeter, R. Tschuncky, and H.-G. Herrmann Eds.: Woodhead Publishing Series in Electronic and Optical Materials: Number 88 2016.

[224] F. G. Tseng, "Advance Micro System Fabrication and Lab - Lecture 13 SEM Techniques," National Tsing Hua University, Hsinchu, Taiwan, 2016.

[225] C. Lechene *et al.*, "High-resolution quantitative imaging of mammalian and bacterial cells using stable isotope mass spectrometry," *Journal of Biology,* vol. 20, no. 5, pp. 20.1-20.30, 2006.

[226] Horiba. "What is Raman Spectroscopy?" Horiba. https://www.horiba.com/en_en/raman-imaging-and-spectroscopy/ (accessed 26 January, 2020).

[227] U. Babeș-Bolyai, "Raman Spectroscopy," Universitatea Babeș-Bolyai, Romania.

[228] Renishaw. "Raman bands explained." Renishaw. https://www.renishaw.com/en/raman-bands-explained--25808 (accessed 26 January, 2020).

[229] N. Corporation. "Lesson 1. Basic of Raman scattering." Nanophoton Corporation. https://www.nanophoton.net/raman-spectroscopy/lessons/lesson-1 (accessed 26 January, 2020).

[230] *ASTM C1421-18 - Determination of Fracture Toughness of Advanced Ceramics at Ambient Temperature*, A. S. f. T. a. M. (ASTM), United States, 2018.

[231] J. Kübler, "Fracture toughness of ceramics using the SEVNB method - round Robin," ETH Zürich, EMPA, Swiss Federal Laboratories for Materials Testing and Research, 37, 1999.

[232] *CEN/TS 14425-5:2004 - Advanced technical ceramics – test methods for determination of fracture toughness of monolithic ceramics. Part 5: Single-edge vee-notch beam (SEVNB) method*, B. S. I. (BSI), 2004.

[233] R. G. R. Damani, R. Danzer, "Critical Notch-Root Radius Effect in SENB-S Fracture Toughness Testing " *Journal of the European Ceramic Society,* vol. 16, 1996.

[234] Y. H. Toshihiko Nishida, "Effect of Notch-Root Radius on the Fracture Toughness of a Fine-Grained Alumina," *Journal of American Ceramic Society,* vol. 77, no. 2, 1994.

[235] X. Wang and A. Atkinson, "On the measurement of ceramic fracture toughness using single edge notched beams," *Journal of the European Ceramic Society,* vol. 35, no. 13, pp. 3713-3720, 2015, doi: 10.1016/j.jeurceramsoc.2015.05.005.

[236] *ASTM E228-17 - Standard Test Method for Linear Thermal Expansion of Solid Materials with a Push-Rod Dilatometer*, A. S. f. T. a. M. (ASTM), United States, 2017.

[237] C. P. Romao, K. J. Miller, C. A. Whitman, M. A. White, and B. A. Marinkovic, "4.07 - Negative Thermal Expansion (Thermomiotic) Materials," in *Comprehensive Inorganic Chemistry II: From Elements to Applications*, vol. 4, J. Reedijk and K. Poeppelmeier Eds.: Elsevier, 2013, pp. 127-151.

[238] J. E. Daw, J. L. Rempe, D. L. Knudson, K. G. Condie, and J. C. Crepeau, "Viability of Pushrod Dilatometry Techniques for High Temperature In-Pile Measurements," Idaho National Laboratory (INL), USA, INL/EXT-07-13120, 2008.

[239] *BS EN 821-1:1995 - Advanced technical ceramics - Monolithic ceramics - Thermo-physical properties. Part 1: Determination of thermal expansion*, B. S. I. (BSI), 1995.

[240] Buehler. "Vickers Hardness Testing." https://www.buehler.com/uk/vickers-hardness-testing/ (accessed December, 2023).

[241] G. Mathers. "Hardness Testing Part 1." TWI Ltd. https://www.twi-global.com/technical-knowledge/job-knowledge/hardness-testing-part-1-074 (accessed 2023).

[242] *ASTM E1876-22 – Standard Test Method for Dynamic Young's Modulus, Shear Modulus, and Poisson's Ratio by Impulse Excitation of Vibration*, A. S. f. T. a. Materials, USA, 2022.

[243] N. Supply. *Dynamic Material Testing: The basics of the Impulse Excitation Technique*. Kansas, USA. [Online]. Available: https://content.ndtsupply.com/assets/Uploads/Basics-of-IET.pdf

[244] O. A. Quaglio, J. M. d. Silva, E. d. C. Rodovalho, and L. d. V. Costa, "Determination of Young's Modulus by Specific Vibration of Basalt and Diabase," *Advances in Materials Science and Engineering,* pp. 1-8, 2020, doi: https://doi.org/10.1155/2020/4706384.

[245] L. Scislo, "Verification of Mechanical Properties Identification Based on Impulse Excitation Technique and Mobile Device Measurements," *Sensors,* vol. 23, no. 12, pp. 5639-5653, 2023, doi: https://doi.org/10.3390/s23125639.

[246] Z. Fan *et al.*, "Oxidation behavior of fine-grained SiC-B4C/C composites up to 1400 °C," *Carbon,* vol. 41, pp. 429-436, 2003.

[247] K. Kobayashi, K. Maeda, H. Sano, and Y. Uchiyama, "Formation and oxidation resistance of the coating formed on carbon material composed of B4C-SiC powders," *Carbon,* vol. 33, no. 4, pp. 397-403, 1995.

[248] Q. Guo, J. Song, L. Liu, and B. Zhang, "Relationship between oxidation resistance and structure of B4C-SiC/C composites with self-healing properties," *Carbon,* vol. 37, pp. 33-40, 1999.

[249] S. Hayun, A. Weizmann, M. P. Dariel, and N. Frage, "Microstructural evolution during the infiltration of boron carbide with molten silicon," *Journal of the European Ceramic Society,* vol. 30, no. 4, pp. 1007-1014, 2010, doi: 10.1016/j.jeurceramsoc.2009.09.021.

[250] S. Hayun, H. Dilman, M. P. Dariel, and N. Frage, "The effect of aluminum on the microstructure and phase composition of boron carbide infiltrated with silicon," *Materials Chemistry and Physics,* vol. 118, no. 2-3, pp. 490-495, 2009, doi: 10.1016/j.matchemphys.2009.08.023.

[251] R. Telle, "Structure and Properties of Si-doped Boron Carbide," in *The Physics and Chemistry of Carbides, Nitrides and Borides*, R. Freer Ed. Netherlands: Kluwer Academic Publishers, 1990, pp. 249-267.

[252] J. A. Costello and R. E. Tressler, "Oxidation Kinetics of Silicon Carbide Crystals and Ceramics: I, In Dry Oxygen," *Journal of American Ceramic Society,* vol. 69, no. 9, pp. 674-681, 1986.

[253] E. Fitzer and R. Ebi, "Kinetic Studies on the Oxidation of Silicon Carbide," in *Silicon Carbide*, J. W. F. R. C. Marshall, C. E. Ryan Ed. Colombia, United States: University of South Carolina Press, 1973, pp. 320-328.

[254] I. Ogawa, K. Kobayashi, and S. Nishikawa, "Oxidation resistance of carbon-ceramics composite materials sintered from ground powder mixtures of raw coke and ceramics," *Journal of Materials Science,* vol. 23, pp. 1363-1367, 1988.

[255] *Technote: Cubed Reaction-Bonded Silicon Carbide*, Delaware, p. 2.

[256] P. Chhillar, M. K. Aghajanian, and D. D. Mer, "The Effect of Si Content on the Properties of B4C-SiC-Si Composite," presented at the Advances in Ceramic Armor III, 2007.

[257] F. L. Galeener, "Raman and ESR Studies of The Thermal History of Amorphous SiO2," *Journal of Non-Crystalline Solids,* vol. 71, pp. 373-386, 1985.

[258] T. Narushima, M. Maruyama, H. Arashi, T. Goto, T. Hirai, and Y. Iguchi, "In-situ Observations of Oxide Film Formed during Thermal Oxidation of SiC-B4C Composite Using Raman Spectroscopy," *Key Engineering Materials,* vol. 113, pp. 99-104, 1996.

[259] A. K. Hassan, L. M. Torell, L. Borjesson, and H. Doweidar, "Structural changes of B2O3 through the liquid-glass transition range: A Raman-scattering study," *Physical Review. B, Condensed matter,* vol. 45, no. 22, pp. 12797-12805, Jun 1 1992, doi: 10.1103/physrevb.45.12797.

[260] W. L. Konijnendijk, "The structure of borosilicate glasses," PhD, Technische Hogeschool Eindhoven, Eindhoven, 1975.

[261] T. Furukawa and W. B. White, "Raman spectroscopic investigation of sodium borosilicate glass structure," *Journal of Materials Science,* vol. 16, pp. 2689-2700, 1981 1981.

[262] G. E. Walrafen, S. R. Samanta, and P. N. Krishnan, "Raman investigation of vitreous and molten boric oxide," *The Journal of Chemical Physics,* vol. 72, no. 1, pp. 113-120, 1980, doi: 10.1063/1.438894.

[263] B. N. Meera and J. Ramakrishna, "Raman spectral studies of borate glasses," *Journal of Non-Crystallien Solids,* vol. 159, pp. 1-21, 1993.

[264] L. Cormier, O. Majerus, D. R. Neuville, and G. Calas, "Temperature-Induced Structural Modifications Between Alkali Borate Glasses and Melts," *Journal of the American Ceramic Society,* vol. 89, no. 1, pp. 13-19, 2006, doi: 10.1111/j.1551-2916.2005.00657.x.

[265] T. W. Bril, "Raman spectroscopy of crystalline and vitreous borates," PhD, Technische Hogeschool Eindhoven, Eindhoven, 1976.

[266] S. Hayun, "Reaction-bonded boron carbide for lightweight armor: The interrelationship between processing, microstructure, and mechanical properties " *American Ceramic Society Bulletin,* vol. 96, no. 6, pp. 20-26, 2017.

[267] S. Hayun, A. Weizmann, H. Dilman, M. P. Dariel, and N. Frage, "Rim region growth and its composition in reaction bonded boron carbide composites with core-rim structure," *Journal of Physics: Conference Series,* vol. 176, 2009, doi: 10.1088/1742-6596/176/1/012009.

[268] T. Furukawa and W. B. White, "Raman Spectroscopy of Heat-Treated B2O3-SiO2 Glasses," *Journal of American Ceramic Society,* vol. 64, no. 8, pp. 443-447, 1981.

[269] R. Martens and W. Müller-Warmuth, "Structural groups and their mixing in borosilicate glasses of various compositions - an NMR study," *Journal of Non-Crystalline Solids,* vol. 265, pp. 167-175, 2000.

[270] J. F. Stebbins, S. Kroeker, S. K. Lee, and T. J. Kiczenski, "Quantification of five- and six-coordinated aluminum ions in aluminosilicate and fluoride-contaning glasses by high-field, high-resolution 27Al NMR," *Jounral of Non-Crystalline Solids,* vol. 275, pp. 1-6, 2000.

[271] A. G. revesz, "A New Model for Defects in Non-Crystalline Silicon Dioxide," *Journal of Non-Crystalline Solids,* vol. 4, pp. 347-356, 1970.

[272] F. J. Norton, "Permeation of Gaseous Oxygen through Vitreous Silica," *Nature,* vol. 191, no. 4789, p. 701, 1961.

[273] C. Tsou, Y.-S. Huang, H.-C. Li, and T.-H. Lai, "Determination of Thermal Expansion Coefficient of Thermal Oxide," *Sensors and Materials,* vol. 17, no. 8, pp. 441–451, 2005.

[274] J. L. Stokes, B. J. Harderd, V. L. Wiesnerd, and D. E. Wolfe, "High-Temperature thermochemical interactions of molten silicates with Yb2Si2O7 and Y2Si2O7 environmental barrier coating materials," *Journal of the European Ceramic Society,* vol. 39, p. 9, 2019.

[275] D. L. Poerschke and C. G. Levi, "Effects of cation substitution and temperature on the interaction between thermal barrier oxides and molten CMAS," *Journal of the European Ceramic Society,* vol. 35, p. 11, 2015.

[276] D. L. Poerschke, D. D. Hass, S. Eustis, G. G. E. Seward, J. S. V. Sluytman, and C. G. Levi, "Stability and CMAS Resistance of Ytterbium-Silicate/Hafnate EBCs/TBCfor SiC Composites," *Journal of American Ceramic Society,* vol. 98, no. 1, pp. 278-286, 2015.

[277] D. L. Poerschke, T. L. Barth, and C. G. Levi, "Equilibrium relationships between thermal barrier oxides and silicate melts," *Acta Materialia,* vol. 120, pp. 302-314, 2016.

[278] N. K. Eils, P. Mechnich, and W. Braue, "Effect of CMAS Deposits on MOCVD Coatings in the System Y_2O_3–ZrO_2: Phase Relationships," *Journal of American Ceramic Society,* vol. 96, no. 10, pp. 3333-3340, 2013.

[279] D. L. Poerschke, G. G. E. Seward, and C. G. Levi, "Influence of Yb:Hf Ratio on Ytterbium Hafnate/Molten Silicate(CMAS) Reactivity," *Journal of American Ceramic Society,* vol. 99, no. 2, pp. 651-659, 2016.

[280] Z. Tian *et al.*, "Corrosion of $RE_2Si_2O_7$ (RE=Y, Yb, and Lu) environmental barrier coating materials by molten calcium-magnesium-alumino-silicate glass at high temperatures," *Journal of the European Ceramic Society,* vol. 39, pp. 4245-4254, 2019, doi: https://doi.org/10.1016/j.jeurceramsoc.2019.05.036.

[281] X. Zhong, W. Wang, Y. Niu, L. Huang, Q. Li, and X. Zheng, "Corrosion behaviors and mechanisms of ytterbium silicate environmental barrier coatings by molten calcium-magnesium-alumino-silicate melts," *Corrosion Science,* vol. 191, 2021.

[282] D. L. Poerschke, "Developments in Thermodynamic Models of Deposit-Induced Corrosion of High-Temperature Coatings," *The Minerals, Metals & Materials Society,* vol. 74, no. 1, 2022.

[283] P. Ptáček *et al.*, "Preparation, kinetics of sinter-crystallization and properties of hexagonal strontium-yttrate-silicate apatite phase: $SrY_4[SiO_4]_3O$," *Ceramics International,* vol. 41, no. 1, pp. 1779-1795, 2015.

[284] W. Zhu, H. Y. Chen, L. Yang, Y. C. Zhou, and G. N. Xu, "Phase field model for diffusion-reactionstress field in the thermal barrier coatings corroded by the molten CMAS," *Engineering Failure Analysis,* vol. 111, 2020.

[285] D. L. Poerschke, J. S. V. Sluytman, K. B. Wong, and C. G. Levi, "Thermochemical compatibility of ytterbia–(hafnia/silica) multilayers for environmental barrier coatings," *Acta Materialia,* vol. 61, pp. 6743-6755, 2013.

[286] A. Iqdari, B. Velde, N. Benalioulhaj, S.-C. Dujon, and N. E. Yamine, "Exchange of light rare earths for Ca in apatite," *Comptes Rendus Geoscience,* vol. 335, pp. 381–390, 2003.

[287] V. L. Wiesner and N. P. Bansal, "Mechanical and thermal properties of calcium–magnesium aluminosilicate (CMAS) glass," *Journal of the European Ceramic Society,* vol. 35, pp. 2907-2914, 2015.

[288] J. Sleeper, A. Garg, V. L. Wiesner, and N. P. Bansal, "Thermochemical interactions between CMAS and $Ca_2Y_8(SiO_4)_6O_2$ apatite environmental barrier coating material," *Journal of the European Ceramic Society,* vol. 39, pp. 5380-5390, 2019.

[289] S. Kramer, J. Yang, C. G. Levi, and C. A. Johson, "Thermochemical Interaction of Thermal Barrier Coatings with Molten $CaO–MgO–Al_2O_3–SiO_2$ (CMAS) Deposits," *Journal of American Ceramic Society,* vol. 89, no. 10, pp. 3167-3175, 2006.

[290] C. Gatzen, D. E. Mack, O. Guillon, and R. Vaßen, "YAlO3—A Novel Environmental Barrier Coating for Al_2O_3/Al_2O_3–Ceramic Matrix Composites," *Coatings,* vol. 9, pp. 609-622, 2019, doi: http://10.3390/coatings9100609.

[291] M. Fritsch, H. Klemm, M. Herrmann, A. Michaelis, and B. Schenk, "The Water Vapour Hot Gas Corrosion of Ceramic Materials," *CFI, Ceramic Forum International/Berichte der DKG (Deutsche Keramische Gesellschaft),* vol. 87, no. 11, pp. E28-E32, 2010.

[292] J. Xiang, Z.-G. Liu, J.-H. Ouyang, and F.-Y. Yan, "Synthesis, structure and electrical properties of rare-earth doped apatite-type lanthanum silicates," *Electrochimica Acta,* vol. 65, pp. 251-256, 2012.

[293] C. Bonhomme, S. Beaudet-Savignat, T. Chartier, A. Maître a, A.-L. Sauvet, and B. Soulestin, "Sintering kinetics and oxide ion conduction in Sr-doped apatite-type lanthanum silicates, $La_9Sr_1Si_6O_{26.5}$," *Solid State Ionics,* vol. 180, pp. 1593-1598, 2009.

[294] A. C. Strzelecki *et al.*, "Structure and thermodynamics of calcium rare earth silicate oxyapatites, $Ca_2RE_8(SiO4)_6O_2$ (RE = Pr, Tb, Ho, Tm)," *Physics and Chemistry of Minerals,* vol. 49, pp. 1-13, 2022.

[295] L.-C. Leu, S. Thomas, M. T. Sebastian, S. Zdzieszynski, S. Misture, and R. Ubic, "Crystal Structure of Apatite Type Rare-Earth Silicate $(Sr_2RE_2)(RE_6)(SiO_4)_6O_2$ (RE = La, Pr, Tb, Tm, and Y)," *Journal of American Ceramic Society,* vol. 94, no. 8, pp. 2625-2632, 2011.

[296] A. S. Risbud, K. B. Helean, M. C. Wilding, P. Lu, and A. Navrotsky, "Enthalpies of formation of lanthanide oxyapatite phases," *Journal of Materials Research,* vol. 16, no. 10, pp. 2780-2783, 2001.

[297] J.-j. Liang, A. Navrotsky, T. Ludwig, H. J. Seifert, and F. Aldinger, "Enthalpy of formation of rare-earth silicates Y_2SiO_5 and Yb_2SiO_5 and N-containing silicate $Y_{10}(SiO_4)_6N_2$," *Journal of Materials Research,* vol. 14, no. 4, pp. 1181-1185, 1999.

[298] G. Costa, B. J. Harder, N. P. Bansal, B. A. Kowalski|, and J. L. Stokes, "Thermochemistry of calcium rare-earth silicate oxyapatites," *Journal American Ceramic Society,* vol. 00, pp. 1-8, 2019.

[299] H. Yoshiokaa, Y. Nojirib, and S. Tanase, "Ionic conductivity and fuel cell properties of apatite-type lanthanum silicates doped with Mg and containing excess oxide ions," *Solid State Ionics,* vol. 179, no. 30, pp. 2165-2169, 2008.

[300] L. G. Martínez-González, E. Rodríguez-Reyna, K. J. Moreno, J. I. Escalante-García, and A. F. Fuentes, "Ionic conductivity of apatite-type rare-earth silicates prepared by mechanical milling," *Journal of Alloys and Compounds,* vol. 476, pp. 710–714, 2009.

[301] L. I. Ardanova *et al.*, "Isomorphous Substitutions of Rare Earth Elements for Calcium in Synthetic Hydroxyapatites," *Inorganic Chemistry,* vol. 49, pp. 10687-10693, 2010.

[302] J. A. Fahey, W. J. Weber, and F. J. Rotella, "An X-Ray and Neutron Powder Diffraction Study of the $Ca_{2+x}Nd_{8-x}(SiO_4)_6O_{2-0.5x}$ System," *Journal of Solid State Chemistry,* vol. 60, pp. 145-158, 1985.

[303] L. W. Schroeder and M. Mathew, "Cation Ordering in $Ca_2La_8(SiO_4)_6O_2$ " *Journal of Solid State Chemistry,* vol. 26, pp. 282-287, 1978.

[304] N. Massoni, R. Hegron, and L. Campayo, "Reinvestigation of the crystal structure of $Ca_2Ce_8(SiO_4)_6O_2$ apatite by Rietveld refinement," *Acta Crystallographica E,* vol. E74, pp. 955-959, 2018.

[305] J. V. Crum, S. Chong, J. A. Peterson, and B. J. Riley, "Syntheses, crystal structures, and comparisons of rare-earth oxyapatites $Ca_2RE_8(SiO_4)_6O_2$ (RE = La, Nd, Sm, Eu, or Yb) and $NaLa_9(SiO_4)_6O_2$," *Acta Crystallographica E,* vol. E75, pp. 1020-1025, 2019.

[306] Y. Wang *et al.*, "Water vapor corrosion behaviors of plasma sprayed RE_2SiO_5 (RE = Gd, Y, Er) coatings," *Corrosion Science,* vol. 167, pp. 108529-108538, 2020.

[307] P. J. Panteix, E. Béchade, I. Julien, P. Abélard, and D. Bernache-Assollant, "Influence of anionic vacancies on the ionic conductivity of silicated rare earth apatites," *Materials Research Bulletin,* vol. 43, pp. 1223–1231, 2008.

[308] A. Serret, M. V. Caban, and M. Vallet-Regí, "Stabilization of Calcium Oxyapatites with Lanthanum(III)-Created Anionic Vacancies," vol. 12, pp. 3836-3841, 2000.

[309] S. K. Kendra M. Grant, Jan P. A. Löfvander, Carlos G. Levi, "CMAS degradation of environmental barrier coatings," *Surface & Coatings Technology,* vol. 202, p. 5, 2007 2007.

[310] S. Kramer, J. Yang, C. G. Levi, and C. A. Johnson, "Thermochemical Interaction of Thermal Barrier Coatings with Molten CaO–MgO–Al2O3–SiO2 (CMAS) Deposits," *Journal of American Ceramic Society,* vol. 89, p. 9, 2006.

[311] H. Mehrer, *Diffusion in Solids: Fundamentals, Methods, Diffusion-Controlled Processes*. Springer.

[312] *ASTM E2109 - 01(Reapproved 2021) - Standard Test Method for Determining Area Percentage Porosity in Thermal Sprayed Coatings*, A. S. f. T. a. M. (ASTM), United States, 2021.

[313] Y. Yong, X. Lou, S. Li, C. Yang, and X. Yin, "Direct simulation of the influence of the pore structure on the diffusion process in porous media," *Computers and Mathematics with Applications,* vol. 67, pp. 412-423, 2014.

[314] A. V. Naumkin, A. Kraut-Vass, S. W. Gaarenstroom, and C. J. Powell. "NIST X-ray Photoelectron Spectroscopy Database." U.S. Department of Commerce. https://srdata.nist.gov/xps/elm_in_comp_res.aspx?elm1=Si (accessed 2023).

[315] D. R. Wheeler and S. V. Pepper, "Angle-resolved X-ray photoelectron spectroscopy of epitaxially grown (100) β-SiC to 1300 °C," *Surface and Interface Analysis,* vol. 10, pp. 153-162, 1987, doi: https://doi.org/10.1002/sia.740100216.

[316] A. Mesarwi, W. C. Fan, and A. Ignatiev, "Oxidation of the Si(100) surface promoted by Sr overlayer: An x-ray photoemission study," *Journal of Applied Physics,* vol. 68, pp. 3609-3613, 1990, doi: https://doi.org/10.1063/1.346321.

[317] C. D. Wanger, W. M. Riggs, L. E. Davis, J. F. Moulder, and G. E. Muilenberg, *Handbook of X-ray Photoelectron Spectroscopy*. Minnesota, USA: Perking-Elmer Corporation, Physical Electronics Division, 1979.

[318] R. Benoit. "La Surface." Centre national de la recherche scientifique (CNRS). http://www.lasurface.com/accueil/ (accessed 2023).

[319] Y. Kanedo and Y. Suginohara, "Observation of Si2p binding energy by ESCA and determination of O, O^{-} and O^{2-} ions in silicates," Tohoku University, Sendai, Japan, 1977.

[320] X.-R. Yu and H. Hantsche, "Vertical differential charging in monochromatized small spot X-ray photoelectron spectroscopy," *Surface and Interface Analysis,* vol. 20, pp. 555-558, 1993, doi: https://doi.org/10.1002/sia.740200702.

[321] Y. Zhong, X. Qiu, J. Gao, and Z. Guo, "Chemical Structure of Si–O in Silica Fume from Ferrosilicon Production and Its Reactivity in Alkali Dissolution," *ISIJ International,* vol. 59, no. 6, pp. 1098-1104, 2019.

[322] W. A. M. Aarnink, A. Weishaupt, and A. v. Silfhout, "Angle-resolved X-ray photoelectron spectroscopy (ARXPS) and a modified Levenberg-Marquardt fit procedure: a new combination for modeling thin layers," *Applied Surface Science,* vol. 45, no. 1, pp. 37-48, 1990, doi: 10.1016/0169-4332(90)90018-U.

[323] F. Arezzo, E. Severini, and N. Zacchetti, "An XPS study of diamond films grown on differently pretreated silicon substrates," *Surface and Interface Analysis,* vol. 22, pp. 218-223, 1994, doi: 10.1002/sia.740220149.

[324] T. J. Šarapatka, "XPS study of light-induced effects on Pd-Si and Pd-SiO2-Si interfaces," *Journal of Electron Spectroscopy and Related Phenomena,* vol. 58, no. 3, pp. 233-245, 1992, doi: 10.1016/0368-2048(92)80022-Z.

[325] A. Cros, R. Saoudi, G. Hollinger, C. A. Hewett, and S. S. Lau, "An x-ray photoemission spectroscopy investigation of oxides grown on Au_xSi_{1-x} layers," *Journal of Applied Physics,* vol. 67, pp. 1826–1830, 1990, doi: https://doi.org/10.1063/1.345610.

[326] J. Hedman *et al.*, "Influence of doping on the electron spectrum of silicon," *Journal of Electron Spectroscopy and Related Phenomena,* vol. 1, no. 1, 1972, doi: 10.1016/0368-2048(72)85007-2.

[327] Y. Tanizawa and T. Suzuki, "Effects of silicate ions on the formation and transformation of calcium phosphates in neutral aqueous solutions," *Journal of the Chemical Society, Faraday Transactions,* vol. 91, no. 19, pp. 3499-3503, 1995, doi: https://doi.org/10.1039/FT9959103499.

[328] J. Ge and M. Chaker, "Oxygen Vacancies Control Transition of Resistive Switching Mode in Single-Crystal TiO2 Memory Device," *Applied Materials and Interfaces,* vol. 9, pp. 16327-16334, 2017.

[329] N. Bosio, A. Schaefer, and H. Grönbeck, "Can oxygen vacancies in ceria surfaces be measured by O1s photoemission spectroscopy?," *Journal of Physics: Condensed Matter,* vol. 34, pp. 174004-174010, 2022, doi: https://doi.org/10.1088/1361-648X/ac4f7b.

[330] H. Zhao *et al.*, "Effects of oxygen vacancy on the electronic structure and multiferroics in sol–gel derived $Pb_{0.8}Co_{0.2}TiO_3$ thin films," *Dalton Transactions,* vol. 42, pp. 10358–10364, 2013.

[331] S. Takatani, H. Miki, K. Kushida-Abdelghafar, and K. Torii, "$Pt/PbZr_xTi_{1-x}O_3$ interfacial reaction and Schottky barrier formation studied by x-ray photoelectron spectroscopy: Effect of H2 and O2 annealing," *Journal of Applied Physics,* vol. 85, no. 11, pp. 7784–7791, 1999, doi: https://doi.org/10.1063/1.370585.

[332] J.-C. Dupin, D. Gonbeau, P. Vinatier, and A. Levasseur, "Systematic XPS studies of metal oxides, hydroxides and peroxides," *Physical Chemistry Chemical Physics Journal,* vol. 2, pp. 1319-1324, 2000.

[333] A. Almamoori, S. Lawson, and F. Rezaei, "Improving Adsorptive Performance of CaO for High Temperature CO2 Capture through Fe and Ga Doping," *Energy & Fuels,* vol. 33, no. 2, 2019, doi: 10.1021/acs.energyfuels.8b03996.

[334] I. Sohn, W. Wang, H. Matsuura, F. Tsukihashi, and D. J. Min, "Influence of TiO_2 on the Viscous Behavior of Calcium Silicate Melts Containing 17 mass% Al_2O_3 and 10 mass% MgO," *ISIJ International,* vol. 52, no. 1, pp. 158–160, 2012.

[335] T. L. Barr, "Recent advances in X-Ray Photoelectron Spectroscopy studies of oxides.," *Journal of Vacuum Science & Technology A,* vol. 9, no. 3, pp. 1793-1805, 1991.

[336] B. Carriere, D. Brion, J. Escard, and J. P. Deville, "X-Ray photoelectron study of some silicon-oxygen compounds," *Journal of Electron Spectroscopy and Related Phenomena,* vol. 10, pp. 85-91, 1977.

[337] H. Idriss and M. A. Barteau, "Active sites on oxides: From single crystals to catalysts," *Advances in Catalysis,* vol. 45, pp. 261-331, 2000.

[338] H. Idriss and E. G. Seebauer, "Effect of oxygen electronic polarisability on catalytic reactions over oxides," *Catalysis Letters,* vol. 66, pp. 139–145, 2000.

[339] H. Idriss, "On the wrong assignment of the XPS O1s signal at 531–532 eV attributed to oxygen vacancies in photo- and electro-catalysts for water splitting and other materials applications," *Surface Science,* vol. 712, pp. 121894-121900, 2021, doi: https://doi.org/10.1016/j.susc.2021.121894.

[340] R. B. Shalvoy, P. J. Reucroft, and B. H. Davis, "Characterization of coprecipitated nickel on silica methanation catalysts by X-ray photoelectron spectroscopy," *Journal of Catalysis,* vol. 56, no. 3, pp. 336-348, 1979.

[341] J. A. Kovacich and D. Lichtman, "A qualitative and quantitative study of the oxides of aluminum and silicon using AES and XPS," *Journal of Electron Spectroscopy and Related Phenomena,* vol. 35, no. 1, pp. 7-18, 1985.

[342] M. R. Alexander, R. D. Short, F. R. Jones, M. Stollenwerk, J. Zabold, and W. Michaeli, "An X-ray photoelectron spectroscopic investigation into the chemical structure of deposits formed from hexamethyldisiloxane/oxygen plasmas," *Journal of Materials Science,* vol. 31, pp. 1879–1885, 1996.

[343] C. D. Wagner, D. A. Zatko, and R. H. Raymond, "Use of the oxygen KLL Auger lines in identification of surface chemical states by electron spectroscopy for chemical analysis," *Analytical Chemistry,* vol. 52, no. 9, pp. 1445–1451, 1980, doi: https://doi.org/10.1021/ac50059a017.

[344] M. L. Miller and R. W. Linton, "X-ray photoelectron spectroscopy of thermally treated silica (SiO2) surfaces," *Analytical Chemistry,* vol. 57, no. 12, pp. 2314–2319, 1985, doi: https://doi.org/10.1021/ac00289a033.

[345] Y. Uwamino, T. Ishizuka, and H. Yamatera, "X-ray photoelectron spectroscopy of rare-earth compounds," *Journal of Electron Spectroscopy and Related Phenomena,* vol. 34, no. 1, pp. 67-78, 1984, doi: 10.1016/0368-2048(84)80060-2.

[346] G. Chiarello, A. Lumachi, F. Parmigiani, P. Ghetti, and G. D. Michele, "An XPS Study of SO_2 on a CaO Surface Derived From $Ca(OH)_2$," *Journal of Electron Spectroscopy and Related Phenomena,* vol. 50, pp. 229-237, 1990.

[347] H. V. Doveren and J. A. T. Verhoeven, "XPS Spectra of Ca, Sr, Ba and their Oxides " *Journal of Electron Spectroscopy and Related Phenomena,* vol. 21, no. 3, pp. 265-273, 1980.

[348] T. T. Eighmy, A. E. Kinner, E. L. Shaw, J. J. Dykstra Eusden, and C. A. Francis, "Chlorapatite ($Ca_5(PO_4)_3Cl$) Characterization by XPS: An Environmentally Important Secondary Mineral," *Surface Science Spectra,* vol. 6, pp. 210-218, 1999, doi: https://doi.org/10.1116/1.1247927.

[349] J. Bai, T. Nagashima, and T. Yajima, "XPS Study of Apatite Formed from Simulated Body Fluid on a Titanium Substrate Surface Nitrided by an Atmospheric Pressure

Nitrogen Microwave Plasma," *Journal of Photopolymer Science and Technology,* vol. 28, no. 3, pp. 455-459, 2015.

[350] P. Selvam, B. Viswanathan, and V. Srinivasan, "XPS studies of the surface properties of CaNi5," *Journal of Electron Spectroscopy and Related Phenomena,* vol. 49, no. 2, pp. 203-211, 1989, doi: 10.1016/0368-2048(89)85009-1.

[351] A. B. Christie, J. Lee, I. Sutherland, and J. M. Walls, "An XPS study of ion-induced compositional changes with group II and group IV compounds," *ApplicationsofSurfaceScience,* vol. 15, p. 224—237, 1983, doi: https://doi.org/10.1016/0378-5963(83)90018-1.

[352] B. D. Padalia, W. C. Lang, P. R. Norris, L. M. Watson, and D. J. Fabian, "X-ray photoelectron core-level studies of the heavy rare-earth metals and their oxides," *Proceedings of the Royal Society of London,* vol. 345, no. 1678, pp. 269-290, 1977, doi: https://doi.org/10.1098/rspa.1977.0067.

[353] K. E. Shafei and N. A. Nasiri, "Corrosion behaviour of rare-earth monosilicates in CMAS exposure," *Corrosion Science,* vol. 202, 2022.

[354] K. E. Shafei, R. Kassem, and N. A. Nasiri, "Diffusion behaviour and corrosion rate of rare earth monosilicate-based EBCs under CMAS exposure," *Ceramics International,* vol. 49, no. 23, Part B, pp. 38544-38555, 2023.

[355] J. A. Duffy and M. D. Ingram, "An Interpretation of Glass Chemistry in Terms of the Optical Basicity Concept," *Journal of Non-Crystalline Solids,* vol. 21, p. 38, 1976.

[356] D. J. Cherniak, "Rare earth element diffusion in apatite," *Geochimica et Cosmochimica Acta,* vol. 64, no. 22, pp. 3871–3885, 2000.

[357] R. I. Webster and E. J. Opila, "Mixed phase ytterbium silicate environmental-barrier coating materials for improved calcium–magnesium–alumino-silicate resistance," *Journal of Materials Research,* vol. 35, no. 17, pp. 2358-2372, 2020, doi: http://10.1557/jmr.2020.151.

[358] E. Kothe and A. Varma, *Bio-Geo Interactions in Metal-Contaminated Soils* (Soil Biology, no. Soil Biology 31). Springer Science & Business Media, 2012.

[359] R. D. Shannon, "Revised Effective Ionic Radii and Systematic Studies of Interatomie Distances in Halides and Chaleogenides," *Acta crystallographica,* vol. A32, pp. 751-767, 1976.

[360] V. L. Stolyarova, E. N. Plotnikov, and S. I. Lopatin, "Bond Energies In Oxide Systems: Calculated and Experimental Data " Institute of Silicate Chemistry of the Russian Academy of Sciences Saint Petersburg, Russia

[361] E. B. Watson, T. M. Harrison, and F. J. Ryerson, "Diffusion of Sm, Sr, and Pb in fluorapatite," *Geochimica et Cosmochimica Acta,* vol. 49, pp. 1813-1823, 1985.

[362] X. Zhong *et al.*, "Effects of microstructure on corrorion behaviors for RE2SiO5 (RE=Gd, Y, Er) environmental barrier coatings against calcium-maghnesium-alumino-silicate melts," *Corrosion Science,* vol. 199, pp. 110174-110186, 2022.

[363] M. Xie *et al.*, "Implementation and evaluation of permeability-porosity and tortuosity-porosity relationships linked to mineral dissolution-precipitation," *Computers & Geosciences,* vol. 19, pp. 655-671, 2015.

[364] Y. X. Kang *et al.*, "Defects/CMAS corrosion resistance relationship in plasma sprayed YPSZ coating," *Journal of Alloys and Compounds,* vol. 694, pp. 1320-1330, 2017.

[365] X. Zhong *et al.*, "Microstructure and Thermal Properties of Atmospheric Plasma-Sprayed $Yb_2Si_2O_7$ Coating," *Journal of Thermal Spray Technology,* vol. 26, pp. 203–210, 2017.

[366] R. Naraparaju *et al.*, "Estimation of CMAS infiltration depth in EB-PVD TBCs: A new constraint model supported with experimental approach," *Journal of the European Ceramic Society,* vol. 39, pp. 2936–2945, 2019.

[367] M. A. Rivera-Gil, J. J. Gomez-Chavez, C. V. Ramana, R. Naraparaju, U. Schulz, and J. Muñoz-Saldaña, "High temperature interaction of volcanic ashes with 7YSZ TBC's produced by APS: Infiltration behavior and phase stability," *Surface & Coatings Technology,* vol. 378, 2019.

[368] S. M. Hosseini, T. Shvareva, and A. Navrotsky, "Energetics of lanthanum silicate apatite: Influence of interstitial oxygen and cation vacancy concentrations in $La_{9.33+x}(SiO_4)_6O_{2+3x/2}$ and $La_{10-x}Sr_x(SiO_4)_6O_{3-0.5x}$," *Solid State Ionics,* vol. 233, pp. 62-66, 2013.

[369] L. B. Kong *et al.*, *Transparent Ceramics: Topics in Mining, Metallurgy and Materials Engineering*. Spinger, 2015.

[370] F. A. Kröger and H. J. Vink, "Relations between the Concentrations of Imperfections in Crystalline Solids," *Solid State Physics,* vol. 3, pp. 307-435, 1956.

[371] J. Zhao *et al.*, "Oxygen vacancy induced electronic structure variation in the $La_{0.2}Sr_{0.8}MnO_3$ thin film," *AIP Advances,* vol. 9, pp. 055208-1-055208-6, 2019.

[372] Z. Tian *et al.*, "Towards thermal barrier coating application for rare earth silicates RE_2SiO_5 (RE = La, Nd, Sm, Eu, and Gd)," *Journal of the European Ceramic Society,* vol. 39, pp. 1463-1476, 2019.

[373] D. J. Morgan, "Photoelectron spectroscopy of ceria: Reduction, quantification and the myth of the vacancy peak in XPS analysis," *Surface and Interface Analysis,* vol. 55, pp. 845–850, 2023, doi: DOI: 10.1002/sia.7254.

[374] L. Yue, H. Pu, S. Pang, H. Li, and Q. Zhang, "Top-gate LZTO thin-film transistors with PMMA gate insulator by solution process," *Europhysics Letters (EPL),* vol. 97, pp. 67006-p1-67006-p5, 2012, doi: doi: 10.1209/0295-5075/97/67006.

[375] T.-M. Pan and W.-S. Huang, "Physical and electrical characteristics of a high-k Yb_2O_3 gate dielectric," *Applied Surface Science,* vol. 255, pp. 4979-4982, 2009.

[376] T. M. Project. "Materials Data on SiO_2 by Materials Project " Lawrence Berkeley National Lab. (LBNL) and U.S. Department of Energy Office of Scientific and Technical Information (USDOE Office of Science, BES). (accessed.

[377] O. C. Gagné and F. C. Hawthorne, "Bond-length distributions for ions bonded to oxygen: alkali and alkaline-earth metals," *Acta Crystallographica Section B: Structural Science, Crystal Engineering and Materials,* vol. 72, no. Pt 4, pp. 602-625, 2016.

[378] T. M. Project. "Materials Data on Lu_2O_3 by Materials Project." Lawrence Berkeley National Lab. (LBNL) and U.S. Department of Energy Office of Scientific and Technical Information (USDOE Office of Science, BES). (accessed 2023).

[379] T. M. Project. "Materials Data on Yb_2O_3 by Materials Project." Lawrence Berkeley National Lab. (LBNL) and U.S. Department of Energy Office of Scientific and Technical Information (USDOE Office of Science, BES). (accessed 2023).

[380] T. M. Project. "Materials Data on Er_2O_3 by Materials Project." Lawrence Berkeley National Lab. (LBNL) and U.S. Department of Energy Office of Scientific and Technical Information (USDOE Office of Science, BES). (accessed 2023).

[381] Y. Li, J. Wang, and J. Wang, "Theoretical investigation of phonon contributions to thermal expansion coefficients for rare earth monosilicates RE2SiO5 (RE = Dy, Ho, Er, Tm, Yb and Lu)," *Journal of the European Ceramic Society,* vol. 40, pp. 2658-2666, 2020.

[382] A. Abdul-Aziz and A. C. Wroblewski, "Durability Analysis and experimental Validation of Environmental Barrier Coating (EBC) Performance Using Combined Digital Image Correlation and NDE," *Coatings,* vol. 6, no. 70, pp. 1-10, 2016.

[383] P. R. Gradl, "Digital Image Correlation Techniques Applied to Large Scale Rocket Engine Testing," *American Institute of Aeronautics and Astronautics,* pp. 1-17, 2016.

[384] P. Gradl, "Optical Measurement Techniques for Rocket Engine Testing and Component Applications: Digital Image Correlation and Dynamic Photogrammetry," NASA Marshall Space Flight Center, Alabama, USA, 2016.

[385] C.-y. Hsu *et al.*, "In-situ measurement of SiC/Si interfacial tensile strength of reaction bonded SiC/Si composite," *Composites Part B,* vol. 175, pp. 107116-107123, 2019.

[386] Q. Zhang and X.-P. Zhang, "The crack nature analysis of primary and secondary cracks: A numerical study based on moment tensors," *Engineering Fracture Mechanics,* vol. 210, pp. 70-83, 2019.

[387] X. Chen, D. Peng, J. P. Morrissey, and J. Y. Ooi, "A comparative assessment and unification of bond models in DEM simulations," *Granular Matter,* vol. 24, no. 29, pp. 1-20, 2022, doi: https://doi.org/10.1007/s10035-021-01187-2.

[388] N. Y. Wong, "Crack Coalescence in Molded Gypsum and Carrara Marble," Doctor of Philosophy (PhD), Department of Civil and Environmental Engineering, Massachusetts Institute of Technology, United States, 2008.

[389] E. Eberhardt, B. Stimpson, and D. Stead, "Effects of Grain Size on the Initiation and Propagation Thresholds of Stress-induced Brittle Fractures," *Rock Mechanics and Rock Engineering,* vol. 32, no. 2, pp. 81-99, 1999.

[390] T. Whitlow, E. Jones, and C. Przybyla, "In-situ damage monitoring of a SiC/SiC ceramic matrix composite using acoustic emission and digital image correlation," *Composite Structures,* vol. 158, pp. 245-251, 2016.

[391] T. T. Ngo, J. K. Park, and D. J. Kim, "Loading rate effect on crack velocity in ultra-high-performance fiber-reinforced concrete," *Construction and Building Materials,* vol. 197, pp. 548-558, 2019.

[392] X. X. Zhang, R. C. Yu, G. Ruiz, M. Tarifa, and M. A. Camara, "Effect of loading rate on crack velocities in HSC," *International Journal of Impact Engineering,* vol. 37, pp. 359-370, 2010.

[393] J. Pittari, G. Subhash, J. Zheng, V. Halls, and P. Jannotti, "The rate-dependent fracture toughness of silicon carbide- and boron carbide-based ceramics," *Journal of the*

European Ceramic Society, vol. 35, no. 16, pp. 4411-4422, 2015, doi: 10.1016/j.jeurceramsoc.2015.08.027.

[394] J. P. III, G. Subhash, A. Trachet, J. Zheng, V. Halls, and P. Karandikar, "The Rate-Dependent Response of Pressureless-Sintered and Reaction bonded Silicon Carbide-Based Ceramics," *International Journal of Applied Ceramics Technology,* vol. 12, no. S2, pp. E207-E216, 2015.

[395] J. Bu, X. Chen, L. Hu, H. Yang, and S. Liu, "Experimental Study on Crack Propagation of Concrete Under Various Loading Rates with Digital Image Correlation Method," *International Journal of Concrete Structures and Materials,* vol. 14, no. 25, pp. 14-25, 2020, doi: https://doi.org/10.1186/s40069-020-00400-5.

[396] P. Forquin, "An optical correlation technique for characterizing the crack velocity in concrete," *The European Physical Journal Special Topics* vol. 206, pp. 89–95, 2012, doi: 10.1140/epjst/e2012-01590-6.

[397] F. Liebold, A. A. Heravi, O. Mosig, Manfred Curbach, V. Mechtcherine, and H.-G. Maas, "Crack Propagation Velocity Determination by High-speed Camera Image Sequence Processing," *Materials,* vol. 13, pp. 4415-4430, 2020, doi: doi:10.3390/ma13194415.

[398] M. E. Launey *et al.*, "Designing highly toughened hybrid composites through nature-inspired hierarchical complexity," *Acta Materialia,* vol. 57, pp. 2919–2932, 2009, doi: http://10.1016/j.actamat.2009.03.003.

[399] J. Delage, "Fracture behaviour of SiC/SiC ceramic matrix composite," Doctor of Philosophy, Department of Mechanical Engineering, Imperial College London, United Kingdom, 2022.

[400] G. D. Quinn, "NIST Recommended Practice Guide: Fractography of Ceramics and Glasses," National Institute of Standards and Technology, Special Publication 960-16e3, 2020. [Online]. Available: https://www.nist.gov/publications/nist-recommended-practice-guide-fractography-ceramics-and-glasses-3rd-edition

[401] V. M. F. Évora, N. Jain, and A. Shukla, "Stress Intensity Factor and Crack Velocity Relationship for Polyester/TiO2 Nanocomposites," *Experimental Mechanics,* vol. 45, pp. 153-159, 2005.

[402] K. H. Schwalbe, J. D. Landes, and J. Heerens, "7.02 - Classical Fracture Mechanics Methods," in *Comprehensive Structural Integrity*, I. Milne, R. O. Ritchie, and B. Karihaloo Eds., no. 7): Elsevier Science, 2003, pp. 3-42.

[403] J. M. Krafft and G. R. Irwin, "Crack velocity considerations, Fract Toughness Testing and Its Applications," ASTM STP, United States, 1965, vol. 381.

[404] W. L. F. J.W. Dally, G.R. Irwin, , "On the uniqueness of stress intensity factor-crack velocity relationship," *International Journal of Fracture,* pp. 159–168, 1985.

[405] S. Pyo, M. Alkaysi, and S. El-Tawil, "Crack propagation speed in ultra high performance concrete (UHPC)," *Construction and Building Materials,* vol. 114, pp. 109-118, 2016.

[406] J. R. Kermode *et al.*, "Low-speed fracture instabilities in a brittle crystal," *Nature Letters,* vol. 455, pp. 1224-1228, 2008, doi: doi:10.1038/nature07297.

[407] X.-K. Zhu and J. A. Joyce, "Review of fracture toughness (G, K, J, CTOD, CTOA) testing and standardization," *Engineering Fracture Mechanics,* vol. 85, pp. 1–46, 2012, doi: https://doi.org/10.1016/j.engfracmech.2012.02.001.

[408] W. L. Khor, P. Moore, H. Pisarski, and C. Brown, "Comparison of methods to determine CTOD for SENB specimens in different strain hardening steels," *Fatigue and Fracture of Engineering Materials and Structures,* vol. 41, pp. 551–564, 2018, doi: 10.1111/ffe.12718.

[409] *ASTM E1820–20 Standard Test Method for Measurement of Fracture Toughness*, A. S. f. T. a. M. (ASTM), USA, 2020.

[410] A. S. f. T. a. M. (ASTM), "ASTM C1327 - Standard Test Method for Vickers Indentation Hardness of Advanced Ceramics," American Society for Testing and Materials (ASTM), United States, 2015.

[411] J. Blaber, B. Adair, and A. Antoniou, "Ncorr: Open-Source 2D Digital Image Correlation Matlab Software," *Experimental Mechanics,* vol. 55, pp. 1105-1122, 2015.

[412] H. Remesan and M. Ramji, "Adaptation of Open Source 2D DIC Software Ncorr for Solid Mechanics Applications," presented at the 9th International Symposium on Advanced Science and Technology in Experimental Mechanics, New Delhi, India, 2014.

[413] X. Fan, X. Deng, W. Mao, Z. Luo, W. Ye, and C. Dai, "In situ characterization of high-temperature mechanical behaviors of freestanding Si, BSAS and Yb_2SiO_5 environmental barrier coatings by three-point bending tests based on digital image correlation," *Results in Surfaces and Interfaces,* vol. 12, pp. 1-14, 2023.

[414] K. E. Shafei and N. A. Nasiri, "Oxidation of reaction-bonded silicon carbide-boron carbide in air," *Ceramics International,* vol. 47, 2021.

[415] T. Chen, C. M. Harvey, S. Wang, and V. V. Silberschmidt, "3 - Dynamic interfacial fracture," in *Dynamic Deformation, Damage and Fracture in Composite Materials and Structures*, V. Silberschmidt Ed., no. Composites Science and Engineering): Elsevier 2023, pp. 29-87.

[416] *Fracture mechanics toughness tests — Part 1: Method for determination of K_{Ic}, critical CTOD and critical J values of metallic materials*, B. Standard, United Kingdom, 1991.

[417] W. Khor, "Crack Tip Opening Displacement (CTOD) in Single Edge Notched Bend (SEN(B))," Doctor of Philosophy, Brunel University London, London, 2018.

[418] *WES 1108 Standard test method for crack-tip opening displacement fracture toughness measurement*, T. J. W. E. Society, Japan, 2016.

[419] M. Rui, Y. Zhang, and J. Ye, "Environment-Friendly Preparation of Reaction-Bonded Silicon Carbide by Addition of Boron in the Silicon Melt," *Materials,* vol. 14, pp. 1090-1099, 2021.

[420] E. S. Antonova, N. A. Golubeva, I. Y. Kelina, L. A. Plyasunkova, T. E. Stakhrovskaya, and A. S. Nechepurenko, "Effect of Original Powder Mixture Fractional Composition and Dispersion on Reaction-Bonded Silicon Carbide Physicomechanical Properties," *Refractories and Industrial Ceramics,* vol. 55, pp. 409-413, 2015.

[421] S. P. Lee *et al.*, "High temperature characterization of reaction sintered SiC based materials," *Journal of Nuclear Materials,* vol. 329, pp. 534-538, 2004.

[422] M. Wilhelm, M. Kornfeld, and W. Wruss, "Development of SiC-Si composites with fine-grained SiC microstructures," *Journal of European Ceramic Society,* vol. 19, pp. 2155-2163, 1999.

[423] G. N. Morscher, "Stress-dependent matrix cracking in 2D woven SiC-fiber reinforced melt-infiltrated SiC matrix composites," *Composites Science and Technology,* vol. 64, no. 9, pp. 1311-1319, 2004.

[424] Z. P. Bažant and R. Gettu, "Rate effects and load relaxation in static fracture of concrete," *ACI Materials Journal,* vol. 89, no. 5, pp. 456–68, 1992, doi: https://doi.org/10.14359/2400.

[425] B. Mahanta, A. Tripathy, V. Vishal, T. N. Singh, and P. G. Ranjith, "Effects of strain rate on fracture toughness and energy release rate of gas shales," *Engineering Geology,* vol. 218, no. 23, pp. 39–49, 2017, doi: https://doi.org/10.1016/j.enggeo.2016.12.008.

[426] Z. X. Zhang, S. Q. Kou, J. Yu, Y. Yu, L. G. Jiang, and P.-A. Lindqvist, "Effects of loading rate on rock fracture," *International Journal of Rock Mechanics and Mining Sciences,* vol. 36, no. 5, pp. 597–611, 1999, doi: https://doi.org/10.1016/S0148-9062(99)00031-5.

[427] Q. B. Zhang and J. Zhao, "Effect of loading rate on fracture toughness and failure micromechanisms in marble," *Engineering Fracture Mechanics,* vol. 102, pp. 288–309, 2013, doi: https://doi.org/10.1016/j.engfracmech.2013.02.009.

[428] Y. Xing, B. Huang, E. Ning, L. Zhao, and F. Jin, "Quasi-static loading rate effects on fracture process zone development of mixed-mode (I-II) fractures in rock-like materials," *Engineering Fracture Mechanics,* vol. 240, pp. 107365-107382, 2020, doi: https://doi.org/10.1016/j.engfracmech.2020.107365.

[429] P. Jannotti, G. Subhash, J. Zheng, and V. Halls, "Measurement of microscale residual stresses in multi-phase ceramic composites using Raman spectroscopy," *Acta Materialia,* vol. 129, pp. 482-491, 2017.

[430] K. Kollins, C. Przybyla, and M. S. Amer, "Residual stress measurements in melt infiltrated SiC/SiC ceramic matrix composites using Raman spectroscopy," *Journal of the European Ceramic Society,* vol. 38, pp. 2784-2791, 2018.

[431] K. Detwiler, R. Hunt, and E. Opila, "In-situ observation of micro-cracking in a SiC/BN/SiC ceramic matrix composite under tension," *Open Ceramics,* vol. 14, pp. 100366-100374, 2023.

[432] B. L. Wing, "Residual Stresses and Oxidation of Silicon Carbide Fiber Reinforced Silicon Carbide Composites," Doctor of Philosophy, Material Science and Engineering, University of Michigan, United States, 2016.

[433] V. I. Ivashchenko, P. E. A. Turchi, and V. I. Shevchenko, "Simulations of the mechanical properties of crystalline, nanocrystalline, and amorphous SiC and Si," *Physical Review. B,* vol. 75, pp. 085209-1-085209-11, 2007.

[434] J. R. Kermode *et al.*, "Low-speed fracture instabilities in a brittle crystal," *Nature Letters,* vol. 455, pp. 1224-1228, 2008, doi: doi:10.1038/nature07297.

[435] I. H. Lin and R. C. Thomson, "Dislocation emission, and shielding for cracks under general loading," *Acta Materialia,* pp. 187-206, 1986.

[436] J. A. Dean, "Section 4 - Properties of Atoms, Radical, and Bonds," in *Lange's Handbook of Chemistry* United States of America: McGraw- Hill, Inc., 1999, pp. 4.1-4.84.

[437] T. Williams, "Development of Pressureless Sintered Silicon Carbide-Boron Carbide Composites for Armour Applications," Engineering Doctorate Department of Materials (Micro and Nano Materials and Technologies), University of Surrey, United Kingdom, 2015.

[438] M. Lodhe, N. Chawake, D. Yadav, and M. Balasubramanian, "On correlation between β→α transformation and densification mechanisms in SiC during spark plasma sintering," *Scripta Materialia,* vol. 115, pp. 137-140, 2016.

[439] C. J. Gilbert, J. J. Cao, L. C. D. Jonghe, and R. O. Ritchie, "Crack-Growth Resistance-Curve Behavior in Silicon Carbide: Small versus Long Cracks," *Journal American Ceramic Society,* vol. 80, no. 9, pp. 2253-2261, 1997.

[440] S. Hayun, M. P. Dariel, N. Frage, and E. Zaretsky, "The high-strain-rate dynamic response of boron carbide-based composites: The effect of microstructure," *Acta Materialia,* vol. 58, pp. 1721–1731, 2010, doi: http://doi:10.1016/j.actamat.2009.11.014.

[441] S. Hayun, D. Rittel, N. Frage, and M. P. Dariel, "Static and dynamic mechanical properties of infiltrated B_4C–Si composites," *Materials Science and Engineering A,* vol. 487, pp. 405-409, 2008, doi: http://doi:10.1016/j.msea.2007.11.062.

[442] T. J. Vogler, W. D. Reinhart, and L. C. Chhabildas, "Dynamic behavior of boron carbide," *Journal of Applied Physics,* vol. 59, no. 8, pp. 4173-4183, 2004, doi: http://0021-8979/2004/95(8)/4173/11/$22.00.

[443] D. E. Grady, "Dynamic Properties of Ceramic Materials," Sandia National Laboratories, California, USA, SAND94-3266, 1995.

[444] D. Sherman, "Macroscopic and microscopic examination of the relationship between crack velocity and path and Rayleigh surface wave speed in single crystal silicon," *Journal of the Mechanics and Physics of Solids,* vol. 53, pp. 2742-2757, 2005.

[445] P. C. Paris, H. Tada, A. Zahoor, and H. Ernst, "The Theory of Instability of the Tearing Mode of Elastic-Plastic Crack Growth," in *ASTM STP 668– Elastic-Plastic Fracture*, Atlanta, Georgia, USA, J. D. Landes, J. A. Begley, and G. A. Clarke, Eds., 1977, pp. 5-36.

[446] S. R. Novak, "ASTM STP 591 - Resistance to Plane-Stress Fracture (R-Curve Behavior) of A572 Structural Steel," presented at the Eighth National Symposium on Fracture Mechanics, Brown University, USA, 1974.

[447] J. M. Barsom, J. F. Sovak, and S. R. Novak, "AISI Project 168–Toughness Criteria for Structural Steels: Fracture Toughness of A572 Steels," U. S. Steel Research Laboratory, USA, 97.021-001(2), 1972.

[448] V. Naglieri, A. P. Tomsia, R. O. Ritchie, and B. Gludovatz, "Developing strength and toughness in bio-inspired silicon carbide hybrid materials containing a compliant phase," *Acta Materialia,* vol. 98, pp. 141-151, 2015, doi: http://DOI:10.1016/j.actamat.2015.07.022.

[449] O. Kolednik, "Load Control vs. Displacement Control – Their Infleunce on the J-Resistance Curve," presented at the ECF8 Fracture Behavior and the Design of Materials and Structures, Torino, Italy, 1990.

[450] G. N. Morsch and J. Hurst, "Stress-Rupture and Stress-Relaxations of SiC/SiC Composites at Imtermediate Temperature " in *25th Annual Conference on Composites, Advanced Ceramics, Materials, and Structures: A: Ceramic Engineering and Science Proceedings*, M. Singh and T. Jessen, Eds., 2001, vol. 22: The American Ceramic Society, doi: https://doi.org/10.1002/9780470294680.ch62.

[451] G. N. Morscher, "Growth of Matrix Cracks During Intermediate Temperature Stress Rupture of a SiC/SiC Composite in Air,," in *21st Annual Conference on Composites, Advanced Ceramics, Materials, and Structures: A: Ceramic Engineering and Science Proceedings*, 2000 2001, vol. 21, no. 3, pp. 423-431.

[452] C. J. Gilbert, J. J. Cao, W. J. Moberylchan, L. C. Dejonghe, and R. O. Ritchie, "Cyclic Fatigue and Resistance-Curve Behavior of an Insitu Toughened Silicon Carbide with Al-B-C Additions," *Acta Metallurgica et Materialia,* vol. 44, no. 8, pp. 3199-3214, 1996.

[453] C. J. Gilbert and R. O. Ritchie, "On the Quantifications of Bridging Tractions During Subcritical Crack Growth Under Monotonic and Cyclic Fatigue Loading in a Grain-Bridging Silicon Carbide Ceramic," *Acta Materialia,* vol. 46, no. 2, pp. 609-616, 1998.

[454] S. K. Lee, Y. C. Kim, and C. H. Kim, "Microstructural development and mechanical properties of pressureless-sintered SiC with plate-like grains using AI_2O_3-Y_2O_3 additives," *Journal of Materials Science,* vol. 29, pp. 5321-5326, 1994.

[455] N. Innovations. "ND-DC Dip Coater." https://nadetech.com/products/dip-coating/nd-dc (accessed December, 2023).

[456] R. O. Ritchie, "Failure of Silicon: Crack Formation and Propagation," in *13th Workshop on Crystalline Solar Cell Materials and Processes*, Colorado, USA, 2003: Berkeley Lab, p. 42.

[457] X. Li *et al.*, "Measurement for fracture toughness of single crystal silicon film with tensile test," *Sensors and Actuators A,* vol. 119, pp. 229–235, 2005, doi: 10.1016/j.sna.2003.10.063.

[458] R. W. Jackson and M. R. Begley, "Critical cooling rates to avoid transient-driven cracking in thermal barrier coating (TBC) systems," *International Journal of Solids and Structures,* vol. 51, no. 6, pp. 1364-1374, 2014, doi: https://doi.org/10.1016/j.ijsolstr.2013.12.029.

[459] M. Begley. "LayerSlayer: Multilayer Analysis Suite." University of California Santa Barbara. https://sites.engineering.ucsb.edu/~begley/LayerSlayer.html (accessed 2024).

[460] M. R. Begley and J. W. Hutchinson, *The Mechanics and Reliability of Films, Multilayers and Coatings*. United Kingdom: Cambridge University Press, 2017, p. 276.